Large Eddy Simulation of In-Cylinder Phenomena
in
Spark Ignition Engines

Von der Fakultät für Ingenieurwissenschaften, Abteilung Maschinenbau und Verfahrenstechnik

der

Universität Duisburg-Essen

zur Erlangung des akademischen Grades

eines

Doktors der Ingenieurwissenschaften

Dr.-Ing.

genehmigte Dissertation

von

Peter Robert Janas
aus
Zabrze (Polen)

Gutachter: Univ.-Prof. Dr.-Ing. Andreas M. Kempf
Univ.-Prof. Dr.-Ing. Christian Hasse
Tag der mündlichen Prüfung: 22.08.2017

Vorwort / Danksagung

Die vorliegende Arbeit entstand während meiner Tätigkeit als wissenschaftlicher Mitarbeiter am Lehrstuhl für Fluiddynamik an der Universität Duisburg-Essen in den Jahren 2012 bis 2016.

Meinem Doktorvater Herrn Prof. Dr.-Ing. Andreas Kempf danke ich für die wertvollen Anregungen zu dieser Arbeit, die vielen konstruktiven Gespräche und die jederzeit gewährte hervorragende Unterstützung bei der Durchführung und Abfassung. Herrn Prof. Dr.-Ing. Christian Hasse möchte ich für die Übernahme des Korreferates und die kritische Durchsicht meiner Arbeit danken. Weiterhin gilt mein Dank dem Vorsitzenden der Prüfungskommission, Herrn Prof. Dr.-Ing. Rüdiger Deike, sowie dem Mitprüfer, Herrn Prof. Dr. Burak Atakan.

Das Ergebnis dieser Arbeit konnte ohne das Mitwirken einer Vielzahl von Personen nicht realisiert werden. An dieser Stelle möchte ich mich zunächst beim Herrn Dr. Irenäus Wlokas bedanken, der mir immer mit Rat und Tat während meiner Promotion, aber auch im privaten Leben, zur Seite stand. Herrn Olaf Hasemann danke ich für seine Unterstützung bei programmiertechnischen Problemen und das offene Ohr für Fragestellungen rund um die Informatik. Ich möchte mich für die stets konstruktiven sowie fachlichen Gespräche bei Dr. Thuong Nguyen bedanken, mit dem ich auch auf zahlreichen Konferenzen eine sehr tolle Zeit verbracht habe. Herrn Prof. Dr. Tommaso Lucchini und Herrn Prof. Dr. Sebastian Kaiser danke ich für die fachlichen Diskussionen über Verbrennungsmotoren. Darüber hinaus möchte ich mich bei allen Teilnehmern des Darmstadt Engine Workshops bedanken. Insbesondere danke ich Prof. Dr. Andreas Dreizler, Dr. Benjamin Böhm und Dr. Brian Peterson.

Weiterhin möchte ich mich bei allen wissenschaftlichen und technischen Mitarbeiterinnen und Mitarbeitern des Lehrstuhles Fluiddynamik für die angenehme Arbeitsatmosphäre sowie den themenübergreifenden Austausch, welcher einen wichtigen Beitrag zum Gelingen dieser Arbeit geleistet hat, bedanken. Insbesondere gilt mein Dank Herrn Patrick Wollny, Herrn Andreas Rittler und Herrn Timo Lipkowicz. Nejra Sikalo danke ich für das Lesen, die Korrekturen und Verbesserungen der Arbeit. Des Weiteren möchte ich mich bei den Studenten, die innerhalb ihrer Abschlussarbeiten und Tätigkeit am Lehrstuhl wichtige Beiträge zu dieser Arbeit geleistet haben, bedanken.

Abschließend bedanke ich mich im Besonderen bei meinen Eltern, meinem Bruder Marius und meiner Frau Teruko, die mich zu jeder Zeit unterstützt haben.

Duisburg, September 2017

Abstract

The motivation for this thesis is the development of a simulation tool that can deliver spatially- and time-resolved information to better understand the highly unsteady and irregular flow motion and combustion inside spark ignition engines. The key element of the method is that the large eddies are directly solved on the computational grid and the smaller structures are modelled, i.e. large eddy simulation (LES). High order numerical schemes for an accurate solution are applied, which are still not state-of-the-art for most of the industrially relevant problems. The simulation tool is integrated into an existing open source software and is successfully validated against Particle Image Velocimetry (PIV) and Magnetic Resonance Velocimetry (MRV) measurements of optically accessible research engines. A generic simulation workflow based on a mapping-strategy is proposed with a mesh-morphing strategy without topological changes in-between the mapping intervals. The simulation workflow includes an automated grid generation for complex engine geometries with inclined valves and the piston top-land crevice. It is applied to three different engine geometries.

A criterion is established for estimating the number of cycles needed in a simulation, if experimental data is available. A visualization strategy is developed and an analysis for the tumble flow based on auto-correlation coefficients is proposed, which allows quantifying the tumble break-down process. The tumble visualization and quantification methods are used to study the sensitivity of the turbulent flow field based on cold-flow multi-cycle simulations of two different cylinder-head geometries.

In a next step, the flow fields of the two different cylinder-head geometries are taken to study the flame propagation by a flame-surface-density modelling approach with different algebraic expressions for the flame wrinkling. Furthermore, fired multi-cycle simulations with internal exhaust gas recirculation are carried out and compared to Mie-scattering images of the flame propagation of the corresponding engine. Finally, undesirable combustion phenomena are studied, like the flame propagation into the piston top-land crevice, which is known as a source for unburnt hydrocarbons.

The developed tool opens the door for high resolution simulations of internal combustion engines.

Zusammenfassung

Ziel dieser Dissertation war die Erarbeitung eines Simulationsmodells, welches räumlich- und zeitaufgelöste Informationen in der Brennkammer eines Ottomotors zur Verfügung stellen kann. Dabei entstand ein Simulationswerkzeug, das in einer bereits vorhandenen, quellfreien Simulationssoftware integriert und erfolgreich mit diversen experimentellen Daten von optisch zugänglichen Motoren validiert werden konnte. Kernstück des Modells ist das direkte Auflösen der großskaligen Wirbel, sowie die gleichzeitige Modellierung kleinerer Wirbelstrukturen. Hierbei erfolgt die Modellierung unter Berücksichtigung der geforderten hohen Qualitätskriterien aus dem akademischen Bereich, wie bspw. die Nutzung von numerischen Diskretisierungsschemata höherer Ordnung. Die Simulationsergebnisse der Zylinderinnenströmung konnten erfolgreich mittels PIV (Particle Image Velocimetry) und MRV (Magnetic Resonance Velocimetry) Messungen an optischen Versuchsmotoren validiert werden.
Um einen vollständigen Motorenzyklus zu simulieren, wurde ein generischer Simulations-Workflow entwickelt. Hierzu wird der Motorenzyklus in Teilintervale zerlegt. Innerhalb der Intervalle werden die Rechengitter abhängig von der Kolben- und Ventilbewegung verzerrt. Das hierheraus resultierende Simulationsergebnis wird für ein neues Intervall auf ein neues unverzerrtes Rechennetz interpoliert. Diese Vorgehensweise wird solange wiederholt bis der gesamte Zyklus beendet ist. Die Erstellung der Rechengitter für die einzelnen Teilintervalle erfolgt automatisiert. Mittels dieser Simulationsstrategie konnten drei unterschiedliche Zylinderkopfgeometrien mit Zündkerzen und Feuerstegen erfolgreich simuliert werden.
Zur Quantifizierung des Tumblewirbelzerfalls wurde ein Kriterium basierend auf Autokorrelationsfunktionen des Strömungsfeldes erarbeitet. Zusätzlich wurde ein Kriterium für die erforderliche Anzahl der zu simulierenden Zyklen entwickelt. Mithilfe einer Visualisierungsstrategie für den Tumblewirbel von nicht-reaktiven Mehrzyklen-Rechnungen konnten zwei unterschiedliche Zylinderkopfgeometrien im Detail analysiert werden. Im Weiteren erfolgte die Auswertung des Simulationsergebnisses respektive des Strömungsfeldes der zwei unterschiedlichen Zylinderkopfgeometrien. Hierzu wurde der Flame-Surface-Density (FSD) Ansatz unter Verwendung unterschiedlicher algebraischer Modelle zur Bestimmung der Flammenfaltung genutzt. Darüber hinaus wurden vollständige Mehrzyklen-Simulationen unter Berücksichtigung der inneren Abgasrückführung und des Restgasanteils aus den vorherigen Zyklen realisiert. Die Simulationsergebnisse wurden mit experimentellen Mie-Streumessungen der Flammenausbreitung verglichen bzw. validiert. Abschließend erfolgte die Untersuchung der Flammenausbreitung in dem Feuersteg, welcher durch die ungewöhnlich tief angeordneten Kolbenringe zu einem sehr großen Quetschspalt zwischen Kolbenhemd und Zylinderwand führt. Diese geometrische Anordnung ist als eine der bekannten Ursachen für unverbrannte Kohlenwasserstoffe zu sehen.
Die Implementierung des Simulationswerkzeugs in eine quellfreie Simulationsumgebung ermöglicht die Berechnung von ottomotorischen Verbrennungsprozessen auf Großrechnerarchitekturen.

Contents

Nomenclature

Lower case latin symbols

a	Coefficients of the linearized system of equations	–
c	Progress variable	–
c_p	Specific heat capacity at constant pressure	$J/(kgK)$
d_q	Two-wall quench distance	m
e_s	Specific sensible internal energy	m^2kg/s^2
f	Interpolation function	–
f_t	Fuel mass fraction	–
g_i	Gravity vector	m/s^2
h	Absolute specific enthalpy	J/kg
h_s	Specific sensible enthalpy	J/kg
k	User defined coefficient for the Sweby limiter	–
k_{sgs}	Sub-grid scales turbulent kinetic energy	m^2/s^2
l	Length to the moving boundaries	m
l_δ	Inner layer thickness	m
l_η	Kolmogorov length scale	m
l_F	Laminar flame thickness	m
l_I	Integral length scales	m
m_a	Mass of air	kg
n_f	Face normal vector	–
n_R	Number of crank revolutions per power stroke	–
p	Pressure	Pa
p_c	Probability density function for Keppeler model	–
p_{ref}	Reference pressure	Pa
q_r	Radiation	W
r	Consecutive gradient	–
t	Time	s
t_I	Eddy turnover time	s
u'_Δ	Sub-grid velocity fluctuations	m/s
$u_{\text{cell,i}}$	Cell velocity vector	m/s
u_i	Velocity vector	m/s
u_η	Turnover velocity of the smallest eddies	m/s
$x_{\text{cell,i}}$	Cell displacement vector	m

Upper case latin symbols

A_s	Sutherland coefficient	–
A_t	Total flame surface	m^2
B_2	Factor for the calculation of the laminar flame velocity	–
B_M	Factor for the calculation of the laminar flame velocity	–

C_ϵ	Constant for compressible Smagorinsky model	–
$C_{\text{res}}, C_{\text{sgs}}$	Resolved and modelled curvature of flame surface density	$1/(ms)$
C_D	Model constant for the Keppeler model	–
C_k	Constant for compressible Smagorinsky model	–
C_R	Model constant for the Keppeler model	–
C_S	Smagorinsky model constant	–
D	Fractal dimension	–
D_k	Diffusion coefficient of the species k	m/s^2
F	Polynomial function for the Keppeler model	–
F/A	Fuel-to-air ratio	–
F_x	Convective face flux in x-direction	kg/s
$J_{i,k}$	Diffusive mass flux of the species k in i-direction	$kg/(m^2 s)$
L	Characteristic length scale	m
N	Crank shaft rotational speed	rpm
N_c	Number of cycles	–
P	Production of flame surface density	$1/(ms)$
P_{in}	Indicated power	kW
Q_{HV}	Fuel heating value	MJ/kg
R	Universal gas constant	$J/(mol\ K)$
S	Rate of strain tensor	$1/s$
S_ϕ	Source term	–
S_d	Displacement velocity	m/s
$S_{L,0}$	Unstrained laminar flame velocity	m/s
S_L	Laminar flame velocity	m/s
T	Temperature	K
$T_{\text{res}}, T_{\text{sgs}}$	Resolved and modelled transport of flame surface density	$1/(ms)$
T_s	Sutherland temperature	K
$T_{u,ref}$	Unburnt reference temperature	K
T_u	Unburnt temperature	K
V	Volume	m^3
V_{kernel}	Volume of flame kernel	m^3
W	Mean molecular weight	kg/mol
Y_k	Mass fraction of species k	–
Y_{air}	Residual gas mass fraction of air	–
Y_{burnt}	Residual gas mass fraction of burnt products	–
Y_{fuel}	Residual gas mass fraction of fuel	–
Y_{igr}	Residual gas mass fraction	–

Lower case greek symbols

α	Thermal diffusivity	m^2/s
δ	Piston clearance	m
δ_l	Laminar flame thickness	m
δ_t	Turbulent flame thickness	m
δ_{ij}	Kronecker delta	–
δ_{PE}	Distance vector between point P and E	m
δ_{Pe}	Distance vector between point P and face e	m
$\dot{\omega}_k$	Chemical reaction rate of the species k	$kg/(m^3 s)$
ϵ	Turbulent dissipation	m^2/s^3
ϵ_0	Outer cut-off length	m

ϵ_{sgs}	Turbulent sub-grid dissipation	m^2/s^3
ϵ_i	Inner cut-off length	m
η	Kolmogorov scale	m
γ	Cell motion diffusion constant	–
γ	Factor for the calculation of the laminar flame velocity	–
λ	Thermal heat conductivity	$W/(m^2K)$
λ_{st}	Stoichiometric air to fuel ratio	–
μ	Dynamic viscosity	$kg/(s\ m)$
μ_t	Turbulent dynamic viscosity	$kg/(s\ m)$
ν	Kinematic viscosity	m^2/s
ν_t	Turbulent kinematic viscosity	m^2/s
ϕ'	Fluctuations of an arbitrary scalar ϕ	–
ϕ'_{rms}	Standard deviation of an arbitrary scalar ϕ	–
ρ	Density	kg/m^3
σ_c	Correction factor for ECFM-LES model	–
σ_i	Singular values	–
τ_η	Kolmogorov time scale	s
τ_{ij}	Anisotropic shear stress tensor	Pa
τ_{kk}	Isotropic shear stress tensor	Pa
θ_{no}	Non-orthogonal angle of the cell interface	–

Upper case greek symbols

Δ	Filter width	m
Γ_ϕ	General diffusion constant	m^2/s
$\hat{\Delta}$	Combustion filter width	m
Φ	Equivalence ratio	–
$\Phi(r)$	Weighting coefficient for a TVD-scheme	–
Ψ	Compressibility	m^2/s^2
Σ	Flame surface density	$1/m$
Θ	Crank angle	–
Θ	Model constant for the Keppeler model	–

Subscripts

E, e	East cell and east face
EA	Ensemble averaged
f	Face
int	Intersection
max	Ensemble averaged
N	Neighbour cell
P	Depending cell
res	Resolved
S	Surface
s	Source
sgs	Sub-grid scale
t	Target
V	Volume
W, w	West cell and west face

Superscripts

^{o}	Old time level $n-1$
^{oo}	Old time level $n-2$
n	Current time level

Operators

$\overline{\phi}$	LES-filtered
$\widetilde{\phi}$	Favre-filtered
$\langle\phi\rangle$	Time averaged
∇	Vector differential operator
∂	Partial derivative

Dimensionsless numbers

Da	Damköhler-number
Ka	Karlowitz-number
Le_η	Lewis-number
Ma	Mach-number
Re	Reynolds-number
Re_η	Kolmogorov Reynolds-number
Sc	Schmidt-number

Abbreviations

AKTIM	Arc and Kernel Tracking Ignition Model
ATF	Artificially Thickened Flame
BDC	Bottom Dead Centre
CCV	Cycle-to-Cycle Variatons
CDS	Central Differencing Scheme
CFD	Computational Fluid Dynamics
CFM	Coherent Flame model
CGT	Counter Gradient Transport
COV	Coefficient of Variation
CPU	Central Processing Unit
DNS	Direct Numerical Simulation
ECFM	Extended Coherent Flame model
EVC	Exhaust Valve Closing
EVO	Exhaust Valve Opening
FSD	Flame Surface Density
FVM	Finite Volume Method
HCCI	Homogeneous Charge Compression Ignition
HO	High Order
IGES	Initial Graphics Exchange Specification
IMEP	Indicated Mean Effective Pressure
IVC	Intake Valve Closing
IVO	Intake Valve Opening
LES	Large Eddy Simulation
LHS	Left Hand Side
LIF	Laser Induced Fluorescence
LO	Low Order
MRV	Magnetic Resonance Velocimetry
OpenFOAM	Open Field Operation and Manipulation

PDE	Partial Differential Equations
PIV	Particle Image Velocimetry
POD	Proper Orthogonal Decomposition
RANS	Reynolds Averaged Navier-Stokes
RHS	Right Hand Side
SAS-SST	Scale Adaptive Simulation Shear Stress Transport
SCL	Space Conservation Law
SI	Spark Ignition
STEP	STandard for the Exchange of Product model data
TDC	Top Dead Centre
TFLES	Thickened Flame Model
TUD	Technical University of Darmstadt
TVD	Total Variation Diminishing
UDE	University of Duisburg-Essen
UHC	Unburnt Hydrocarbon Emissions
URANS	Unsteady Reynolds Averaged Navier-Stokes
WALE	Wall Adapting Local Eddy

1

Introduction

1.1 Motivation and background

The internal combustion engine has a long history going back to the year 1891, when Nicholas Otto was the first who applied the concept of the "four stroke combustion engine" in a piston-cylinder assembly. Since then, the combustion engine was continuously improved in terms of engine power output and reduction of pollutant emissions. Nowadays, 1.2 billion [8] vehicles are driving all around the world, powered by thermal engines. Unfortunately, they are contributing to the global warming by emitting CO_2, decreasing the air quality in urban regions and producing noise. Emission regulations aim to control new technologies in order to lower the amount of the hazardous emissions into the environment. These regulations need to be met by the car industry, before they can launch a new car in the market. Some of the recent technologies, which are of key importance to meet today's emission regulations are turbo-charging, down-sizing, low friction in-cylinder materials, variable valve timing and direct injection systems. However, all the necessary technology has made the engine such a complex system, that the margin for further improvements became very small and has finally made the community to look for alternative solutions. The ideal powertrain is meant to be less complex as the conventional combustion engine, while achieving better performance, higher drivability, durability and being environmentally more friendly. A possible solution could be the replacement of thermal engines by electrical motors. They do not emit "any" harmful pollutants directly and produce only a fraction of the noise that a thermal engine produces. They seem to be the solution to the problem, but only if electricity is produced by renewable energy sources, like solar or wind. Furthermore, the capacity and lifetime of the batteries is limited and contributes a significant amount to the full price of the electrical vehicle. Therefore, a pure electrical vehicle will be no global solution to the environmental problem in the short term. However, taking the best of both worlds - combustion engine and electrical motor - can be a smart approach to increase the overall efficiency. Cars that are using a combination of a thermal engine and an electrical motor are called hybrid vehicles. The hybridisation can be seen as a transition technology until the technology for a full electrical vehicle is mature enough and affordable to average people, including a charging station network and energy from renewable sources. Since the full electrification of the vehicle powertrains is not likely to happen soon, the combustion engine and in particular the spark ignition engine, which is also used in most hybrid powertrains, will play a major role in the transportation sector and requires further improvements. Here, a deep understanding of local and time dependent in-cylinder phenomena is of paramount importance to improve the efficiency of today's spark ignition engines and will require high resolution experiments and simulations in space and time, such as large-eddy simulations (LES).

1.2 Literature review on LES for SI-engines

Unstable engine operating conditions such as knock and cyclic variations appear very irregularly and are triggered by local time dependent events, which can be caused by high temperature spots, leading to self ignition, or by undesirable flow conditions in the vicinity of the spark plug. A better understanding of their origins can lead to a higher engine efficiency and lower pollutant emissions, but requires measurement techniques and numerical methods, which allow to resolve in-cylinder physics in space and time. Since experiments inside the combustion chamber are difficult to perform, numerical simulations, such as the large eddy simulation (LES) are becoming more and more popular for engine applications. This trend can be followed in review papers, e.g. by Haworth [85], Drake et al. [49], Rutland [164], or more recently by Fansler et al. [56] and Hasse [82].

Cold-flow engine simulation
First LES simulations of in-cylinder physics were carried out under motored operating conditions. They mainly focused on the validation of the applied strategy and their ability to study cycle-to-cycle variation, as shown by an early work of Haworth et al. [86] in 1996. The first LES, however, of realistic engine geometries were made by Moreau et al. [141] in 2004, who used the AVBP CFD-code [2]. Also for mixing-dominated processes, the great potential of LES to predict the air-fuel-stratification was topic of earlier studies, as shown by Sone et al. in 2001 [175] or later by Goryntsev et al. [75] in 2005. Both of them used KIVA as CFD-code [7]. The awareness of LES, being a predictive tool for studying cycle-to-cycle variations increased with the years, but also raised new questions, for example, which turbulence sub-grid scale model should be used, which numerics and boundary conditions shall be applied, which mesh motion strategy is suitable for the large displacement of the piston and inclination of the valves, what happens at the walls (a notorious weakness of LES) or simply how many cycles need to be calculated. These open questions are addressed in the scope of this thesis (see chapter 6).

The difficulty in studying cycle-to-cycle variations (CCV) lies in the clear distinction between the small scale turbulence and the cycle variations. Recent advancements in the quantification of CCV can be found in the work of Buhl et al. [31], who studied cycle-to-cycle variations of coherent structures inside a simplified piston engine [199] and inside the TCC-engine [173] by a new Proper Orthogonal Decomposition (POD) based conditional averaging method. This method allowed the separation of the large-scale fluctuations from the classical turbulent scales. Furthermore, interesting observations by Keskinen et al. [102] have shown that, by removing the residual turbulence from the intake port, the cycle-to-cycle variations have increased, which implies the importance of the intake port regions and the turbulence for making the process more deterministic and controllable. The influence of the intake region was also recently investigated by Li et al. [119], who performed LES simulations with tumble flaps in the intake ports: for closed tumble flaps, they found an enhanced intensity of the coherent flow structures, which favoured a lower cyclic variation of the tumble ratio and its rotational centre. Understanding the sequences of the formation of the in-cylinder flow will be the key to understand cycle-to-cycle variations, but will require new post-processing methods to quantify or even visualize them.

Different sub-grid scale models were applied for engine simulations, where most authors used the standard or dynamic Smagorinsky-model. More advanced models are the Sigma-model [136] or the Wall Adapting Local Eddy model (WALE) [154]. But also scale adaptive

simulations (SAS-SST) were conducted, which are improved URANS formulations (Unsteady Reynolds-Averaged-Navier-Stokes), that allow the resolution of the turbulent spectrum in unstable flow conditions by the introduction of the von Karman length-scale. The SAS models adjust dynamically to resolve the turbulent structures, yielding an LES-like behaviour in unsteady regions of the flow [31]. Keskinen et al. [102] performed LES engine simulations without a sub-grid scale model, where the turbulent viscosity was supposedly replaced by the numerical diffusion coming from a total-variation-diminishing scheme (TVD). Within the aforementioned studies, the simulation results for the velocity fields for all models did not change significantly during the intake stroke, but during the compression stroke. During the compression stroke Misdariis et al. [136] observed lower turbulent viscosities for the Sigma-model compared to the standard and dynamic Smagorinsky-model, because the Sigma-model was developed to avoid any over-prediction of the turbulence in shear layers and in solid rotation zones and more generally to two-dimensional flows and rotation, as it is found for the tumble flow (on the tumble symmetry plane).

Various numbers of cold-flow cycles were calculated to obtain a sufficient number of samples, where for example Nguygen et al. [146] calculated 15 cycles, Enaux et al. [55] 25 cycles, di Mare et al. [130] 30 cycles, Goryntsev et al. [74] and Baumann et al. [19] 50 cycles, or Buhl et al. 120 cycles [31], where a cold-flow cycle took around 1-3 days to solve, depending on the rpm and intake pressure. Cycle parallelization strategies were employed to overcome the long simulation time by simulating many sequential cycles at the same time with different inlet turbulence conditions, as applied by Goryntsev et al. [74] and Baumann et al. [19]. The simulation time for one cycle depends on many parameters for example on the available computational resources, on the mesh resolution, on the used models, applied numerics or on the efficiency of the CFD-code itself. The simulation time also depends on the complexity of the engine, where research engines with one intake and one exhaust valve without inclination, will be easier to handle in terms of meshing and mesh motion than a pent-roof spark ignition engine with four valves. Examples for optically accessible research engines taken for LES simulations are the simplified piston-cylinder assembly with one stationary, open valve by Whitelaw et al. [199] and the TCC-engine operated by the Sick engine group at the University of Michigan [173], which features a pancake combustion chamber with one intake and one exhaust valve. More realistic engines are operated by the Dreizler engine group [18] from the Technical University of Darmstadt, by the group of Kaiser [20] at the University of Duisburg-Essen, or by the research institute IFP-energies nouvelles [136]. All of them are single cylinder research engines with optical access for laser diagnostics.

Fired engine simulations

Adding combustion to the engine simulation is a very challenging task, because the combustion process has to happen in a predefined time window and has to account for (a) the flame kernel growing from ignition, (b) the transition to a freely propagating flame and (c) for the flame quenching at the cold chamber walls. Since the combustion primarily depends on the turbulent flow field, it is highly important that the turbulent flow is correctly predicted, which requires an adequate numerical high order scheme, such as central differencing for the convection terms of the momentum equation and a high order temporal discretisation. One of the first reactive LES simulation in a "realistic" engine geometry was performed by Richard et al. [160] and Thobois et al. [183] in 2007, where combustion simulations where performed with the Coherent Flame Model (CFM) [34] and Thickened Flame Model (TFLES), respectively. Both models include a transport equation

for the flame-surface-density (FSD). Later, in the work of Vermorel et al. [188], real multi-cycle LES simulations of 10 consecutive cycles with the Extended Coherent Flame Model (ECFM) [40] were carried out, which also includes a FSD-transport equation.
From 2010 on, many researchers started to perform reactive LES simulations of spark ignition engines, for example Enaux et al. [54], who calculated 25 cycles with combustion for an operational point with low CCV and concluded that the flow field at the spark timing and the early flame kernel growth are responsible for CCV. Laget et al. [113] calculated a full four-cylinder engine with intake and exhaust manifolds to understand the interdependency of the different cylinders and mixing processes inside the manifolds. Both authors used AVBP. Goryntsev et al. [73] simulated 50 cycles, including fuel injection inside a direct injection engine with tumble flaps. They used KIVA-3V with the standard Smagorinsky model, a standard Arrhenius-based combustion model coming within the KIVA-3V code and ignited the mixture by gradually increasing the energy during the ignition phase in some cells in the vicinity of the spark plug.
Fontanesi et al. [62, 61] studied the origin of CCV inside a downsized engine under full load with the commercial CFD-code Star-CD [11]. They considered the fuel injection by a Lagrangian approach and used the ECFM combustion model with a modified version of the Arc-and-Kernel Tracking-Ignition-Model [53] (AKTIM) to initiate the flame kernel growth. Flame quenching was considered by nullifying the production terms in the flame surface density transport equation at a distance of y^+ of 50 from the solid walls. Different correlations between global and local flow variables were evaluated, but no clear trend could be observed. In a later work, Fontanesi et al. [60] investigated the sensitivity of cycle-to-cycle variations and knock to the location and orientation of the spark plug, where the knock was predicted by an approach suggested by Lafossas et al. [112]. They showed that the orientation of the electrodes was rather insensitive to the combustion stability, but a change of the spark-plug position increased CCV.
Koch et al. [107] studied CCV at a full-load point by calculating 40 cycles with the G-equation for the flame propagation with Star-CD and have also related the early stage of combustion to CCV. Tatschl et al. [182] used the CFD-code AVL-Fire [3] and calculated 20 cycles using the CFM combustion model, including the fuel injection and a coupling of a 1D code, which provided boundary conditions at the inlet and the outlet of the CFD domain. They used a unique approach for the ignition, where the flame kernel was imposed after 0.3 ms after the ignition event. The size of this flame kernel was correlated to the cross-flow velocity at the spark plug electrode. Schmitt et al. [171] studied the mixture and the combustion process inside a methane fuelled, direct-injection engine, using the level-set approach for the flame propagation. They have observed that a supersonic injection enhanced the tumble motion and therefore decreased the CCV. Nguyen et al. [146] calculated five fired multi-cycle simulations of the optically accessible research engine of the University of Darmstadt and obtained a good qualitative comparison of the flame propagation to Mie-scattering images. They used the PsiPhi in-house code of the research group of Kempf and modelled the flame propagation with the flame surface density approach with an algebraic expression for the flame wrinkling proposed by Muppala et al. [142].
Lecocq et al. [116] proposed a new model to predict the knock based on the Tabulated-Kinetics-for-Ignition (TKI) and ECFM-LES models, which were later used by Robert et al. [162, 163] for simulating a realistic spark ignition engine. They were the first who could quantitatively predict knock. The work of Granet et al. [78] represents a state-of-the-art reactive LES simulation of spark ignition engines, which involves 75 consecutive cycles that are in a quantitively good agreement with the measured CCV for two different operational

conditions.

1.3 Objectives and scope of the thesis

The objective of this thesis is the development of a simulation workflow, which allows the calculation of unsteady in-cylinder phenomena inside spark ignition engines by means of multi-cycle large-eddy simulations. A stringent requirement for the workflow is that it has to be generic, meaning that the workflow can be applicable to different engine geometries, which requires an efficient pre-processing (e.g. automated meshing). The workflow needs to be incorporated into the existing open source software library OpenFOAM. The usage of an open source tool has the advantage that the workflow can be applied on computer clusters with many CPUs at reasonable licensing cost.

In the scope of this thesis, three different engine geometries are considered for cold and for fired LES simulations to address the following questions:

- How many cycles need to be simulated for the assessment of the in-cylinder flow field? (see chapter 6.4)
- How do different turbulence sub-grid closure models perform on different grids compared to experimental evidences? (see chapter 6.4)
- How does the tumble vortex look like and how can the tumble break-down be quantified? (see chapter 6.4.5)
- Can the enlarged piston top-land crevice of optically accessible research engines be neglected? (see chapter 7.5.1)
- How sensitive is the formation of the tumble-flow to the geometry of the valve seat? (see chapter 8.5.1)
- Can the combustion process be described by algebraic flame-surface-density closure models? (see chapters 7.5.2 and 8.5.4)
- What is the influence of the internal gas recirculation of the burnt gases on the flame propagation? (see chapter 7.5.3)
- Can the flame propagate into the piston top-land crevice? (see chapter 9)

1.4 Thesis outline

In the first chapter, a brief introduction and motivation is given and some relevant previous studies of cold-flow and reactive LES simulations of spark ignition engines are presented. Chapter 2 introduces the working principle of the spark ignition engine and undesired issues associated with today's spark ignition engines. In chapter 3, the compressible governing equations are introduced to describe the turbulent flow field inside the spark ignition engine together with the applied turbulence sub-grid scale closures. The flamelet concept for turbulent premixed flames is presented and models, such as the flame-surface-density model, are shown. In chapter 4, the numerical methods for solving the governing equations are introduced. The grid generation and the workflow for the multi-cycle simulations are

also explained. Parts of this chapter were published in the "SAE International Journal of Engines" [145]. Chapter 5 gives a brief overview about the three engine configurations, which were simulated in the scope of this work. Chapter 6 is a reprint of a paper published in the journal "Flow, Turbulence and Combustion" [94]. It includes cold-flow multi-cycle simulations of an optically accessible research engine with different sub-grid scale models on two different grid sizes. The flow fields are compared against experimental evidences. Furthermore, post-processing and visualization strategies for the analysis of the tumble flow are proposed. Chapter 7 presents a numerical study of the combustion process inside the same engine as used in chapter 6. Additional cold-flow multi-cycle simulations are performed, including the piston top-land crevice. The flow fields of the cold-flow simulations are then used as starting conditions to study the flame front propagation with different algebraic flame surface density models. Furthermore, fired multi-cycle simulations with internal gas recirculation are presented and compared against Mie-scattering images of the flame propagation inside the corresponding engine. In chapter 8, a comparison of the flow field of two different cylinder-head geometries to PIV and MRV measurements is presented. The developed tools for the tumble visualization - introduced in chapter 6 - are applied on different flow fields of two different cylinder-head configurations. Finally, the flame front propagation inside the two different engine geometries is studied and compared against each other. Chapter 9 is a reprint of a paper published in the "JSAE - International Journal of Engines" [92] and shows a numerical and experimental study of the flame propagation into the piston top-land crevice. Chapter 10 is the last chapter of this thesis and presents a summary of the main achievements together with an outlook for possible next steps towards more realistic LES engine simulations.

2

Theoretical Background of SI-Engines

This chapter provides the working principle of the spark ignition engine. In particular, emphasis is put on the importance of the in-cylinder flow-field for combustion and on unavoidable in-cylinder phenomena, namely cycle-to-cycle variations and knock.

2.1 Working principle

The spark ignition engine is a reciprocating engine with internal combustion and external ignition source, which necessitates an exchange of the working medium after each completed cycle. It can be either naturally aspirated or super-charged via a compressor. The fuel can be directly injected into the combustion chamber or into the intake ports. In order to complete one engine cycle, the crank-shaft rotates two times around its axis (720°CA). The piston is connected via the conrod to the crank-shaft to convert the translation into a rotational motion. [185]. The full cycle can be sub-divided into four stroke as illustrated in figure 2.1.

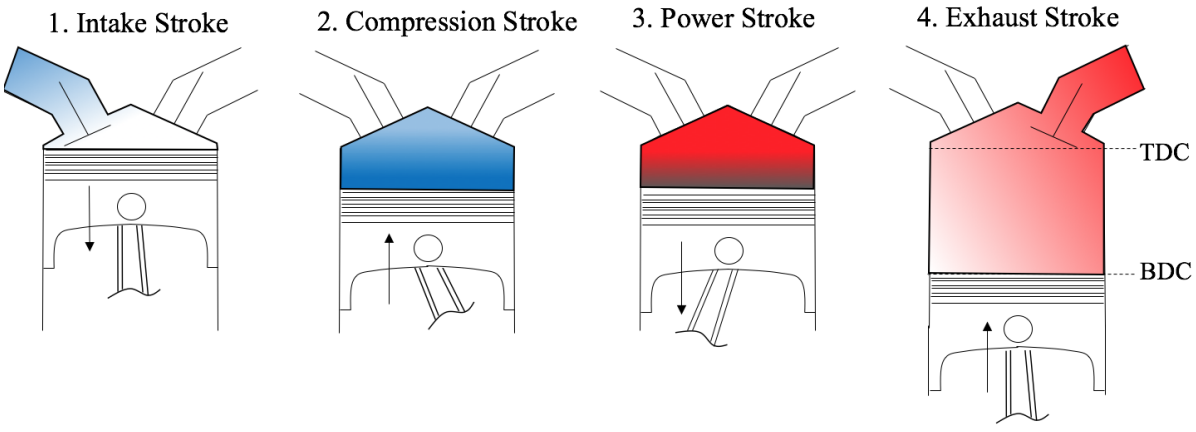

Figure 2.1: Schematic of the working principle of the four strokes of a gasoline spark ignition engine.

The four strokes, namely the intake, compression, expansion and exhaust stroke have the following functions:

1. **Intake stroke**
   The piston is at TDC, the intake valves are opened and the exhaust valves are closed. Due to the downward motion of the piston, an under-pressure is created and the air/fuel mixture is sucked in. The inducted mass of air is controlled by a throttle-body upstream of the intake valves. Coherent vortex structures, such as the tumble-vortex, will develop inside the combustion chamber. The vortex structures are important for the combustion process.

2. **Compression stroke**
   The intake valves are closed and the piston moves up again and compresses the air/fuel mixture. Towards the end of the compression, the tumble flow breaks up into a highly turbulent field. At the end (or after) the compression stroke, the mixture is ignited by the spark plug. A turbulent flame brush is propagating through the combustion chamber and consuming the air/fuel mixture, leaving the burnt products behind.

3. **Power stroke**
   The hot burnt products are expanding and forcing the piston to move downwards. The work, which is created by the expansion, is around five times bigger than the work needed to rise the piston, as a result of the pressure rise caused by the heat-release.

4. **Exhaust stroke**
   Before the piston has reached the BDC position again, the exhaust valves open and the exhaust gasses stream out of the cylinder, due to a favourable pressure difference between the cylinder and the exhaust manifold. In the actual exhaust stroke, the exhaust gasses are pushed out by the upwards moving piston to free the cylinder for the next cycle.

Two strokes can overlap each other by changing the valve closing and opening times. For example, for an early opening of the intake valves during the exhaust stroke and a late closing of the exhaust valves within the intake stroke. A valve overlap can be used to re-circulate the exhaust gases back into the combustion chamber. A higher amount of exhaust gases will lower the in-cylinder temperature after the combustion and therefore lowering pollutant emissions, such as thermal NOx.

All four-strokes have to be optimized and considered for a high power output, even-though the work is only created during the power stroke. In particular the formation and understanding of the turbulent in-cylinder flow field is of key importance, because the turbulence is used to wrinkle the flame front, hence to speed up the combustion process. In a combustion engine, it is not enough to just burn the air/fuel mixture, it has to burn at the right moment and with the right speed, which is illustrated by the following example: Assuming an engine runs at 3000 rpm, has a cylinder radius of 4.1 cm, a centrally mounted spark plug and contains a mixture of iso-octane with an equivalence ratio of Φ=1 (laminar flame velocity 41 cm/s at ambient conditions), the flame would need 0.1 seconds to reach the combustion chamber walls in the absence of turbulence. Bearing in mind that one rotation (360°CA) at 3000 rpm requires 0.02 seconds and that combustion should not exceed a duration of ∼120°CA, a lot of fuel would be unburnt and expelled during the exhaust stroke. The only reason why the fuel can be burnt in time is due to the in-cylinder flow field, which is highly turbulent and wrinkling the flame front to enhance the combustion process. Fortunately, the turbulence level of the flow field scales with the mean piston

speed, which ensures the working of the engine even at higher rotational speeds. Typically, the turbulence level follows $\frac{\sqrt{\overline{u'u'}}}{\overline{u}}$, which is constant in engines.

During the engine's operation, the only way to change the indicated power output P_{in} is either by increasing the combustion efficiency or by inducting more air [87]:

$$P_{\text{in}} = \frac{n_f m_{\text{air}} N Q_{\text{HV}} (F/A)}{n_R} \tag{2.1}$$

In eqn. 2.1, m_{air} denotes the inducted mass of air, n_f the fuel conversion efficiency, N the rotational speed of the crank-shaft, Q_{HV} the fuel heating value, (F/A) the air-to-fuel ratio and n_R the number of crank revolutions per power stroke (for a four-stroke engine, n_R=2).

2.2 Flow field

The flow field close to TDC, as well as the combustion efficiency, are entirely determined by the flow conditions at intake valve closure (IVC) time. Therefore, it is important to understand how the flow is issuing into the combustion chamber and not only the amount of the air itself. Inside a spark-ignition engine the valves are usually mounted with an inclination to the cylinder head. This orientation will favour a rotational flow pattern around the x-axis according to figure 2.2. This rotational flow is denoted as the tumble flow. It is the main flow feature of the spark ignition engine and defines a coherent (organized) flow structure in a disorganised turbulent surrounding [125]. The tumble formation and its characterization is explained in greater detail in chapter 6 and its sensitivity to the geometry of the valve seat region is presented in chapter 8.

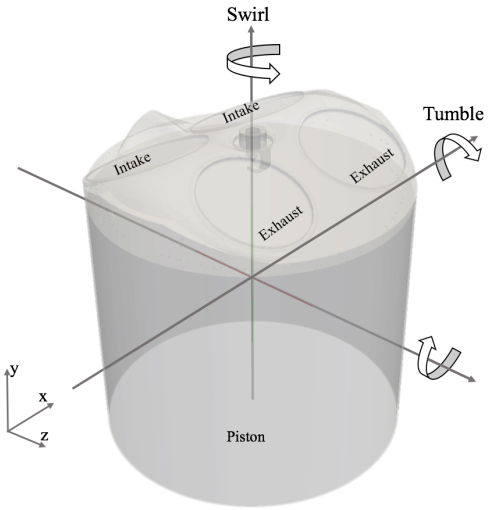

Figure 2.2: Definition of the tumble and swirl flow.

Figure 2.3 shows a cut through the mid-valve plane of two schematics of spark ignition engines with opened and inclined intake valves. For both configurations, the flow is mainly passing through the upper tip of the valve and forming a big coherent vortex inside the combustion chamber. However, for the configuration with a tumble blade (A) in the intake port, the rotational flow inside the combustion chamber is stronger. The tumble blade forces more flow to enter the engine through the upper valve seat as compared to the case

without tumble blade (B), which finally leads to a stronger rotational vortex (indicated by the thick arrow). During the compression stroke, the rotational vortex (tumble) becomes squeezed by the upwards coming piston and will break up into a small scale turbulent flow field [125]. The stronger the tumble flow, the more turbulence will be available for the combustion at the end of the compression stroke. Hence, the flame inside an engine with tumble blade, will propagate faster than in an engine without tumble blade (under the same operating conditions).

A rotational flow around the y-axis, as illustrated in figure 2.2, is denoted as swirl and not used in conventional spark ignition engines. The swirling flow is typically used in Diesel engines.

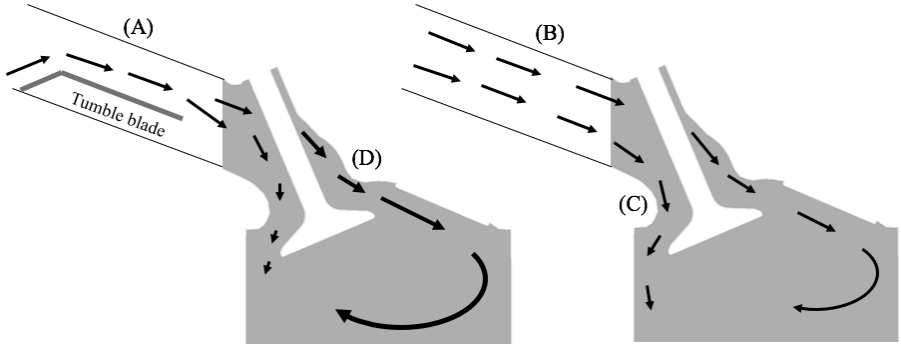

Figure 2.3: Different intake port designs with (A) and without (B) tumble blade and the influence of the flow distribution in the underflow (C) and overflow (D) region inside the valve seat region.

2.3 Combustion in spark ignition engines

Inside a conventional gasoline engine, the working medium is a premixed air/fuel mixture, which has to be ignited by an external heat source, from where a flame kernel starts growing until it turns into a self-sustaining flame front. This phase is denoted as the ignition event, where the flame is rather laminar and highly prone to extinction, due to heat losses and to locally too high turbulence. It has to be mentioned, that having the proper turbulent features at the correct location and time is a delicate issue for the design of the spark ignition engine. After the ignition event has survived, the flame has to interact with the highly turbulent surrounding and propagate through the combustion chamber until the combustible mixture is consumed or until the flame is quenched at the chamber walls. The whole process, which is also known as "conventional combustion mode", can be subdivided into: (1) ignition, (2) flame kernel growing, (3) flame propagation (deflagration) and (4) extinction of the flame [87].
An essential feature of the conventional combustion mode is, that the air/fuel mixture has to be sufficiently mixed, ideally homogeneously distributed and lying in-between the flammability limits (for gasoline $0.6 < \Phi < 1.5$), where the classical gasoline engine is mostly operated at stoichiometric conditions (three-way catalyst working regime). The fuel is injected either in the intake port upstream of the intake valves during the intake stroke or directly into the combustion chamber. In terms of mixture preparation, more variability exists for the direct-injection systems compared to the port fuel injector engines. For the direct-injection engines, the fuel can be injected multiple times and used to enhance

the tumbling motion. The direct injection system can also be used to operate the engine in a stratified mode, where the injected fuel spray is directly ignited by the spark plug (lately in the compression stroke). The fuel jet will burn locally very rich, but globally combustion can happen even under the flammability limits. Thus in the stratified combustion mode, the spark ignition engine can be controlled by the injected fuel mass and the throttle-body can be set widely opened. This has the advantage that pumping losses can be lowered at part-load-conditions. However, the difficulty of applying this combustion strategy lies in controlling the stratification of the injected fuel with the turbulent in-cylinder air flow, which is exposed to strong cyclic fluctuations [133].
Other advanced combustion strategies are lacking in controllability. For instance, for the homogeneous charge compression ignition (HCCI) combustion mode [208], combustion is supposed to happen simultaneously inside the combustion chamber, yielding a lower temperature rise and consequently a reduction of the NOx emissions. A simultaneous auto-ignition event will require a homogeneous mixture with very low temperature stratification, which is very difficult to obtain and even more difficult to control. It will require the measurement of the in-cylinder temperatures at different locations. A review of HCCI in engines can be found in the work of Yao et al. [204]. Recently, the fuel octane number was suggested to become a control parameter for the design of new combustion modes. The octane number defines the resistance of the fuel against self-ignition. Two different gasoline fuels with different octane numbers can be injected by distinct injectors, yielding an octane number for an optimum spark timing (maximal break torque point) and a reduction of knock [24].
Even though different combustion strategies exist aiming at higher combustion efficiency and lower pollutant emissions, the "conventional combustion mode" is still used in most of the spark ignition engines, since it can be (at least to some extent) controlled. However, the flame propagation within the conventional combustion mode is highly prone to cycle-to-cycle variations and needs to be better understood.

Influences of the piston top-land crevice to the unburnt hydrocarbon emissions
One of the most important crevice volumes is the piston-top land crevice, defined as the volume between the piston skirt, cylinder liner and first piston ring. The importance of the piston top-land crevice was already identified in the late 70's by Wentworth [196] and is illustrated in figure 2.4.

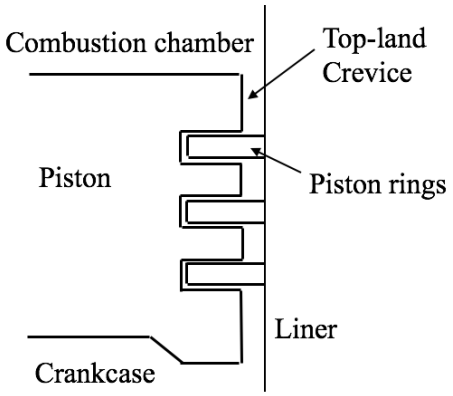

Figure 2.4: Sektch of the piston top-land crevice volume.

The function of the piston top-land is to protect the first ring from overheating. Its size depends on the piston material, the piston ring groove and the cooling system. The height

of the piston top-land is usually 2-10 % of the piston diameter with a decreasing trend [128]. Due to the thermal expansion of the piston, the radial clearance gap is limited to ∼0.18 mm in production engines and to ∼0.5 mm in optically accessible research engines. Wentworth emphasised the sensitivity of the unburnt hydrocarbon (UHC) emissions to the piston top-land crevice, piston-ring gap-orientation and blow-by and experimentally proved the reduction of the UHC exhaust emissions [197] due to the usage of a modified sealed piston-ring. Thus, controlling the piston-ring package will help in reducing the exhaust tailpipe UHC emissions.

The UHC from the piston top-land undergo a complex path after leaving the crevice, which includes: (a) the post-oxidation during the expansion stroke, (b) the interaction with the turbulent flow field at exhaust valve opening (EVO) and (c) piston displacement during the exhaust stroke. For a running engine, the UHC emissions are usually measured in the exhaust pipe during the exhaust stroke, which makes the analysis of the history of the crevice content very difficult. In the work of Tabaczynski [180], two UHC peaks have been detected at EVO and exhaust valve closure (EVC). He associated the first peak with the head-on-quenching during the exhaust blowdown and the second one to the roll-up vortex, which is imposed by the upwards coming piston. Fendell [58] has shown with 1D calculations, that almost all of the UHC emissions, which are formed inside the quench layers at the cylinder walls, will be post-oxidized during the expansion and the exhaust stroke. He stated that the piston-top land crevice is the main source of the UHC emissions measured during the exhaust stroke. Furthermore, to enable flame propagation into the piston-top land crevice, he proposed increasing the wall temperature of the crevice. Adamczyk [13] quantified the amount of UHC emissions with a gas chromatograph by sequentially filling the main crevice volumes of a combustion bomb (non-moving piston) under engine relevant conditions. He quantified that around 80 % of the total amount of UHC emissions are coming from the crevice volume. He also studied the influence of the spark plug location and concluded, that the highest UHC emissions were observed with centrally mounted spark plug [58].

Later, numerous experimental analyses were conducted of the sensitivity of the piston-top-land geometry to the exhaust pipe UHC emissions [22, 15, 200, 135]. The main conclusions drawn from these studies were: (a) a critical radial clearance distance exists, where the flame can penetrate into the crevice and (b) for radial clearance distances lower than the two-wall quenching distance the engine-out UHC emissions vary linearly with the crevice volume. Empirical relations for the two-wall quenching distance were derived by Lavoie [115] and later by Ishizawa [90] (see section 9.2), who used ion-probes mounted in the piston to detect flame penetration into the top-land crevice volume. Saika et al. [166] proved the existence of flame penetration with ion-probes mounted in the moving piston. A detailed review of combustion crevice-induced UHC emissions can be found in the work of Alkidas [14].

2.4 Undesirable in-cylinder phenomena

Undesirable in-cylinder phenomena are reducing the engine efficiency and are limiting its operational range. They mostly come together with a required (desired) phenomenon, such as turbulence, which is needed for the working principle of the engine. In the following, the undesired in-cylinder phenomena are described.

2.4.1 Cycle-to-Cycle Variation

One of the most important unavoidable in-cylinder phenomena are the cycle-to-cycle variations. Their appearance is most obvious in the in-cylinder pressure traces under fired operating conditions, where some cycles will show a high in-cylinder pressure and a fast combustion and some cycles a slower combustion and a lower peak in-cylinder pressure. A misfired cycle can also appear after many successfully fired cycles, which drastically decreases the engine efficiency. It is a common practice to quantify CCV by a coefficient of variation (COV) of the peak in-cylinder pressure:

$$\mathrm{COV} = \frac{\sigma_{p_{\max}}}{\langle p_{\max} \rangle} \tag{2.2}$$

In eqn. 2.2, $\langle p_{\max} \rangle$ denotes the mean peak in-cylinder pressure for the number of investigated cycles and $\sigma_{p_{\max}}$ the standard deviation of the mean peak in-cylinder pressure. Instead of the peak in-cylinder pressure, the indicated mean effective pressure (IMEP) can also be used to quantify CCV, which is a direct measure of the work output.

In order to understand CCV and the contribution of the flow field to it, the turbulent flow field itself needs to be investigated and understood. Controlling the turbulence and achieving a reproducibility of the flow conditions will be a first step of limiting CCV. Since the flow field is highly irregular, statistical methods must be used for the evaluation of CCV.

Even though turbulence is said to be highly instationary, it can be treated as stationary in a statistical sense, by looking at mean and fluctuating values after sufficiently long time. For an arbitrary scalar ϕ, the mean value taken over a time interval Δt is defined as:

$$\langle \phi \rangle = \lim_{\Delta t \to \infty} \frac{1}{\Delta t} \int_0^{\Delta t} \phi(t)\, dt \tag{2.3}$$

The fluctuations ϕ' and the standard deviation (root mean square) of ϕ are given by:

$$\phi'(t) = \phi(t) - \langle \phi \rangle \tag{2.4}$$

and

$$\phi_{\mathrm{rms}} = \lim_{\Delta t \to \infty} \sqrt{\frac{1}{\Delta t} \int_0^{\Delta t} (\phi(t)^2 - \langle \phi \rangle^2)\, dt} \quad , \tag{2.5}$$

respectively.

Unfortunately, the flow field cannot be simply averaged over a long period of time to determine the mean flow and the velocity fluctuations of one particular cycle, because the flow inside the engine is not stationary. Within a cycle i and particular crank angle Θ the instantaneous velocity U can be written as:

$$U(\Theta, i) = \langle U(\Theta, i) \rangle + u'(\Theta, i) \tag{2.6}$$

with $\langle U(\Theta, i) \rangle$ being the individual cycle mean value of one specific cycle i at a given crank angle Θ, which can be obtained by a moving average [125], which takes into account the size of the combustion chamber and the mean piston velocity. Figure 2.5 shows schematically the instantaneous velocity of an individual cycle at a fixed position inside the

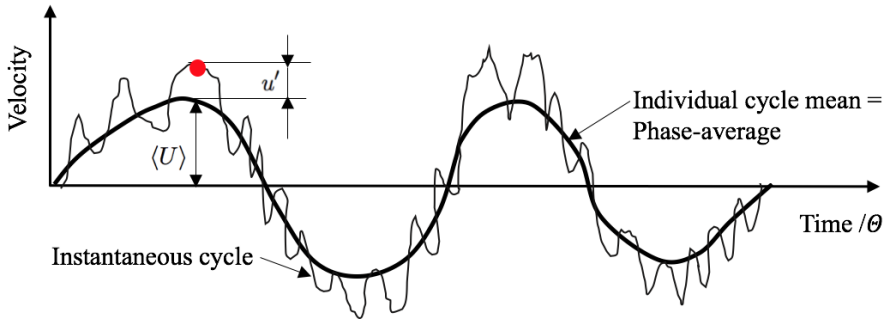

Figure 2.5: Instantaneous velocity U (solid wiggled fine line) at a fixed position inside the combustion engine tracked over some crank angles Θ and its cycle mean value (solid smooth line) according to Heywood [87]. No cyclic variations are present (phase-average = individual cycle mean).

combustion chamber over some crank angles Θ and the corresponding cycle mean velocity $\langle U \rangle$. The scenario in figure 2.5 denotes a situation where no cycle-to-cycle variations are present, hence the individual cycle mean is equal to the phase-average velocity, which can be calculated by:

$$\langle U_{\mathrm{PA}}(\Theta) \rangle = \frac{1}{N_c} \sum_{i=1}^{N_c} U(\Theta, i) \tag{2.7}$$

with N_c being the total number of cycles [125] [87].

The problem with the flow field averaging is that one cannot distinguish between the cyclic and the turbulence-induced variations once CCV is present, which is actually always the case for spark ignition engines. This becomes clear by looking at figure 2.6, where the time history of the velocity of one particular position inside the combustion chamber is plotted for some crank angles. The solid oscillating line represents the instantaneous velocity and

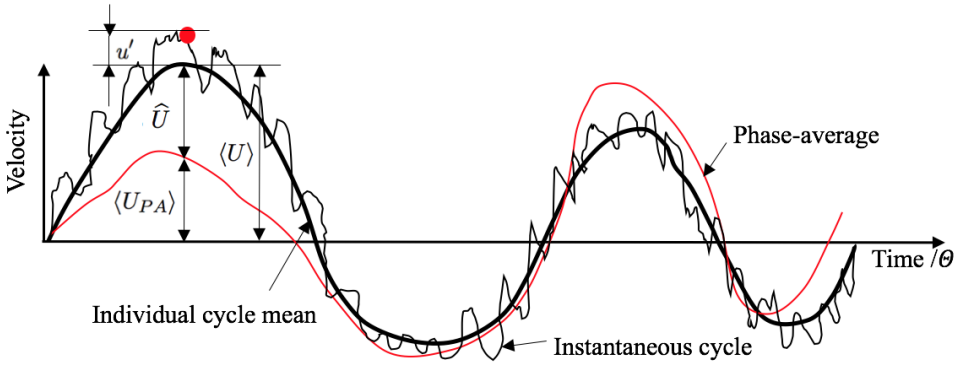

Figure 2.6: Instantaneous velocity U (solid wiggled fine line) at a fixed position inside the combustion engine tracked over some crank angles Θ, its cycle mean value (solid black smooth line) and the phase-average velocity (red solid line) according to Heywood [87]. Cycle-to-cycle variations are present.

the thicker smooth line represents the corresponding mean value of this specific cycle.

Considering now the smooth red solid line, which represents the phase-averaged velocity obtained from many cycles (according to eqn. 2.7), significant difference to the individual cycle mean of the particular engine cycle (thick black line) is obtained. This difference denotes the cycle-to-cycle variations $\widehat{U}$ and can be written as:

$$\widehat{U}(\Theta, i) = \langle U(\Theta, i) \rangle - \langle U_{\mathrm{PA}}(\Theta) \rangle \tag{2.8}$$

Hence, the instantaneous velocity $U(\Theta, i)$ of a particular cycle i can be decomposed as:

$$U(\Theta, i) = \langle U_{\mathrm{PA}}(\Theta) \rangle + \widehat{U}(\Theta, i) + u'(\Theta, i) \tag{2.9}$$

In eqn. 2.9, the phase-averaged velocity $\langle U_{\mathrm{PA}} \rangle$ is only a function of the crank angle, but the cyclic variation of the mean velocity $\widehat{U}$ and the turbulent fluctuations u' are functions of the crank angle and the corresponding cycle i. Unfortunately, it is not straightforward to calculate the mean of a particular cycle and therefore the phase-averaged fluctuation intensity $u'_{\mathrm{PA}}(\Theta)$ is determined along this study from:

$$u'_{\mathrm{PA}}(\Theta) = \left(\frac{1}{N_c} \sum_{i=1}^{N_c} \left[U(\Theta, i)^2 - \langle U_{\mathrm{PA}}(\Theta) \rangle^2 \right] \right)^{1/2} \tag{2.10}$$

Cycle-to-cycle variations are responsible for the unevenness of the running engine. Its suppression could yield a higher overall efficiency, but the origin of the variations is still not fully understood [125].

2.4.2 Knock

Another undesired phenomenon inside the spark-ignition engine is caused by spontaneous self-ignition of the end-gas (mixture of the fresh charge and hot residual gases) before or after the spark ignition. This can lead to a rapid increase of the heat release, which is accompanied with high pressure fluctuations and shock waves that are traveling back and forth through the combustion chamber and can cause severe damage to the engine. These pressure fluctuations are transmitted through the solid engine parts to the outside and become noticeable by a "knocking" noise. Knock can be smooth and controllable, but also strong enough to break the piston. The knock, which can be controlled, is caused by auto-ignition of the end-gas after the spark ignition. In this case, the auto-ignition delay time of the end-gas becomes so short, that the end-gas will ignite independent of the main flame propagation, which is initiated by the spark plug. Retarding the spark timing helps omitting this kind of knock. Knock depends on the local mixture distribution, containment and, in particular, on the temperature stratification, which is controlled by the turbulent mixing.
Knock can also be caused by surface self-ignition, which cannot be controlled anymore. In that case, the end-gas will be ignited at hot surfaces (the spark plug or exhaust valves). Therefore, knock must be already taken into account during the design process of an engine. The tendency for knock can be reduced, for example, by well cooled exhaust valves or smaller crevices, where less deposits can be accumulated or by a high octane-number. The higher the octane number is, the higher is the resistance to self-ignition of the fuel [87].

3

Theory and Modelling of Turbulent Flow and Combustion

This chapter is dedicated to the physical modelling of the fluid motion and combustion. First, the governing equations of a compressible flow are presented and the concept of turbulence is introduced. Finally, the flame surface density concept to premixed flames is presented and closure models are discussed.

3.1 Governing equations

The governing equations are expressed as balance equations for an arbitrary fixed control volume, which is an open system, through which mass may flow. The net rate of accumulation and the convective transport of this volume will be always balanced by the volume and the surface forces acting on it [189].

Continuity equation
The mass in a control volume V of a single-phase flow can change only, when it is transported in or out of the volume. Thus, the balance of the mass is described by the continuity equation, with ρ being the density of the fluid:

$$\frac{\partial \rho}{\partial t} + \frac{\partial (\rho u_j)}{\partial x_j} = 0 \tag{3.1}$$

Momentum equation
The change of momentum is equal to the forces, which are acting on the fluid. The conservation of the momentum is expressed by the Navier-Stokes equations and reads:

$$\frac{\partial (\rho u_i)}{\partial t} + \frac{\partial (\rho u_i u_j)}{\partial x_j} = \frac{\partial \tau_{ij}}{\partial x_j} - \frac{\partial p}{\partial x_i} + \rho g_i \tag{3.2}$$

On the right hand side of eqn. 3.2, the pressure p and viscous forces are found. The viscous forces are expressed by the shear stress tensor τ_{ij} and can be modelled for a Newtonian fluid as:

$$\tau_{ij} = -\frac{2}{3}\mu \frac{\partial u_k}{\partial x_k}\delta_{ij} + \mu \left(\frac{\partial u_i}{\partial x_j} + \frac{\partial u_j}{\partial x_i} \right) \tag{3.3}$$

In eqn. 3.3, δ_{ij} stands for the Kronecker delta and μ denotes the dynamic viscosity. The only volume force that is considered in this work is the gravitational force ρg_i. Other types of volume forces are: Coriolis, centrifugal or electromagnetic.

Conservation of species
For the combustion processes, it is important how the mixture is distributed inside the engine and also consumed. The the total rate of change of a species k is balanced by the diffusive flux $J_{k,j}$ and the consumption/production rate $\dot{\omega}_k$ due to combustion:

$$\frac{\partial \rho Y_k}{\partial t} + \frac{\partial \rho u_j Y_k}{\partial x_j} = -\frac{\partial J_{k,j}}{\partial x_j} + \dot{\omega}_k \tag{3.4}$$

The diffusive fluxes can be approximated by Fick's law as:

$$J_{k,j} = -\rho D_k \frac{\partial Y_k}{\partial x_j} \tag{3.5}$$

where D_k denotes the diffusion coefficient and can be related to the Schmidt-number Sc_k, which describes the relation of the dynamic viscosity of the mixture to the diffusion coefficient D_k of the individual species k by:

$$Sc_k = \frac{\mu}{\rho D_k} \tag{3.6}$$

Substituting eqn. 3.5 and eqn. 3.6 into eqn. 3.4 yields:

$$\frac{\partial \rho Y_k}{\partial t} + \frac{\partial \rho u_j Y_k}{\partial x_j} = \frac{\partial}{\partial x_j}\left(\frac{\mu}{Sc_k}\frac{\partial Y_k}{\partial x_j}\right) + \dot{\omega}_k \tag{3.7}$$

Eqn. 3.7 is also used as a basis for the combustion model used in this work, which is based on a transport equation for a progress variable. The transport equation for the progress variable describes in turn the transport of the combustible products. This will be elaborated in sections 3.4, 9.3 and 8.3.2.

Energy equation
The balance equation for the sensible energy can be expressed, either with the sensible internal energy e_s or with the sensible enthalpy h_s. Eqn. 3.8 shows the transport equation for the total internal energy, which includes the kinetic energy ($K = 1/2u_i^2$) [151] [155]:

$$\frac{\partial(\rho e_s)}{\partial t} + \frac{\partial(\rho u_j e_s)}{\partial x_j} + \frac{\partial(\rho K)}{\partial t} + \frac{\partial(\rho K u_j)}{\partial x_j} = \frac{\partial}{\partial x_j}\left(\alpha \frac{\partial e_s}{\partial x_j}\right) - \frac{\partial}{\partial x_j}(p u_j) + \tau_{ij}\frac{\partial u_i}{\partial x_j} + q_R + \dot{\omega} \tag{3.8}$$

The left hand side (LHS) of equation 3.8 denotes the total rate of change of the total internal energy. The first term on the right hand side describes the heat conduction, with α being the thermal diffusivity. The second term is the convective change of the pressure, which is important for the interaction of the pressure waves. The thermal diffusivity is expressed as:

$$\alpha = \frac{\lambda}{\rho c_p} \tag{3.9}$$

In eqn. 3.9, λ is the heat conductivity and c_p is the specific heat capacity. The frictional heating is denoted by the third right hand side (RHS) term and the heat losses due to radiation by q_R. The last term on the RHS, is the reaction source term $\dot{\omega}$, which describes the heat release due to combustion.

The balance equation for the sensible enthalpy is obtained by substituting $e_s = h_s - p/\rho$

into eqn. 3.8:

$$\frac{\partial(\rho h_s)}{\partial t} + \frac{\partial(\rho u_j h_s)}{\partial x_j} + \frac{\partial(\rho K)}{\partial t} + \frac{\partial(\rho K u_j)}{\partial x_j} = \frac{\partial}{\partial x_j}\left(\alpha \frac{\partial h_s}{\partial x_j}\right) + \frac{\partial p}{\partial t} + \tau_{ij}\frac{\partial u_i}{\partial x_j} + q_R + \dot{\omega} \quad (3.10)$$

The absolute enthalpy h is used for the simulation with combustion, which consists of the chemical bond energy, that is contained in the reference enthalpy $h_{k,\mathrm{ref}}$ of the species k and the sensible enthalpy:

$$h_k = h_{k,\mathrm{ref}} + \int_{T_{\mathrm{ref}}}^{T} c_{p,k} dT \quad (3.11)$$

In the case with combustion, the enthalpy of the mixture contained in the system, is the sum of the mass fractions of the corresponding species k multiplied with their absolute enthalpies h_k:

$$h = \sum_{k=1}^{n} Y_k h_k \quad (3.12)$$

Using the absolute enthalpy instead of the sensible energy in 3.10 has the advantage, that the reaction source term $\dot{\omega}$ vanishes. Radiation and frictional heating are not considered in this work.

3.2 Constitutive equations

The ideal gas law is used to relate the pressure to the temperature and the density. It is derived from the kinetic theory of gases [88] and is valid for gases that consist of a large number of molecules, which are negligibly small in size compared to the occupied volume and are in a random motion according to Newton's laws of motion:

$$p = \rho \frac{RT}{W} \quad (3.13)$$

In eqn. 3.13, R is the universal gas constant and W the mean molecular weight of the mixture consisting of N number of species k, with Y_k being the mass fraction and W_k the molecular weight of the species k:

$$W = \left(\sum_{k=1}^{N} \frac{Y_k}{W_k}\right)^{-1} \quad (3.14)$$

The dynamic viscosity is obtained by the standard kinetic gas theory or fitted by the Sutherland formula for Newtonian fluids [178]:

$$\mu = \frac{A_s \sqrt{T}}{1 + T_s/T} \quad (3.15)$$

In eqn. 3.15, A_s denotes the Sutherland coefficient and T_s the Sutherland temperature [178].

3.3 Turbulence Modeling

The state of the flow can be determined with the Reynolds-number Re, which defines the ratio of the inertia forces to the viscous forces:

$$Re = \frac{u_i L}{\nu}, \tag{3.16}$$

with L being a characteristic length scale and ν the kinematic viscosity [45]. When the inertia forces are bigger compared to the viscous forces (e.g. for the intake flow inside the intake pipes and in the combustion chamber), the flow is defined by a chaotic 3D high velocity motion. (Polymer flows in extruders are an example for a viscosity-dominated flow, where the flow is rather slow and smooth.) These two flow states are defined as turbulent and laminar, respectively. A flow is said to be fully turbulent, when a critical Reynolds-number is exceeded. The critical Reynolds-number for a flow in a pipe is 2300 and for a flow above a flat plate 500000. In most industrially relevant problems, the flow is turbulent. One of the main reasons is, that the turbulent mixing is much faster than the molecular mixing by the diffusion. Hence, mixing-dominated processes can be designed compact and realized in a shorter time, which decreases the costs.

Different length scales exist within the turbulent flow. The biggest scales depend on the geometry, which is for the engine the bore diameter. The smallest scales depend on the viscosity of the fluid and the dissipation ϵ, which was introduced by Kolmogorov in 1941 [109] within the concept of the energy cascade according to Richardson [161]. The concept of the energy cascade says that the biggest eddies are breaking down into smaller ones, until they are dissipated into heat. Otherwise the energy would accumulate and the turbulence would never die out. This is not the case as the turbulence is always dissipative and needs energy to be maintained. Assuming that the energy, which is contained at the largest scales l_I, is proportional to u'^2, where u' are the turbulent velocity fluctuations and the turnover time of the biggest eddies is $t_I = l_I/u'$, their ratio will define the dissipation rate ϵ at the smallest scales:

$$\epsilon \sim \frac{u'^3}{l_I} \tag{3.17}$$

Knowing the dissipation energy at the smallest scales allows the estimation of the smallest length scales (also known as the Kolmogorov length scales l_η) by relating them to the viscosity as:

$$l_\eta = \left(\frac{\nu^3}{\epsilon}\right)^{1/4} \tag{3.18}$$

The biggest scales are also known as the integral length scales l_I, which are obtained by calculating the auto-correlation coefficients at two points in the flow with variable distance between them. The equation for the normalized auto-correlation coefficients R_x reads:

$$R_x(r) = \frac{\langle u'(x)u'(x+r)\rangle}{\langle u'(x)^2\rangle} \tag{3.19}$$

The integration of the auto-correlation curves leads to the integral length scale:

$$l_I = \int_0^\infty R_x dr \tag{3.20}$$

The velocity fluctuations must be either measured simultaneously at two different locations or obtained from 3D-simulations of hundreds or even thousands of consecutive cycles.

Energy spectrum

A Fourier transformation of the auto-correlation coefficients yields the turbulent energy spectrum $E(\kappa)$ in wave number space $\kappa = 2\pi/l$. Figure 3.1 shows the energy spectrum, where the maximum is attained at the integral length scale and the last steep decay at the Kolmogorov scale. The energy transfer from the biggest to the smallest vortices takes place within the inertial subrange, where the energy spectrum decreases following the $\kappa^{-5/3}$ law [157].

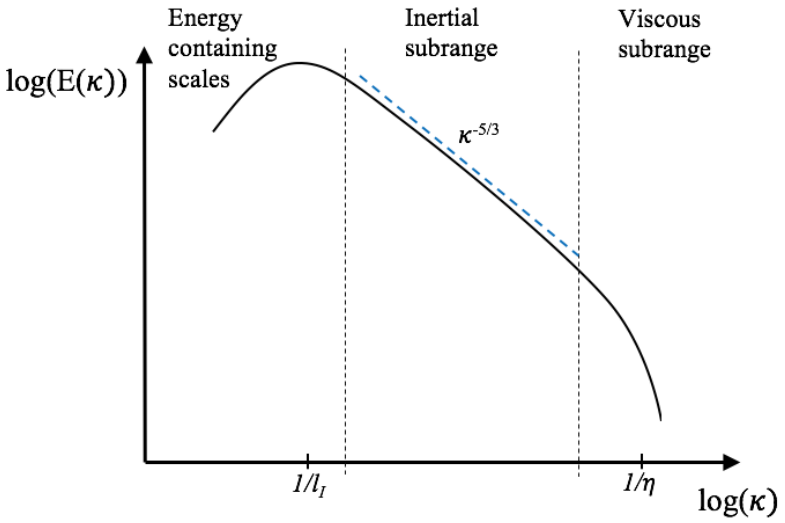

Figure 3.1: Energy spectrum of the decay of isotropic homogeneous turbulence [151].

Strategies to model turbulent flows

Simulation techniques that can resolve the full energy spectrum are called Direct Numerical Simulations (DNS), which require a spatial discretisation up to the size of the Kolmogorov scales. For most of the industrially relevant problems, these techniques are not feasible, also not for the combustion engine, where up to now, only DNS of engine like geometries without combustion and relatively low engine speeds were performed [167].

Another possibility is to model the complete spectrum, which is done in the Reynolds-Averaged-Navier Stokes (RANS) approach. This method introduces the Reynolds decomposition of the governing equations (see chapter 3.1) to the fields of interest and a temporal averaging. The Reynolds decomposition yields a new unclosed term, which is known as the Reynolds-stresses $\rho\langle u_i' u_j' \rangle$. This term can be modelled with an artificial turbulent viscosity according to the hypothesis of Boussinesq [25], who suggested that the Reynolds-stresses might be proportional to the mean rate of deformation, which is intrinsically analogous to the momentum transfer by the molecular viscosity. In this case, the momentum transfer is forced by the turbulent eddies and the molecular viscosity is changed by the turbulent viscosity μ_t. There are different modelling approaches to calculate the turbulent viscosity:

mixing length models proposed by Prandtl, transport equation models for the turbulent kinetic energy or dissipation [114] or transport equations for all six components of the Reynolds-stress tensor [189]. Due to the much lower computational effort, compared to DNS, RANS is still widely used for many industrial applications. However, it fails in predicting the time dependent events, since it only gives the time averaged results. In the scope of reciprocating engine simulations, unsteady-RANS (URANS) has been applied successfully to calculate the ensemble mean values and is able to capture (to some extent) the dynamic behaviour of the ignition process, fuel injection or flame propagation. However, it will not be possible to calculate all of the cyclic induced variations $\widehat{U}(\Theta, i)$, as shown in eqn. 2.9, simply because they are not included in the model. However, an U-RANS might be interpreted as a very coarse large eddy simulation (LES), in which the dynamics of the pressure waves inside the manifolds will be damped out by the very high turbulent viscosities, yielding different in-flow conditions (which then manifest in some cyclic variations). Another disadvantage of this method is that it requires some effort in the identification of the model parameters and their validation that will only be valid for one particular engine. A method which is less computationally demanding as DNS, but more accurate as RANS and less model-dependent with the capability to resolve time dependent events, is the large-eddy simulation (LES). LES is used in the scope of this thesis.

3.3.1 Large Eddy simulation

The main idea behind the large eddy simulation is to directly resolve the big eddies and to model the smaller ones, which tend to be isotropic and therefore easier to model. The separation of the scales is achieved by a filtering operation, which is mathematically speaking, expressed as a convolution of the field of interest, with a filter kernel $\mathcal{G}$.

$$\overline{\phi}(x_i) = \int_V \phi({x_i}^*)\mathcal{G}(x_i, {x_i}^*, \Delta)d{x_i}^* \tag{3.21}$$

In the scope of this work, the overline " $-$ " denotes LES-filtered quantities. The solution is split into a resolved part and an unresolved part. The scales associated with the unresolved part will be denoted as sub-grid scales (sgs).

$$\phi = \overline{\phi} + \phi^{\mathrm{sgs}} \tag{3.22}$$

Many expressions for the filter function $\mathcal{G}$ exist and can be found in the books of Pope [157] or Sagaut [165]. However, most of them are not used in CFD-codes, because they are practically very difficult to implement. Especially on unstructured moving grids, as it is the case for many engine simulations. In the scope of this work, no filter function is applied. The filtering is implicitly included by the LES grid, where the filter width can be expressed by the cubic-root of the local computational cell volume:

$$\Delta = \sqrt[3]{\Delta_i} \tag{3.23}$$

It has to be mentioned that expressing the filter width with eqn. 3.23 can lead to errors for high aspect ratios, as it might be the case for large cell displacements on moving grids (e.g. piston displacement).

For compressible flows with big density changes in combustion engine, it is convenient to

use the Favre-filtering [57], which refers to a density-weighted filtering and reads:

$$\widetilde{\phi} = \frac{\overline{\rho\phi}}{\overline{\rho}} \tag{3.24}$$

3.3.1.1 Filtered governing equations

The Favre-averaging is applied to the continuity, momentum, species and energy conservation equations. The viscous heating and radiation are neglected within the scope of this thesis. Furthermore, for the energy equation, the variant with the total enthalpy h is depicted without the kinetic energy K. The Favre-averaging of the other variants of the energy equations can be applied analogously. The Favre-filtered conservation equations for mass, momentum, species and energy read:

$$\frac{\partial(\overline{\rho})}{\partial t} + \frac{\partial(\overline{\rho}\widetilde{u}_j)}{\partial x_j} = 0 \tag{3.25}$$

$$\frac{\partial\left(\overline{\rho}\widetilde{u}_i\right)}{\partial t} + \frac{\partial(\overline{\rho}\widetilde{u}_i\widetilde{u}_j)}{\partial x_j} = \frac{\partial\overline{\tau_{ij}}}{\partial x_j} - \frac{\partial\overline{p}}{\partial x_i} + \overline{\rho}g_i - \frac{\partial\overline{\rho}(\widetilde{u_i u_j} - \widetilde{u}_i\widetilde{u}_j)}{\partial x_j} \tag{3.26}$$

$$\frac{\partial\overline{\rho}\widetilde{Y}_k}{\partial t} + \frac{\partial\overline{\rho}\widetilde{u}_j\widetilde{Y}_k}{\partial x_j} = \frac{\partial\overline{J}_{k,j}}{\partial x_j} + \overline{\dot{\omega}_k} - \frac{\partial\overline{\rho}(\widetilde{Y_k u_j} - \widetilde{Y}_k\widetilde{u}_j)}{\partial x_j} \tag{3.27}$$

$$\frac{\partial(\overline{\rho}\widetilde{h})}{\partial t} + \frac{\partial(\overline{\rho}\widetilde{u}_j\widetilde{h})}{\partial x_j} = \frac{\partial}{\partial x_j}\left(\overline{\alpha\frac{\partial h}{\partial x_j}}\right) + \frac{\partial\overline{p}}{\partial t} - \frac{\partial\overline{\rho}(\widetilde{u_j h} - \widetilde{u}_j\widetilde{h})}{\partial x_j} \tag{3.28}$$

The Favre-averaged governing equations (eqn. 3.25 - eqn. 3.28) contain additional unclosed terms: the unresolved Reynolds-stresses $(\widetilde{u_i u_j} - \widetilde{u}_i\widetilde{u}_j)$ in eqn. 3.26, the unresolved species $(\widetilde{Y_k u_j} - \widetilde{Y}_k\widetilde{u}_j)$ and the enthalpy fluxes $(\widetilde{h u_j} - \widetilde{h}\widetilde{u}_j)$ in eqn. 3.27 and in eqn. 3.28 and the filtered reaction source term $\overline{\dot{\omega}_k}$ in eqn. 3.27, which need to be modelled. The closure for the filtered reaction source term $\overline{\dot{\omega}}$ will be introduced in section 3.4.

3.3.1.2 Sub grid modeling

Unresolved Reynolds stresses

The unresolved Reynolds stresses ($\tau_{ij} = \widetilde{u_i u_j} - \widetilde{u}_i\widetilde{u}_j$) are modelled according to the Boussinesq hypothesis (like in the RANS approach, see section 3.3), which models the turbulent transfer of the momentum with a turbulent eddy viscosity ν_t and is closed by:

$$\tau_{ij} - \frac{1}{3}\delta_{ij}\tau_{kk} = -\mu_t\left(\frac{\partial\widetilde{u}_i}{\partial x_j} + \frac{\partial\widetilde{u}_j}{\partial x_i} - \frac{2}{3}\delta_{ij}\frac{\partial\widetilde{u}_k}{\partial x_k}\right) = -2\mu_\mathrm{sgs}\left(\widetilde{S}_{ij} - \frac{1}{3}\widetilde{S}_{kk}\delta_{ij}\right) \tag{3.29}$$

Different models for the eddy viscosity exist, which are either based on algebraic equations or transport equations for the turbulent kinetic energy. In this work the standard Smagorinsky model [174] is applied with an extension to compressible flows and a more advanced model, the σ-Nicoud model [147].

Compressible Smagorinsky model

The turbulent viscosity is calculated as:

$$\nu_t = C_k \Delta \sqrt{k_{\text{sgs}}} \tag{3.30}$$

where C_k is a model constant and k_{sgs} is the sub-grid scale kinetic energy, which corresponds to half of the isotropic sub-grid scale shear stress tensor $k_{\text{sgs}} = \tau_{kk}/2$. For incompressible flows, it is often absorbed into the filtered pressure $\overline{p}$ [155]. The sub-grid scale turbulence is modelled similar to an expression proposed by Yoshizawa [206]:

$$k_{\text{sgs}} = \frac{2C_k}{C_\epsilon} \Delta^2 \widetilde{S}^2 \tag{3.31}$$

In eqn. 3.31, C_ϵ denotes another model constant and $\widetilde{S}$ the resolved shear stresses, which are defined as:

$$\widetilde{S} = 2\sqrt{\widetilde{S}_{ij}\widetilde{S}_{ij}} \quad \text{with} \quad \widetilde{S}_{ij} = \frac{1}{2}\left(\frac{\partial \widetilde{u}_j}{\partial x_i} + \frac{\partial \widetilde{u}_i}{\partial x_j}\right) \tag{3.32}$$

Substituting eqn. 3.31 into eqn. 3.30 leads to the final expression of the turbulent viscosity, which resembles the formulation of the standard Smagorinsky model [174], with the model constant C_S.

$$\nu_t = \left(\underbrace{\sqrt{\frac{2C_k^{1.5}}{C_\epsilon^{0.5}}}}_{C_S} \cdot \Delta \right)^2 \sqrt{2\widetilde{S}_{ij}\widetilde{S}_{ij}} \tag{3.33}$$

For homogeneous isotropic turbulence C_S is typically set to 0.2 [155].

Advanced subgrid models

The weakness of the Smagorinsky model is that it relies on a model constant that must be adapted from case to case. To overcome this restriction, a dynamic procedure by Germano [69] was introduced, which calculates the appropriate model constant during the simulation. Another drawback of the Smagorinsky model is that the turbulent viscosity is over-predicted near the walls. Therefore, damping functions for the turbulent viscosity have been proposed, e.g. the van Driest damping [187]. New models have been recently developed, such as the WALE-model (Wall adapting local Eddy viscosity) [147] or the σ-model [148] where turbulent viscosity vanishes near the wall. In the scope of this work, the σ-model was used in chapter 6 to calculate the cold flow gas exchange and is compared against the compressible Smagorinsky model. It fulfils the following requirements of the turbulence [184]:

- Turbulent shear stress should decay towards the solid boundaries.
- The differential operator $\mathcal{D}_m$ should be zero for 2D flows $\left(\nu_t = (C_S\Delta)^2 \mathcal{D}_m(\mathbf{u})\right)$.
- The turbulent viscosity should be zero, in the case where the resolved scales are purely isotropic or anisotropic.

The σ-model combines all the aforementioned properties and is based on a single value decomposition of the velocity gradient tensor G_{ij} into three singular values ($\sigma_{i=1,2,3}$), which are the square roots of the eigenvalues of the tensor G_{ij}:

$$G_{ij} = \frac{\partial \widetilde{u}_k}{\partial x_i} \frac{\partial \widetilde{u}_k}{\partial x_j} \tag{3.34}$$

The differential operator $\mathcal{D}_m$ is then expressed as:

$$\mathcal{D}_m = \frac{\sigma_3(\sigma_1 - \sigma_2)(\sigma_2 - \sigma_3)}{\sigma_1^2} \quad \text{with} \quad \sigma_1 \geq \sigma_2 \geq \sigma_3 \geq 0. \tag{3.35}$$

Unresolved species and enthalpy fluxes
The unresolved species and enthalpy fluxes are modelled via a gradient assumption [155] and read:

$$(\widetilde{Y_k u_j} - \widetilde{Y}_k \widetilde{u}_j) = -\frac{\nu_t}{Sc_t} \frac{\partial \widetilde{Y}_k}{\partial x_j}, \tag{3.36}$$

$$(\widetilde{h u_j} - \widetilde{h} \widetilde{u}_j) = -\frac{\nu_t}{Sc_t} \frac{\partial \widetilde{h}}{\partial x_j} \tag{3.37}$$

with Sc_t being the turbulent Schmidt-number.

3.4 Premixed Turbulent Combustion Modeling

Depending on the intensity of the turbulence and the flame thickness, turbulent premixed combustion can be classified in different zones and regimes [151]. Figure 3.2 shows such a regime diagram for premixed turbulent flames. Inside this diagram, the boundaries of the different regimes are defined by the Damköhler-number (Da) and Karlowitz-number (Ka):

$$Da = \frac{\tau_l}{\tau_c} = \frac{l_l \; S_L}{l_F u'} \quad \text{and} \quad Ka = \frac{\tau_c}{\tau_\eta} = \frac{l_F \; u_\eta}{\eta S_L}. \tag{3.38}$$

In eqn. 3.38, τ_c is the chemical time scale, which describes the time that is needed for the flame to propagate with the laminar flame speed S_L, along a distance, which is equal to the laminar flame thickness l_F. The turnover time of the large eddies, with the size l_l and velocity u', is defined as $\tau_l = l_l/u'$ and for the smallest scales with $\tau_\eta = \eta/u_\eta$.

Within the combustion regime diagram, the thin reaction zone (a) denotes a region where the smallest vortices are smaller than the laminar flame thickness, but larger than the inner reaction zone. In the corrugated flamelet (b) and the wrinkled flamelet (c) regimes, the smallest scales are bigger than the reaction zone, thus are only able to push the flame front back and forth. It has to be mentioned that in the wrinkled flamelet regime, the turnover velocity of the biggest eddies cannot compete with the laminar flame velocity, meaning that the laminar flame propagation dominates this regime. In the broken reaction zones regime the Kolmogorov eddies are smaller than the inner layer thickness l_δ and can extinguish the flame.

It is difficult to define a unique combustion regime i.e. for the spark ignition engine, because

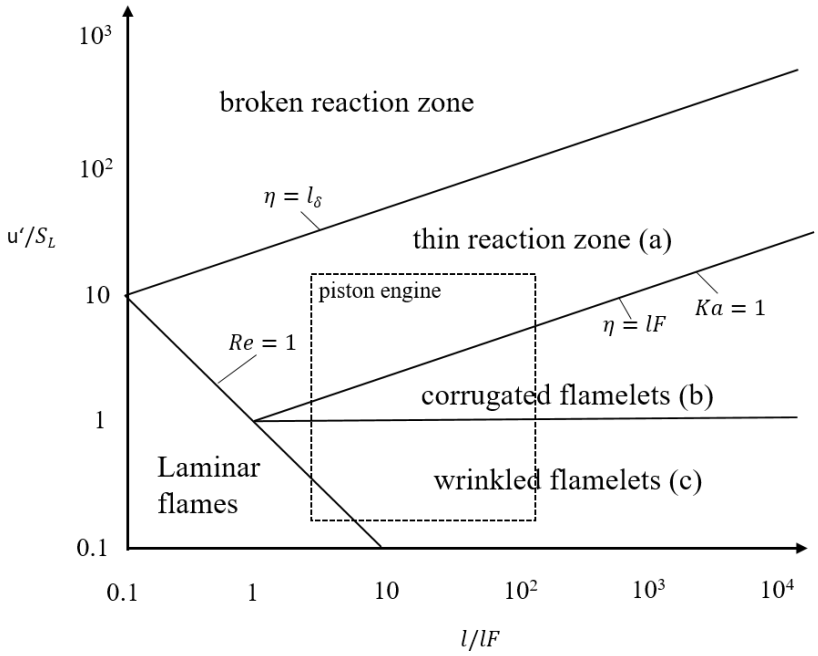

Figure 3.2: Premixed turbulent combustion regime diagram according to Peters [151]. The dashed box denotes the region of piston engines according to Poinsot [155].

it is operated at different engine speeds, different turbulent velocities, but also at different loads, which can cause a high amount of internal gas recirculation, hence decreasing the laminar flame speed. Under low to a mid-range engine speed and loads, the turbulent Reynolds-number is about Re ∼100-1000, the Damköhler-number Da ∼100 [155] and the smallest turbulent eddies are smaller than the laminar flame thickness. Here, the flame can be put into the flamelet regime. A flamelet is a thin reactive-diffusive layer, convoluted by the turbulent flow. In this regime the flame propagation time is smaller than the turnover time of the Kolmogorov eddies and the flame itself is thinner than the Kolmogorov scales. Hence, the eddies cannot penetrate into the thin reaction layer and are only able to wrinkle it. Since the reaction time is short and the reaction layer thin compared to the Kolmogorov scales, the flamelet approach can focus on the position of the flame, rather than on the complex chemistry in the reaction layer. The flamelet concept reduces the computational cost for the calculation of the chemistry, which can take a considerable amount of the total calculation time. Furthermore, this approach decouples the chemistry from the turbulence, since no chemical time scales will enter the calculation of the mean reaction rate [151].

3.4.1 Flame surface density modelling

In the context of the premixed combustion, the flamelet concept is based on a non-reactive progress variable $\widetilde{c}$, which defines a flame brush, bounded by $\widetilde{c}$ =0, which corresponds to a fully unburnt mixture and $\widetilde{c}$=1, for a fully burnt one. Since the progress variable describes the transformation of the unburnt mixture into burnt products, it is usually expressed with an unburnt ($\widetilde{Y_u}$) and burnt mass fraction ($\widetilde{Y_b}$) of a species that monotonically evolves through the flame brush. In a case where the flame is insensitive to heat losses, a definition

based on the unburnt temperature ($\widetilde{T}_u$) and burnt temperature ($\widetilde{T}_b$) is often used:

$$\widetilde{c} = \frac{\widetilde{Y} - \widetilde{Y_u}}{\widetilde{Y_b} - \widetilde{Y_u}} \quad \text{or} \quad \widetilde{c} = \frac{\widetilde{T} - \widetilde{T_u}}{\widetilde{T_b} - \widetilde{T_u}} \tag{3.39}$$

Within the scope of this thesis, the unburnt and burnt mass fractions and temperatures rely on a one-step chemistry mechanism. A mixture of iso-octane and air is taken for the reactive simulations, using the following global irreversible reaction [132]:

$$C_8H_{18} + \frac{1}{\Phi}12.5(O_2 + 3.76N_2) \rightarrow 8CO_2 + 9H_2O + \frac{3.76}{\Phi}12.5N_2 + 12.5\ (\frac{1}{\Phi} - 1)O_2 \tag{3.40}$$

The transport equation for the progress variable field reads:

$$\frac{\partial(\overline{\rho}\widetilde{c})}{\partial t} + \frac{\partial(\overline{\rho}\widetilde{u}_j\widetilde{c})}{\partial x_j} + \frac{\partial}{\partial x_j}\left(\overline{\rho}\widetilde{u_j c} - \overline{\rho}\widetilde{u}_j\widetilde{c}\right) = \frac{\partial}{\partial x_j}\overline{\left(\rho D\frac{\partial c}{\partial x_j}\right)} + \overline{\dot{\omega}} \tag{3.41}$$

On the right hand side of 3.41, the molecular diffusion with the diffusion coefficient D and the mean reaction rate $\overline{\dot{\omega}}$ appears, which can be modelled as:

$$\frac{\partial}{\partial x_j}\overline{\left(\rho D\frac{\partial c}{\partial x_j}\right)} + \overline{\dot{\omega}} \approx \rho_u S_L \Sigma_{\text{gen}} \tag{3.42}$$

In eqn. 3.42, Σ_{gen} denotes the generalized flame surface density (FSD) and can be obtained either from algebraic expressions or by a transport equation.

3.4.2 Algebraic flame surface density models

Many different algebraic FSD-models exist, for example by Angelberger [16], Boger [23], Charlette [38], Colin [41], Fureby [67] or Zimont [209], which all assume an equilibrium of the production and destruction of the flame surface. The performance of these models has been tested by Ma et al. [126]. In the scope of this thesis, the Keppeler [100], Muppala [142] and Weller [194] algebraic models are used.

Keppeler model

The most recent model is the Keppeler model [100], which is based on the fractal characteristics of the flame surface and assumes a self-similarity of the flame wrinkling between the small and the large scales. It was developed for flames within the corrugated and wrinkled flamelet regimes at elevated pressures (validated up to 20 bars). The implementation was generously provided by the Pfitzner research group (University of the Armed Forces, Munich) and was adapted from the regress-variable ($\widetilde{b} = 1 - \widetilde{c}$) to the progress variable notation. (The regress variable notation is widely used within the standard framework of OpenFOAM.)The Keppeler FSD-model reads:

$$\Sigma_K = \left(\mathcal{B} + (1-\mathcal{B})\,C_R\left(\frac{2.2\Delta}{l_F\ max(Ka_\Delta^{-1/2}, 2)}\right)^{(D-2)}\widetilde{c}(1-\widetilde{c})F(\widetilde{c})^{-1}\right)\left|\frac{\partial\widetilde{c}}{\partial x_j}\right| \tag{3.43}$$

with C_R being a model constant, which is set to 4.5. $\mathcal{B}$ is a blending function that reads:

$$\mathcal{B} = \exp(-\frac{\Delta}{\epsilon_i}\Theta) \tag{3.44}$$

where Θ is a model constant and set to 2.2, Δ is the filter width and ϵ_i the inner cut-off length. The blending function ensures that the flame surface density reduces to $|\nabla\widetilde{c}|$ for $\Delta \to 0$ and for $u'_\Delta \to 0$ [36]. More information about the Keppeler model can be found in section 7.3.2.1.

Muppala model
The second model is the Muppala model, which is chosen due to a pressure dependence in its formulation and reads:

$$\Sigma_M = \left[1 + \frac{0.46}{Le} Re_\Delta^{0.25} \left(\frac{u'_\Delta}{S_L}\right)^{0.3} \left(\frac{p}{p_0}\right)^{0.2}\right] \left|\frac{\partial\widetilde{c}}{\partial x_j}\right| \tag{3.45}$$

where Le denotes the Lewis number, u'_Δ are the turbulent sub-grid fluctuations and Re_Δ is the Reynolds number inside a computational cell. More information and its performance compared to the Keppeler model is shown in chapter 7.

Weller model
Finally, the Weller model [194] is used, which comes with the standard OpenFOAM version and was only rewritten and adapted to the commonly used progress variable notation found in the literature and reads:

$$\Sigma_\mathrm{W} = 1 + 2\widetilde{c}\left(1 + 0.62\sqrt{\frac{u'_\Delta}{S_L}} Re_\eta\right) \left|\frac{\partial\overline{c}}{\partial x_j}\right| \tag{3.46}$$

where Re_η denotes the Kolmogorov Reynolds-number. Unlike to the Keppeler and Muppala models, the gradient of the Reynolds-averaged progress variable field is used, which requires the additional modelling of the counter-gradient-transport (CGT) [126]. The Weller model is described additionally in greater detail in chapter 9.

3.4.3 Transport of the flame surface density

The algebraic models for the flame surface density assume that the sub-grid production and the destruction of the flame brush is in equilibrium, which is not always true. For example, the ignition phase describes an extreme case, where the algebraic equations will fail in predicting the flame kernel growth. In order to include non-equilibrium states, a balance equation for the flame surface density was introduced by Pope [156], Candel and Poinsot [34] and is known as the coherent flame model (CFM). It was extended by Colin et al. [40] (ECFM) for RANS simulations of highly stratified combustion in spark ignition engines, together with the Arc-and-Kernel-Tracking-Ignition model (AKTIM) [53]. It was later adapted by Richards et al. [160] to LES (ECFM-LES). Recently, the ECFM-LES was coupled with an ignition model by Colin and Truffin [42], which accounts for a better description of the flame kernel growth (Imposed Stretch Spark Ignition Model - ISSIM).

Since many other authors and different engine CFD-codes have included the ECFM-LES model for the simulation of the spark ignition engines, the ECFM-LES is presented here

for the sake of completeness and its closed form according to Richard et al. [160] reads:

$$\frac{\partial \Sigma}{\partial t} = T_{\text{res}} + T_{\text{sgs}} + S_{\text{res}} + S_{\text{sgs}} - P + C_{\text{res}} + C_{\text{sgs}} \tag{3.47}$$

with T_{res} being the resolved transport of the flame surface, which reads:

$$T_{\text{res}} = -\frac{\partial}{\partial x_j}\left(\widetilde{u_j}\Sigma\right) \tag{3.48}$$

The sub-grid scale contribution of the transport of the flame surface is calculated by:

$$T_{\text{sgs}} = \frac{\partial}{\partial x_j}\left(\sigma_c \nu_t Sc_t^{-1} \frac{\partial \Sigma}{\partial x_j}\right) \tag{3.49}$$

where σ_c denotes a correction factor to ensure that enough grid points are placed inside the flame, which depends on the chosen combustion filter $\hat{\Delta}$ (similar to the AFT approach in section 3.4.4). The resolved strain rate is expressed by:

$$S_{\text{res}} = \left(\frac{\partial \widetilde{u_j}}{\partial x_j} - (n_i n_j)\frac{\partial \widetilde{u_i}}{\partial x_j}\right)\Sigma \tag{3.50}$$

and the unresolved strain rate by:

$$S_{\text{sgs}} = \sigma_c^{-1}\Gamma(\hat{u}' S_L^{-1}, \hat{\Delta}\delta_l^{-1})\hat{u}'\hat{\Delta}^{-1}\Sigma \tag{3.51}$$

where $\hat{u}'$ are the turbulent fluctuations at the combustion filter scale and n_j is the normal vector of the iso-surface of the filtered progress variable. The resolved propagation part reads:

$$P = \frac{\partial}{\partial x_j}(S_d n_j \Sigma) \tag{3.52}$$

and the resolved curvature of the flame reads:

$$C_{\text{res}} = S_d \frac{\partial n_j}{\partial x_j}\Sigma \tag{3.53}$$

with S_d being the flame displacement speed. The unresolved part of the flame curvature is expressed by:

$$C_{\text{sgs}} = \beta S_L (c^* - \overline{c})\overline{c}^{-1}(1-\overline{c})^{-1}(\Sigma - \Sigma^{\text{lam}})\Sigma \tag{3.54}$$

according to Veynante et al. [191].

It has to be mentioned that, due to the high complexity of this model, implementing it to a CFD-code is prone to implementation errors. Due to lacking in validation data and limited time, the ECFM-LES model was omitted in the scope of this thesis. However, it has been implemented into the engine simulation workflow proposed here within a Master Thesis project [192] under the authors supervision and applied to the same engine.

3.4.4 Artificial flame thickening

One drawback of the FSD approach is, that there is no control of the flame brush thickness, where the flame thickness is purely governed by the size of the grid and may even become smaller than the laminar flame thickness with $\Delta_x < l_F$. Most of the time, the grids are too coarse to describe the flame brush properly and an increase of the spatial resolution is not affordable. In order to circumvent these problems, the flame can be literally thickened on the computational mesh by introducing a thickening factor $\mathcal{F}$ as proposed by Butler and O'Rourke [33]. By taking the model from Williams [201] and Kuo [111] to express the laminar flame speed and thickness, the idea of the flame thickening can be illustrated. They state that the laminar flame thickness l_F and flame speed S_L is related to the diffusion coefficient D and reaction rate $\dot{\omega}$ by:

$$S_L \sim \sqrt{D\dot{\omega}} \tag{3.55}$$

$$l_F \sim \sqrt{\frac{D}{\dot{\omega}}} \tag{3.56}$$

Multiplying the diffusion coefficient by $\mathcal{F}$ and dividing the reaction rate by $\mathcal{F}$ in eqn. 3.55 and 3.56, only the flame thickness will be increased without affecting the flame speed. The disadvantage of this method is, that it affects the turbulence-chemistry interaction, which can be explained with the definition of the Damköhler number (see eqn. 3.38). Depending on the value of $\mathcal{F}$, the chemical length scales become more important than the flow-dependent length scales, which leads to a smoother flame front as it was also observed by DNS calculations of a turbulent premixed flame by Angelberber et al. [16] and Colin et al. [41]. In order to account for this effect, an efficiency function $\mathcal{E}$ has been proposed by Colin et. al [41] and Charlette et al. [38], who introduce a dependency on the grid size, turbulent sub-grid fluctuations and laminar flame speed. Later, a flame sensor was added to the efficiency function $\mathcal{E}$ by Legier et al. [117] to assure that the thickening is solely applied in the reaction region. The artificial thickening is applied to the species transport equation and absolute enthalpy equation as:

$$\frac{\partial \rho Y_k}{\partial t} + \frac{\partial \rho u_j Y_k}{\partial x_j} = \frac{\partial}{\partial x_j}\left(\mathcal{E}\mathcal{F} D_k \frac{\partial Y_k}{\partial x_j}\right) + \frac{\mathcal{E}\dot{\omega}_k}{\mathcal{F}} \tag{3.57}$$

$$\frac{\partial (\rho h)}{\partial t} + \frac{\partial (\rho u_j h)}{\partial x_j} = \frac{\partial}{\partial x_j}\left(\mathcal{E}\mathcal{F}\alpha \frac{\partial h}{\partial x_j}\right) + \frac{\partial p}{\partial t} \tag{3.58}$$

4

Numerical Approach

In this chapter, the numerical methods, needed to solve a system of partial differential equations, are presented and demonstrated for a transport equation of an arbitrary scalar. Furthermore, approximations for the temporal and spatial terms are discussed, where the accuracy and stability of the convective fluxes for engine flows are emphasised. A switch between a low- and high accuracy scheme based on the local Mach-number is proposed, to overcome problems at valve opening and closing. Furthermore, the solution algorithm, which couples pressure, velocity and density together, for compressible flows at arbitrary Mach-number, is shown. Finally, the simulation and the meshing workflow for LES engine simulations based on the CFD-code OpenFOAM are presented.

4.1 Finite Volume Method

In order to solve the governing equations described in section 3, the Finite Volume Method (FVM) is applied, where the integral form of the governing equations is discretized over a finite number of volumes. Figure 4.1 illustrates a discretized box by cell elements. Note that those grids can consist of any kind of shaped cells, which obey certain grid quality criteria, which are discussed in the subsection 4.2 [95].

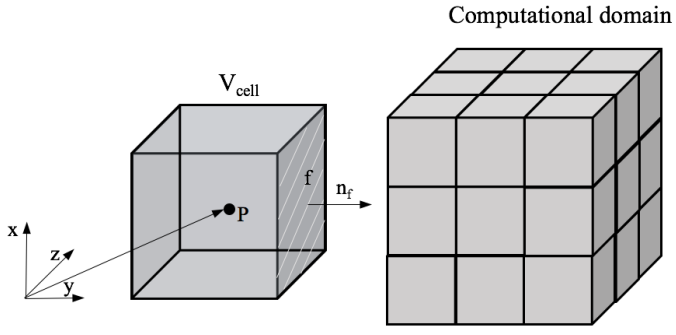

Figure 4.1: Example of a spatially discretized box by cubic volumes (cells).

Equation 4.1 represents a transport equation for an arbitrary scalar ϕ, where the first term is the temporal accumulation, the second term determines the convective transport of ϕ in and out of the volume with the convection velocity u_i, the third term describes the diffusion of ϕ with the general diffusion constant Γ_ϕ and the last term S_ϕ is the corresponding source

term, which can be dependent or independent of ϕ.

$$\underbrace{\frac{\partial \rho\phi}{\partial t}}_{\text{Accumulation}} + \underbrace{\frac{\partial(\rho\phi u_i)}{\partial x_j}}_{\text{Convection}} - \underbrace{\frac{\partial}{\partial x_j}\left(\Gamma_\phi \frac{\partial \phi}{\partial x_j}\right)}_{\text{Diffusion}} = \underbrace{S_\phi}_{\text{Source term}} \tag{4.1}$$

The Gauss theorem [140] is applied to transform eqn. 4.1 into the integral form:

$$\frac{\partial}{\partial t}\int_{V_p} \rho\phi dV + \int_{V_p} \frac{(\rho\phi u_i)}{\partial x_j} dV - \int_{V_p} \frac{\partial}{\partial x_j}\left(\Gamma_\phi \frac{\partial \phi}{\partial x_j}\right) dV = \int_V S_\phi dV \tag{4.2}$$

According to the Gauss theorem, the volume integral of the divergence of a vector field is related to a net flux of the vector field over the closed surface S of the corresponding volume.

$$\left(\frac{\partial \rho\phi}{\partial t}\right)_p + \oint_S \mathbf{n}_f (\rho\phi u_i)_f dS - \oint_S \mathbf{n}_f (\Gamma_\phi)_f \left(\frac{\partial \phi}{\partial x_j}\right)_f dS = \int_V (S_\phi)\, dV \tag{4.3}$$

In Equation, 4.3 the divergence operators are replaced by the surface fluxes, where n_f denotes the vector normal to the surface S. The subscripts f and P denote the corresponding values evaluated either at the cell face or at the cell centre.
The information is transferred from cell to cell by the face fluxes, therefore the value of ϕ depends on the neighbouring cells. This leads to a coupled system of equations - one equation for each dependent variable of the control volume. One way to solve this set of equations is by linearization and conversion into algebraic equations of the following form [189]:

$$a_p \phi_P + \sum_N a_N \phi_N = R_P \tag{4.4}$$

In eqn. 4.4, the subscript N denotes all neighbouring cells of the cell P and R_P the source terms. The coefficients a_p and a_N depend on the approximations of the diffusion and convection fluxes of eqn. 4.3.

4.2 Spatial discretization

According to eqn. 4.3, the face fluxes are evaluated at the face centres. Since the values of the dependent variables are stored in the middle of the cell within the FVM approach, the cell value has to be interpolated on the face. Several approximations exist with different stability and accuracy properties. If we consider an upwind differencing scheme (UDS), the value of the face would be calculated only by the upstream cell. This assumption might be correct for super-sonic flows (Ma>1), where the transport of any information is only affected by the upstream side (hyperbolic problem). For small Mach-numbers (Ma$\ll$1), a point in the domain will be affected by all surrounding points (elliptic problem). Figure 4.2 shows three cells P, W and E, with the corresponding interfaces w and e. Assuming that the values of ϕ at the grid points are known, the value ϕ_e at the interface e can be obtained by linear interpolation:

$$\phi_\mathrm{e} = f_\mathrm{e}\phi_\mathrm{P} + (1 - f_\mathrm{e})\phi_\mathrm{E} \tag{4.5}$$

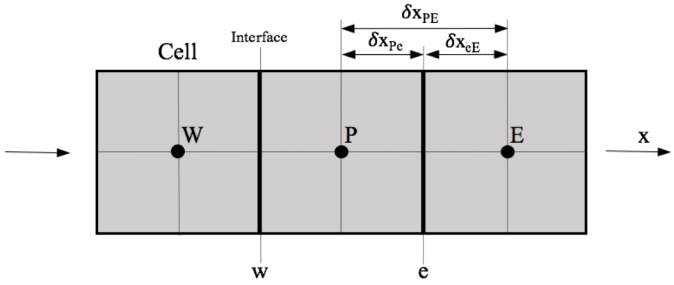

Figure 4.2: Three cells with interfaces w and e.

where f_e denotes the interpolation function and reads for a **central differencing scheme** (CDS):

$$f_\mathrm{e} = \frac{\delta x_\mathrm{eE}}{\delta x_\mathrm{PE}} \tag{4.6}$$

This scheme is second-order in space, but can lead to oscillations for abrupt changes of the fluxes. A more robust, but also more dissipative scheme, is the **upwind differencing scheme** (UDS), which assigns directly the cell value to the interface [95] dependent of the flow direction F_x:

$$\phi_\mathrm{e} = \phi_\mathrm{E}, \; F_x < 0 \tag{4.7}$$

$$\phi_\mathrm{e} = \phi_\mathrm{P}, \; F_x \geq 0 \tag{4.8}$$

The Total Variation Diminishing (TVD) schemes combine a high-order (HO) numerical scheme and a lower-order (LO) differencing scheme by a weighting coefficient $\Phi(r)$ according to the following equation [95]:

$$\phi_\mathrm{e} = (\phi)_\mathrm{LO} + \Phi(r)\left[(\phi)_\mathrm{HO} - (\phi)_\mathrm{LO}\right] \tag{4.9}$$

For $\Phi(r)$ a vast number of different limiter functions exist. A detailed description of the limiter functions can be found in the books of Ferziger and Perić [59] or Versteeg and Malalasekera [189]. Within this work the Sweby limiter [179] was chosen, which reads:

$$\Phi(r) = \max\left(\max\left(\frac{2r}{k}, 1\right), 0\right) \tag{4.10}$$

where k is an user defined $0 \geq k \geq 1$. For k=1, eqn. 4.9 is TVD conforming (meaning that the total variation of the discrete solution has to diminish with the time) and working at the edge of the Sweby TVD limit region. The weighting $\Phi(r)$ can be interpreted as a flux-limiting function, with r being the consecutive gradients of the dependent variable. Following the notation introduced in figure 4.2, the function for r reads [95]:

$$r = \frac{\phi_P - \phi_W}{\phi_E - \phi_P} \tag{4.11}$$

Also the gradients need to be evaluated at the interfaces between the cells. The gradient of ϕ on an orthogonal grid is obtained from:

$$\mathbf{n}_f \, (\nabla\phi)_f = |\mathbf{n}_f| \frac{|\phi_P - \phi_E|}{\overline{PE}}, \tag{4.12}$$

where $\overline{PE}$ denotes the distance between the cells P and E.

Non-orthogonal correction

Figure 4.3 illustrates a case with a non-orthogonal grid, which requires a correction in order to maintain the second-order accuracy. In particular during the valve motion, the

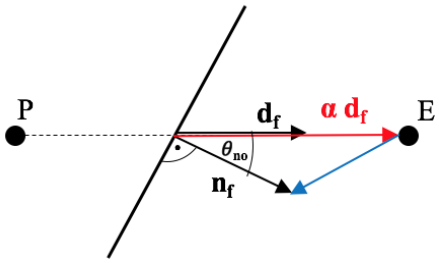

Figure 4.3: Correction procedure for the calculation of the gradients on the cell faces for non-orthogonal grids.

mesh non-orthogonality may increase [95]. The gradient on the faces of a non-orthogonal grid can be calculated by:

$$\mathbf{n}_f \left(\frac{\partial\phi}{\partial x_j}\right)_f = \underbrace{\alpha\mathbf{d}_f \left(\frac{\phi_P - \phi_E}{|\mathbf{d}|}\right)}_{\text{orthogonal}} + \underbrace{(\mathbf{n}_f - \alpha\mathbf{d}_f)\left(\frac{\phi_P - \phi_E}{|\mathbf{d}|}\right)}_{\text{non-orthogonal}} \tag{4.13}$$

In eqn. 4.13, $\mathbf{n}_f$ denotes the surface normal vector of the interface, $\mathbf{d}$ the distance vector between the cell centres of cell P and E, $\mathbf{d}_f$ is the projection of $\mathbf{n}_f$ on $\mathbf{d}$ and α a weighting coefficient defined as a function of the mesh orthogonality θ_{no} as:

$$\alpha = \frac{1}{\cos(\theta_{\text{no}})} \tag{4.14}$$

As the mesh non-orthogonality increases, the stability decreases, because the non-orthogonal correction part is treated explicitly, whereas the orthogonal part is treated implicitly. It is therefore recommended to use the correction only for $\theta_{\text{no}} < 60°$. For higher values of θ_{no}, the correction can be switched off. A detailed description of the discretization methods implemented in OpenFOAM can be found in the PhD thesis of Jasak [95].

CDS-TVD switch for engine simulations

The discretization of the divergence of ρu_i in the momentum equation has to be approximated as accuratly as possible, because it will be used for the convective transport in all consecutive transport equations. It is inevitable to discretize this term with a CDS-scheme for an accurate LES of a reactive flow. A TVD-scheme would be already too diffusive, which may lead to an incorrect turbulent intensity inside the combustion chamber, thus leading to weak flame wrinkling and therefore to a wrong flame propagation. Unfortu-

nately, for steep velocity gradients or even high velocities ($Ma > 0.3$), a CDS-scheme can lead to strong oscillations, which can lead to unphysical results, too. Inside an engine, the velocities are usually quite low ($Ma < 0.1$), but can exceed a Mach-number of one at the opening and closing events. In this case, a CDS-scheme might not be appropriate due to possible numerical oscillations. Therefore, a CDS-TVD switch was implemented as a function of the local Mach-number. It is based on the *limitedLinear* discretisation scheme of OpenFOAM, which is basically a TVD-scheme that uses a CDS-scheme for the higher order discretization term (eqn. 4.9) and for $\Phi(r)$, it uses the Sweby limiter (eqn. 4.10) function. For $Ma > 0.3$, $\Phi(r)$ is set to 1 and the LO-scheme of 4.9 will be cancelled out. CDS is imposed everywhere else in the domain.

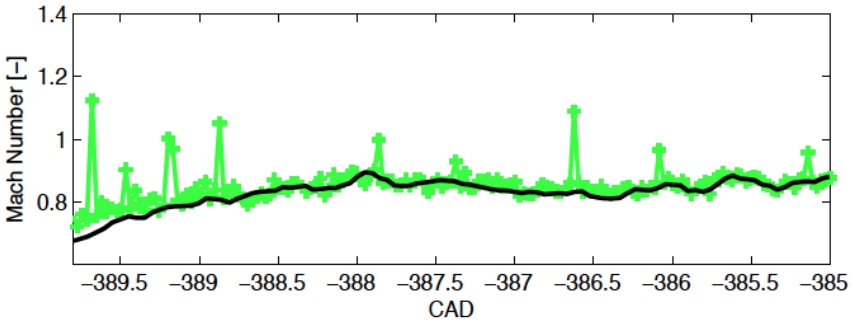

Figure 4.4: Maximum Mach-number plotted over the °CA within the intake stroke, for a pure CDS-scheme (green) and the CDS-TVD switch (black) [145].

The scheme was first tested for a cold flow LES engine simulation [145] of the optical research engine of the University of Duisburg-Essen. In Figure 4.4, the evolution of the maximum Mach-number is plotted over a few crank angle degrees within the intake stroke with opened intake valves. The Mach-number is oscillating and peaking with the CDS-scheme, but stays rather smooth for the CDS-TVD scheme. It must be stressed that, the switch only kicks in at the valve seat region during the opening and closing events, so that a TVD-scheme is applied. The CDS-scheme is applied everywhere for the convective fluxes of the momentum equation.

4.3 Temporal discretization

In eqn. 4.15 the semi-discretized form of the transport equation (eqn. 4.1) using the explicit Euler method is shown:

$$\frac{\rho\phi_P^n - \rho\phi_P^o}{\Delta t}V_p + \sum_f F\phi_f - \sum_f (\Gamma_\phi)_f \mathbf{n}_f S_f \cdot (\nabla\phi)_f = S_u V_P + S_P V_P \phi_P \tag{4.15}$$

where F denotes the convective fluxes, Δt the time step width and S_u and S_P the source terms, which can be either dependent or independent of ϕ. It is first order accurate in time and uses only values from the previous time step t^o. Since only values from the old time step t^o are used to evaluate the dependent variables of the new time step t^n, the time step Δt width has to comply with the Courant-Friedrichs-Lewy (CFL) stability criterion,

where the CFL-number has to be lower than one:

$$\mathrm{CFL} = \frac{u_i \Delta t}{\Delta x} \tag{4.16}$$

A CFL-number lower than one means that for a given time step width Δt, the information is not travelling over more than one cell of the size Δx.

In order to circumvent the problem of too small time step widths caused by high velocities or small cell sizes (complying with CFL=1), the time derivatives can be solved implicitly. Implicit methods yield a stable solution without a restrictions to a CFL-number. They require an iterative solution procedure, because values of the given time step are involved, which are usually not known. The Euler backward scheme belongs to the implicit methods, is second-order accurate in time and uses values from three time levels, from the current time step ϕ^n, the previous time step ϕ^o, and even one before ϕ^{oo}:

$$\frac{\frac{3}{2}\rho\phi_P^n - 2\rho\phi_P^o + \frac{1}{2}\rho\phi^{oo}}{\Delta t} V_\mathrm{p} + \sum_f F\phi_f^n - \sum_f (\Gamma_\phi)_f \mathbf{n}_f \cdot (\nabla\phi)_f^n = S_u V_P + S_P V_P \phi_P^n \tag{4.17}$$

In the scope of this thesis, the Euler backward implicit scheme was chosen in order to benefit from a bigger time step size, because the differences in the velocity and geometrical scales can be sometimes very big inside an engine within a given time step (for example during the gas exchange phase). The highest velocities usually appear within a few cells in the valve seat region, where the flow is rather streaming straight through it, thus using a CFL-number bigger than one, might be acceptable.

4.4 Pressure-Velocity-Density coupling

The fluid is exposed to compression and expansion ($Ma \ll 1$) by the piston and, during opening and closing events, even to compression shocks ($Ma > 1$), which require the solution of the fully compressible flow equations for mass, momentum and total energy (see section 3.1). For compressible flows the ideal gas equation can be used to combine pressure, temperature and density. The fully compressible formulation does not require a special algorithm to iteratively find the pressure field and is therefore easier to implement in CFD-codes. Unfortunately, the stability criterion is now not only based on the convective fluid velocity, but also on the speed of sound. Issa [91] and later Demirdžić et al. [46] developed a flow solver for arbitrary Mach-numbers based on the PISO-algorithm, which is widely used to calculate the gradient of the pressure for incompressible flows. The main difference to the classical PISO-method is, that a state equation is invoked to couple density, pressure and temperature. The pressure equation can be derived by applying the divergence to the semi-discretized momentum equation and combining it with the continuity equation (see eqn. 4.21). For the sake of clarity, this method will be denoted as pressure-based approach. The complete derivation of the pressure equation can be found in the work of Demirdžić et al. [46] and in the book of Ferziger [59]. It must be noted that the time derivative is kept, (which is not the case for the incompressible Poisson-pressure equation) and that the compressibility effects are introduced by Ψ:

$$\Psi = \frac{d\rho}{dp} = \frac{1}{RT} \tag{4.18}$$

It must be stressed that this formulation can handle low and high Mach-number regimes. However, sharp gradients, as they will appear along a shock, will not be predicted as accurately as with the classical density-based approach. For an engine simulation, this formulation can be seen as a good compromise between accuracy and computational costs. The approach was tested against a real density-based compressible flow solver for a cold flow engine simulation of an optically accessible spark-ignition engine [145]: even though the density-based solver was much faster during one time step, it suffered from very low time step sizes, five times lower than those for the pressure-based approach, during the compression and expansion phase. The overall computational cost was similar and therefore the pressure-based algorithm chosen within the scope of this thesis.

Solution algorithm
The pressure-based algorithm will be briefly explained. The notation is based on the implementation by Jasak [95].

1. Solve the momentum equation with the pressure field from the previous time step (Momentum predictor).

2. Extract the coefficients a_p and the off-diagonal terms H of the linearized momentum equation. H denotes all the coefficients a_N of the linearized momentum equation, including the source terms, but excluding the pressure.

3. Recalculate the velocity from the coefficients H and a_p:

$$u_i = \frac{H}{a_p} \tag{4.19}$$

4. Recalculate the fluxes (note: flux field is not divergence free):

$$\phi_d = \Psi \left(\rho \frac{H}{a_p} \right) \frac{1}{\rho} \tag{4.20}$$

5. Solve for the pressure with non-divergence free fluxes. The compressibility is in Ψ:

$$\frac{\partial(\Psi p)}{\partial t} + \nabla \cdot (\phi_d \, p) - \nabla \cdot \left(\frac{\rho}{a_p} \nabla p \right) = 0 \tag{4.21}$$

6. Correct the velocity field:

$$u_i = \left(\frac{H}{a_p} \right) - \left(\frac{1}{a_p} \nabla p \right) \tag{4.22}$$

For the PISO-algorithm, steps 2-5 are repeated at least two times. If the convergence of the flow field cannot be obtained, the loop will start from step 1 with the last corrected flux.

4.5 Mesh Motion

The motion of the mesh is one of the main reasons why CFD simulations of internal combustion engines may not be so advanced as simulations of non-moving systems. In particular, the large displacement of the piston and the inclined valves are severe constraints

to the mesh morphing. During the years, different approaches have been used and adapted for the motion of the engine parts. These methods can be classified into:

- Mesh morphing without topological changes of the grid [160] [54]
- Mesh morphing and additional topological changes (addition and removal of cells) [123] [138]
- Immersed-boundary methods [190] [137] [145]
- Run-time meshing [172]

The mesh morphing methods without topological changes can be seen as the easiest way to deal with the moving parts. Only the mesh nodes are moved based on the motion or displacement of the piston and the valves. An advantage of this method is that the number of cells is not changing, making this method easy to implement, even in CFD-codes that are using unstructured grids. However, this approach would lead to an undesirable stretching or compressing of the cells, if one would use it for the entire displacement of the piston. Therefore, the cycle of the engine has to be split into several intervals. For each interval, the mesh is morphed up to a predefined time and the results are then mapped to a new grid, which is conform with the piston and the valve positions of the previously morphed mesh. This approach is currently used by different groups [160], where the number of intervals is governed by the engine geometry and the structure of the mesh. For example, Enaux et al. [54] used 41 grids to cover a complete cycle of a single-cylinder spark ignition engine, using tetrahedral cells with an average grid spacing of 0.8 mm. The influence of the mesh motion on the results and on the sub-filter modelling was studied by Keskinen et al. [103], Leonard et al. [118] and Toledo et al. [186], stating that only minor influences of the mesh motion on the flow field are observed, for not too large displacements (that also depend on the cell structure).

In order to avoid the tremendous effort of generating many computational grids, people often manipulate the topology of the mesh by removing and adding cells. For the motion of the piston, layers of cells are added in the expansion and removed in the compression stroke. This technique requires cell layers with a constant layer height that are perfectly aligned with the piston. Since the topology of the mesh changes due to the addition and removal of the cells, the CFD-codes became very complex. This is especially evident when dealing with parallel computations, where the communication between the boundaries for the topologically changing domains has to be taken into account. Engine simulations with topological changes based on OpenFOAM technology, were performed by Lucchini et al. [123], or recently by Montorfano et al. [138]. In terms of the computational performance, the dynamically changing meshes can lead to load balancing problems during the simulation, where some processors will have a static number of cells and others only a few or many. Mesh motion capabilities with and without topological changes are provided also by commercial CFD-codes, like Ansys [1], Star-CD [11], AVL-Fire [3] or KIVA [7].

The immersed-boundary method is a very elegant way of dealing with the moving objects, since no meshing is required. Only a background mesh on which the moving or non-moving solid parts are immersed has to be created. The difficulty lies in the sharp representation of the surfaces. Engine simulations with immersed boundaries have been successfully run by Verzicco et al. [190], Mittal et al. [137] or Nguyen et al. [145].
Alternatively, new grids can be generated during run-time after each time step. Obviously

the meshing has to be done in a very efficient way. One example for a run-time meshing approach for an engine simulation using the CFD-code Converge [4], can be found in the work of Senecal et al. [172].

Influence of the mesh motion on the governing equations

Due to the cell motion, the cell volume V_{cell} might change by ΔV_{cell}, which has to be taken into account by the governing equations. In order to have a consistent set of governing equations on a moving grid, the change of the control volume to the coordinate frame velocity has to obey the space conservation law (SCL) [47]:

$$\frac{d}{dt}\int_V dV - \oint_S (\mathbf{n}_f \cdot u_{\text{cell},j})\, dS = 0 \tag{4.23}$$

where $u_{\text{cell},j}$ is the velocity of the moving cell volume. If the SCL is not satisfied, errors will occur by adding artificially mass to the system. In OpenFOAM, the SCL is applied directly to the governing equation by adjusting the convective face flux, with the velocity of the corresponding moving face:

$$F_{\text{rel}} = \rho_f \mathbf{n}_f \cdot (u_j - u_{\text{cell},j})\, S_f \tag{4.24}$$

The discretized form of eqn. 4.25 on a moving grid reads:

$$\frac{3\rho_p\phi_P^n V_p^n - 4\rho_p\phi_P^o V_p^o + \rho_p\phi_p^{oo} V_p^{oo}}{2\Delta t} + \sum_f F_{\text{rel}}\phi_f^n - \sum_f (\Gamma_\phi)_f \mathbf{n}_f S_f \cdot (\nabla\phi)_f^n = S_{\text{u}} V_P^n + S_P V_P^n \phi_P^n \tag{4.25}$$

Now the displaced volumes for the two time levels ^{o} and ^{oo} must be calculated and stored.

Displacement vs. velocity mesh motion strategies

In the presented work, a mesh motion strategy without topological changes is applied. A Laplace equation is solved, which yields either a smooth mesh deformation velocity field $u_{\text{cell},j}$:

$$\frac{\partial}{\partial x_j}\left(\gamma \frac{\partial u_{\text{cell},j}}{\partial x_j}\right) = 0\ , \tag{4.26}$$

or a cell displacement field $x_{\text{cell},j}$

$$\frac{\partial}{\partial x_j}\left(\gamma \frac{\partial x_{\text{cell},j}}{\partial x_j}\right) = 0 \tag{4.27}$$

In eqn. 4.26, γ denotes a user-defined stiffness of the mesh motion, which can be expressed as a function of the distance between the moving boundaries and is used to control the mesh motion. Here, the stiffness-constant is calculated as the quadratic inverse distance l^2 to the cylinder head and piston:

$$\gamma = \frac{1}{l^2} \tag{4.28}$$

The boundary conditions for eqn. 4.26 are no-slip conditions for the non-moving parts, except for the stems of the valves and the liner, were a zero-gradient boundary condition is applied. For the moving boundaries, the velocity ($u_{b,j}$) of the piston and the valves is

directly imposed. For the cell displacement formulation, the displacement of the moving boundary $x_{\mathrm{disp},j}$ is directly applied (relative to a reference position ($x_{\mathrm{ref},j}$)). After solving the mesh motion equation, the displacement of the nodes is calculated from the velocity-based formulation as:

$$x_j^{\mathrm{new}} = x_j^{\mathrm{old}} + u_{b,j}\ \Delta t, \tag{4.29}$$

or from the cell-displacement formulation as:

$$x_j^{\mathrm{new}} = x_{\mathrm{ref},j} + x_{\mathrm{disp},j}. \tag{4.30}$$

As mentioned previously, the velocity of the moving boundaries is used together with the time step width to calculate the displacement. Hence, the displacement of the moving boundary is only first-order accurate in time, therefore a small time step is needed to ensure a good overlapping between the grids. A good overlapping between the grids is important to avoid losing or adding any mapped quantities. In figure 4.5, the in-cylinder volume and the in-cylinder mass for a portion of the compression and expansion stroke (from 20°bTDC to 40°aTDC) is shown. Both quantities were calculated with the cell- and velocity-based mesh motion strategies with different CFL-numbers. The results were mapped every 5°CA on a new mesh. In the upper graph of figure 4.5, the in-cylinder volume seems to be a continuous function at the intersections of the mapping intervals. However, from the in-cylinder mass, one may notice that the mass is not conserved during the mapping. The difference of the mass during the mapping intervals is caused by a mismatch of the source and the target grids, which is attributed to the first-order approximation in time (eqn. 4.29). Obviously, with smaller time steps, a better grid overlapping is achieved, which is demonstrated for CFL=2 and CFL=0.5. Independently on the CFL-number, the cell displacement formulation (eqn. 4.27) yields an almost perfect overlap and no mass is lost or added during the mapping.

4.6 Grid generation

The requirements for the computational grids of an engine simulation are tremendous, not only because they have to comply with the mesh motion strategy, but also because high-order numerical schemes must be applicable, different flow orientations taken into account and an accurate description of geometrical features must be enabled (such as the valve seat region). Fulfilling all these requirements lead to an enormous time-consuming job - bearing in mind that for the mesh motion strategy with mapping, more than 100 grids are often necessary. Therefore, the application of the mapping approach can only be justified if the grid generation can be performed automatically. Fortunately, fully-automated grid generators exist, for example snappyHexMesh, which is the automated grid generator of OpenFOAM. Alternatively, the meshing can be done with commercial grid generators, like Gambit [1], which can be controlled and automated. This method was used at the beginning of this thesis for the research engine of the University of Duisburg-Essen [93]. In terms of industrial applicability and costs, an approach based on open source products can be attractive, thus snappyHexMesh was finally used. The effort of building a "low-oriented" grid for a combustion engine is considerable and even more difficult to embed into an automated meshing work-flow. Therefore, it was decided to keep the cells inside the complete combustion chamber equidistant, refined and adapted only to the walls. This strategy has proven to be quickly applicable to a new engine geometry, and possible errors in the calculation of the shear stresses of the intake jet have been tolerated.

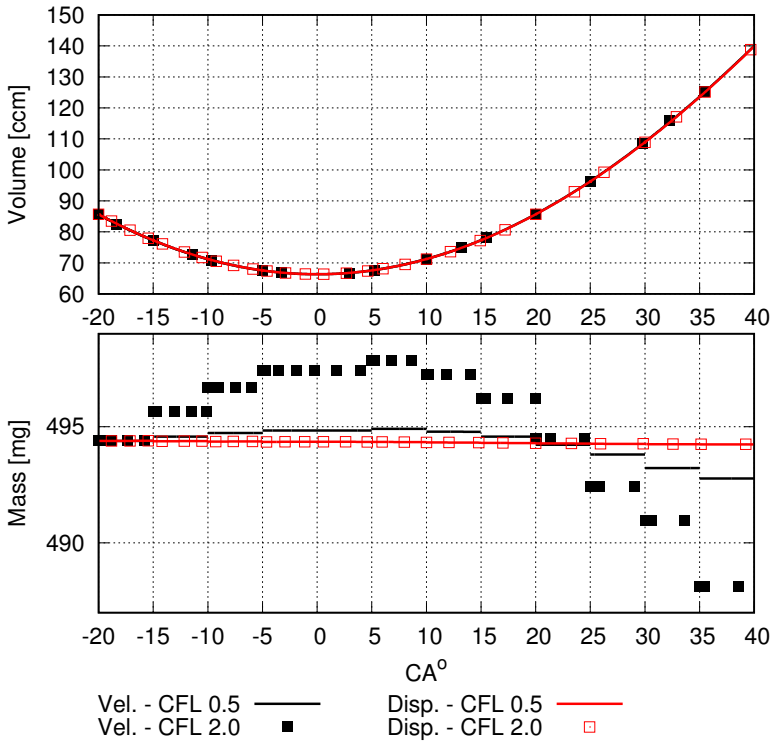

Figure 4.5: Displacement volume and in-cylinder mass of the "Darmstadt" optical research engine within the compression and expansion stroke (20°bTDC → 40 °aTDC) calculated with the velocity- and displacement-based mesh motion approach with different CFL-numbers.

SnappyHexMesh - Working principle

Based on snappyHexMesh, a mesh generation strategy for engine simulations was developed. The most important steps will be now briefly elaborated.

SnappyHexMesh needs a STL (STereoLithography) file of the geometry. By the STL file, the surface of the geometry is described by triangles, saved as a list, where the individual triangles are represented by three points and a normal vector. All triangles of the STL have to create a "watertight" closed surface. Around the STL geometry, a hexahedral background mesh that fully covers the STL geometry needs to be provided. SnappyHexMesh than detects the intersections of the background mesh with the surfaces of the STL geometry. Depending on the resolution of the background mesh, the cells at the intersection with the STL, can be refined for a better representation of the geometry. One refinement level cuts the cell into halves in each direction - one cell is cut into 8 cells. All cells, inside or outside the STL geometry, can be kept. The outside or the inside part is then simply removed from the grid. Local refinement can be performed on user-defined regions, which cannot be captured by the background mesh. Up to this point, the boundaries are represented by a "stair-step-like" grid, which will be "snapped" (morphed) to the actual surface of the geometry, in the a next step. Finally, boundary layers at the walls can be added. In the scope of this thesis, no boundary layers to the walls were applied.

STL file of the engine
The STL file of the engine can be directly extracted from the raw CAD data of the engine with a CAD tool. Ideally, the CAD geometry has been already cleaned and divided into patches (important for the meshing with snappyHexMesh and the CFD simulation). It has to be stressed that, the triangles of the STL must be sufficiently small/dense to capture all the details of the engine, such as the curvature of the liner. Figure 4.6 shows the cylinder-head and the ports of the spark ignition engine operated at the Technical University of Darmstadt. The different colours denote the different patches where the mesh refinement is performed.

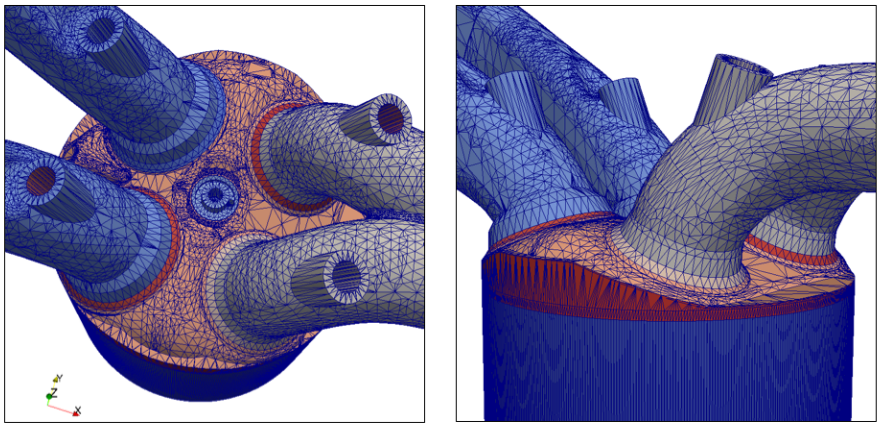

Figure 4.6: The top and side view of the optically accessible single cylinder engine of the Darmstadt research group.

A tool, moveEngineSTL (based on Lib-ICE technologies [6]) was developed to manipulate the points of the piston and the valves of the STL-file, as a function of the °CA. It writes out new STL geometries, with the corresponding piston and the valve position, which can then be used by snappyHexMesh to create the target grids for the mapping. The interval size was chosen to be no less than 5 °CA - corresponding to a piston motion of no more than 4 mm. The valves are closed by curtains, (which are internal walls around the valve seat) or by completely detached ports.

Engine Grids
The complete meshing work-flow is automated and performed exclusively by open-source tools. Two different engines were meshed with this approach: the optical research engine of the University of Duisburg-Essen [97] and the optical research engine of the Technical University of Darmstadt [18], with two different cylinder head geometries (wall-guided and spray-guided cylinder head). The spark-plug was included and refined (0.125 - 0.25 mm) in all geometries. Furthermore, grids with and without crevice volumes were created, where for the grids without the crevice volume, the clearance height at TDC had to be increased in order to comply with the geometrical compression ratio. The resolution inside the crevice was $\sim$ 0.115 mm in radial direction and 0.6 mm in vertical direction. The grid was coarsened to $\sim$1-3 mm upstream of the intake valves and downstream of the exhaust valves. The cell size inside the combustion chamber varied from 0.5 mm to 1 mm. The key-parameters for the different grid setups are summarized in table 4.1. Additional information on the engine grids are found in the section 9.4 for the "Duisburg-Engine" and in sections 6.3 and 8.3.3 for the "Darmstadt-Engine".

Table 4.1: Specification of the engine grids.

Nr	Engine	Δx_{cyl}	Crevice	Intervals	Number of cells
1	Darmstadt Wall-Guided	1.0 mm	no	144	0.9 - 1.2 Mio. [94]
2	Darmstadt Wall-Guided	0.5 mm	no	144	2.0 - 5.7 Mio. [94]
3	Darmstadt Wall-Guided	1.0 mm	yes	147	2.8 - 3.2 Mio.
4	Darmstadt Spray-Guided	1.0 mm	yes	151	2.5 - 3.2 Mio.
5	Duisburg	0.5 mm	no	100	0.5 - 5.3 Mio [145]
6	Duisburg	0.85 mm	yes	144	1.1 - 2.2 Mio [92]

4.7 Mapping

In-between the mesh motion intervals, the results have to be mapped from the source mesh on to the target grid. This is done by a conservative cell volume-weighted procedure:

$$m_t = \frac{1}{\sum_{i=1}^{n_{\text{nb}}} V_{\text{int},i}} \sum_{i=1}^{n_{\text{nb}}} m_{s,i}\, V_{\text{int}} \tag{4.31}$$

In equation 4.31, m denotes the quantity to be mapped, with the subscripts s and t standing for the source and target grid, respectively. V_{int} describes the intersection volume of the target cell with all neighbouring n_{nb} source cells. Figure 4.7 schematically shows an overlap between the source mesh (black), with the cell values $m_{s,i}$, and the target grid with a different topology (red).

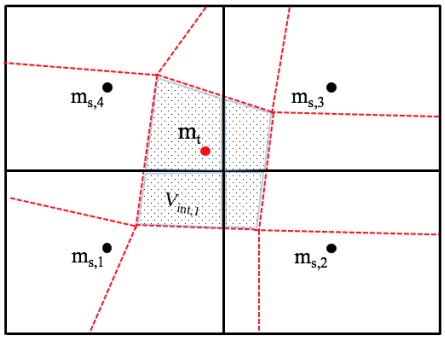

Figure 4.7: Overlapping between the the target mesh (red) and the source mesh (black)

In Figure 4.8, the mesh motion strategy is demonstrated on the computational grids. It can be seen that the distortion of the mesh from -300°CA to -295°CA is very small, therfore errors that may be induced by the subsequent mapping on the new (undistorted) grid at -295°CA can be assumed to be small. For each mapping interval, the error was $\sim 0.002\%$. A similar error was reported by Lucchini et al. [122], who also used a mesh motion and mapping approach with OpenFOAM.

4.8 OpenFOAM

In this thesis, the tool applied for the LES engine simulations is OpenFOAM. OpenFOAM is a class library written in C++ for solving continuum mechanics-related problems, where FOAM denotes Field Operation and Manipulation [195]. It has been developed in the early 90's by Henry Weller at the Imperial College, as a finite volume object-oriented C++ CFD

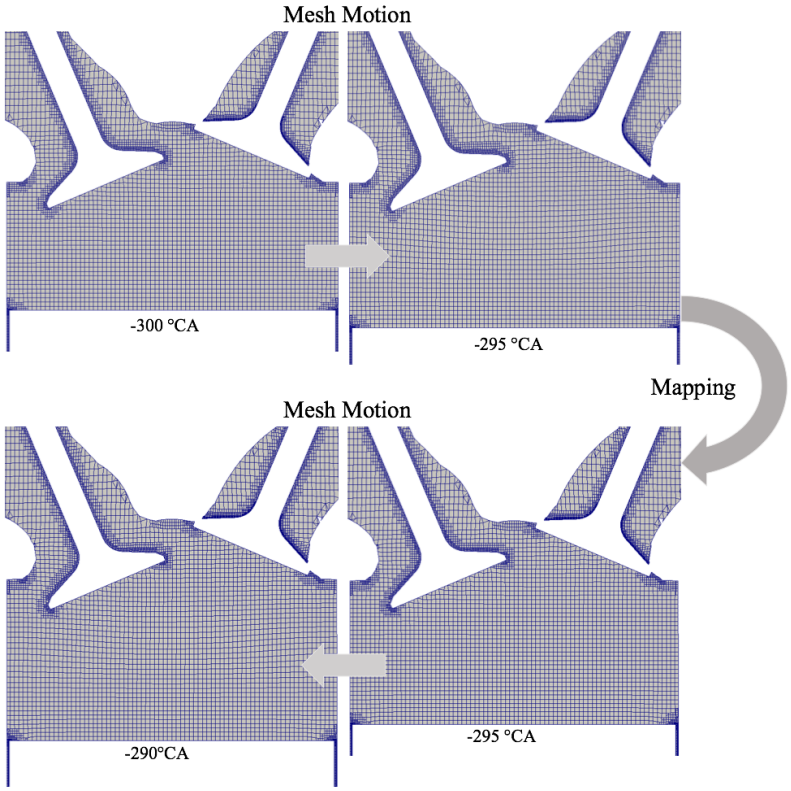

Figure 4.8: Mesh motion and mapping procedure for one mapping interval at -295 °CA.

software in the research group of Prof. David Gosman. In 2004, the software was commercialised by the company Nabla Ltd. and named FOAM. Only after 2004, FOAM was released under General Public License (GNU) by the company OpenCFD [9] and renamed in OpenFOAM. Since the source code was publicly available, the OpenFOAM community continuously increases, with users all around the world, mostly from academic research, but also from the industry. In 2012, OpenCFD was acquired by the ESI Group [5] and since 2014 completely managed by the OpenFOAM foundation [10].

A top level-syntax was developed to be as close as possible to the conventional mathematical notation, which was achieved by the object-oriented technique offered by C++. The merit of OpenFOAM is that the mathematical language (e.g. formulas) is abstracted by objects and classes. For instance, the velocity can be expressed with the variable `U` and its magnitude simply by `mag(U)`, where `U` is defined as an object of the type "volVectorField" and `mag()` is method defined within a base class of OpenFOAM. Any other vector field can be simply assigned with this class and will automatically inherit all its properties. Divergence operators, time derivatives and many other physical models are abstracted by classes, which then can be reused and combined. This allows the user to write complete solvers with a few lines, since all the physics and mathematics are encapsulated (hidden) in the classes and only need to be called. An example of a transport equation for an arbitrary scalar q, which is convected by a flux ϕ and diffused with the diffusion coefficient D is shown below in a conventional mathematical notation (nabla notation):

$$\frac{\partial q}{\partial t} + \nabla \cdot (\phi q) - \nabla \cdot (D \nabla q) = 0 \tag{4.32}$$

and in the corresponding OpenFOAM high level syntax:

```
fvm::ddt(q) + fvm::div(phi,q) - fvm::laplacian(D, q)
```

The base class `fvm` (finite volume method) creates a matrix representation of an operator using the finite volume discretisation (see eqn. 4.4). The operators are abstracted by `ddt()`, `div()` and `laplacian()` functions, which contain the discretisation methods. Nowadays, OpenFOAM includes a variety of solvers and libraries, which can deal with incompressible and compressible flows, heat transfer, buoyancy-driven flows, conjugated heat transfer, multiphase flows, turbulence modelling (LES and RANS), sprays, wall-film modelling or fluid-structure interaction. Due to the vast different examples of fully working libraries and executables, users with little experiences in C++ programming can quickly learn the structure of the code, modify and extend it. A big community of users exist, with a strong commitment to share their own developments and experiences with other users, which is certainly one of the reasons why OpenFOAM became so successful and popular in academia and industry over the years. The official version of OpenFOAM is maintained professionally by the OpenFOAM foundation [10], making it faster, more accurate and extended by new functionalities.

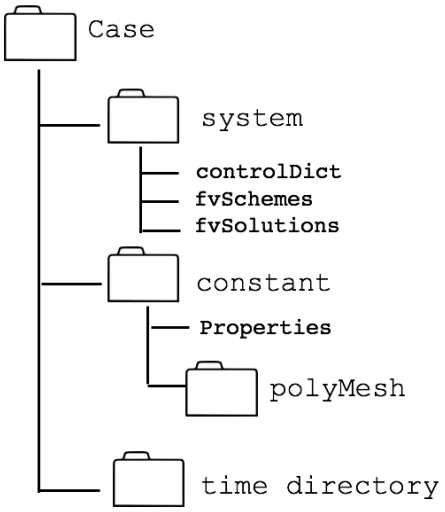

Figure 4.9: OpenFOAM case file structure [9].

A simulation case is defined by a simple file structure, which is shown in figure 4.9. The case folder contains all the files needed to perform a simulation. All the files for the numerical set-up are stored inside the system folder. The configurations are made by dictionary entries, that are read by the different libraries of OpenFOAM. For instance, the controlDict dictionary contains all settings related to "controlling" the simulation, such as the definition of the start and termination times of the simulation or the time step size. Inside the fvSolution dictionary, the numerical setup, such as the temporal discretization schemes or approximations for the divergence or Laplace operators, is chosen. In the fvSolution dictionary, the solution algorithms for the linearized equations need to be specified. The constant folder contains all the dictionaries needed for the thermodynamic properties, physical models and the grid information. Finally, the time folder is required, which contains all the physical boundary conditions and the initialisation of the fields

(for example, the temperature, pressure or velocity). The results are also stored in such time-folders and are named by the time or crank-angle degree at which they were written.

4.9 Engine Simulation Workflow

The solution algorithms for the governing equations, mesh generation, mesh motion and mapping strategy must be combined together in order to perform LES simulations of an engine as automatic as possible. The relevant steps for the automatisation are illustrated in figure 4.10 and will be elaborated in this section.

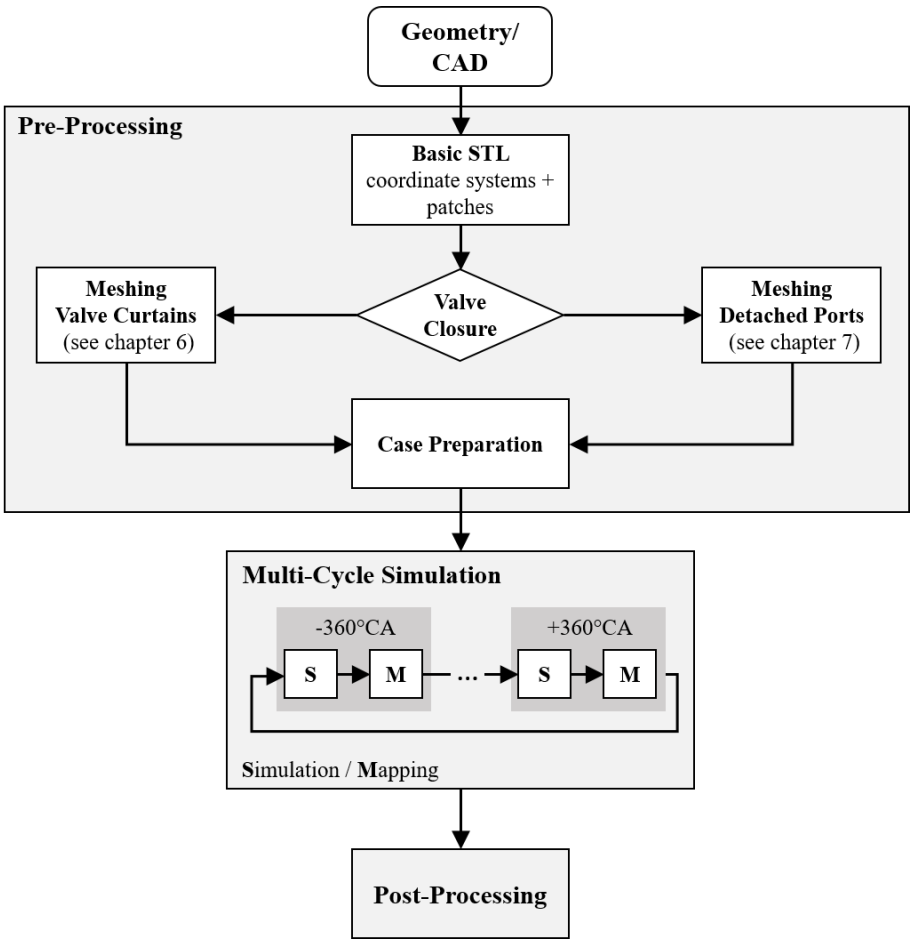

Figure 4.10: Flow-chart of the workflow for the pre-processing, simulation and post-processing.

The geometry of the engine is usually fixed and provided by a third party, (e.g. by an engine manufacture or academic research group) and given in the CAD file formats IGES or STEP. These formats must be converted to the STL file format and adapted to the meshing procedure, which requires the separation of the entire geometry into individual engine parts (patches). Important patches for the meshing and the mesh motion are the piston, cylinder-head, intake and exhaust valves. Furthermore, the global coordinate system has to be defined. It is recommended to set the origin of the global coordinate system at the piston position at TDC and the valves to the closed (minimum valve lift) position. The global coordinate system and the relevant patches are shown in figure 4.11.

This configuration is denoted as the "Basic STL" according to figure 4.10 and is used for

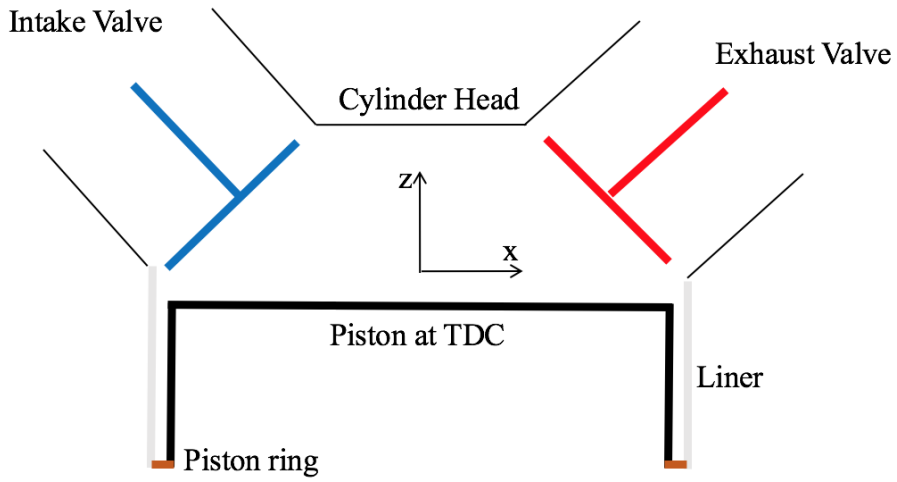

Figure 4.11: Sketch with the important patches for the mesh motion and the corresponding coordinate systems.

the meshing. Two meshing workflows that differ in the treatment of the valve closure, were applied. The valves can be either closed by curtains acting as an internal wall around the valve seat (see chapter 6.3.1) or by detaching by detaching the intake and the exhaust port at closing events (see chapter 8.3.3). The advantage of the valve curtain approach is that only one basic STL file, which contains the entire engine geometry with intake and exhaust ports, is needed. Figure 4.12 shows the basic structure of the STL for the valve curtain approach, where the black line stands for the engine with intake and exhaust ports and the green lines denote the curtain surfaces, which can be added to the geometry whenever the valves are closed. For the detached-ports approach, four different STL geometries

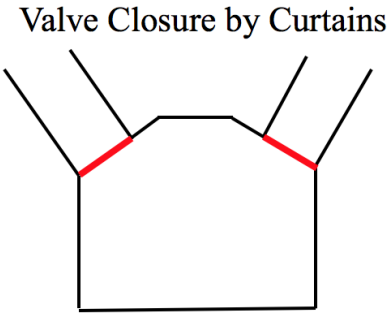

Figure 4.12: Valve closure with curtains (red).

need to be assigned, the intake and the exhaust ports separately meshed and combined together. The advantage of the detached ports is, that a higher grid quality at the closed-valve position can be ensured, because the narrow gap at minimal valve lift is excluded. Figure 4.13 shows the possible mesh configurations for this method, where the black lines denote the four different basic STL configurations and the blue and red lines denote the detached intake and exhaust ports, respectively. Furthermore, this approach allows to completely disregard the intake and the exhaust port, whenever they are not attached to

the combustion chamber. On the one hand, this saves computational resources, but on the other hand, the dynamic inside the manifolds is not taken into account anymore. For the meshing of each configuration, a shell-script file was created, with all the necessary operations to build the different grids. A shell-script is a program, which is run by the Unix shell and used to manipulate and execute other programs. The tasks are executed sequentially.

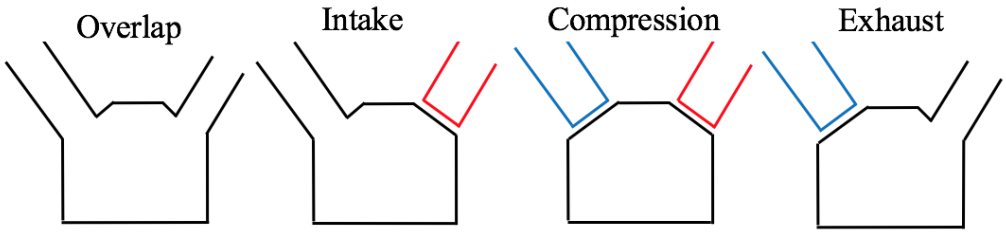

Figure 4.13: Possible mesh configurations for the meshing work-flow with detached ports. The black line denotes the engine grids and the red and the blue lines the intake and the exhaust ports, respectively.

Once the grids are generated, they can be used to create the individual simulation cases, which is denoted by the step "Case Preparation" in the flow chart shown in figure 4.10. Assuming that a new grid is used every 5°CA, 144 cases are needed to cover a full cycle (720°CA). Therefore, the preparation of the cases, which includes the generation of the required data structure of OpenFOAM, is done with bash script-files. Before the simulation is started, the number of CPUs on which the simulation will be executed and the domain decomposition must be predefined. Good performances were achieved with around 13000 cells per CPU. After the grids are decomposed, the simulation can be started. The STL preparation, the meshing and the case preparation belong to the pre-processing and are exclusively done by open-source tools, e.g. Blender [21] and OpenFOAM [9]. After the case preparation and the field decomposition, the simulation can be started. The simulation and the mapping procedure are systematically shown in the box "Multi-Cycle Simulation" of the flow-chart in figure 4.10, which consists of a sequence of the simulation and the mapping intervals (every $\sim$ 5°CA).

5

Optically accessible research engines

In this chapter the engines that are used for the LES simulations are presented and their main characteristics discussed.

5.1 Introduction to research engines

An optically accessible research engine is an engine that enables a direct view into the combustion chamber from outside (for example through a transparent glass liner), which is normally not possible for a conventional full-metal engine. A milestone in the history of the optically accessible engines was the development of an extended piston design by Bowditch in 1960 [26]. The Bowditch-type piston design allowed to view the combustion chamber from below during the full cycle through the piston by a 45° inclined mirror. The new piston design opened the door for the application of laser diagnostics and cameras to the engines.
In the past, the design of new combustion chambers relied entirely on the experience and know-how of the engine manufacturers and required a lot of tests and modifications, which costs time and money. Optically accessible engines nowadays can be applied during the development phase of new combustion strategies or to find an optimal fuel injector position to avoid any wall-impingement. Another important field of their application lie in understanding the formation of the in-cylinder flow field and validation of engine CFD-codes, which is one of the main objective of this thesis.

There is one truth about optically accessible engines, which sometimes seems to be forgotten or not stressed enough, that these engines are not 100 % representative of a full-metal engine. Due to the lower heat conductivity of the transparent parts, compared to their metal counterparts, the heat losses to the piston and the liner wall will be different. Bigger and new clearance volumes might be found at the sealing surface of the cylinder head and at the glass liner, or in the piston-top land volume, due to very low mounted piston rings (discussed in 9). The operating conditions of optically accessible research engines are limited to the mechanical and thermal resistance. In order to avoid any damage of the transparent parts. a work-rest strategy is applied, where after some (∼100) fired cycles, the engine is set back to motored operation. A comparison of optical engines to all-metal engines is provided by Kashdan et al. [98]. The geometrical modifications and different operating conditions have to be kept in mind, by using the experimental data for the validation of the 3D CFD-tools, which will be later used to design "real" engines.

5.2 Characteristics of the investigated research engines

In the scope of this work, the data of two different optical research engines is used for the validation of the presented CFD-tool and for the further investigation of the in-cylinder flow and the combustion. The first investigated engine was the optical research engine of the University of Duisburg-Essen [20], operated by Prof. Kaiser (IVG, Prof. Schulz), where RANS [93] (not shown in this thesis) and LES engine simulations of the flow-field and the combustion were made. Another engine chosen for this thesis, is operated by the engine group of Prof. Dreizler [18] at the Technical University of Darmstadt. It is part of the "Darmstadt engine workshop" (www.rsm.tu-darmstadt.de), which takes place every 4-6 months. In the scope of this workshop, different research groups, which are simulating this engine, gather together and discuss their progress and issues. Throughout this study, the cylinder-head for this engine was changed from a wall-guided head to a spray-guided head, which was also possible to studied (due to the efficient engine simulation workflow). For the sake of convenience, the research engine of the University of Duisburg-Essen will be denoted as DUE, and the optical research engine of the Technical University Darmstadt with the wall-guided head as TUDw and with the spray-guided head with TUDs, respectively.
Figure 5.1 shows the different cylinder head geometries of the wall- and spray-guided heads of the University of Darmstadt and of the engine of the University of Duisburg-Essen. All cylinder heads have a pent-roof design, with inclined intake and exhaust valves. The inclination is important for the development of the tumble flow. For all heads, the blue valves stand for the intake valves and the red valves for exhaust valves, where only for the spray-guided head (TUDs) the intake valves are smaller than the exhaust valves. Since the TUDs and UDE head have a centrally-mounted fuel injector, the spark plug is shifted from the centre of the cylinder head. The valve lift profile for the TUDw and TUDs is fixed by a conventional cam-shaft, where the UDE engine exhibits a variable valve lift and phasing for the intake side, with a maximum valve lift of 9.7 mm. The major geometrical characteristics of the three engines are summarized in table 5.2. All engines use a Bowditch-

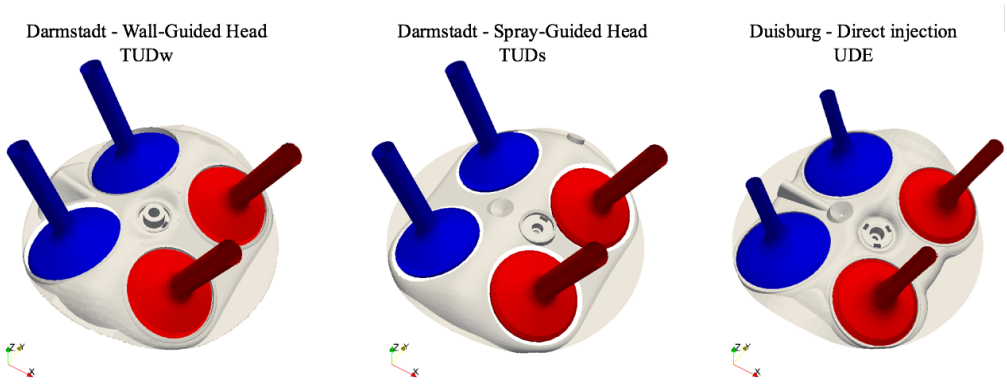

Figure 5.1: Cylinder heads of the optical research engines of the Technical University of Darmstadt and the University of Duisburg-Essen.

type extended piston design, with a lowered piston ring package, in order to avoid contact with the piston-rings and the glass liner. The first ring for the UDE engine is mounted 31.5 mm underneath the piston head and 74.4 mm for the TUDs and TUDw engines. In Figure 5.2, the geometrical design at BDC is shown for the TUDw and UDE engine, including the piston-top land dimensions and transparent liner part. The radial clearance for all engines is 0.5 mm (at ambient temperature) between the piston and the liner.

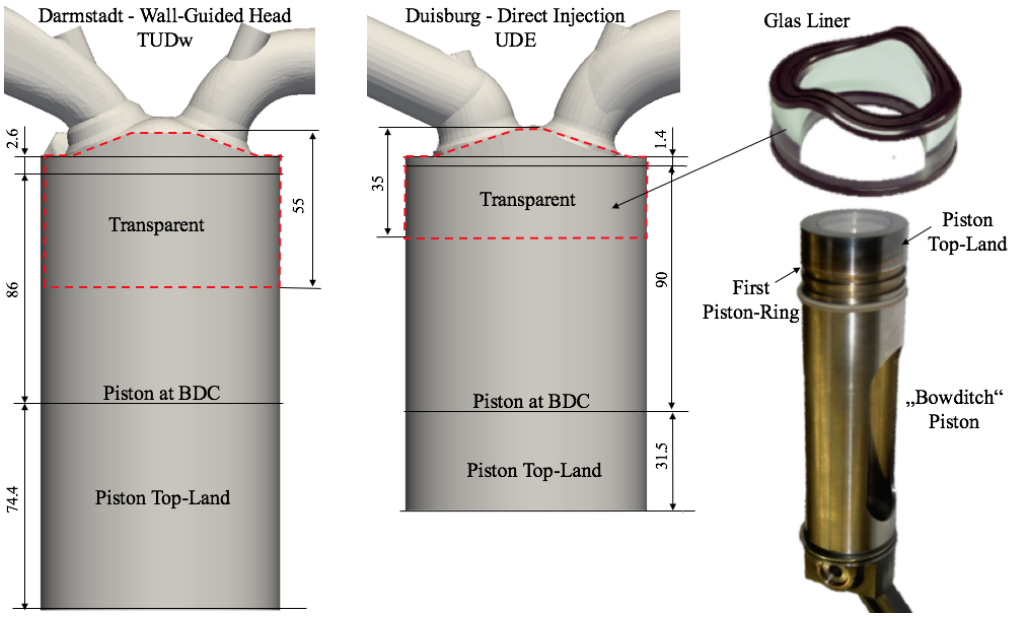

Figure 5.2: Geometrical details of the cylinder piston assembly of the optical engines. The transparent part of the liner is spotted by a red box.

Table 5.1: Main characteristics of the optically accessible engines.

Specification	TUDw	TUDs	UDE
Bore/Stroke	86/86 mm	86/86 mm	84/90mm
Displacement	499 cm^3	499 cm^3	499 cm^3
Clearance height	2.6 mm	2.6 mm	1.4 mm
Compression ratio	8.5:1	8.7:1	10:1
Clearance Volume	66.5 cm^3	64.9 cm^3	55.4 cm^3
IVO	325°aTDC	325°aTDC	350 °aTDC
IVC	125°bTDC	125°bTDC	176 °bTDC
EVO	105°aTDC	105°aTDC	172 °aTDC
EVC	345°bTDC	345°bTDC	320 °bTDC
Int./exh. max. lift	9.5 mm	9.5 mm	0-9.7 / 3.5 mm
Int./exh.valves diameter	33/31 mm	29/31 mm	32/28 mm
Int./exh. port diamete	60 mm	60 mm	30/35 mm
°CA at max. intake valve lift	250 °aTDC	250 °aTDC	variable

6

On the evolution of the flow field in a spark ignition engine

Authors: P. Janas, I. Wlokas, B. Böhm, A. Kempf
This chapter including all figures and tables was previously published in Flow, Turbulence and Combustion, On the Evolution of the Flow Field in a Spark Ignition Engine, Volume 98, 2017, pp 237-264, Peter Janas and Irenäus Wlokas and Benjamin Böhm and Andreas Kempf. "With permission of Springer". The author P. Janas developed the code, ran all the simulations, wrote the paper and generated all figures and tables. The authors A. Kempf, I. Wlokas and B. Böhm contributed corrections, discussions and proof-reading.

6.1 Introduction

The turbulent flow field at the time of spark ignition is known to be of key importance for the efficiency of combustion in gasoline engines. The flow field has to mix the fuel with the oxidizer homogeneously in order to provide a combustible mixture at the spark plug and moreover to wrinkle the flame front to enhance the consumption rate. Therefore, turbulence is crucial for the working principal of the spark ignition engine, but only if it is available at the right amount and at the right place inside the combustion chamber, meaning that too strong eddies could lead to missfire or unstable working conditions. Even after many years of experimental and numerical investigations, the development of the in-cylinder flow field is still not fully understood. A deeper understanding of the formation of the turbulent environment will be a relevant step towards the reduction of cycle-to-cycle variations (CCV), which lower the efficiency of the spark ignition engine. The negative side effects of turbulence, like CCV, are known for many years but due to the poor optical accessibility, the focus had to be put first on the development of appropriate tools to study in-cylinder processes. Experiments inside the combustion chamber of optical accessible single cylinder research engines are nowadays available and 3D computational fluid dynamics (CFD) simulations are able to resolve the full unsteady turbulent flow field. Both approaches depend on each other and the boundary conditions, assumptions and limitations have to be known from both sides (experiment and simulation). From the simulation perspective, only LES simulations can cope at the moment with the unsteady turbulent flow inside the combustion engine with acceptable cost-to-time performance. During the last 20 years, LES simulations were applied to study the in-cylinder aerodynamics and combustion processes in reciprocating engines [74, 18, 54, 188, 141, 145], where one of the first LES engine simulations was performed in 1992 by Naitho et al. [144]. A motivation of the application of LES to engine flows is given by Haworth et al. [85] and a review about numerical simulations of engines and experimental measurement techniques as such

by Drake et al. [49].

The challenge in better understanding in-cylinder phenomena does not only lie in the application of the measurement techniques and numerical models to the engine, it is also about how to post-process, visualize and analyze the produced data. In-cylinder flow dynamics are judged and studied by integral quantities like the swirl, tumble number, turbulence intensity or discharge coefficients, which are very useful for the engineers in the preliminary design of an engine, but they do not give any insight about local flow structures. More advanced analyses include the measurement of integral length scales of the turbulent flow field. For a direct measurement of the length scales, the velocity has to be simultaneously measured at different locations. By applying the temporal or spatial auto-correlation function to these velocities, the integral time and length scales can be obtained. Corcione and Valentino [43] applied the two-point laser Doppler velocimetry (LDV) to calculate the integral length scales inside a diesel engine. Hong and Chen [89] applied these techniques to a single cylinder research engine with a pent-roof combustion chamber and measured a lateral length scale of about 3.9 mm at 30° before top dead centre (bTDC). They have analyzed the cross- and longitudinal-correlations, with a variable distance between the two probe volumes of a maximum of 7.5 mm and concluded that the integral length scale is influenced by the in- and outflow jets and by the piston motion. In the work of Auriemma et al. [17] and later by Reitz et. al [159], experimentally obtained lateral length scales were compared to a 3D RANS (Reynolds averaged Navier Stokes) simulation, where the turbulent length scales were directly obtained from the k-ϵ turbulence model - so that only the length scale of the assumed fully developed turbulence could be computed. Unsurprisingly, a good agreement was only achieved by adjusting the turbulent kinetic energy, implying a limited ability of the RANS approach to properly model the length scales inside the engine. In other areas of turbulent combustion, integral lengths scales are commonly considered [38, 41, 99]. Di Mare et al. [131] examined different quality criteria for LES of in-cylinder aerodynamics, where one of the criteria was based on the integral length scale.

For further insight of the flow structures in the combustion chamber, Particle Image Velocimetry (PIV) was applied in many experimental studies. This technique requires modifications to the engine and provides velocity information inside a predefined part of the combustion chamber. Accompanying the optical research engines, the aerodynamics can also be studied in stationary flow benches. Here, the cylinder head with a fixed open valve is mounted on a cylinder with the bore and diameter of the corresponding engine. The flow bench is then fed with compressed air under engine relevant conditions. Unfortunately, this approach only gives global flow quantities like the discharge coefficient of the valves or the tumble and swirl number. Although only a small time interval of the intake stroke can be covered by this approach, the complexity of the measurement compared to a reciprocating engine is dramatically reduced, which offers the possibility to use different experimental equipment and a wider interrogation window. Recently, the Magnetic Resonance Velocimetry (MRV) has been applied to a 1:1 full scale dummy of an optical research engine by Freudenhammer et al. [64]. The MRV measurements provide full 3D velocity data inside the upper part of the combustion chamber and the intake ports. Freudenhammer et al. compared their MRV measurements to PIV [18] data obtained from the corresponding engine and showed a good quantitative agreement among the experiments. Hence, MRV measurements should be well suited for the validation of the 3D flow fields predicted by CFD.

This chapter was previously published [94] and is reprinted with permission of the journal.

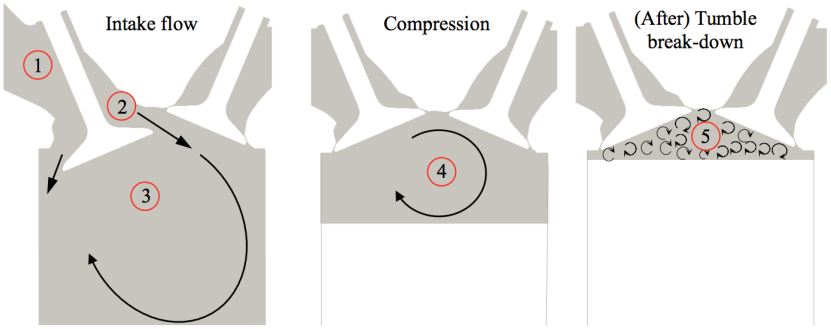

Figure 6.1: Sketch of the evolution of the (turbulent) flow field: flow upstream of the intake valves (1), flow around the valve seat (2), tumble flow inside the combustion chamber during the intake stroke (3), tumble compression (4) and (after) tumble break-down (5).

In this work, multi-cycle LES simulations are presented for motored operating conditions. The numerical approach delivers complete 3D velocity fields throughout the entire combustion chamber, valve seat regions and intake and exhaust ports without modifications to the real engine geometry. The focus of this work is on the development of the (turbulent) flow inside the combustion chamber. In figure 6.1, the different zones and phases, which are important for the development of the flow, are drawn schematically [87]. The flow upstream of the intake valves (zone 1) and around the valve seat (zone 2) will be discussed and compared to MRV measurements. Especially the valve seat region is of paramount interest, since turbulence is generated there, convected to the combustion chamber, and causes the big coherent structures (zone 3). Afterwards, the tumble motion will be investigated by tracking its rotational centre throughout the complete combustion chamber (zone 4) and the tumble-break down will be monitored by two-point velocity correlations in the compression stroke.

6.2 Engine and experiment

The optical research engine, which is part of the "Darmstadt engine workshop" (www.rsm.tu-darmstadt.de), operated by Dreizler and coworkers [18] has been chosen for this investigation, due to the extensive available data base for the flow field validation. This spark ignition engine features a pent-roof cylinder head with two inclined intake and exhaust valves. Optical access is provided through the piston and liner. The key-parameters of this optical engine are shown in table 1. Instantaneous velocity fields on the tumble symmetry plane inside the combustion chamber were measured by two-dimensional two-component particle image velocimetry (PIV) [18] at 800 rpm.

For the flow bench measurement, a 1:1 scaled Polyamide model of the same engine was investigated by Freudenhammer et al. [64] using Magnetic Resonance Velocimetry (MRV). This measurement technique is able to resolve the ensemble averaged velocity field in a confined geometry. It is usually applied for medical research, for instance to study the flow in blood vessels. Since MRV does not require an optical access, it is well suited for very complex geometries. For the MRV measurements, water was used as a working medium. The flow rate of the MRV measurement was adjusted to mimic the inflow conditions at 270°bTDC (800 rpm) of the corresponding optical research engine. Two flow rates of 2 m^3/h and 4 m^3/h for the MRV measurement were chosen, yielding Reynolds-numbers

This chapter was previously published [94] and is reprinted with permission of the journal.

Table 6.1: Specifications of the optical research engine operated by the Dreizler-group and operating conditions for the PIV measurement [18]. TDC is denoted within the power-stroke, where a stands for after and b for before TDC.

Bore/Stroke	86/86 mm
Displacement	499 cm^3
Clearance height	2.6 mm
Compression ratio	8.5:1
Intake valve opening (IVO)	325°aTDC
Intake valve closing (IVC)	125°bTDC
Exhaust valve opening (EVO)	105°aTDC
Exhaust valve closing (EVC)	345°bTDC
Intake/exhaust max. lift	9.5 mm
Intake/exhaust valves diameter	33/29 mm
Intake/exhaust port diameter (d_p)	60 mm
Average intake pressure	0.95 bar
Average exhaust pressure	1 bar
Intake temperature	296 K
Maximum intake valve lift	9.5 mm at 250°bTDC
Engine speed	800 rpm
Fluid	Air seeded with silicon droplets
Number of cycles	2700

of 22500 and 45000, respectively. The two MRV measurements can be scaled to match the velocity fields of the corresponding PIV measurement, with velocity scaling factors of 41.70 and 20.64 [64]. The Mach-number inside the valve gap for the PIV measurement was estimated to be 0.066 for a valve lift of 9.21 mm, so that compressibility effects can be neglected. Since the MRV technique is only able to measure mean velocities, the intake valves were kept at a fixed position and the piston replaced by an outlet. At 270°bTDC, one can assume that the flow is not accelerated, as the piston is not accelerated then.

A comparison of the PIV and MRV measurements is shown in figure 6.2, illustrating a good agreement of both measurements in the upper half of the cylinder and strong deviations in the lower half. The differences arise from the missing piston in the MRV measurement, so that the flow is not redirected by the piston towards the cylinder head. (The different velocity scales arise from the different working fluids for the PIV and MRV measurement, ensuring Reynolds-similarity.)

6.3 Numerical modelling

For the simulation of the in-cylinder aerodynamics, the open source tool box Openfoam is used, to solve the Favre-filtered equations for mass (8.1), momentum (8.2), and energy (8.3) on a moving grid:

$$\frac{\partial(\overline{\rho})}{\partial t} + \frac{\partial(\overline{\rho}\widetilde{u}_j)}{\partial x_j} = 0 \tag{6.1}$$

This chapter was previously published [94] and is reprinted with permission of the journal.

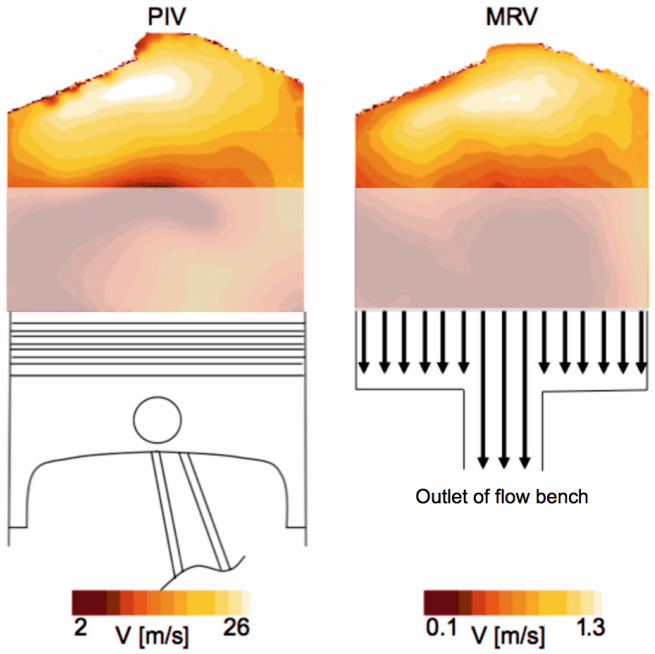

Figure 6.2: Contour plot of the (phase) averaged velocity magnitude at 270°bTDC within the tumble symmetry plane from PIV (left) [18] and the MRV (right) [64]. A good agreement in the upper half of the cylinder is achieved, which makes MRV well suited to provide additional information in the valve seat region. (The deviating region of the flow field is faded out.)

$$\frac{\partial\left(\overline{\rho}\widetilde{u}_i\right)}{\partial t}+\frac{\partial(\overline{\rho}\widetilde{u}_i\widetilde{u}_j)}{\partial x_j}=\frac{\partial\overline{\tau_{ij}}}{\partial x_j}+\frac{\partial\tau_{ij}^{\mathrm{sgs}}}{\partial x_j}-\frac{\partial\overline{p}}{\partial x_i} \tag{6.2}$$

$$\frac{\partial(\overline{\rho}\widetilde{e})}{\partial t}+\frac{\partial(\overline{\rho}\widetilde{u}_j\widetilde{e})}{\partial x_j}+\frac{\partial(\overline{\rho}\widetilde{K})}{\partial t}+\frac{\partial(\overline{\rho}\widetilde{K}\widetilde{u}_j)}{\partial x_j}=\frac{\partial}{\partial x_j}\left(\alpha_{\mathrm{eff}}\frac{\partial\widetilde{e}}{\partial x_j}\right)-\frac{\partial}{\partial x_j}(\overline{p}\widetilde{u}_j) \tag{6.3}$$

Within the governing equations, the overline $<->$ denotes LES filtered and the tilde $<\tilde{}>$ Favre filtered quantities, with $\overline{\rho}$ as the density, $\widetilde{u_j}$ as the velocity vector, $\overline{p}$ as the pressure and $\overline{\tau}_{ij}$ as the viscous shear stress tensor. In order to account for the mesh motion, all convective fluxes were calculated relative to the moving grid [47]. For the unresolved subgrid stresses τ_{sgs}, the standard Smagorinsky model [174] with a model constant of 0.062 was chosen and the Sigma model [148] with a model constant of 1.35, which was previously tested for engines by Misdariis et al. [136] and by Nguyen et al. [146]. The molecular viscosity is calculated by the Sutherland law [178]. The total internal energy consists of the internal energy $\widetilde{e}$ and the kinetic energy $\widetilde{K}= 1/2\ \widetilde{v}_i^2$. The sum of laminar and turbulent thermal diffusivity is denoted as α_{eff}. The pressure is calculated by a pressure-velocity-density coupling for flows at arbitrary Mach-number proposed by Demirdžić [46, 59]. This approach does not limit the time step size according to the speed of the sound, hence allows to progress in time with bigger steps, using an implicit second-order scheme. The convective scalar-fluxes are discretized with a total variation diminishing scheme (TVD-scheme), using the Sweby limiter [179]. For the momentum equation, a switch between a central differencing scheme (CDS) and TVD-scheme is applied: a CDS is normally used, which is replaced by a TVD-scheme in regions with Mach-numbers greater than 0.3 to

This chapter was previously published [94] and is reprinted with permission of the journal.

avoid numerical problems [145] on the one hand, and to avoid the unacceptable numerical dissipation that would come with a pure TVD-scheme on the other hand.

6.3.1 Numerical setup

Simulations of internal combustion engine require special attention to the grid quality and structure, since the cells inside the combustion chamber have to adjust to the piston and valve motion. A high grid quality in terms of high orthogonality, low skewness and small expansion rates is a stringent requirement for LES, in particular to avoid numerical instabilities and dissipation that would lead to insufficient turbulent levels. A mesh motion strategy is applied without topological changes on multiply grids, on which the mesh quality stays high. The results are then mapped to the new grid. Target grids for every 5°CA are created prior to the simulation, where 5°CA corresponds to a piston motion of less than 4 mm. For the mesh motion, a Laplace equation is solved that yields a smooth mesh deformation velocity field $u_{cell,k}$:

$$\frac{\partial}{\partial x_k}\left(\gamma \frac{\partial u_{cell,k}}{\partial x_k}\right) = 0 \tag{6.4}$$

Each mesh point is then just shifted by the deformation velocity multiplied with the width of the time step. The boundary conditions for equation (6.4) are effectively no-slip conditions, with the exceptions of expanding boundaries (valve stem and cylinder liner), where the condition $\frac{\partial u_{cell,k}}{\partial x_k} = 0$ is applied. An artificial stiffness for the mesh motion is introduced by the diffusion coefficient γ, to control the mesh motion [96].

The complete meshing work-flow is automated and performed exclusively by open source tools [93, 145, 92]. The valves are closed by "curtains", which are internal walls around the valve seat. The grids are based on hexahedral cells with a local mesh refinement at the spark plug and valve seat region. The effort of building a "flow-oriented" grid for a combustion engine is considerable and even more difficult to embed into an automated meshing work-flow. Furthermore, it will be more difficult to apply higher order schemes on it, which is crucial for an LES. Therefore, we have kept the cells inside the complete combustion chamber equidistant, refined and adapted to the walls only at the boundaries. However, we would like to note that this can lead to slightly larger errors in the calculation of the shear stress of the intake jet. For the coarse grid, inside the combustion chamber, the average cell size is 1 mm, inside the valve seat region it is 0.125 to 1 mm, and at the spark plug 0.25 mm. Inside the inlet and outlet manifolds, away from the valves, the mesh resolution was reduced to 2 mm. A second, refined grid uses a cell size of 0.5 mm inside the combustion chamber. In total, 144 grids are used for the full cycle with 0.9 to 1.2 millions of grid cells for the coarse mesh and 2.0 to 5.7 millions of cells for the fine mesh at TDC and BDC, respectively. The refinement of two inside the combustion chamber (from 1 mm to 0.5 mm) means that the number of cells has been increased by 8, the time-step width reduced by 2, and the computational effort increased by 16. The piston top-land crevice volume was blocked and the geometric compression ratio adapted, accordingly. Figure 6.3 shows the coarse mesh on a cut through the valves with an open intake valve, the cylinder head of the fine grid, and the complete computational domain.

Since the grid size determines the local filter size and the spacing of our mesh is changing during compression, expansion and valve motion, it will have a direct impact on the results. Fortunately, the cells inside the combustion chamber experience a piston displacement of

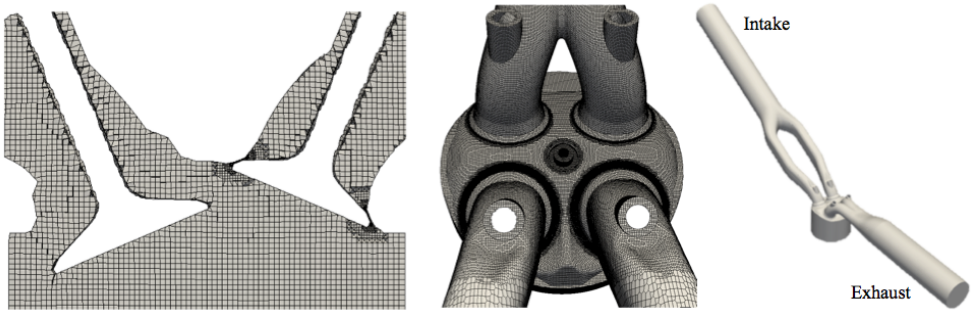

Figure 6.3: From left: Engine grid on a cut through the valves with opened intake valve (coarse mesh), top view of the cylinder head (fine mesh) and full computational domain.

no more than 4 mm, where we assume that the error in the local filter size is small. We would like to stress, that the mapping strategy with this small displacement intervals is the reason for the relative high amount of mapping intervals (144). As comparison, Enaux et al. [54] uses 41 grids to cover a complete cycle of a similar engine, with an average grid spacing of 0.8 mm. It has to be guaranteed that the moving grids are overlapping precisely on the target grids to not lose mass or momentum. Here, the mesh motion can be based on either imposing the displacement of the moving boundaries or using its velocity. In our approach, as mentioned above, the velocity of the moving boundaries is used together with the time step width to calculate the displacement. Hence, the displacement of the moving boundary is only first-order in time accurate, so that a small time step is needed to ensure a good overlapping between the grids.

6.3.2 Simulation setup

The simulation is started at 360°bTDC, when the intake and exhaust valves are open and the fluid assumed to be at rest in the entire domain. A time-varying absolute pressure is imposed at positions of 530 mm upstream of the intake valves and 360 mm downstream of the exhaust valves, where the pressure is known from measurements. The inlet temperature is set to 295 K. A no-slip boundary condition is applied to all walls, for which the temperature was fixed to 333 K. No additional wall modelling was added for the heat transfer. Ten consecutive cold flow engine cycles were calculated on the coarse and seven on the fine grid.

The time step was calculated from a maximum CFL number of 2 based on the convective velocity. The most time consuming part of the simulation is the opening and closing of the valves, when the mesh inside the valve gap has a resolution of 0.125 mm and velocities around 300 m/s occur, leading to time steps smaller than one micro second. However, once the valves are closed, the time step size increases to almost 50 micro seconds. Table 2 shows how much computational time is required for the different phases of the cycle on the fine and coarse mesh, performed on 16 CPUs (AMD Opteron - Type 6234) with a total of 192 cores.

6.4 Results

The in-cylinder pressure evolution is discussed first. The numerical model has a compression ratio of 8.5:1, which conforms to the engine specification. Figure 6.4 shows the simulated in-cylinder pressure of the motored test case for the fine and coarse mesh con-

Table 6.2: Computational time for one engine cycle performed with 196 CPUs on the fine and coarse mesh presented for the different time intervals: valve overlap, intake valve closing, exhaust valve closing.

Interval	Fine / Coarse [days]	% of total time	CAD
Full cycle	6.5 / 2.7	100 / 100	720
Intake valve closing	1.1 / 0.4	18 / 16	30
Exhaust valve opening	2.4 / 0.7	38 / 28	45
Overlapping	0.5 / 0.4	7 / 13	50
Rest	2.4 / 1.2	37 / 43	595

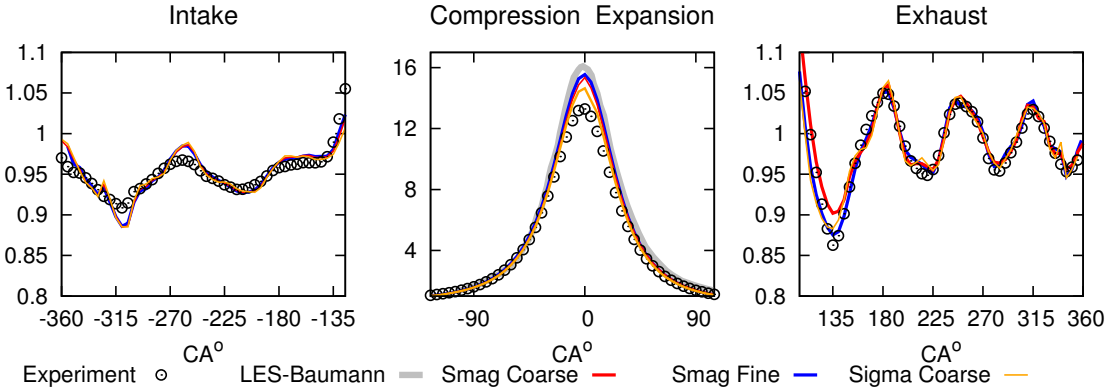

Figure 6.4: In-cylinder pressure [bar] evolution for the complete cycle given by a LES on a fine grid (blue) with the Smagorinsky model and on coarse grid with the Smagorinsky (red) and Sigma model (orange). Simulation results are compared against experiment (black) and another engine cold-flow simulation of the same engine under the same operating conditions performed by Baumann et al. [19].

figuration. Both curves have a very similar in-cylinder pressure distribution compared to the measurement for the intake and exhaust stroke, but overpredict the peak-pressure by 17%. At the closure of the inlet valves the simulated pressure is in very good agreement with the measurement, however, this does not imply that the in-cylinder mass is correct. Since only the in-cylinder trapped mass (mass coming into the engine) can be estimated from the flow meter of the test bench, the total in-cylinder mass (trapped mass + residual gas) remains unknown. A temperature measurement inside the combustion chamber would help for a better estimate of the in-cylinder mass at intake valve closure, which unfortunately does not exist. The work of Baumann et al. [19] confirms our simulation, as they first calculated a very similar, too high peak-pressure. They then lowered the in-cylinder mass by adjusting the intake pressure to make the peak-pressure fit. We do not follow this approach, because the in-cylinder pressure at inlet valve closure in our simulation agrees well with the experiment. The in-cylinder mass in our simulations at IVC was ∼542 mg for the simulations on the fine and coarse mesh using the Smagorinsky model and ∼536 mg on the coarse mesh using the Sigma model.

To ensure that our simulations and the work by Baumann do not share a (unknown) common mistake leading to the overprediction of pressure, we have calculated the in-cylinder pressure resulting from an isentropic compression under different assumptions. For this purpose, a 0D model for the compression and expansion of the optical engine was made,

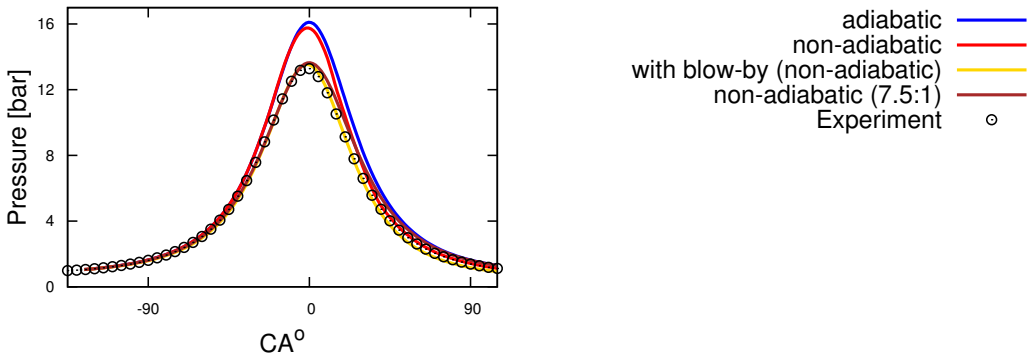

Figure 6.5: Estimation of the in-cylinder pressure during the compression and expansion stroke (IVC → EVO) given by a 0D simulation for an adiabatic case (blue), with heat transfer (red), with blow-by (gold), and with reduced compression ratio (dashed line) compared to a measured in-cylinder pressure (black) under motored operating conditions.

which includes an empirical model for the convective heat transfer proposed by Woschni [202] and a simplified blow-by model [150]. The 0D simulations are initialized with the measured in-cylinder pressure at intake valve closure of 1.055 bar and air of 300 K. In figure 6.5 the results of the 0D simulations are presented and compared to the experiment. It is observed that for isentropic compression and expansion, the peak in-cylinder pressure is overpredicted by 28% to the measurement, whereas our non-adiabatic 3D-CFD simulation lead to an overprediction of 17%. In fact, around 20% of the total in-cylinder mass should be removed by blow-by gasses to justify the lower measured in-cylinder pressure. Recent studies underline our observations of the missmatch of the peak-pressure inside optical research engines, where Rakopoulos et al. [158] used a blow-by model within a CFD simulation of an optical engine, to match the experimental data. For the case investigated here, we find that the geometrical compression ratio for isentropic compression and expansion should be lowered from 8.5:1 to 7.5:1 to fit the measurement.

Blow-by, as another likely explanation for a deviating peak pressure, is hard to quantify. The alternative explanation of a strong effect of heat transfer is also not trivial to assess in an LES, where accurate boundary layer modeling for momentum and heat transfer is still not fully solved [170, 168, 169]. (It should however be pointed out that the wall heat transfer is somewhat less critical in motored operation.) Decreasing the compression ratio should also not be a desired solution, since it will require (a) modifications to the engine geometry, that may influence the in-cylinder flow field and (b) will change the temperature evolution during compression, hence the viscosity and consequently the turbulence [167]. It is, however, perceivable that large amounts of gas are trapped between the piston-rings and in the piston top-land crevice (piston top-ring is 74.5 mm positioned underneath the piston head), lowering the in-cylinder mass temporally during the compression stroke, while releasing it partially to the cylinder back during the expansion phase. Given the great uncertainty in this explanation, we have chosen to simulate the case as it is and to accept the resulting deviation in the peak-pressure. (We would like to stress that not capturing the peak-cylinder may not be critical under motored conditions, but certainly under fired operation.)

This chapter was previously published [94] and is reprinted with permission of the journal.

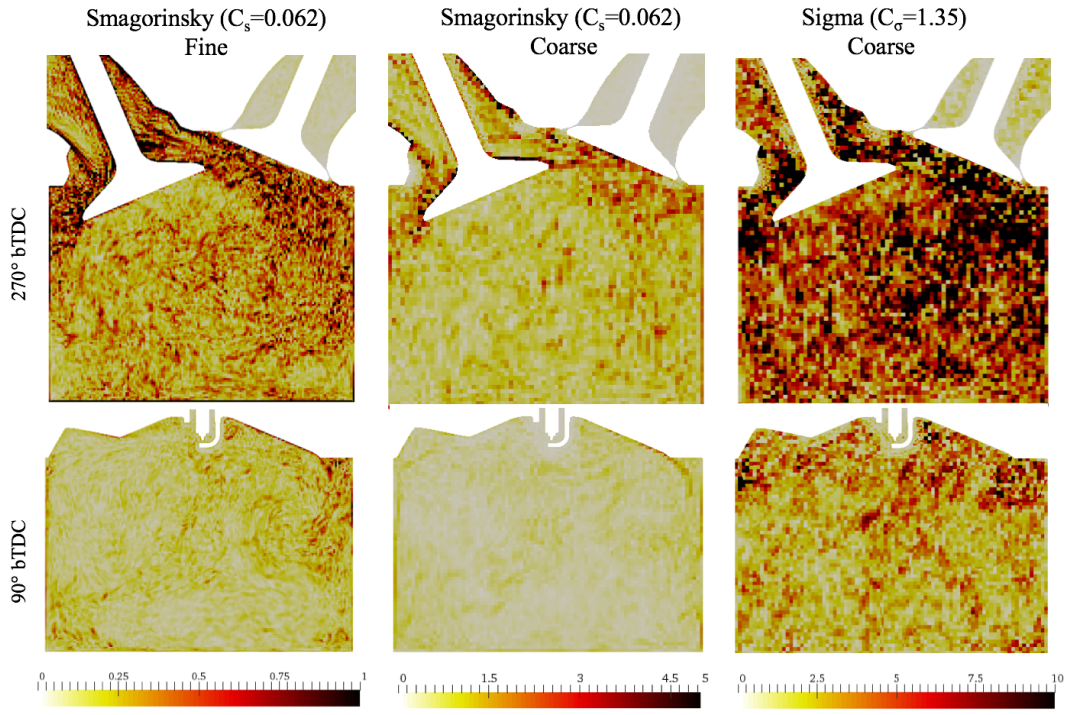

Figure 6.6: Contour plots of the turbulent to laminar viscosity ratio of single cycles within the valve plane at 270°bTDC (upper row) and symmetry tumble plane at 90°bTDC for the fine simulation and coarse simulation using the Smagorinsky model and for the coarse simulation with the Sigma model.

6.4.1 Engine LES Quality assessment

The mesh adequacy was assessed by investigating the turbulent to laminar viscosity ratio. Figure 6.6 shows the contour plots of the instantaneous turbulent to laminar viscosity ratio (ν_t/ν_l) in the valve plane at 270°bTDC and within the tumble symmetry plane at 90°bTDC for the Smagorinsky model on the coarse and fine grid and for the Sigma model on the coarse grid. The ratio stays lower than 20 in all simulations, with the exception of certain points when the Sigma model is used. Like similar criteria, this criterion should not be seen as a sufficient criterion for an "accurate or good LES " and can only be seen as an indicator [70, 152, 105, 104]. Alternatives for the assessment of the quality of a LES are the length scale resolution parameter [153], which was recently used by Montorfano et al. [139] to estimate the quality of a LES in a valve/piston assembly or the resolution index [157], which was used by Baumann et al. [19]. The length scale resolution parameter requires the size of the Kolmogorov scales, which is not known for the engine in this investigation and therefore rejected as quality criterion. Also the resolution index requires the local kinetic energy inside the combustion chamber, which is difficult to calculate based on cycle averaged data, because the motion of the large scale motion (tumble vortex) has to be taken into account, too, which is not trivial, since the centre of the tumble is changing from cycle to cycle. We therefore omitted this criterion, too.

Figure 6.7 shows the velocity fluctuations at 90°bTDC on the tumble symmetry plane for the fine and coarse simulation performed with the Smagorinsky model and on the coarse mesh with the Sigma model. The results converge nicely with grid refinement for the

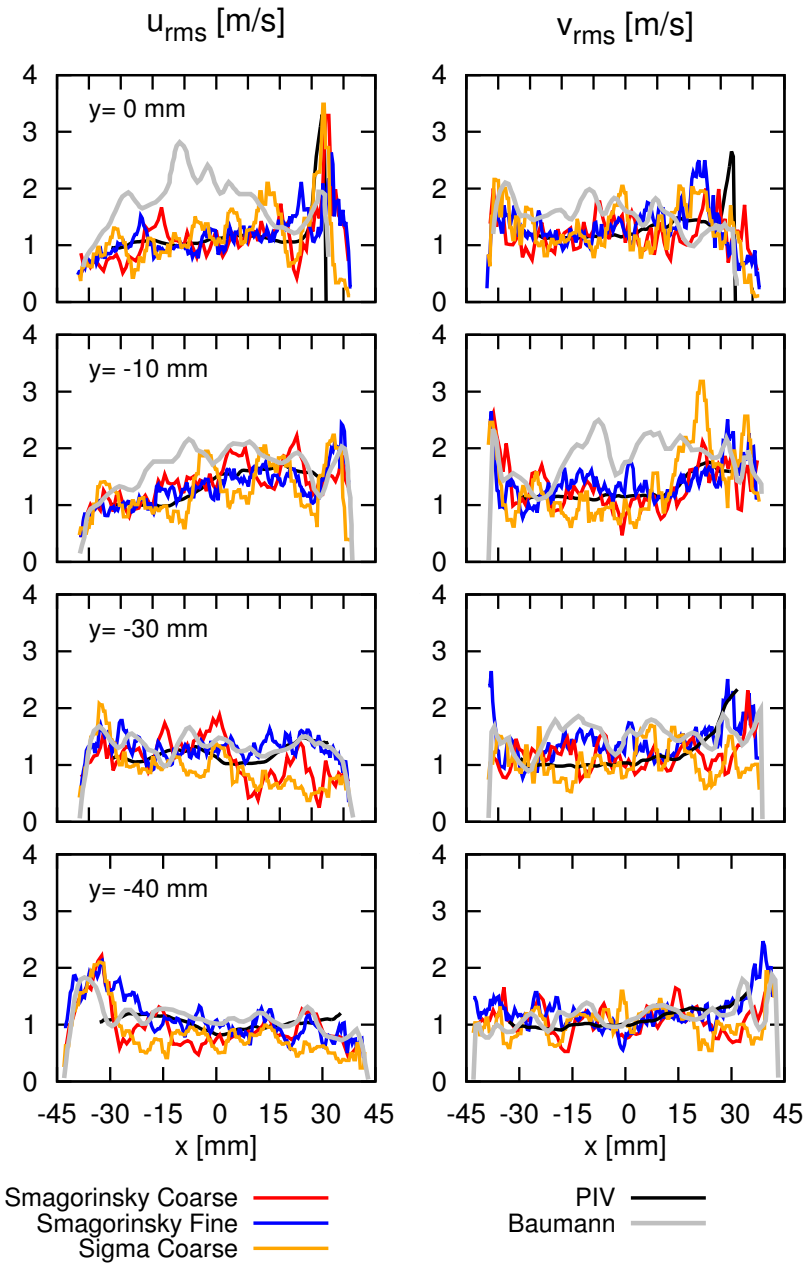

Figure 6.7: Velocity fluctuations taken from the fine (20 cycles) and coarse grid (10 cycles) using the Smagorinsky model and from simulations using the Sigma model (10 cycles), compared to the PIV measurements and from the fine grid simulations (0.8 mm, 50 cycles) of Baumann et al. [19]. (The fluctuations have been sampled within the tumble symmetry plane on horizontal lines underneath the fire deck.)

This chapter was previously published [94] and is reprinted with permission of the journal.

simulations with the Smagorinsky model. It is clear that the number of necessary samples is strongly dependent on the quantity that needs to be studied. Where a mean flow field in stable engine operation will be well sampled after very few cycles, higher moments of velocity or scalars will require more, the statistical analysis of cyclical variations might even require thousands of cycles. At stable engine operation, assuming statistical independence of Gaussian distributed samples u_i', the standard error σ^* of the mean $\overline{u}$ due to the finite number n of samples is given as:

$$\sigma^* = \frac{\sigma}{\sqrt{n}} \quad with\ \sigma = \sqrt{\frac{1}{n}\sum_{j=1}^{n}(u_j - \overline{u})^2} \tag{6.5}$$

This means that the statistical error only drops with the square root of the number of samples - a larger number of samples has a small effect. The engine experiments by Baum et al. [18] show that the error indeed drops like $1/\sqrt{n}$, providing indirect evidence that the samples in the investigated engine are statistically independent.

Based on this information, we would like to propose a criterion for the necessary number of cycles required in a simulation, if the experimental data is known. We suggest that in a simulation, it is not efficient to drive the statistical sampling error $\sigma_{s,\phi} = \sigma^*$ of a mean quantity ϕ to a significantly smaller value than the combined modeling and numerical error. This combined modeling and numerical error $\sigma_{m,n,\phi}$ can be estimated by the difference of a mean ϕ_s from the simulation and the mean from the experiment ϕ_e(assuming a large number of samples in the experiments). In other words, a sufficient number of samples has been achieved once $e_{s,\phi} \approx |\phi_s - \phi_e|$ is reached, with $e_{s,\phi} \approx \sigma/\sqrt{n}$, where σ would be estimated from the available samples.

In practice, this criterion could be tested by drawing error bars at a distance from the mean results of a simulation. The simulation would then have to be continued as long as most experimental data points lie within the narrowing error bars ($1/\sqrt{n}$), but can be stopped when the error bars have become so narrow that most experimental data points lie outside the error bars. In other words, the simulation would be run until it becomes clear that a really good agreement with the experiments is no longer likely.

Figure 6.8 shows the u- and v-velocity components, phase averaged over 5 and 20 cycles at 270°bTDC at 10 and 30 mm underneath the fire deck together with the error bars derived. It can be seen that the error from 5 to 20 cycles decreases and that there are already points for which the statistical error is small compared to the deviation from the experiment - so that based on the proposed criterion, 20 cycles would be sufficient to assess how well the simulation agrees with the experiment.

6.4.2 Valve seat region

An important area inside the combustion engine is the valve seat region, from where the flow enters the combustion chamber, thus governing the development of the (turbulent) flow field (see figure 6.1). Therefore, the flow field on curtain planes around the valves is evaluated first and compared to the MRV measurement. A cylindrical coordinate system is introduced with its origin in the centre of the intake valve and along the valve stem. The radial velocity component was calculated for both intake valves, accordingly. The curtain surface has a radius r of 16.5 mm and a height h of 10 mm. This surface covers the

This chapter was previously published [94] and is reprinted with permission of the journal.

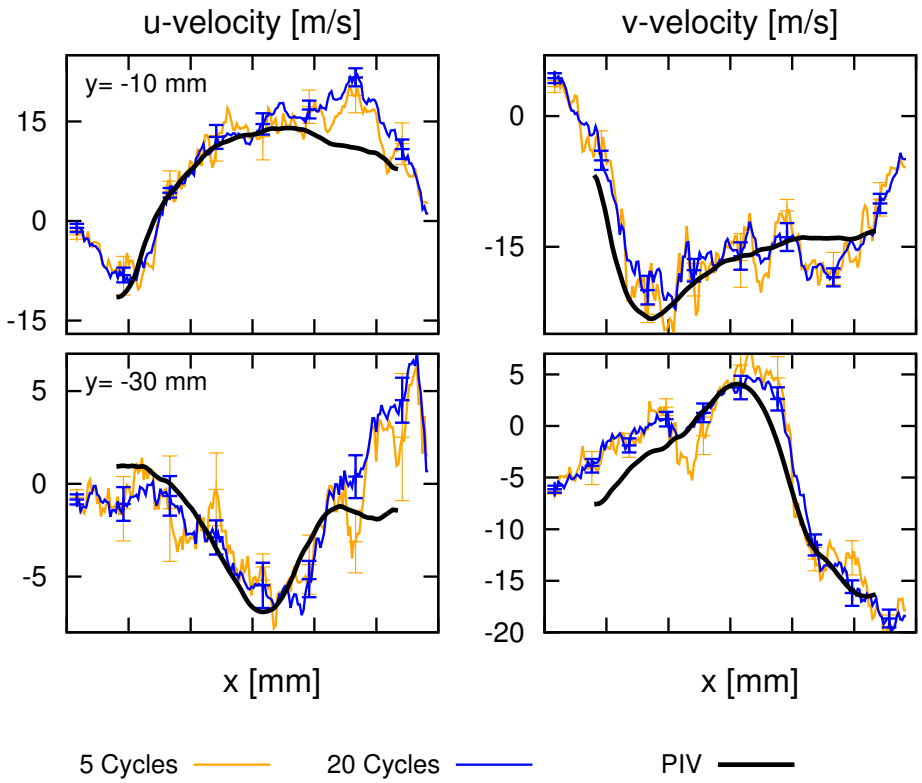

Figure 6.8: Phase averaged velocity components taken from 5 (orange) and 20 (blue) cycles, simulated on the fine mesh with the Smagorinsky model at 270°bTDC within the tumble symmetry plane at -10 and -30 mm underneath the fire deck compared to the PIV measurement.

This chapter was previously published [94] and is reprinted with permission of the journal.

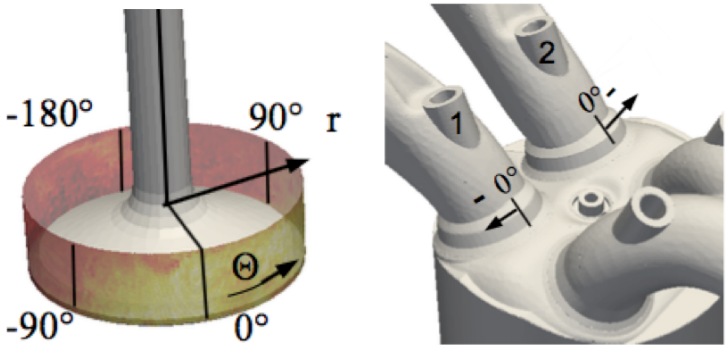

Figure 6.9: Valve curtain in cylindrical coordinate system for valve 1 and the cylinder head with the position of valves 1 and 2.

complete entrance area around the valve from the top of the valve to the cylinder head. Figure 6.9 shows the annular valve seat plane, where the range of -90° $< \theta <$ 90° will be denoted as overflow region and the rest of the curtain as underflow.

Figure 6.10 shows the ensemble averaged radial velocity field within the unwound valve curtain of valve 1 of the MRV measurement and the phase averaged radial velocities obtained from 10 LES cycles (coarse grid, Smagorinsky model) of valve 1 and the instantaneous radial velocity fields of both intake valves. It is clear that the flow is gradually increasing from $\theta = -180°$ to $\theta = -90°$, where regions with negative radial velocities (backflow) are observed at the upper part of the valve curtain next to the cylinder head, indicating flow separation. (A detailed description of flow separation in the valve seat region can be found in the work of Weclas et al. [193].) The instantaneous velocity fields in figure 6.10 show large amounts of turbulent fluctuations, in particular in the underflow region. In the average fields, the highest velocities appear in the overflow region.

Figure 6.11 shows the percentage of the mass flow passing the valve curtain of valve 1 for the LES and MRV for bins of 10°. In the window of -50° $< \theta <$ 50°, around 72% of the total mass is inducted according to the MRV and LES. In the range of -180° $< \theta < -90°$, the mass flow profile for the MRV and LES is smoother than on the positive θ side, where the two intake streams merge, which may cause instabilities in the flow.

6.4.3 Valve plane

The flow passes the valve curtain and enters the combustion chamber (zone 3 in figure 6.1) and starts forming a large tumble vortex. Figure 6.12 shows the contour plot of the velocity magnitude as obtained by the MRV measurement (Re=45000) and LES (Re=32200) in a cut through the valves. The Reynolds-number in the LES was calculated for the inlet pipe, 100 mm upstream of the bifurcation, consistent with the position in the MRV measurement. The flow passing the upper tip of the valve is denoted as overflow and the lower stream as underflow, according to Freudenhammer et al. [64] and illustrated in figure 6.12. The fluid enters the combustion chamber as a "planar jet-like" flow, where the highest flow velocities are obtained in the valve seat area. In the upper part of the cylinder head, the velocity fields from the MRV and LES are qualitatively comparable to each other, but in the MRV measurement a bigger penetration length of the upper jet is observed in the overflow region. The flow detaches at the upper tip of the intake valve and forms a

This chapter was previously published [94] and is reprinted with permission of the journal.

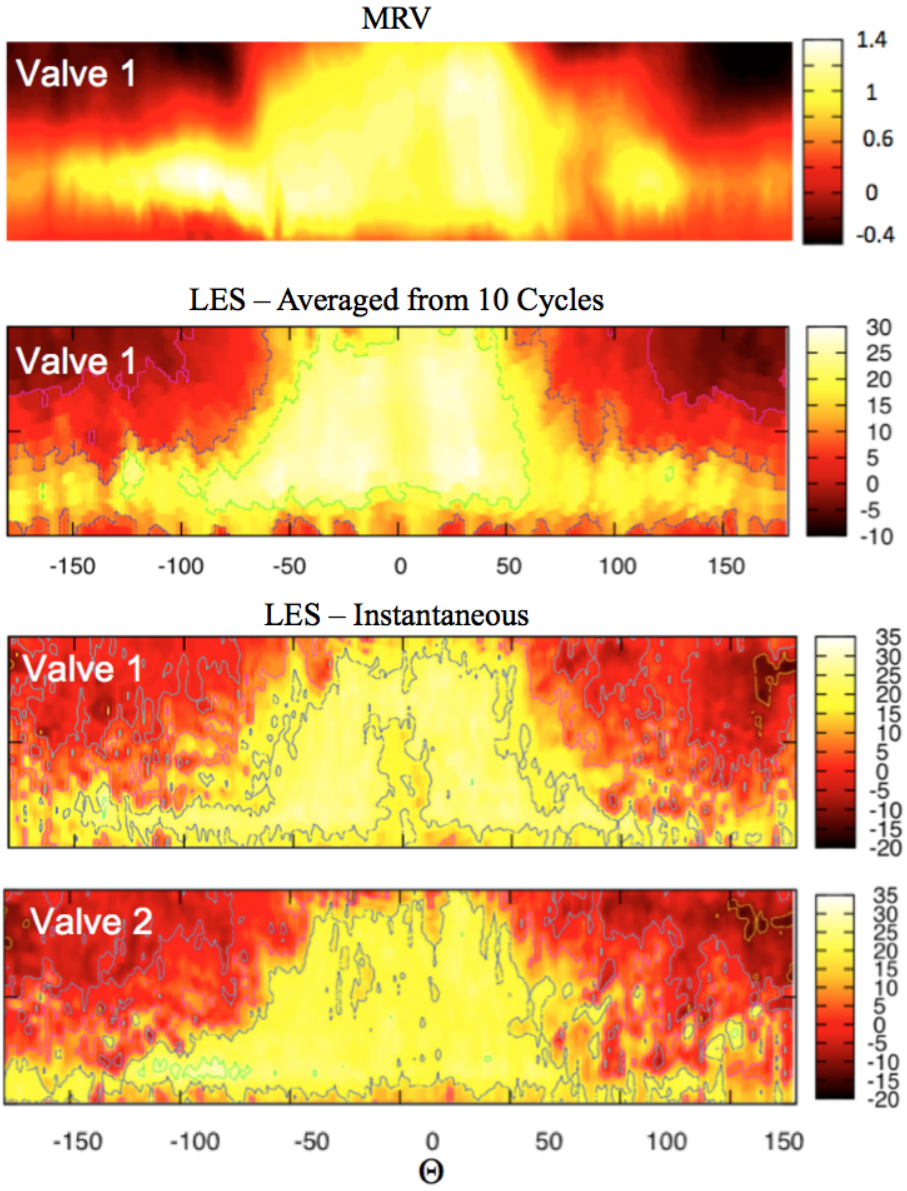

Figure 6.10: Rolled-upped ensemble averaged radial velocity on the valve curtain of valve 1 given by the MRV measurement (Re=45000) and averaged and instantaneous radial velocity contour plots from the intake valve curtains given by the LES obtained from 10 cold flow LES (Smagorinsky model) cycles on the coarse grid.

This chapter was previously published [94] and is reprinted with permission of the journal.

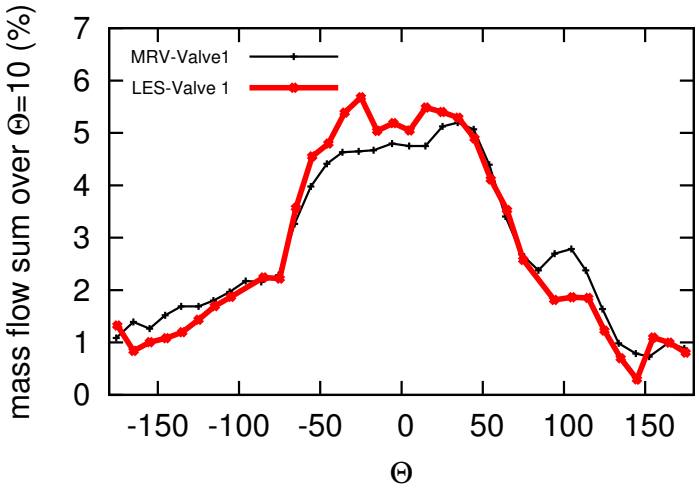

Figure 6.11: Percentage of the total mass flow over the inlet valve 1 of a mean from 10 LES cycles (coarse) at 270°bTDC and the MRV measurement, determined for bins of 10°.

recirculation zone underneath it.

In the underflow region, the flow changes significantly across the valve seat. It is not accelerated over the full cross-sectional area, only in a small layer along the lower tip of the valve. The smaller velocities and backflow at the lower valve seat area are caused by recirculation zones created by the sharp edge of the intake port in the underflow region. Those recirculation zones induce losses (less in-cylinder filling), but they also force the flow to pass the upper part of the valve seat to enter the combustion chamber, which enhances the tumble motion. In the cross-tumble plane (figure 6.12), the flow is accelerated after the valve stem and branches towards the liner wall and center line. The branch towards the liner, impinges at the wall and spreads towards the exit (or towards the piston in the LES). In the middle of the cross-tumble plane, the flow in-between the two intake valves merges together, locally forming a single planar jet. The coalescence of the two jets in-between the intake valves leads to oscillations of the merged single jet in the LES, which will reduce the reproducibility of the flow field inside the engine. Furthermore, in the LES results, the flow impinges on the liner wall at a lower position, and a thicker layer with higher velocities is predicted. This needs further investigations, since the wall modeling for LES is a challenging problem and not touched in the scope of this work.

6.4.4 Tumble plane

Figure 6.14 shows the phase averaged flow fields, calculated from ten LES cycles on the coarse mesh (Smagorinsky model), the phase averaged flow fields given by the PIV measurements at 270°bTDC and the MRV data (Re=45000) in the tumble symmetry plane. A good agreement between the PIV and LES is achieved. As in this flow bench measurement, the piston was replaced by a steady outlet manifold, only the upper part of the combustion chamber to the position y=-20 mm should be taken for a comparison to the PIV measurement and LES. However, above the y=-20 mm position, a good agreement is achieved for the MRV measurement compared to the LES and PIV measurement. In the LES simulation, the spark plug was not removed, which caused a recirculation zone downstream of it.

This chapter was previously published [94] and is reprinted with permission of the journal.

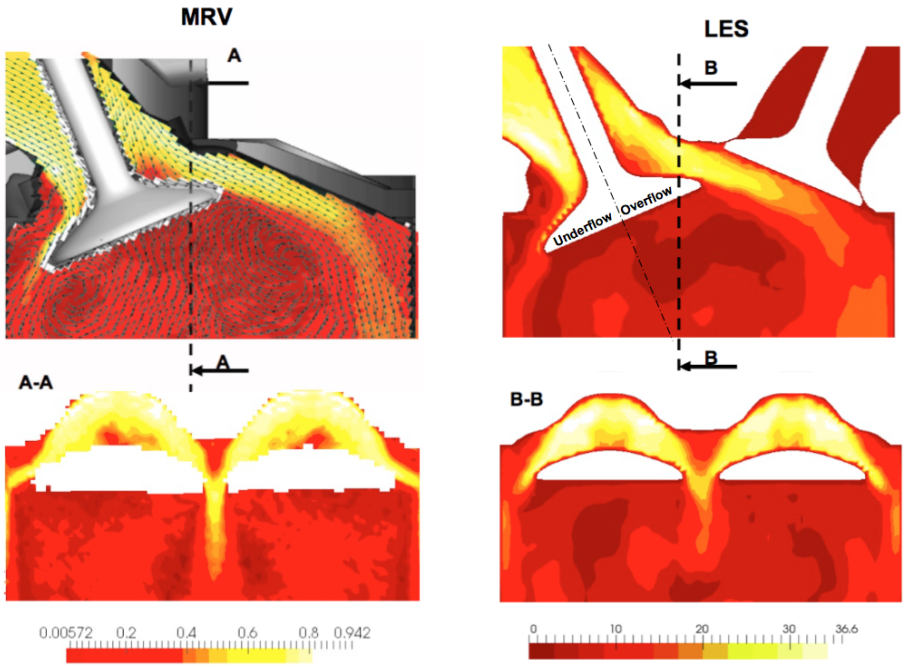

Figure 6.12: Contour plot of the ensemble average velocity magnitude [m/s] for the MRV experiment (left) and for the LES (right) phase average at 270°CA over ten cold flow engine cycles (coarse mesh, Smagorinsky model), on a cut through valves (top) and on the cross-tumble plane (bottom).

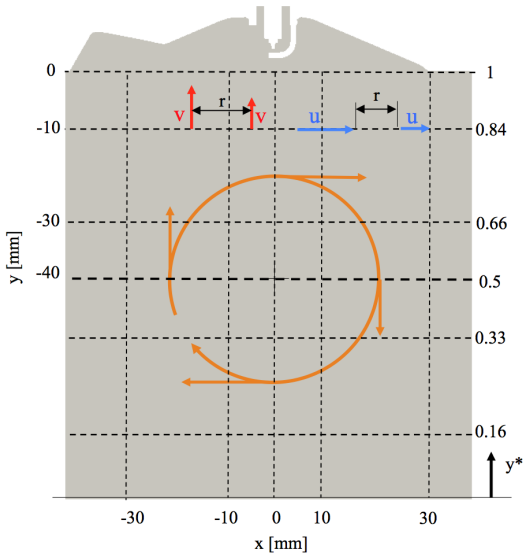

Figure 6.13: Sample positions on the tumble symmetry plane for the comparison of velocity profiles along (a) vertical lines at positions in x-direction at ±30 mm, ±10 mm and 0 mm and (b) along horizontal lines in y-direction at 0 mm, -10 mm, -30 mm and -40 mm. The coordinate y* is normalized by the current height of the combustion chamber, ranging from 0 on the piston head to 1 at the fire deck. In the centre of the tumble plane, a big vortex is shown and velocity vectors u and v for the illustration of the definition of the auto-correlation functions.

This chapter was previously published [94] and is reprinted with permission of the journal.

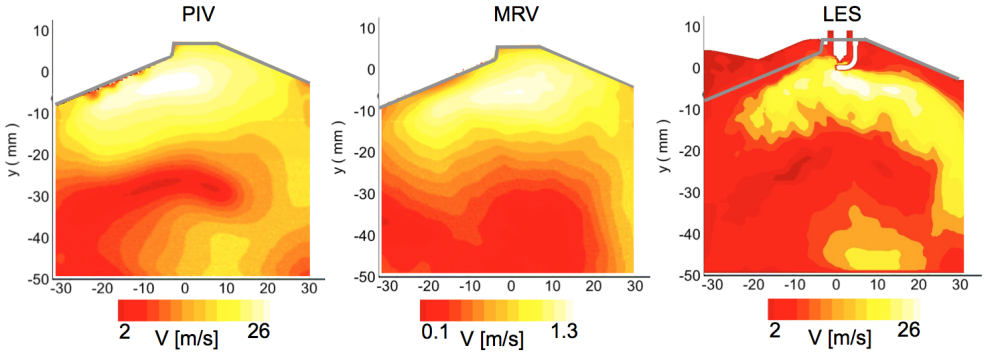

Figure 6.14: Velocity magnitude plot given by the PIV measurement taken from an average of 2700 motored cycles (left), by the MRV (middle) and the velocity magnitude contour plot obtained from an average of ten cycles from the LES (coarse grid, Smagorinsky model, right) within the tumble symmetry plane. Note that the MRV velocity data deviates due to the use of a different fluid.

In figure 6.15, the velocity components in the x- and y-directions are plotted for all measurements and LES results at 270°bTDC and in figure 6.16, for the LES and PIV at 90°bTDC, along the lines indicated in figure 6.13. A good agreement among the measurements and simulations is achieved, where at 270°bTDC the vertical velocity profiles from LES and PIV deviate to the MRV data below 20 mm of the fire deck, due to the missing piston in the MRV measurement. Interestingly, the velocity profiles calculated with the Sigma model are deviating at 90°bTDC to the experiment, where the simulations performed with the Smagorinsky model still match the experiment well. The velocity profiles from the cycles with the Sigma model rather follow the trend of the simulation by Baumann et al. [19], who used the Smagorinsky model, but with a higher model constant ($C_s = 0.165$). Apparently, the velocity fields seem to be more sensitive to the turbulence model and model constant in the compression phase, as in the intake phase. The comparison of the present LES data to that of Baumann et al. [19] and to the PIV and MRV measurements shows that the flow field is captured sufficiently well to justify the further analysis presented in the following sections.

6.4.5 Tumble vortex identification

For the identification of the large scale vortex motion, a 2D tracking algorithm proposed by Graftieaux et al. [77] is used. It was already applied in the past to instantaneous velocity fields of an optical research engine, for example by Druault et al. [52], who studied the cycle-to-cycle variability of the in-cylinder flow and more recently by Stiehl et al. [177] for the interaction of the engine flow to the fuel spray inside a stratified direct injection engine. The vortex identification function Γ in the integral form is defined as:

$$\Gamma(\vec{x}) = \frac{1}{V} \int_V \left(\frac{\vec{x^*}}{|\vec{x^*}|} \times \frac{\vec{u^*}}{|\vec{u^*}|} \right) \cdot \vec{n} \, dV \tag{6.6}$$

In equation 7.20, V denotes the 2D integration domain, $\vec{x}$ the position at which the function Γ is evaluated, $\vec{x^*}$ the location of any point within the integration domain, $\vec{u^*}$ the velocity at $\vec{x^*}$ and $\vec{n}$ the normal vector to the 2D integration domain. The 2D vortex tracking

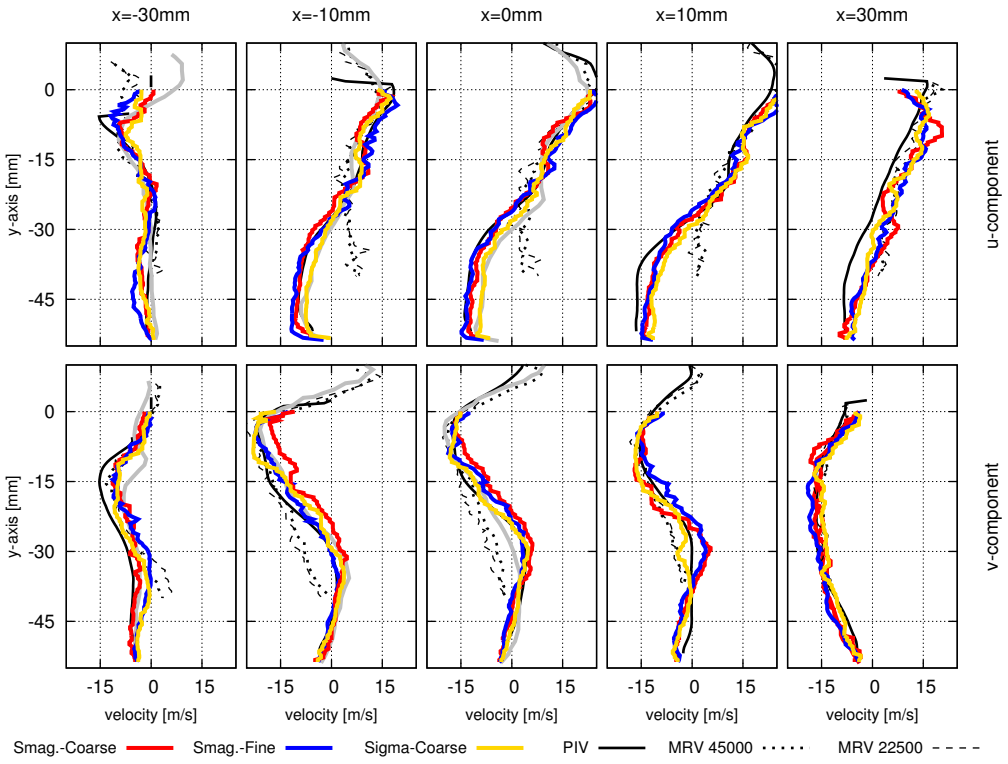

Figure 6.15: Mean velocity profiles on vertical lines under the fire deck, phase averaged over ten LES engine cycles with the Smagorinsky model on the coarse mesh (red), twenty LES cycles with the Smagorinsky model on the fine mesh (blue), ten LES cycles with the Sigma model (orange), from the LES by Baumann [19], from PIV and from MRV at Re=22500 and 45000 at 270°bTDC.

This chapter was previously published [94] and is reprinted with permission of the journal.

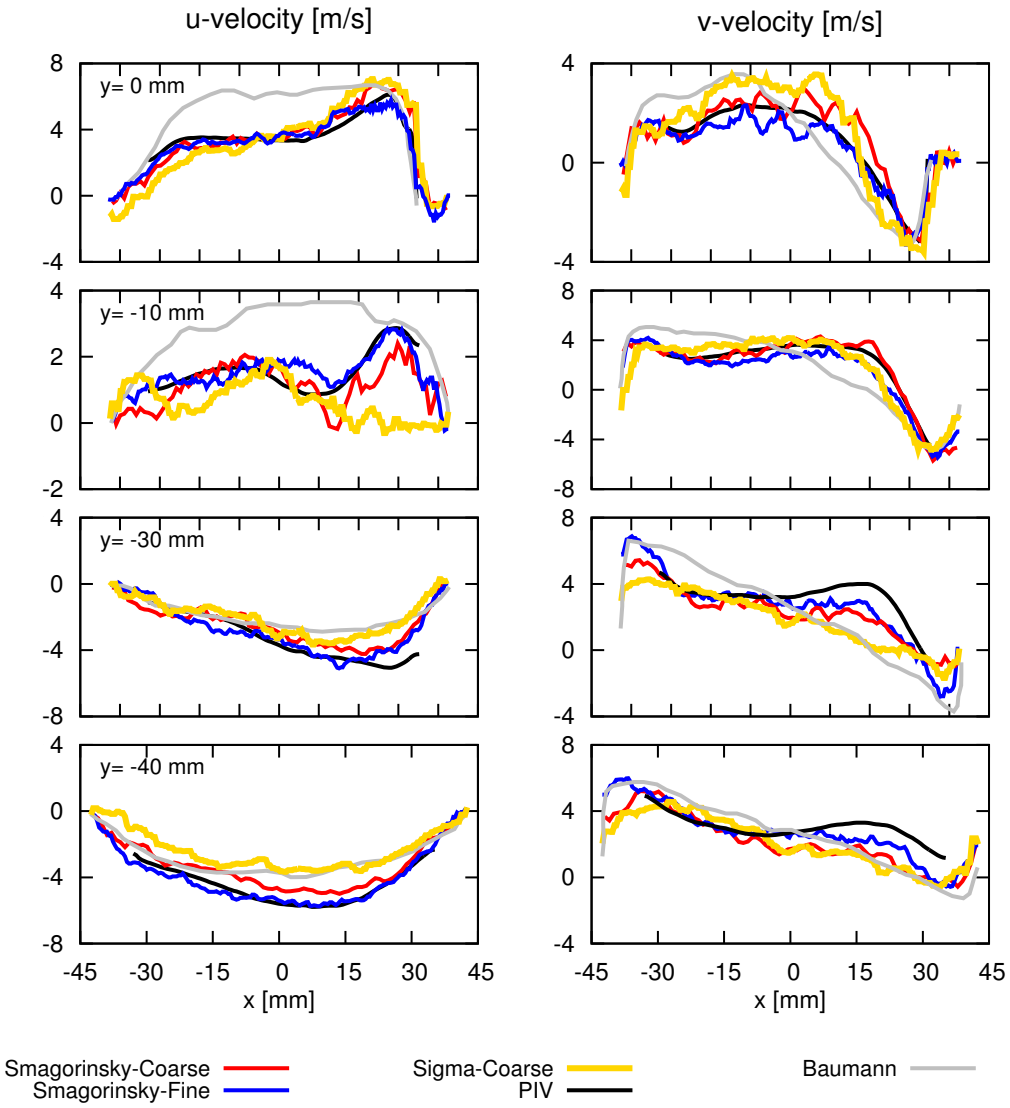

Figure 6.16: Phase averaged velocity components in x- and y-directions obtained from ten LES cycles on the coarse grid (red) and twenty LES cycles on the fine mesh (blue) using the Smagorinky model, from ten cycles with the Sigma model on the coarse grid (orange), from the fine grid LES simulation by Baumann et al. [19] (gray) and the corresponding PIV-measurement (black) within the tumble symmetry plane at 90°bTDC.

This chapter was previously published [94] and is reprinted with permission of the journal.

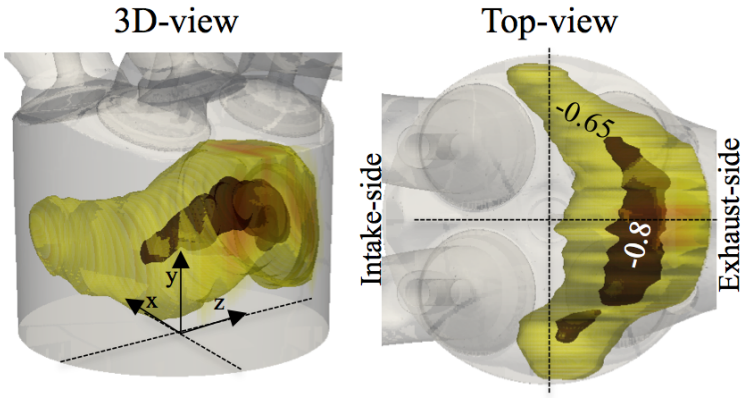

Figure 6.17: A 3D representation of the Γ-field obtained by the 2D vortex detection algorithm at 90°bTDC for the fine mesh simulation. The light yellow color represents an iso-value of the Γ-field of -0.65 and the dark brownish color an iso-value of -0.8.

algorithm is applied on 2D planes separated by 1 mm in z-direction, throughout the entire combustion chamber for multiple cycles (coarse LES) within the compression stroke. For each 2D plane a contour field of the centre of the tumble vortex is obtained, which is bounded between -1< Γ <1. The negative Γ-values indicate the location of a clock-wise turning vortex (towards the exhaust side) and positive Γ-values a counter clock-wise vortex. For $\Gamma = \pm 1$, the centre of a "perfect circular 2D vortex" would be obtained, which is hardly achievable, since the flow field is very complex. In figure 6.17, two instantaneous iso-contour plots of the volumetric Γ-field are shown (fine mesh). The tumble flow has a "croissant-like" shape and branches towards the positive and negative z-direction. Bücker et al. [30] also applied the Γ-criterion for the flow field of an optical research engine and found a "c-shaped" tumble vortex during the compression stroke, which looks very similar to our "croissant-liked" shape. However, they have applied it to a pseudo volumetric velocity field obtained by multiple stereoscopic PIV measurements at different planes, which cannot be used to study cyclic variability of the tumble vortex.

In figure 6.18, a top view of the "tumble-croissant" at 90°bTDC is shown for 6 different LES cycles (coarse mesh, Smagorinsky model). In each cycle, the shape is different, which illustrates the complexity and variability of the flow field. In order to trail the tumble trajectory, the maximum Γ-value within the tumble symmetry plane was tracked from 180°bTDC to 20°bTDC. The tumble centre is plotted for 4 different cycles in figure 6.19, where the dots represent the position of the tumble centers and its color defining the corresponding °CA within the compression stroke. For all 4 cycles, the tumble centre starts at different positions and follows a different path, but moves consistently for all cycles towards the exhaust side. The movement towards the exhaust side of the tumble vortex is governed by the rotational direction of the tumble and by the piston which pushes the tumble upwards. At around 90°bTDC the tumble centre changes its direction and moves towards the spark plug (intake-side). The trend of the trajectory is well captured by the LES. For a better representation in the high scatter of the tumble trajectories, the tumble trajectories of 7 cycles are shown together in figure 6.20 and compared to the PIV measurements. The trajectories are very similar for all cycles, except for cycle 7, which follows a very different path. This shows that sudden flow field irregularities from one cycle to the next cycle appear - as an example of cyclic variations.

This chapter was previously published [94] and is reprinted with permission of the journal.

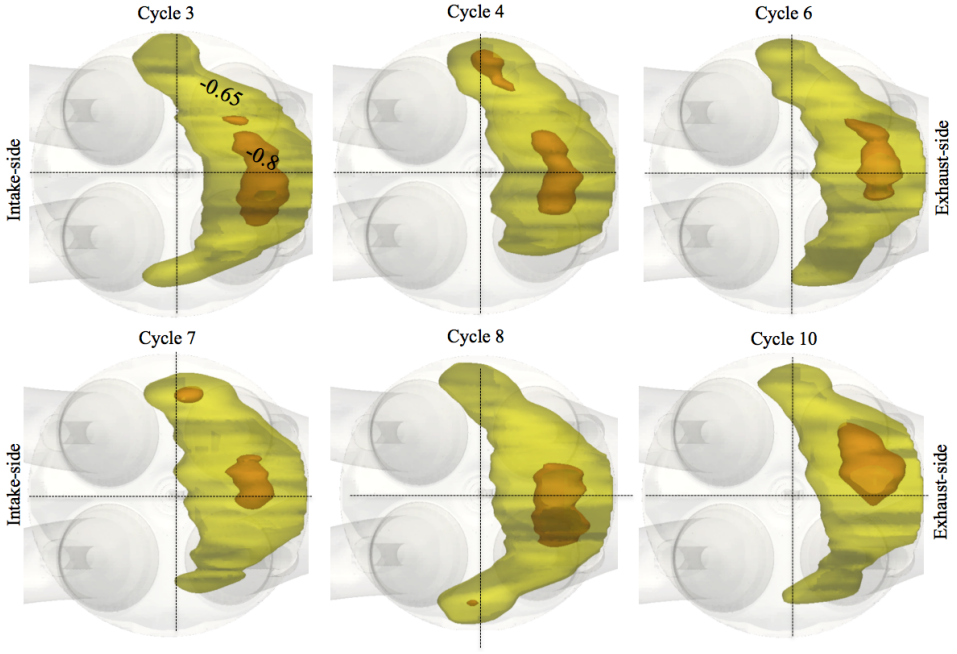

Figure 6.18: The Γ iso-contour (-0.65 and -0.8) plots obtained by the LES (coarse) at 90°bTDC for different cycles.

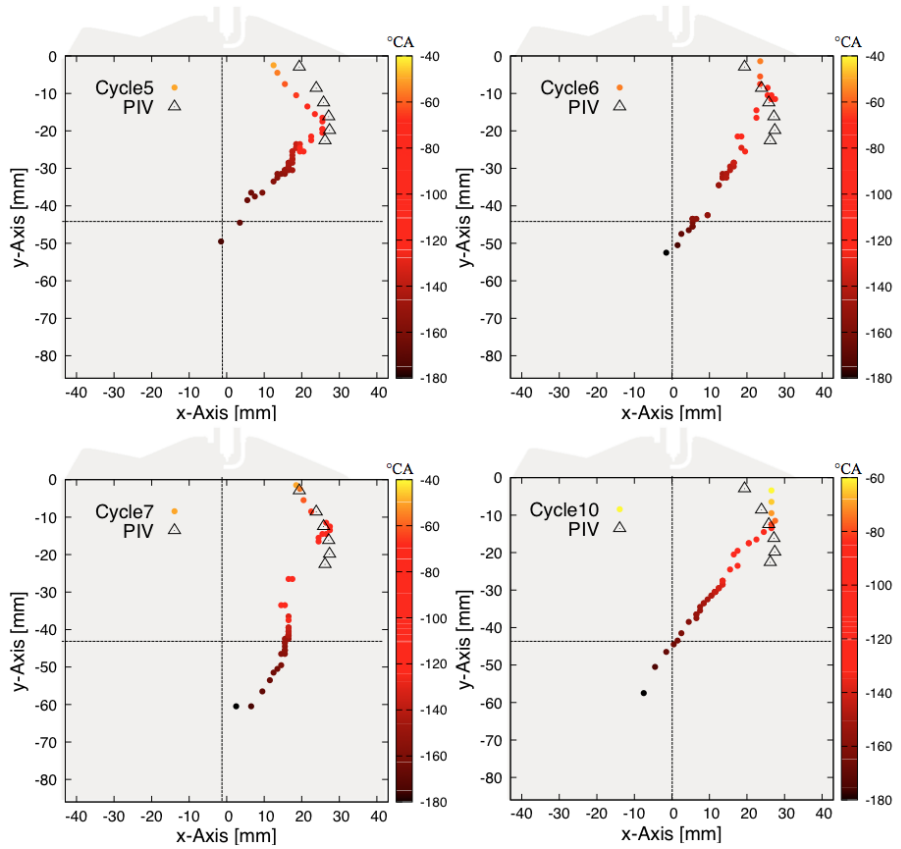

Figure 6.19: Tumble trajectory from 180°bTDC to 20°bTDC within the tumble symmetry plane for four LES cycles compared to the averaged trajectory from the PIV measurement.

This chapter was previously published [94] and is reprinted with permission of the journal.

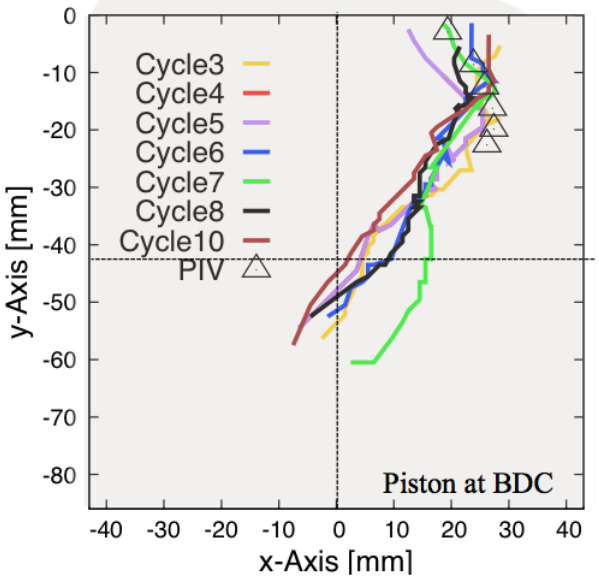

Figure 6.20: Tumble trajectory from 180°bTDC to 20°bTDC within the tumble symmetry plane for different cycles and compared to the averaged tumble trajectory from the PIV measurement.

The tumble vortex is compressed by the upward motion of the piston, reducing its size. In figure 6.21, the volume of the "tumble-croissant" for an iso value of Γ=-0.65 is plotted for the compression stroke. At 90°bTDC the tumble volume starts to collapse to the same value for each cycle. From here, the tumble center starts to change its direction towards the spark plug and branches towards the negative and positive z-axis as seen in figure 6.17.

6.4.6 Two-point velocity correlation

The two-point correlation functions of the velocity fluctuations along horizontal lines inside the combustion chamber are computed for the fine grid. They relate two velocity vector components to each other as a function of their distance r [157]. In total, 5 different locations were chosen within the tumble symmetry plane, for the sampling of the velocity at the (normalized) y*-coordinates shown in figure 6.13. The normalized two-point correlation function reads:

$$R_\alpha(r) = \frac{\langle u'_\alpha(x) u'_\alpha(x+r)\rangle}{\langle u'_\alpha(x)^2\rangle} \tag{6.7}$$

In equation 6.7, the velocity fluctuations u' are defined as the deviation of the instantaneous velocities $\widetilde{u}$ of a cycle k from the LES phase average $\langle\widetilde{u}\rangle$ over N cycles, where α denotes a velocity component in the direction α (Einstein summation is not implied).

$$u' = \widetilde{u} - \langle\widetilde{u}\rangle, \text{ with } \langle\widetilde{u}\rangle = \frac{1}{N}\sum_{k=1}^{N}\widetilde{u}_k \tag{6.8}$$

The classical two-point correlation should be applied on homogeneous, isotropic turbulence with enough statistics for a fully converged result (thousands of consecutive cycles,

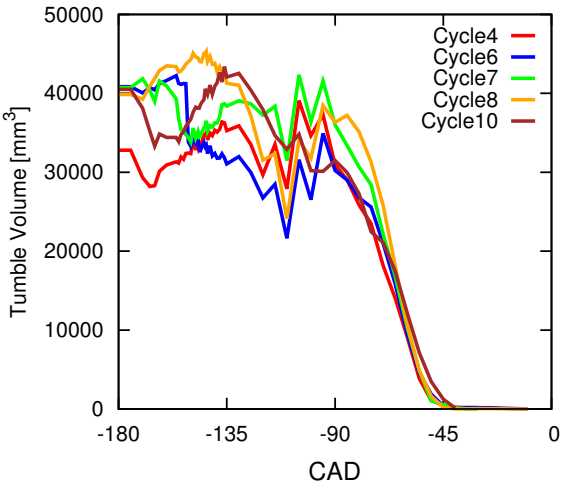

Figure 6.21: Volume of the tumble vortex for an iso-value of -0.65 of the Γ-field for different cycles within the compression stroke.

according to Baum et al. [18]). These requirements are almost impossible to meet in an engine or an LES. However, the correlation function can provide useful insight into the tumble break-down process, if we alter the definition such that it will include the tumble vortex and subsequent coherent structures. Therefore, we propose a modified version of the classical two-point correlation function, which also considers coherent structures and not just the turbulent fluctuations:

$$R_\alpha^\delta(r) = \frac{\langle u_\alpha^\delta(x) u_\alpha^\delta(x+r)\rangle}{\langle u_\alpha^\delta(x)^2\rangle} \tag{6.9}$$

Equation 6.9 shows the adjusted correlation function, which only differs in the use of a different velocity fluctuation u^δ. This u^δ denotes the deviation of the instantaneous resolved velocities $\widetilde{u}$ from the spatial mean $\overline{\widetilde{u}}$ along the reference line in x-direction with the length l, which is bounded by the liner walls. For the tumble plane the integration bounds are equal to the size of the bore ($l = 86mm$). This means that the velocity fluctuations u^δ are defined relative to a line moving with the mean velocity, resulting from compression only.

$$u^\delta = \widetilde{u} - \overline{\widetilde{u}}, \text{ with } \overline{\widetilde{u}} = \frac{1}{l}\int_{-l/2}^{l/2} \widetilde{u}\, dx \tag{6.10}$$

A perfect correlation of 1 appears, when the velocities at a specific distance are always identical, which is obviously true for r=0. In order to illustrate the two-point correlation, a vortex is sketched in figure 6.13, where the orange velocity vectors at y*=0.5 exhibit a negative (cross) correlation (pointing in opposed directions). Thus, a change in the sign of the correlation functions, can be interpreted as the "radius" of a vortex. The cross-correlation relates the velocity components in y-direction at two points separated in x-direction to each other (red arrows at y*=0.84 in figure 6.13).

In figure 6.22, the normalized two-point correlation coefficients along the 5 horizontal lines underneath the cylinder head are plotted from 125°bTDC (IVC) to 0°bTDC for every 25°CA with the classical (R_α) and modified version of the correlation function (R_α^δ). The piston position for the corresponding °CA is marked with arrows underneath the cross-

This chapter was previously published [94] and is reprinted with permission of the journal.

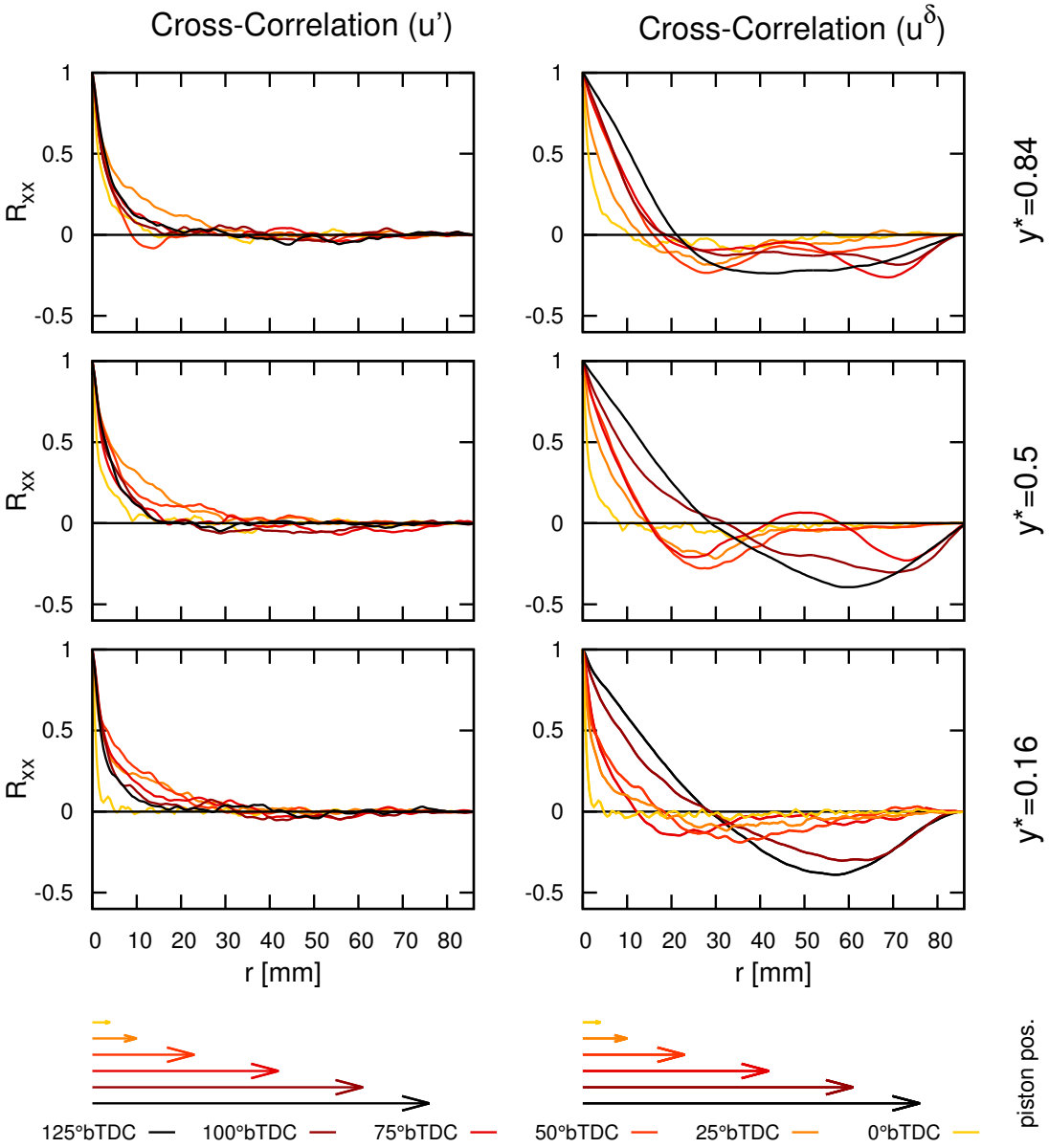

Figure 6.22: Lateral two-point auto-correlation coefficients of the (turbulent) velocity fluctuations u' (classical formulation, left column) and for the velocity fluctuations u^{δ} (right column), for an average of twenty cycles obtained by the LES simulation on the fine grid, along the horizontal reference lines within the tumble symmetry plane. The distance of the piston head to its location at top dead center is illustrated by arrows, representing the biggest possible vortex that could fit inside the combustion chamber.

This chapter was previously published [94] and is reprinted with permission of the journal.

correlation plot and shall demonstrate the "biggest possible vortex size" that would fit inside the combustion chamber. Figure 6.22 shows a very noisy pattern for the cross-correlation coefficients obtained by the classical auto-correlation function (R_α), which is to be expected due to the combination of few samples and small turbulent length scales. The cross-correlation coefficients R_α^δ, however, show a smooth pattern and imply that the integral length scale is decreasing with compression. Interestingly, the classical and modified correlation functions are very similar at TDC, giving evidence that the tumble motion is completely transferred to turbulence.

The further discussion will be based on the results of the modified correlation function R_α^δ. From 125°bTDC (IVC) to 100°bTDC the cross-correlation changes only one time its sign and stays negative for all 5 sampling locations, which implies the appearance of only one big vortex. If we assume that the tumble centre will be in the middle of the plane (y*=0.5), it will have a diameter of around 60 mm at 125°bTDC. At 75°bTDC the cross-correlation curves start changing its sign, which indicates the appearance of new vortices. In fact, 3 vortices can be suspected at y*=0.5 at 75°bTDC with a vortex diameter of around 20 mm each. By approaching the end of the compression stroke, the diameter of the vortices are in the order of the piston-to-cylinder head distance and the cross-correlation curves get a "wiggling" pattern. At 50°bTDC the first minima of the cross-correlation curve is roughly at the same position as the corresponding piston-to-cylinder head distance (orange arrow). From here, the tumble occupies the entire combustion chamber, and will have contact to liner walls, piston-top and cylinder head. In figure 6.17, it is clearly seen that the tumble is already at 90°bTDC constricted by the geometry. Now, the piston will effectively compress the tumble and the large scale motion will break-down into a highly irregular flow field with multiple vortices - the break-down of the tumble into smaller scales. The highly turbulent flow field with many small vortices is shown for the cross-correlation curves for 0°bTDC.

From the normalized two-point correlation coefficients R_α^δ, the integral length scale L_δ was calculated for the 5 horizontal sampling positions during compression, according to equation (6.11), with q as the distance where the autocorrelation function firstly intersects with the zero line.

$$L_\delta = \int_0^q R_\alpha^\delta(r)\, dr \tag{6.11}$$

Figure 6.23 shows the lateral integral length scales obtained from the cross-correlation function R_α^δ for 7 instantaneous cycles. It has to be mentioned, that this length scales should not be confused with the integral length scales of the turbulent fluctuations, rather be seen as a characteristic length scale of big coherent structures. The length scales are scattering for the different cycles, showing the biggest deviations to each other at 50°bTDC (tumble vortex touches the walls) and the lowest scatter at TDC. The lower scatter of the length scales at TDC can be explained by the length scales itself, where smaller vortices tend to behave more equally than big vortices. Overall, however, the lateral length scales are continuously decreasing, reaching values of 15 mm at intake valve closure to 0.8 mm at TDC.

This chapter was previously published [94] and is reprinted with permission of the journal.

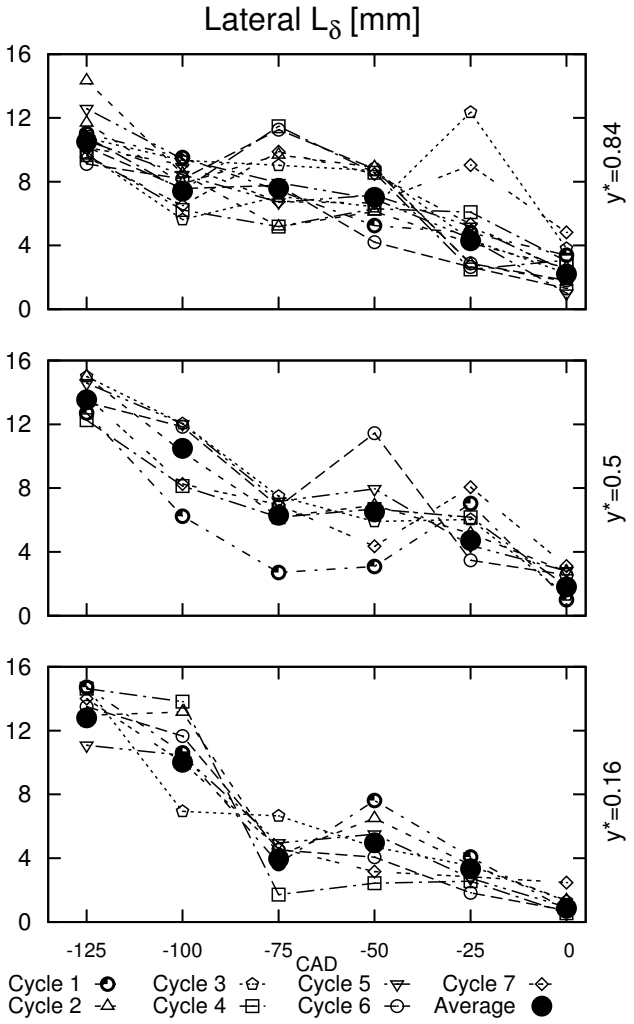

Figure 6.23: Lateral length scales calculated from the auto-correlation coefficient curves R^{δ}_{α}, provided by the LES on the fine grid along horizontal lines within the tumble symmetry plane for 7 instantaneous cycles and the average of twenty cycles.

This chapter was previously published [94] and is reprinted with permission of the journal.

6.5 Conclusions

Large-eddy simulations of an optical research engine were performed for motored operation with two different grid spacings of 1 mm (coarse) and 0.5 mm (fine) inside the combustion chamber. The in-cylinder pressure distribution for the full cycle was examined, showing a good agreement for the LES on both grids during the gas exchange, in particular at the opening and closing events, compared to the experiment. However, an overprediction of the peak in-cylinder pressure was obtained by 17%. A theoretical study of the compression and a comparison to an independent LES simulation of the same engine provided considerable evidence for the correctness of our simulation.
A criterion for an estimate of the needed number of cycles has been proposed and tested on our simulation data sets of 20 cycles.
The predicted velocity agreed qualitatively and quantitatively well with the PIV data and in the upper part of the cylinder volume also with the MRV data, even though MRV was conducted under stationary conditions and with water as a fluid. To the best of the authors' knowledge, this is the first comparison of PIV and LES velocity fields to MRV data in the valve seat region. The mass flow around the valve curtain area was in good agreement. Recirculation zones within the valve seat region reduce the in-cylinder filling. Around 72 % of the total mass flow comes via the overflow region into the cylinder. However, looking on instantaneous contour plots around the valve seats, the highest velocities are observed in small spots in the underflow area. The standard Smagorinsky (C_s=0.062) model worked well, considering the complexity of the engine flow. The direct comparison with the Sigma model and the simulation by Baumann et al. [18] revealed sensitivities of the turbulence models and model constants during the compression phase, which were not seen during the intake stroke. A good match between the MRV, PIV measurements and the LES simulation was achieved.

The tumble shape and its motion was calculated by a 2D vortex identification algorithm on 2D slices throughout the entire combustion chamber. During the compression it takes a "croissant-like" shape that branches towards the positive and negative z-axis until it collapses and disappears. Its shape and trajectory is different form cycle to cycle during the compression. The tumble is moving towards the exhaust side and changes its direction at around 90°bTDC. From the shift in direction, the tumble volume drops as the vortex cannot move freely and is guided by the upwards moving piston.

With the help of the modified definition of the velocity fluctuations for the two-point autocorrelation, it was possible to better observe the tumble break-down. The cross-correlations of the velocity fluctuations along horizontal lines within the tumble symmetry plane showed the reduction of the tumble size, while approaching the end of the compression phase. The tumble has the biggest diameter at the start of the compression (125°bTDC) of around 60 mm with a piston-to-cylinder head distance of 75 mm. The cross-correlation curves show that once the tumble has been "squeezed" sufficiently, the big vortex is split into several smaller vortices, which can be already seen as the onset of tumble break-down - when one big tumble vortex breaks down into several smaller vortices. In this picture of tumble break-down, the tumble would have a natural tendency to stay "circular" rather than "ellipsoid", leading to a break-down of the one major vortex into several sub-vortices. A big advantage of this method is that first quantifications of the tumble break-down process can be already obtained with a low number of samples (cycles).

7

Numerical investigation of the flame propagation inside a spark ignition engine

This chapter presents a numerical investigation of the flame propagation inside the optically accessible research engine of the Technical University of Darmstadt using the wall-guided cylinder-head configuration and is an extension to a previous work [94] (see chapter 6) where only the cold in-cylinder flow field was studied. In this work, reactive multi-cycle simulations are performed based on a single- and multi-cycle approach. The single cycle approach uses different in-cylinder flow field conditions prior to ignition for the initialization of individual combustion simulations. The different in-cylinder flow conditions are extracted from 15 multi-cycle cold-flow in-cylinder simulations of the wall-guided head configuration, where the piston top-land crevice is included in the numerical model (not included in the previous work [94]). The Keppeler [100] and Muppala [142] algebraic flame surface density models are used to describe the flame wrinkling throughout the entire combustion duration with the single-cycle approach. No ignition modelling is used, nor the flame-to-wall interaction considered. The flame is allowed to penetrate into the piston top-land crevice. For the reactive-multi cycle approach 6 consecutive cycles - only using the Keppeler model - with combustion are calculated on. The influence of the internal gas recirculation (IGR) on the laminar flame speed is taken into account. Finally, the results of the flame propagation are compared to Mie-scattering [48] images of the corresponding engine.

7.1 Introduction

In order to reduce pollutant emissions and increase the efficiency of internal combustion engines, a detailed understanding of the in-cylinder phenomena is crucial. Combustion in a spark-ignition engine occurs in the corrugated or wrinkled flamelet regime according to the combustion diagram by Borghi and Peters [151], emphasizing the importance of the local flow structures for the flame itself. Several modelling approaches have been developed to cope with flames in these regimes [155]. This work applies the flame surface density approach to model the flame front propagation, which describes the corrugated unresolved flame by a wrinkling factor, that can be interpreted as the ratio of the turbulent to laminar flame speed [68] [83]. Flame surface density models permit a computationally efficient flame speed closure for modelling turbulent premixed combustion in essentially premixed systems, like a port injection gasoline or gas engine. A comparison of state of the art flame surface density models is given by Ma et al. [127] and Chakraborty et al. [37], providing

an idea of which models work well and less well based on a priori and a posteriori analysis. The algebraic Keppeler [100] and Muppala [142] flame surface density models are used here to model the reaction rate; the Muppala model was chosen for its simplicity and good performance in a posteriori testing [127] and the Keppeler model, because it has shown good performances for flames at elevated pressures up to 20 bars.
The ideal combustion model for spark-ignition engines has to represent: (a) the ignition phase, (b) the free flame propagation and (c) the flame behaviour at the walls. Algebraic flame surface density models cannot predict the ignition phase, because they are assuming an equilibrium of the flame production end destruction. However, during the free flame phase (no influence of the walls), their application is justified. A state of the art combustion model that can predict non-equilibrium effects is the extended coherent flame model (ECFM), combined with the Imposed Stretch Spark Ignition Model (ISSIM) proposed by Colin and Truffin [42]. It applies a transport equation for the flame surface density and includes several closures. It is not easy to apply a complex model such as the ECFM to an engine, because there are many uncertainties, which may have a bigger impact on the results. Uncertainties inside the engine are: (a) the turbulent flow field (i.e. tumble break-down), (b) the amount of the in-cylinder trapped mass, (c) heat transfer to the walls, (d) wall-effects (extinction) or even geometrical details, such as the size of piston top-land crevice.

This work is an extensions of a previous work [94], where the turbulent flow field of the same engine was studied and compared to flow field measurements. The mean flow field was in a good qualitative and quantitative agreement with the experiment, which justifies the next step of studying the turbulent flame propagation, which is highly affected by the in-cylinder aerodynamics. The ignition phase will be "skipped" by imposing an initial flame kernel volume that complies with Mie-scattering images of the burnt gases of the corresponding engine [48]. It will be also demonstrated that small geometrical variations, such as neglecting the piston top-land crevice, have a big influence on the integral quantities (already at motored condition). Finally, the influence of the residual gases to the flame propagation is assessed.

7.2 Engine and experiment

For the combustion simulation, the wall-guided head configuration of the optically accessible research engine of the Technical University of Darmstadt is chosen, due to the availability of experimental data of the flame propagation. The piston top-land crevice is taken into account, because it contributes to about 16 % of the complete combustion chamber volume at TDC. The main characteristics of the engine can be found in table 7.1.

The flame propagation inside the wall-guided head was measured by a step change in the density of silicon oil droplets by Ding [48]. The measured blow-by under fired conditions was 12 g/h, which contributed to around 0.1% of the intake mass flow rate [29]. For the flame tracking experiment, the engine was running at 800 rpm, and was fed with a mixture of iso-octane and air at an air to fuel ratio (λ) of 1.2. The fuel was injected into the intake port far upstream of the intake valves, so that it could mix with the air and the silicon oil droplets before entering the combustion chamber. The intake pressure was set to 950 mbar and the intake temperature to 320 K. Mie-scattering [48] images within the tumble symmetry plane and in a horizontal cut underneath the spark-plug were made from 300 cycles from the start of ignition until TDC.

Table 7.1: Main characteristics of the wall-guided head engine configuration [18].

Bore/Stroke	86/86 mm
Piston	85 mm
Fireland height	74.4 mm
Displacement	499 cm^3
Clearance height	2.6 mm
Compression ratio	8.5:1
Clearance Volume	66.5 cm^3
IVO / IVC	325°aTDC / 125°bTDC
EVO / EVC	105°aTDC / 345°bTDC
Int./exh. max. lift	9.5 mm
Int./exh. valves diameter	33/31 mm

7.3 Numerical modelling

For the simulations under motored and fired operating conditions two different numerical modelling approaches are used and will be now briefly introduced. Both cases are simulated with the open-source code OpenFOAM [10].

7.3.1 Motored operating conditions

For the cold-flow engine cycles, the Favre-filtered equations for mass (8.1), momentum (8.2) and energy (8.3) are solved on a moving grid, which read:

$$\frac{\partial(\overline{\rho})}{\partial t} + \frac{\partial(\overline{\rho}\widetilde{u}_j)}{\partial x_j} = 0 \tag{7.1}$$

$$\frac{\partial\left(\overline{\rho}\widetilde{u}_i\right)}{\partial t} + \frac{\partial(\overline{\rho}\widetilde{u}_i\widetilde{u}_j)}{\partial x_j} = \frac{\partial\overline{\tau_{ij}}}{\partial x_j} + \frac{\partial\tau_{ij}^{\mathrm{sgs}}}{\partial x_j} - \frac{\partial\overline{p}}{\partial x_i} \tag{7.2}$$

$$\frac{\partial(\overline{\rho}\widetilde{e})}{\partial t} + \frac{\partial(\overline{\rho}\widetilde{u}_j\widetilde{e})}{\partial x_j} + \frac{\partial(\overline{\rho}\widetilde{K})}{\partial t} + \frac{\partial(\overline{\rho}\widetilde{K}\widetilde{u}_j)}{\partial x_j} = \frac{\partial}{\partial x_j}\left(\alpha_{\mathrm{eff}}\frac{\partial\widetilde{e}}{\partial x_j}\right) - \frac{\partial}{\partial x_j}(\overline{p}\widetilde{u}_j) \tag{7.3}$$

where the tilde $<\tilde{}>$ describes Favre-filtered and the overline $<->$ LES-filtered quantities, $\overline{\rho}$ the density, $\widetilde{u_j}$ the velocity vector, $\overline{p}$ the pressure, $\widetilde{e}$ the internal energy and $\overline{\tau}_{ij}$ the viscous shear stress tensor. Heat conductivity is expressed with the thermal diffusivity α_{eff}, which consists of the molecular and turbulent diffusivities. The kinetic energy is given as $\widetilde{K} = 1/2\widetilde{u}_j^2$ and the molecular viscosity of the mixture is calculated with the Sutherland law [178]. The unresolved turbulent sub-grid stresses τ_{ij}^{sgs} are calculated with the Smagorinsky model with a model constant of 0.062 (a suitable value as shown in a previous work [94]). In a previous work [94], it is shown that with a more advanced turbulence model, such as the Sigma model [148], the mean velocity field does not change significantly. The major difference is found at the walls, where a lower turbulent viscosity is observed. Since the wall-modeling is a notorious weakness of LES, in particular for engine simulations with moving meshes, it is decided to proceed with the standard Smagorinsky model.

The compressibility of the flow is taken into consideration by a pressure-velocity-density approach proposed by Demirdžić [46, 59]. This approach allows to progress in time with time steps that comply with the CFL-number criterion for convection and not to the prop-

agation of acoustic waves. An implicit second-order scheme is used for the time integration. In order to avoid numerical instabilities at flows with a high Mach-number at valve opening and closing events, a switch between a central differencing scheme (CDS) and a total variation diminishing (TVD) scheme is applied. For $Ma > 0.3$, the convective fluxes of the momentum equations are discretized with the TVD-scheme and elsewhere by CDS. This switch was successfully applied in [145] [92] [94]. For the TVD-scheme the Sweby limiter [179] is used to discretize the convective fluxes.

7.3.2 Fired operating conditions

For the simulations including combustion, the absolute enthalpy $\widetilde{h}$ is used instead of the sensible internal energy $\widetilde{e_s}$, which has the advantage that no reaction source term needs to be modelled:

$$\frac{\partial(\overline{\rho}\widetilde{h})}{\partial t} + \frac{\partial(\overline{\rho}\widetilde{u}_j\widetilde{h})}{\partial x_j} + \frac{\partial(\overline{\rho}\widetilde{K})}{\partial t} + \frac{\partial(\overline{\rho}\widetilde{K}\widetilde{u}_j)}{\partial x_j} = \frac{\partial}{\partial x_j}\left(\alpha_{\text{eff}}\frac{\partial\widetilde{h}}{\partial x_j}\right) + \frac{\partial\overline{p}}{\partial t} \tag{7.4}$$

The absolute enthalpy $\widetilde{h}$ is composed of the sensible and the chemical enthalpy of the mixture. The distinction between the unburnt and the burnt mixture is made by the progress variable $\widetilde{c}$, which is denoted with 0 for the unburnt gases and with 1 for the burnt gases. The flame brush zone is found for $0 < \widetilde{c} < 1$. The composition inside the engine can be described with the unburnt fuel mass fraction $\widetilde{Y}_{\text{fuel, unburnt}}$, which reads:

$$\widetilde{Y}_{\text{fuel,unb.}} = \frac{m_{\text{fuel}}}{m_{\text{fuel}} + m_{\text{air}}} \tag{7.5}$$

and is defined as the ratio of the unburnt fuel mass (m_{fuel}) to the total mass. The mass fractions for the fuel, air and burnt products throughout the combustion can be defined as [10]:

$$\widetilde{Y}_{\text{fuel}} = \left((1-\widetilde{c})\widetilde{Y}_{\text{fuel,unb.}} + \widetilde{c}\left(\widetilde{Y}_{\text{fuel,unb.}} - \frac{1-\widetilde{Y}_{\text{fuel,unb.}}}{\lambda_{\text{st}}}\right)\right)\cdot(1-\widetilde{Y}_{\text{igr}}) \tag{7.6}$$

$$\widetilde{Y}_{\text{air}} = \left((1-\widetilde{Y}_{\text{fuel,unb.}}) - (\widetilde{Y}_{\text{fuel,unb.}} - \widetilde{Y}_{\text{fuel}})\lambda_{\text{st}}\right)\cdot(1-\widetilde{Y}_{\text{igr}}) \tag{7.7}$$

$$\widetilde{Y}_{\text{burnt}} = 1 - \widetilde{Y}_{\text{fuel}} - \widetilde{Y}_{\text{air}} \tag{7.8}$$

The mean molecular weight of the mixture W_m is defined as the sum of the mass fractions of the fuel $\widetilde{Y}_{\text{fuel}}$, the air $\widetilde{Y}_{\text{air}}$ and the burnt gases $\widetilde{Y}_{\text{burnt}}$, divided by their molecular weights, where $\widetilde{Y}_{\text{igr}}$ denotes the mass fraction of the burnt residual gases of the previous cycle:

$$\frac{1}{W_m} = \frac{\widetilde{Y}_{\text{fuel}}}{W_{\text{fuel}}} + \frac{\widetilde{Y}_{\text{air}}}{W_{\text{air}}} + \frac{\widetilde{Y}_{\text{burnt}}}{W_{\text{burnt}}} \tag{7.9}$$

The absolute enthalpy of the mixture $\widetilde{h}$ is expressed with the JANAF polynomials [32], which read:

$$\frac{\widetilde{h}W_m}{R\widetilde{T}} = a_{1m} + \frac{a_{2m}}{2}\widetilde{T} + \frac{a_{3m}}{3}\widetilde{T}^2 + \frac{a_{4m}}{4}\widetilde{T}^3 + \frac{a_{5m}}{5}\widetilde{T}^4 + \frac{a_{6m}}{\widetilde{T}} \tag{7.10}$$

The coefficients $a_{i,m}$ of the mixture can be expressed for a control volume i as functions of the JANAF coefficients of the fuel ($a_{i,\text{fuel}}$), air ($a_{i,\text{air}}$) and the burnt products ($a_{i,\text{burnt}}$), according to eqn. 7.11, where the coefficients for the burnt products ($a_{i,\text{burnt}}$) rely on an one-step reaction mechanism, involving air and iso-octane [87]:

$$\frac{a_{i,m}}{W_m} = \frac{a_{i,\text{fuel}}}{W_{\text{fuel}}} + \frac{a_{i,\text{air}}}{W_{\text{air}}} + \frac{a_{i,\text{burnt}}}{W_{\text{burnt}}} \tag{7.11}$$

The flame propagation is described with a transport equation for the progress variable field $\widetilde{c}$ and reads:

$$\frac{\partial(\overline{\rho}\widetilde{c})}{\partial t} + \frac{\partial(\overline{\rho}\widetilde{u}_j\widetilde{c})}{\partial x_j} + \frac{\partial}{\partial x_j}\left(\overline{\rho}\widetilde{u_j c} - \overline{\rho}\widetilde{u}_j\widetilde{c}\right) = \rho_u S_L \Sigma_{\text{gen}} \tag{7.12}$$

Here, ρ_u is the unburnt density, S_L is the laminar flame speed and Σ_{gen} is the generalized flame surface density. For the unburnt density ρ_u, a transport equation for the total unburnt enthalpy $\widetilde{h}_u$ is solved, which only takes the temperature rise due to the compression into account and reads:

$$\frac{\partial(\overline{\rho}\widetilde{h_u})}{\partial t} + \frac{\partial(\overline{\rho}\widetilde{u}_j\widetilde{h_u})}{\partial x_j} + \left(\frac{\partial(\overline{\rho}\widetilde{K})}{\partial t} + \frac{\partial(\overline{\rho}\widetilde{K}\widetilde{u}_j)}{\partial x_j}\right)\left(\frac{\overline{\rho}}{\overline{\rho}_u}\right) = \frac{\partial}{\partial x_j}\left(\alpha_{\text{eff}}\frac{\partial\widetilde{h_u}}{\partial x_j}\right) + \frac{\partial\overline{p}}{\partial t}\left(\frac{\overline{\rho}}{\overline{\rho}_u}\right) \tag{7.13}$$

The flame surface density (FSD) is calculated by the the Keppeler [100] and Muppala [142] FSD-models. Both models belong to the algebraic models and include a pressure dependency. The Keppeler model is a very recent model and its implementation into OpenFOAM was generously provided by the Pfitzner research group. In the following subsection, the Keppeler model will be described in greater detail.

7.3.2.1 Keppeler Model

The Keppeler Model belongs to the algebraic combustion models and is an extension of the Lindstedt-Váos model [120] (RANS model). It was taken as basis due to a good agreement between the combustion simulations of flames near walls in stagnating turbulence [27]. The Keppeler model relies on the fractal dimension approach, which follows the fractal theory by Mandelbrot [129] and assumes a self-similarity of the flame wrinkling between the small and the large scales. Previous experiments [149] and DNS simulations [84] support this assumption. The Keppeler model was developed for flames at elevated pressure conditions and validated up to 20 bars [100].

According to Gouldin [76], the flame surface A_t can be expressed according to eqn. 7.14, with D being the fractal dimension:

$$\frac{A_t}{L^3} \sim \frac{\epsilon_i^{2-D}}{L^{1-D}} \tag{7.14}$$

In eqn. 7.14, the minimum length scale for the flame wrinkling is denoted as ϵ_i and the biggest as L. For L, the grid size or the filter width Δ is often used in the context of LES and here denoted as the outer cut-off length ϵ_0:

$$L = \epsilon_0 = 2.2\Delta \tag{7.15}$$

The inner cut-off length ϵ_i is calculated with eqn. 7.16 and limited to $2l_F$ according to experimental observations by Driscoll [51] and DNS data of Chakraborty and Klein [36],

where ϵ_i was always larger than the laminar flame thickness l_F.

$$\epsilon_i = l_F \; max(Ka_\Delta^{-1/2}, 2) \tag{7.16}$$

In eqn. 7.16, Ka_Δ denotes the Karlowitz number at the filter size level and is computed by:

$$Ka_\Delta = \left(\frac{u'_\Delta}{S_L}\right)^{3/2} \left(\frac{\Delta}{l_F}\right)^{-1/2} \tag{7.17}$$

In eqn. 7.17, the sub-grid fluctuations are computed by $u'_\Delta = \sqrt{\frac{2}{3}k_{\mathrm{SGS}}}$, where k_{SGS} is the turbulent kinetic energy of the sub-grid scales. The laminar flame speed S_L is modelled according to Metghalchi and Keck [134] and takes the dilution by the mass fraction of the residual burnt gases ($\widetilde{Y_{\mathrm{igr}}}$) into account and reads:

$$S_L = S_{L,0} \left(\frac{T_u}{T_{u,\mathrm{ref}}}\right)^{\gamma} \left(\frac{p}{p_{\mathrm{ref}}}\right)^{\beta} \left(1 - 2.1\widetilde{Y_{\mathrm{igr}}}\right) \tag{7.18}$$

$$S_{L,0} = B_M + B_2 \left(\phi - \phi_M\right)^2 \tag{7.19}$$

$$\gamma = 2.18 - 0.8(\phi - 1) \tag{7.20}$$

$$\beta = -0.16 + 0.22(\phi - 1) \tag{7.21}$$

In equation 7.18, the unburnt reference temperature $T_{u,\mathrm{ref}}$ is set to 298 K and the reference pressure p_{ref} to 1 atm. The model constants γ and β are calculated using equations 7.20 and 7.21 and $S_{L,0}$ is calculated according to eqn. 7.19, with B_2=-84.72 cm/s, B_M=26.32 cm/s and ϕ_M=1.13 [87].

It has been shown by experiments and theoretical investigations that the fractal dimension D is bounded between 2 and 8/3, where the extreme cases can be found for a planar flame inside the computational cell for $D = 2$, or for a computational cell entirely occupied by the unresolved flame for $D = 3$. A dependency of D on $u'_\Delta/S_{L,0}$ was observed by Kobayashi et al. [106], North et al. [149] and Murayama et al.[143] and therefore the fractal dimension is calculated as a function of the Karlowitz-number:

$$D = \frac{8/3 Ka_\Delta + 2C_D}{Ka_\Delta + 2C_D} \tag{7.22}$$

Eqn. 7.22 was tuned with the model constant C_D=0.3 in order to obtain a good agreement with previous models for D proposed by Giacomazzi et al. [71] and by Keppeler et al. [101].

Under the assumption that the flame will not be always inside the computational cell, but rather moving within the flame brush, a probability density function was introduced by Gouldin [76] to describe the turbulent flame brush thickness:

$$p_c = \widetilde{c}(1 - \widetilde{c})\frac{L}{\delta_t} \tag{7.23}$$

Applying eqn. 7.23 to eqn. 7.14 yields the final formulation for the flame surface density with a proportionality constant C_R:

$$\Sigma = C_R \left(\frac{\epsilon_i}{\epsilon_0}\right)^{2-D} \frac{\widetilde{c}(1-\widetilde{c})}{\delta_t} \tag{7.24}$$

The turbulent flame thickness δ_t represents the locally-resolved flame brush and is approximated by $\delta_t = |\nabla\widetilde{c}|F(\widetilde{c})^{-1}$. $F(\widetilde{c})$ is a polynomial function that makes the expression $\widetilde{c}(1-\widetilde{c})F(\widetilde{c})^{-1}$ to 0.22 in almost the entire flame brush [100]. The full flame surface density model according to Keppeler at al. [100] reads:

$$\Sigma_K = \left(\mathcal{B} + (1-\mathcal{B})\, C_R \left(\frac{2.2\Delta}{l_F\ \max(Ka_\Delta^{-1/2}, 2)}\right)^{(D-2)} \widetilde{c}(1-\widetilde{c})F(\widetilde{c})^{-1}\right) |\nabla\widetilde{c}| \tag{7.25}$$

$$\mathcal{B} = \exp(-\frac{\Delta}{\epsilon_i}\Theta) \tag{7.26}$$

with C_R being a model constant, which is set to 4.5. $\mathcal{B}$ is a blending function, with Θ being a model constant which is set to 2.2. The blending function ensures that the flame surface density reduces to $|\nabla\widetilde{c}|$ for $\Delta \to 0$ and for $u'_\Delta \to 0$ [36].

The scalar sub-grid flux term $[\overline{\rho}(\widetilde{u_j c} - \widetilde{u}_j\widetilde{c})]$ in eqn. 8.5 is modelled by a gradient assumption without Counter-Gradient-Transport (CGT) contribution, which reads:

$$[\overline{\rho}(\widetilde{u_j c} - \widetilde{u}_j\widetilde{c})] = \alpha_{\text{eff}} \left(\frac{\partial\widetilde{c}}{\partial x_j}\right) \tag{7.27}$$

Since the Keppeler model uses the Favre-filtered progress variable for the calculation of the gradient in eqn. 7.25, it implicitly includes the effects of CGT, which was shown in the work of Ma et al. [126].

7.3.2.2 Muppala Model

The Muppala flame surface density model [142] belongs to the algebraic flame surface density models and was validated for premixed flames of different fuel mixtures (lean methane-air, ethylene-air, and propane-air mixtures) under various flow and turbulent inlet conditions up to 10 bar and reads:

$$\Sigma_M = \left[1 + \frac{0.46}{Le} Re_\Delta^{0.25} \left(\frac{u'_\Delta}{S_L}\right)^{0.3} \left(\frac{p}{p_0}\right)^{0.2}\right] |\nabla\widetilde{c}| \tag{7.28}$$

It is based on three parameter, which were fitted to the experimental results of different Bunsen type-flames provided by Kobayashi et al. [106]. The pressure is explicitly included in its formulation by p, where p_0 denotes a reference pressure (p_0=1 bar). Furthermore, it assumes unity Lewis number (Le) and uses the local cell Reynolds number Re_Δ.

Also the Muppala model uses the Favre-filtered progress variable for the calculation of the gradient in eqn. 7.28, which implicitly includes the effects of CGT [126].

7.3.3 Numerical setup

The simulations are performed on multiple moving grids without topological changes, with an interval size of no more than 5°CA. In-between the intervals, the results are mapped from the deformed grid to the new target grid with a second-order volume-weighted mapping method. Instead of the internal walls for the valve closure events [94], the intake- and exhaust ports are completely detached from the cylinder volume. Furthermore, the piston top-land crevice volume was included. The grid is locally refined at the spark plug to 0.25 mm and the piston top-land crevice filled with 3-4 stretched cells across the radial gap, with an aspect ratio of $\sim 1/5$. Resolving the piston top-land crevice has increased the number of the grid cells by a factor of ~ 2.5 compared to the configuration without the crevice volume [94]. The intake and the exhaust ports are meshed with a grid resolution of 2 mm. Table 7.2 shows the main characteristics of the engine grids with and without piston-top land crevice.

Table 7.2: Comparison of the engine grids with and without piston top-land crevice.

Δx_{cyl}	Crevice	Intervals	Number of cells
1.0 mm	no	144	0.9 - 1.2 Mio. [94]
1.0 mm	yes	147	2.8 - 3.2 Mio.

Due to the high number of meshing intervals, the meshing workflow had to be automated. The mesh is not aligned with the flow at the valve seat region, which would have increased the complexity of the meshing work-flow tremendously. It is shown in [94] that with a high grid quality (equidistant cubic cells) combined with a second-order discretization scheme (CDS), a good agreement of the intake flow can be achieved (regardless the grid orientation). For the mesh motion, a Laplace equation for a vector $x_{\text{disp},j}$ is solved, which describes the displacement of the grid points and reads:

$$\frac{\partial}{\partial x_j}\left(\gamma \frac{\partial x_{\text{disp},j}}{\partial x_j}\right) = 0 \tag{7.29}$$

with γ being a user-defined stiffness to control the mesh motion. The new coordinates of the grid points are then obtained by $x_j^{\text{new}} = x_{\text{ref},j} + x_{\text{disp},j}$, with $x_{\text{ref},j}$ being a reference point taken at the beginning of the simulation interval. The boundary conditions for eqn. 8.10 are no-slip conditions for the non-moving parts, except for the stems of the valves and the liner, where a zero-gradient boundary condition is applied. For the moving boundaries, the displacement of the moving walls $x_{\text{disp},j}$ is directly imposed (relative to the reference position $x_{\text{ref},j}$) for the given time step.

7.4 Simulation setup

The simulation setups under motored and fired operating conditions are presented in the following subsections. Furthermore, it will be distinguished between a "single-cycle" and "multi-cycle" approach for the fired simulations.

7.4.1 Motored operating conditions

The cold-flow simulation of the wall-guided head with piston top-land crevice is started at 360°bTDC and initialized with instantaneous flow-, temperature- and pressure fields from

a cold-flow simulation of the wall-guided head after 20 consecutive engine cycles that was investigated in detail before [94] and hence available. A time-varying pressure is imposed 360 mm downstream of the exhaust valves and 530 mm upstream of the intake valves, at the location of the pressure sensors [18]. The engine is fed with air preheated to 295 K. The intake port temperature is also set to 295 K and the temperature of the remaining walls is assumed to be 333 K. The valve closure and opening events of the experiment are found in table 7.1. The same closure and opening events are used for the simulations, but with a sudden opening and closing with a minimum valve lift of 0.35 mm. On all stationary walls, a non-slip boundary condition is applied. On the piston and valves, their moving velocity is imposed and the face flux ($\overline{\rho}\widetilde{u}$) set to zero. Fifteen consecutive cycles are simulated with a maximum CFL number of 2.

7.4.2 Reactive single-cycle simulation

Combustion simulations are performed with two different approaches, which are denoted in the scope of this work as single-cycle and multi-cycle approach. For the single-cycle approach, the flow fields of the cold-flow engine simulations are directly used for the initialization and only the combustion process from 20°bTDC to EVO (110°bTDC) is considered. The air/fuel mixture is assumed to be homogeneously distributed inside the combustion chamber with air at an air to fuel ratio (λ) of 1.2. The engine is running at 800 rpm and all walls have a fixed temperature of 333 K. Furthermore, no dilution by residual gases is considered ($\widetilde{Y}_{\mathrm{igr}}$=0). The mixture is ignited at 16°bTDC by super-imposition of a spherical profile for the progress variable field in-between the spark plug gap (∼1.4 mm):

$$\widetilde{c}_{\mathrm{ign}} = c_0 \left(1 - \tanh\left(\frac{|x_i - x_{i,\mathrm{sp}}|}{\Delta_{\mathrm{sp}}}\right)\right) \tag{7.30}$$

In eqn. 7.30, Δ_{sp} is the cell size in the vicinity of the spark plug, $x_{i,\mathrm{sp}}$ is the spark location and c_0 is a model constant, which is set to 0.01. It has to be stressed, that within this work the profile is purely seen as an initialisation of the $\widetilde{c}$-field and does not have a physical meaning. Also the transition of the rather laminar spherical flame kernel into a wrinkled self-sustaining flame front is not taken into account, because the dynamics of the ignition kernel would have required the solution of a transport equation for the flame surface density, which is used for example in the Imposed Stretch Spark Ignition Model (ISSIM) [42]. In addition to the $\widetilde{c}$-profile, an ignition reaction source term is introduced, to avoid any misfire, which would be questionable due to the missing physical ignition model. The ignition reaction source term is denoted as $\overline{\dot{\omega}}_{ign}$ and reads:

$$\overline{\dot{\omega}}_{\mathrm{ign}} = \overline{\rho}\frac{\widetilde{c}_{\mathrm{ign}}}{\Delta t} \tag{7.31}$$

The ignition reaction term $\overline{\dot{\omega}}_{\mathrm{ign}}$ should not be seen as a physical ignition model but rather as a way to initialize the $\widetilde{c}$-field. One can also argue that, having a good ignition model without modelling the spark plug itself, may lead to unknown compensating errors. Cyclical variations that dependent on any of the ignored phenomena cannot be predicted .The ignition reaction source term is used for a duration of 5°CA after ignition, which is enough to avoid any misfire. The post-oxidation of the fuel, the flame quenching at the walls or the reduction of the flame speed close to the walls due to heat losses [28] are not taken into account.

7.4.3 Reactive multi-cycle simulation

The difficulty of the reactive multi-cycle simulation lies in (a) the re-initialisation of $\widetilde{c}$ without loosing the thermodynamic properties of the mixture, (b) in the big pressure gradient between the cylinder volume and the exhaust port at EVO and (c) the treatment of the residual gases. The flame propagation and the state of the mixture (burnt or unburnt) is described by the progress variable field $\widetilde{c}$. In the end of the power stroke, all the air/fuel mixture is ideally burnt, meaning that the progress variable field will be 1 in the complete combustion chamber. In the real world, not all the mixture will be burnt and pockets of fresh charge ($\widetilde{c}$ <<1) will remain before the exhaust valves open. At EVO, the mixture of unburnt and burnt gases will be expelled. Since the combustion model relies on the gradient of the progress variable field $\widetilde{c}$, the flame will keep burning even in the exhaust port. In order to prevent the unphysical flame propagation during the exhaust stroke, the reaction source term of eqn. 8.5 is set to 0. The transport of the burnt gases is described by:

$$\frac{\partial(\overline{\rho}\widetilde{c})}{\partial t} + \frac{\partial(\overline{\rho}\widetilde{u}_j\widetilde{c})}{\partial x_j} + \frac{\partial}{\partial x_j}\left(\alpha_{\text{eff}}\frac{\partial\widetilde{c}}{\partial x_j}\right) = 0 \tag{7.32}$$

After the exhaust stroke has finished the intake valves open and fresh gases ($\widetilde{c}$=0) will be inducted into the cylinder, which mix with the residual burnt gases inside the combustion chamber according to eqn. 7.32. The FSD-approach, used in this study requires at spark ignition timing a progress variable field of zero in the complete combustion chamber. Since the mixing of the residual gases with the fresh mixture is described by the progress variable field itself, it will lead to local gradients of the progress variable. A local gradient of the progress variable can lead to uncontrolled self-ignition events when the reaction source term of eqn. 8.5 is considered. In order to prevent the self-ignition events which are induced by local gradients of the progress-variable, the progress variable field needs to be reset to zero at spark ignition timing. The problem with a reset of the progress variable to zero is that the thermodynamic properties of the residual gases of the previous cycle would be gone. Therefore, the passive scalar $\widetilde{Y}_{\text{igr}}$ (see eqn. 7.6 and 7.7) is introduced to define the burnt gas mass fraction of the previous cycle. By assigning $\widetilde{Y}_{\text{igr}}$:= $\widetilde{c}$ and $\widetilde{c}$:=0 before spark ignition timing, the thermodynamic properties will be unchanged and a "cleaned" progress variable field will be available for the next combustion phase of the ongoing cycle. The transport equation for the residual gases during combustion reads:

$$\frac{\partial(\overline{\rho}\widetilde{Y}_{\text{igr}})}{\partial t} + \frac{\partial(\overline{\rho}\widetilde{u}_j\widetilde{Y}_{\text{igr}})}{\partial x_j} + \frac{\partial}{\partial x_j}\left(\alpha_{\text{eff}}\frac{\partial\widetilde{Y}_{\text{igr}}}{\partial x_j}\right) = 0 \tag{7.33}$$

Figure 7.1 systematically demonstrates the treatment for the mass fraction of the residual burnt gases from the previous cycle.

For the multi-cycle simulations the same ignition strategy is applied, the same wall temperatures imposed and the same engine speed used, as for the single-cycle reactive simulations. The air/fuel mixture is assumed to be homogeneously distributed inside the combustion chamber with air at an air to fuel ratio (λ) of 1.2. The initialization of the first cycle is done based on results of the last cold-flow cycle.

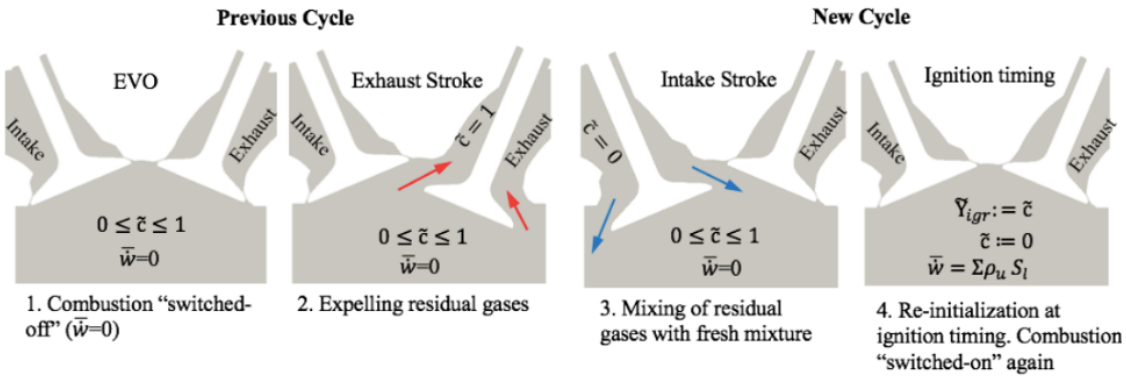

Figure 7.1: Working principle of the reactive multi-cycle simulation based on the progress-variable field and a tracer for the residual burnt gas mass fraction of the previous cycle.

7.5 Results and discussion

First the results of the cold-flow simulations will be presented and then the reactive single-cycle and multi-cycle simulations discussed. A detailed validation and discussion of the velocity fields of the cold-flow simulations can be found in the previous work of this study [94] and only the influence of the crevice volume to the in-cylinder pressure is discussed. For the single-cycle reactive simulations, the results for the two different algebraic flame surface density models are discussed based on a simulation-to-simulation comparison. Finally, the reactive multi-cycle simulations will be compared to Mie-scattering images of the flame front propagation inside the same engine.

7.5.1 Cold-flow simulations - In-cylinder pressure

The Figure 7.2 shows the simulated in-cylinder pressure for the compression and expansion stroke of the LES with and without the piston top-land crevice [94] compared to the experiment. Even though all configurations have the same compression ratio, different in-cylinder pressures are observed. The biggest deviation is observed at TDC, where the peak in-cylinder pressure without piston-top land crevice is roughly 2 bar higher. The explanation for the difference can be found in figure 7.3, where the temperature field in a cross-section through the cylinder and the crevice at TDC is shown. It can be observed, that the temperature of the crevice content is around two times lower than the temperature of the gases inside the combustion chamber. Therefore, the overall temperature will also be lower, hence leading to a lower in-cylinder pressure. During the compression phase, the in-cylinder gas is pushed into the large piston top-land crevice and exposed to high heat losses to the walls, due to a higher surface-to-volume ratio of the narrow crevice.

7.5.2 Combustion - Single-cycle approach

Figure 7.4 shows the in-cylinder pressure, flame surface and the combustion progress obtained with the Keppeler and Muppala models. The results represent an average taken from 15 combustion simulations using the single-cycle approach. Up to 8°bTDC, the pressure curves obtained with the Muppala and Keppeler model show a similar pressure, but then the in-cylinder pressure obtained with the Keppeler model starts rising faster and reaching a peak in-cylinder pressure of $\sim$ 37 bar at 9°aTDC. The in-cylinder pressure calculated with the Muppala model peaks 6° later and reaches a maximum pressure of only $\sim$

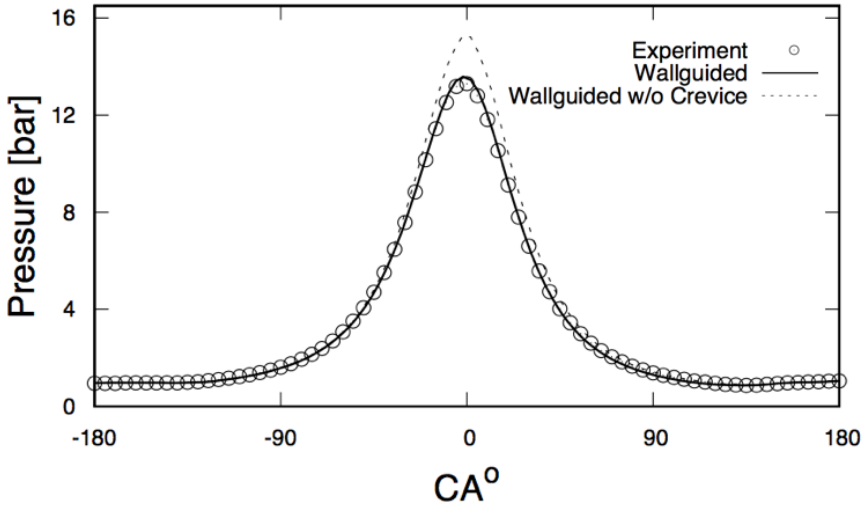

Figure 7.2: In-cylinder pressure during the compression and the expansion phase from LES simulations of the wall-guided head and the temperature under motored operating conditions.

32 bar. The differences in the in-cylinder pressure curves can be explained by plotting the total flame surface inside the combustion chamber, which can be splitted into a resolved part and a modelled part. The total flame surface inside the combustion chamber V_{comb} can be calculated by:

$$S_{\text{tot}} = \int_{V_{\text{comb}}} \Sigma \, dV \tag{7.34}$$

The resolved part of the total flame surface can be described by:

$$S_{\text{res}} = \int_{V_{\text{comb}}} |\nabla \widetilde{c}| \, dV \tag{7.35}$$

Figure 7.4b) shows the total (solid lines) and the resolved (dashed lines) flame surfaces obtained with both models. The total flame surface with the Keppeler model rises sharply from $\sim 10°$bTDC and reaches its maximum of 0.011 m^2 at 4°aTDC - some degrees before the maximal in-cylinder pressure was obtained. The same holds for the total flame surface obtained with the Muppala model, but with a slightly lower maximum total flame surface some degrees later. The evolution of the two distinct flame surfaces explains the difference of the in-cylinder pressure, where a faster increase of the flame surface is also related to a higher consumption rate, leading to a stronger heat release, which finally manifests in a higher in-cylinder pressure. The linear increase of the flame surface denotes the undisturbed flame propagation - no impact of the wall on the flame. At the peak values, the flame has partially burnt to the liner, cylinder head or piston head. Since no wall modelling was applied, the flame is allowed to burn completely to the walls and into the piston top-land crevice. The subsequent decrease of the flame surface denotes the extinction phase at the combustion chamber walls. However, for both models the flame surface curves do not go to zero, because there is still air/fuel mixture inside the piston top-land crevice left. The resolved flame surface curves follow a trend similar to the total flame surface curves for both models and reach their maximal values at the same °CA, where the total flame

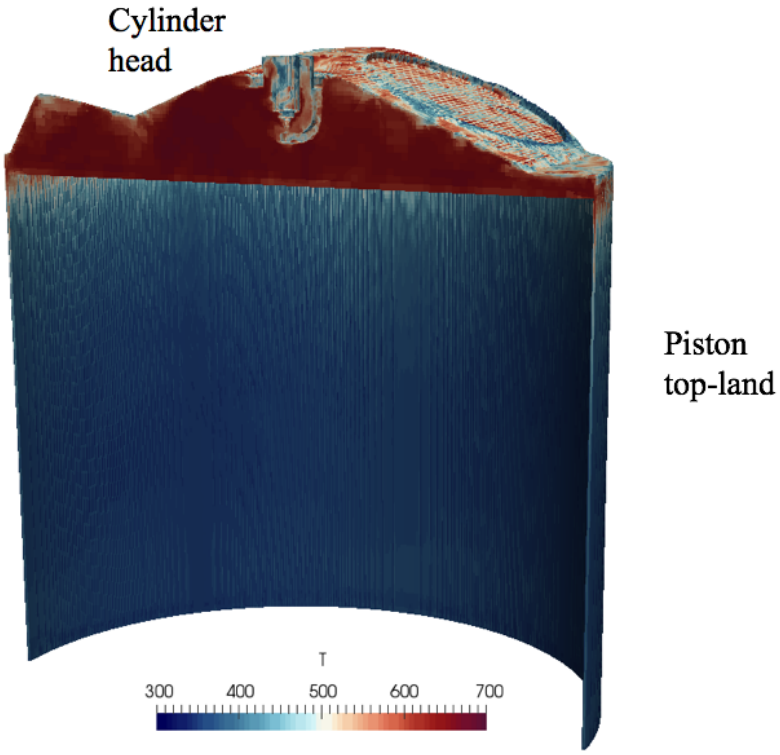

Figure 7.3: In-cylinder temperature field within the tumble plane.

surface curves peaks as well

Figure 7.4c) shows the combustion progress, where the low increase for the Keppeler model from ∼TDC and for the Muppula model from ∼15, is attributed to the aforementioned slow combustion inside the piston top-land crevice and contributes to around 10% of the total in-cylinder charge. The contribution of the modelled flame surface ($S_{\mathrm{mod}} = S_{\mathrm{total}} - S_{\mathrm{res}}$) to the total flame surface is shown in figure 7.5. It represents around 65 % of the total flame surface for the Keppeler model and roughly 35 % for the Muppala model slightly after ignition. These values have to be interpreted with caution, because the inital flame kernel growth cannot be predicted with the algebraic FSD-models. The higher modelled values could also be a reason why the flame surface is increasing faster with the Keppeler model. The contribution of the modelled flame surface for the Keppeler model is decreasing up to the point where the flame reaches the piston top-land crevice (12°aTDC) and then again increasing for the flame inside the crevice. For the Muppala model, an almost linear increase of the modelled flame surface from the ignition phase over the free flame phase to the propagation into the piston top-land crevice, is obtained.

7.5.3 Combustion - Multi-cycle simulation

The Mie-scattering images of the flame propagation inside the wall-guided head [48] are compared to the reactive multi-cycle LES simulations. Since the computational effort for the multi-cycle simulations has increased by a factor of ∼3 compared to the single-cycle combustion approach, only six cycles were computed with the Keppeler model, which were sufficient to observe first trends. The computational time for a full-cycle simulation

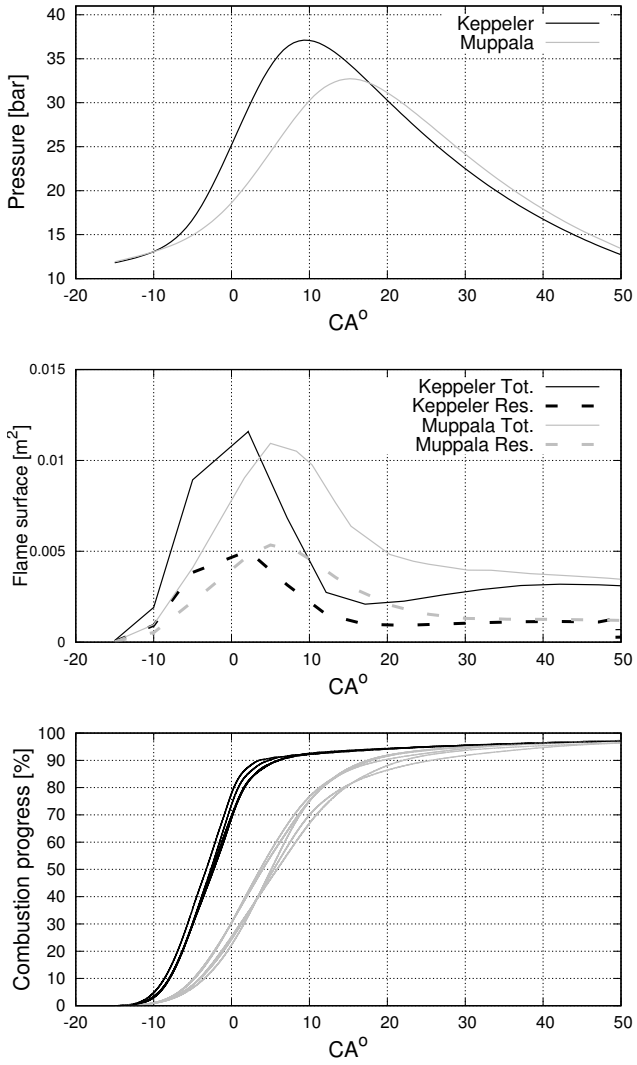

Figure 7.4: a) In-cylinder pressure b) total and resolved flame surface averaged over 15 cycles and c) combustion progress calculated with the Keppeler and Muppala-FSD models plotted over the crank angle for some LES cycles.

including combustion using 192 CPUs required 8-9 days, where the most time-consuming part was the opening of the exhaust valves. A pressure difference of $\sim$ 4:1 bar (combustion chamber to exhaust manifolds) was responsible for supersonic conditions inside the exhaust valve seats.

Figure 7.6 shows the in-cylinder pressure of sequentially solved reactive multi-cycle LES simulations against the experiment. The in-cylinder pressure of the first simulated cycle starts rising much faster and with a steeper gradient then the experiment. Due to back flow of the burnt gases into the combustion chamber, the consecutive cycles contain residual gases of the previous cycles. The residual burnt gas content for all cycles was around 15 % of the total trapped mass. The dilution of the burnt gases with the fresh mixture decreased the laminar flame speed (see eqn. 7.18), which has led to a slower-rising pressure compared to the cycle without residual gases. Compared to the experimentally observed in-cylinder pressure traces, a good agreement is achieved until crevice and wall-effects become important. Since no influence on the wall to the flame is modelled, the over-prediction of

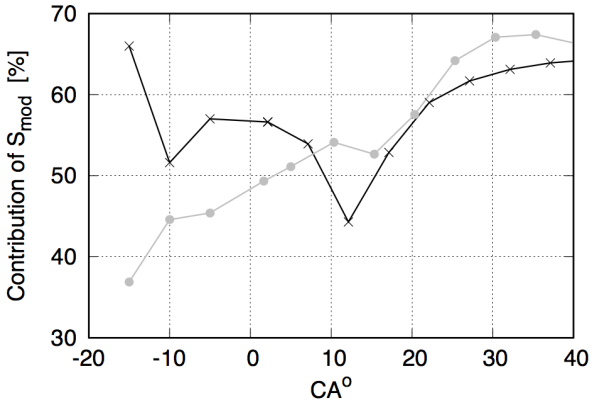

Figure 7.5: Contribution of the resolved flame surface to the total flame surface for the Keppeler and Muppala FSD-models (average of 15 cycles).

the peak pressure can be attributed to an overly high predicted value of the flame surface at the walls.

Figure 7.7 shows the phase-averaged progress variable field obtained after six consecutive

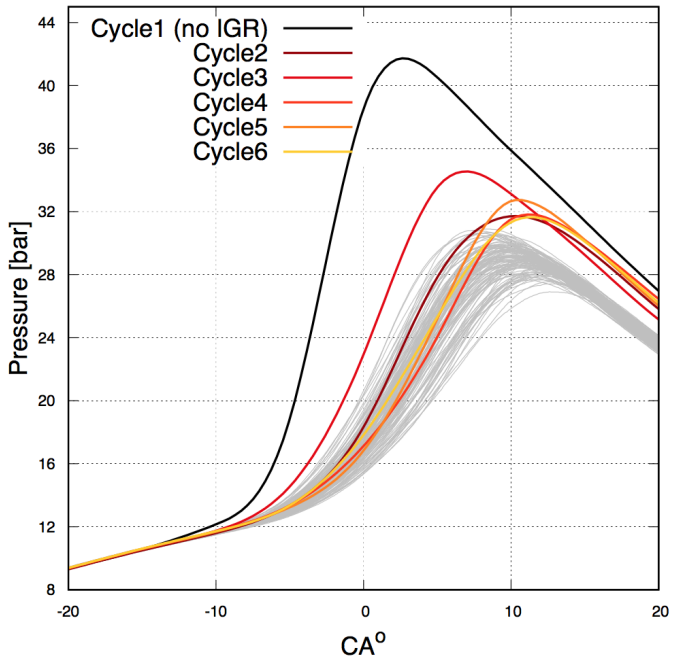

Figure 7.6: In-cylinder pressure from the experiment (light grey) and 6 consecutive multi-cycle LES simulation. The engine speed is 800 rpm, λ=1.2 and spark timing at 16°bTDC.

cycles (where the first cycle is discarded) against the Mie-scattering images averaged over 300 cycles within the tumble symmetry plane and in a horizontal cut underneath the spark plug. Overall, the simulation is in a good qualitative agreement with the experimentally observed burnt gas distribution, implying a good prediction of the turbulent flame speed during the free-flame propagating phase.

7.6 Conclusions

The piston top-land crevice volume was included in the numerical model, which enabled for a very good prediction of the in-cylinder pressure under motored conditions, which was uo to now an unknown uncertainty related to this particular engine.

In the scope of this work, the algebraic FSD models were applied already during the ignition phase, thus their performance in this early state will favour a fast or slow combustion. The predicted total flame surface with the Keppeler model increased faster than it did with the Muppala model and has led to a higher peak in-cylinder pressure.
The multi-cycle simulation with the Keppeler model has revealed that, by considering the influence of the residual gases on the laminar flame speed, the results of the flame propagation during the free-flame phase (without the wall effects) were in a good qualitative agreement with Mie-scattering images. The results were also in a quantitatively good agreement with the in-cylinder pressure, implying that the Keppeler model worked reasonably well during the ignition phase, since the "right" timing for the free-flame propagation was achieved.

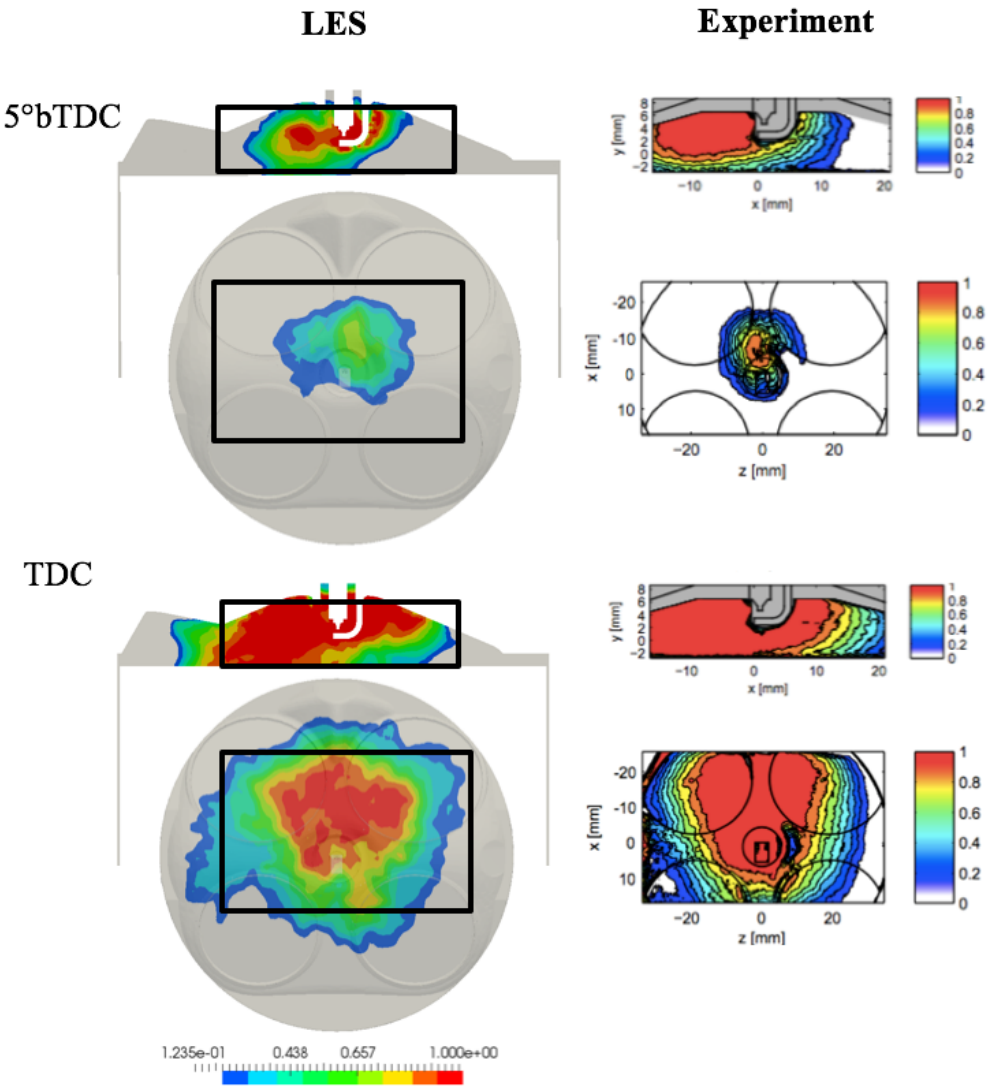

Figure 7.7: Phase-averaged progress variable field obtained from 5 consecutive multi-cycles LES simulation (left) and Mie-scattering images averaged over 300 cycles within the tumble-symmetry plane and on a horizontal cut underneath the spark plug for the wall-guided head configuration at 5°bTDC.

8

Comparison of the in-cylinder flow and flame propagation of two different cylinder-head geometries

In the present chapter, a comparison of LES simulations of the two different cylinder-head configurations of the optical engine of the Technical University of Darmstadt against MRV and PIV data is shown. For each cylinder-head configuration, 15 consecutive cold-flow cycles were calculated. Sensitivities of the intake flow to the tumble formation were investigated based on the Γ*-criterion and on auto-correlation coefficient curves. Finally, the flow fields were taken as starting conditions for combustion simulations using the Keppeler model, in order to investigate the sensitivity of the flow field to the flame propagation. The results were presented at the LES4ICE-2016 Congress in Rueil-Malmaison.*

8.1 Introduction

The flow field at ignition timing, as well as the combustion efficiency, are entirely determined by the flow conditions at intake valve closure (IVC) time [125]. Therefore, it is important to understand how the flow is issuing into the combustion chamber. Inside a spark-ignition engine the valves are mounted with an inclination to the cylinder head. This orientation favours a rotational flow pattern, which is known as tumble-flow. During the compression stroke, the rotational vortex (tumble) becomes squeezed by the upwards coming piston and will break-up into a small scale turbulent flow field. The small scale turbulent flow field is of key-importance for the flame wrinkling, which enhances the consumption rate. Thus, during the development of a new engine, the intensity of the tumble must be considered as a design parameter. Unfortunately, it is not easy to visualize the tumble formation, nor to quantify its break-up.

The flow conditions upstream and around the valves were topic of recent research activities, as for example by Keskinen et al. [102], who studied the influence of the turbulence inside the intake port to the cyclic variability of the in-cylinder flow field or by Hartmann et al. [80], who studied numerically and experimentally the vortex shedding behind the valve stem.

Usually the tumble-number is measured on stationary flow-benches [87] in order to characterize the intensity of the tumble-flow. However, the dynamics of the engine are totally disregarded and the tumble break-up is not present at all (no piston). Laser diagnostics applied inside optically accessible research engines can measure the flow field, but they are

mostly restricted to a 2D plane inside the combustion chamber [18]. Additional measurements to the laser diagnostics, such as magnetic resonance velocimetry (MRV) [64] [65], are able to deliver a full 3D representation of the mean flow field including the valve seat region. Unfortunately, there is no piston present and only one particular moment during the intake stroke can be studied. Therefore, 3D computational fluid dynamics (CFD) simulations are an inevitable supplement to the experimental investigation, because the full 3D flow-field can be studied (including the valve seat region) under operating engine conditions. Furthermore, the geometry of the cylinder-head can be easily changed.

Within this work, the influence of two different cylinder head geometries (spray-guided and wall-guided head), with respect to the tumble formation using Large-Eddy-Simulations (LES), is studied. The main differences of the two heads concerned the shape of the valve seat region and position of the injector, which was centrally mounted for the spray guided head and between the intake valves for the wall-guided head. Particle Image Velocimetry (PIV) measurements of the flow field with the corresponding cylinder-head geometries were provided by the Dreizler group through the "Darmstadt engine workshop" (www.rsm.tu-darmstadt.de). Since the operating conditions were kept identical for both cylinder heads, the datasets are ideally suited to study the effect of the geometry to the tumble formation and tumble break-up. Unfortunately, no experimental data under fired operating conditions was available for the same operating conditions for both cylinder-head configurations. Therefore, the flame propagation is discussed only on a simulation-to-simulation comparison. The simulation-to-simulation comparison will enable obtaining first trends of the interaction between the flow field and the flame propagation.

8.2 Engine and experiment

The main difference of the two cylinder-heads of the Technical University of Darmstadt lies in the position of the injectors. For the wall-guided head configuration the injector is sidewards and in-between the intake valves mounted and for the spray-guided head configuration centrally placed. Due to the re-location of the injector for the spray-guided head, the spark-plug was shifted towards the exhaust side. Furthermore, the diameter of the intake valves of the spray-guided head was decreased from 33 mm to 29 mm. The main characteristics of the two different cylinder-head geometries can be found in table 8.1 and a top view of both heads including the intake and the exhaust valves is shown in figure 8.1.

There is another difference between the two heads, which does not appear at first glance and requires a closer look on a cut through the mid-valve plane, which is shown in figure 8.2. Here, the contours of the mid-valve planes for both heads are super-imposed on each other with widely-opened intake valves and one can clearly distinguish differences in the valve seat region. The valve seat region for the spray-guided head has much smoother and rounded edges than the wall-guided head. This modification will largely influence the angle between the intake jet and cylinder-head and affect the mass flow distribution around the valve entrance, changing the impact on the liner walls and the jet-to-jet interaction within the tumble-symmetry plane. These are very important design parameters and have to be considered.

For the PIV measurements, the engine was motored at a speed of 800 rpm and fed with

Table 8.1: Main characteristics of the two different cylinder-heads.

Specification	Wall-guided	Spray-guided
Bore/Stroke	86/86 mm	86/86 mm
Piston	85 mm	85 mm
Fireland height	74.4 mm	74.4 mm
Displacement	499 cm^3	499 cm^3
Clearance height	2.6 mm	2.6 mm
Compression ratio	8.5:1	8.7:1
Clearance Volume	66.5 cm^3	64.9 cm^3
IVO / IVC	325°aTDC / 125°bTDC	325°aTDC / 125°bTDC
EVO / EVC	105°aTDC / 345°bTDC	105°aTDC / 345°bTDC
Int./exh. valves diameter	33/31 mm	29/31 mm

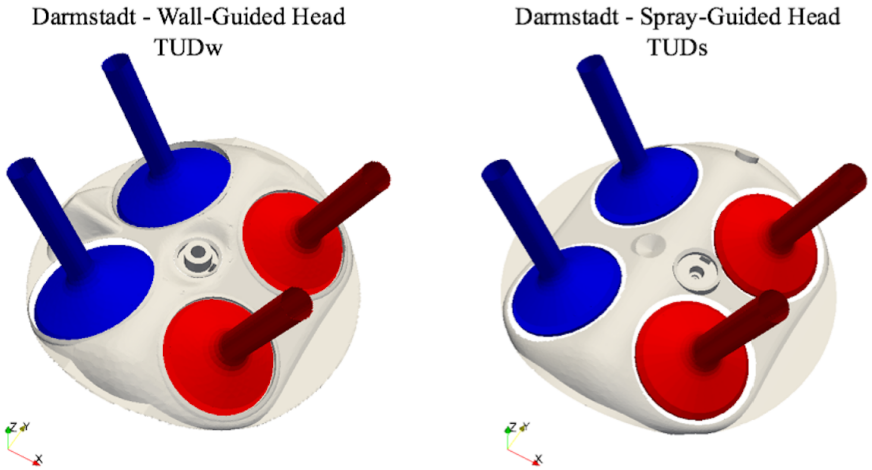

Figure 8.1: Wall-guided (left) and spray-guided (right) cylinder-heads with intake (blue) and exhaust (red) valves.

air at 0.95 bar and a temperature of 296 K. The PIV data mainly covered an interrogation window of 60x70 mm^2 within the tumble symmetry plane, where phase averages of the 2D velocity fields at 270°bTDC (intake stroke) and 90°bTDC (compression stroke) are available. The measured blow-by under motored condition was 4 g/h, which contributes to roughly 0.02% of the intake mass flow rate [29]. In addition to the PIV data, the MRV data will be used for the validation of the upper part of the cylinder-head, including the valve seat region [65]. Although the MRV data are generated under stationary conditions, representing only one particular moment within the intake stroke - mimicking 270°bTDC of the corresponding engine experiment - this method has proven to yield good qualitative and quantitive agreements compared with the flow fields obtained by PIV and LES, as shown by Freudenhammer et al. [64] [65] and in a previous study of this work [94], respectively.

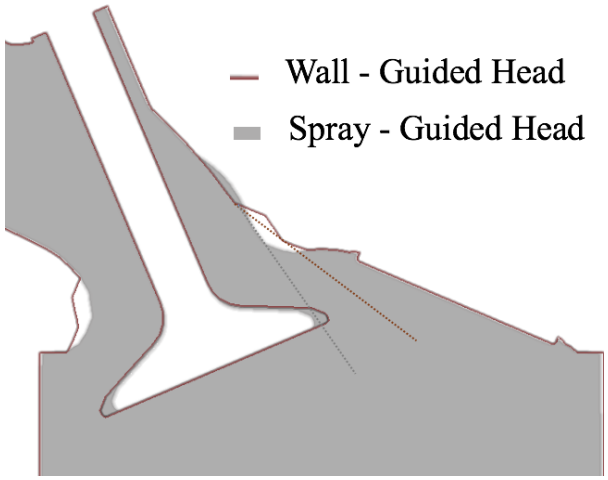

Figure 8.2: Cut through the mid-valve plane of the spray- and wall-guided head at 270°bTDC. The extended dotted lines highlight the different angles with the cylinder-head.

8.3 Numerical modelling

For the simulations under motored and fired operating conditions two different numerical modelling approaches are used. Both cases are simulated with the open-source code OpenFOAM.

8.3.1 Motored operating conditions

For the cold-flow engine cycles of the two different engine head configurations, the Favre-filtered equations for mass (8.1), momentum (8.2) and energy (8.3) are solved on a moving grid, which read:

$$\frac{\partial(\overline{\rho})}{\partial t} + \frac{\partial(\overline{\rho}\widetilde{u}_j)}{\partial x_j} = 0 \tag{8.1}$$

$$\frac{\partial\left(\overline{\rho}\widetilde{u}_i\right)}{\partial t} + \frac{\partial(\overline{\rho}\widetilde{u}_i\widetilde{u}_j)}{\partial x_j} = \frac{\partial\overline{\tau_{ij}}}{\partial x_j} + \frac{\partial\tau_{ij}^{\mathrm{sgs}}}{\partial x_j} - \frac{\partial\overline{p}}{\partial x_i} \tag{8.2}$$

$$\frac{\partial(\overline{\rho}\widetilde{e})}{\partial t} + \frac{\partial(\overline{\rho}\widetilde{u}_j\widetilde{e})}{\partial x_j} + \frac{\partial(\overline{\rho}\widetilde{K})}{\partial t} + \frac{\partial(\overline{\rho}\widetilde{K}\widetilde{u}_j)}{\partial x_j} = \frac{\partial}{\partial x_j}\left(\alpha_{\mathrm{eff}}\frac{\partial\widetilde{e}}{\partial x_j}\right) - \frac{\partial}{\partial x_j}(\overline{p}\widetilde{u}_j) \tag{8.3}$$

where the tilde $<\widetilde{\ }>$ describes Favre-filtered and the overline $<->$ LES-filtered quantities, $\overline{\rho}$ the density, $\widetilde{u_j}$ the velocity vector, $\overline{p}$ the pressure, $\widetilde{e}$ the internal energy and $\overline{\tau}_{ij}$ the viscous shear stress tensor. Heat conductivity is expressed with the thermal diffusivity α_{eff}, which consists of the molecular and turbulent diffusivities. The kinetic energy is given as $\widetilde{K} = 1/2\widetilde{u}_j^2$ and the molecular viscosity of the mixture is calculated with the Sutherland law [178]. The unresolved turbulent sub-grid stresses τ_{ij}^{sgs} are calculated with the Smagorinsky model with a model constant of 0.062. The pressure is calculated by a pressure-velocity-density coupling for flows at arbitrary Mach-number proposed by Demirdžić [46, 59]. This approach does not limit the time step size according to the speed of the sound, hence allows to progress in time with bigger steps, compared to a density-based approach.

8.3.2 Fired operating conditions

For the simulations including combustion, the sensible internal energy $\widetilde{e_s}$, is replaced by the absolute enthalpy $\widetilde{h}$, which has the advantage that no reaction source term needs to be modelled:

$$\frac{\partial(\overline{\rho}\widetilde{h})}{\partial t} + \frac{\partial(\overline{\rho}\widetilde{u}_j\widetilde{h})}{\partial x_j} + \frac{\partial(\overline{\rho}\widetilde{K})}{\partial t} + \frac{\partial(\overline{\rho}\widetilde{K}\widetilde{u}_j)}{\partial x_j} = \frac{\partial}{\partial x_j}\left(\alpha_{\text{eff}}\frac{\partial\widetilde{h}}{\partial x_j}\right) + \frac{\partial\overline{p}}{\partial t} \tag{8.4}$$

The absolute enthalpy $\widetilde{h}$ is composed of the sensible and the chemical enthalpy of the mixture. The distinction between the unburnt and the burnt mixture is made by the progress variable $\widetilde{c}$, which is denoted with 0 for the unburnt gases and with 1 for the burnt gases. The flame brush zone is found for $0 < \widetilde{c} < 1$. The composition inside the engine can be described with the unburnt fuel mass fraction $\widetilde{Y}_{\text{fuel,unb.}}$, which is defined as the ratio of the fuel mass to the total mass. A detailed description about the calculation of the mixture composition inside the engine is found in a previous study of this work [92].
The absolute enthalpy of the mixture $\widetilde{h}$ is expressed with the JANAF polynomials [32], where the coefficients for the burnt products rely on an one step reaction mechanism, involving air and iso-octane [87].

The flame propagation is described with a transport equation [155] for the progress variable field $\widetilde{c}$ and reads:

$$\frac{\partial(\overline{\rho}\widetilde{c})}{\partial t} + \frac{\partial(\overline{\rho}\widetilde{u}_j\widetilde{c})}{\partial x_j} + \frac{\partial}{\partial x_j}\left(\overline{\rho}\widetilde{u_j c} - \overline{\rho}\widetilde{u}_j\widetilde{c}\right) = \rho_u S_L \Sigma_{\text{gen}} \tag{8.5}$$

where ρ_u is the unburnt density, S_L is the laminar flame velocity and Σ_{gen} is the generalized flame surface density. For the unburnt density ρ_u, a transport equation for the total unburnt enthalpy $\widetilde{h}_u$ is solved, which only considers the temperature rise due to the compression and reads:

$$\frac{\partial(\overline{\rho}\widetilde{h_u})}{\partial t} + \frac{\partial(\overline{\rho}\widetilde{u}_j\widetilde{h_u})}{\partial x_j} + \left(\frac{\partial(\overline{\rho}\widetilde{K})}{\partial t} + \frac{\partial(\overline{\rho}\widetilde{K}\widetilde{u}_j)}{\partial x_j}\right)\left(\frac{\overline{\rho}}{\overline{\rho}_u}\right) = \frac{\partial}{\partial x_j}\left(\alpha_{\text{eff}}\frac{\partial\widetilde{h_u}}{\partial x_j}\right) + \frac{\partial\overline{p}}{\partial t}\left(\frac{\overline{\rho}}{\overline{\rho}_u}\right) \tag{8.6}$$

8.3.2.1 Keppeler model

The flame surface density (FSD) is calculated by an algebraic model proposed by Keppeler [100]. It was developed for flames at elevated pressure conditions and validated up to 20 bars [100]. It is a very recent model and assumes a self-similarity of the flame wrinkling between the small and the large scales. Its implementation into OpenFOAM was generously provided by the Pfitzner research group and reads:

$$\Sigma_K = \left(\mathcal{B} + (1-\mathcal{B})\,C_R\left(\frac{2.2\Delta}{l_F\ max(Ka_\Delta^{-1/2}, 2)}\right)^{(D-2)}\widetilde{c}(1-\widetilde{c})F(\widetilde{c})^{-1}\right)|\nabla\widetilde{c}| \tag{8.7}$$

$$\mathcal{B} = \exp(-\frac{\Delta}{\epsilon_i}\Theta) \tag{8.8}$$

with C_R being a model constant, which is set to 4.5. $\mathcal{B}$ is a blending function with Θ being a model constant which is set to 2.2. The blending function ensures that the flame surface

density reduces to $|\nabla\widetilde{c}|$ for $\Delta \to 0$ and for $u'_\Delta \to 0$ [36]. Furthermore, in eqn. 8.7, Ka is the Karlowitz number, l_F is the laminar flame thickness and $F(\widetilde{c})$ is a polynomial function that makes the expression $\widetilde{c}(1-\widetilde{c})F(\widetilde{c})^{-1}$ to 0.22 in almost the entire flame brush [100].

The Keppeler model applies the Favre-filtered progress variable for the calculation of the gradient, which implicitly includes the counter-gradient-transport (CGT) [126]. Thus, the scalar sub-grid flux term $[\overline{\rho}(\widetilde{u_j c}-\widetilde{u}_j\widetilde{c})]$ in eqn. 8.5 can be modelled by a gradient assumption without CGT contribution, which reads:

$$[\overline{\rho}(\widetilde{u_j c} - \widetilde{u}_j\widetilde{c})] = \alpha_{\text{eff}} \left(\frac{\partial \widetilde{c}}{\partial x_j} \right) \tag{8.9}$$

8.3.3 Numerical setup

The simulations for both cylinder-head configurations are carried out on multiple moving grids without topological changes, with an interval size of no more than 5°CA. The results are mapped from the morphed grid to the new target grid using a second-order volume-weighted mapping method. The intake- and exhaust ports are completely detached from the cylinder volume and the piston top-land crevice volume is included. The grids are locally refined at the spark-plug to 0.25 mm and the piston top-land is filled with 3-4 stretched cells across the radial gap, with an aspect ratio of $\sim 1/5$. The intake and the exhaust ports are meshed with a gird resolution of 2 mm. Table 8.2 shows the main characteristics of the grids of the two different cylinder-head configurations. The meshing

Table 8.2: Specification of the engine grids.

Cylinder-head	Δx_{cyl}	Crevice	Intervals	Number of cells
Wall-Guided	1.0 mm	yes	147	2.8 - 3.3 Mio.
Spray-Guided	1.0 mm	yes	151	2.5 - 3.2 Mio.

is automated and explained in greater detail in a previous studies of this work [94] [92] [145]. For the mesh motion, a Laplace equation for a cell displacement field $x_{\text{disp},j}$ is solved and reads:

$$\frac{\partial}{\partial x_j} \left(\gamma \frac{\partial x_{\text{disp},j}}{\partial x_j} \right) = 0 \tag{8.10}$$

with γ being a user-defined damping to control the mesh motion. The new cell position can be then obtained by $x_j^{\text{new}} = x_{\text{ref},j} + x_{\text{disp},j}$, with $x_{\text{ref},j}$ being a reference point taken at the beginning of the simulation interval. No-slip boundary conditions are applied for the non-moving parts, except for the stems of the valves and the liner, where a zero-gradient boundary condition is applied. The displacement of the moving walls $x_{\text{disp},j}$ is directly imposed for all moving boundaries.
For the time integration, an implicit second-order backward scheme is chosen. The convective scalar-fluxes are discretized with a TVD-scheme, which uses the Sweby limiter [179]. For the momentum equation, a switch between a CDS and TVD-scheme is applied. A CDS is normally used, which is replaced by a TVD-scheme for Mach-numbers greater than 0.3 to avoid numerical problems caused by large density changes or even shoch waves. A non-slip boundary condition is applied on all stationary walls and on the piston and valves, its velocity imposed. For both cylinder-heads, 15 consecutive cycles are simulated with a CFL number of 2, which is based on the convective velocity of the flow.

8.4 Simulation setup

The simulation setup for the two cylinder-heads is the same as for the simulation of the wall-guided head without piston top-land crevice, which is presented in a previous work [94]. The same intake and exhaust pressure boundary conditions are used, since the experimentally obtained pressure profiles for the spray-guided head were not available at the time the simulations were performed.

8.4.1 Motored operating conditions

The cold flow simulations for the spray- and wall-guided head are started at 360 °bTDC and are both initialized with instantaneous flow-, temperature- and pressure fields from a cold flow simulation of the wall-guided head after 20 consecutive engine cycles [94] without piston top-land crevice. A time varying pressure is imposed 360 mm downstream of the exhaust valves and 530 mm upstream of the intake valves, at the location of the pressure sensors [18]. The inlet temperature is 295 K. The intake port temperature is also set to 295 K and the remaining walls have a fixed temperature of 333 K. A sudden opening and closing of the valves with a minimum valve lift of 0.35 mm is applied according to the valve opening and closing timings shown in table 8.1.

Table 8.3 shows the computational time for one cold-flow cycle of the spray- and wall-guided head. The simulations are performed on 192 cores on the super computer of the University of Duisburg-Essen (MagnitUDE). It takes around 3 days for one cold-flow cycle for each cylinder-head configuration.

Table 8.3: Computational time for one engine cycle performed with 196 CPUs for the wall- and spray-guided head for the different time intervals: valve overlap, intake valve closing and exhaust valve closing.

Interval	Wall. /Spray. [days]	% of total time	CAD
Full cycle	2.8 / 3.1	100 / 100	720
Intake valve closing	0.4 / 0.3	13 / 11	30
Exhaust valve opening	0.5 / 0.6	16 / 22	45
Overlapping	0.4 / 0.5	15 / 18	50
Rest	1.5 / 1.7	56 / 60	595

8.4.2 Fired operating conditions

The flow fields of the cold-flow engine simulations are directly used for the initialization and only the combustion process from 20°bTDC to EVO (110°bTDC) is considered. The engine is running at 800 rpm and a homogeneously distributed air/fuel mixture with a fuel-mass-fraction of 0.0623 is assumed for both cylinder-heads. All walls have a fixed temperature of 333 K. No dilution by residual gases is considered. The mixture is ignited at 16°bTDC by super-imposition of a spherical profile for the progress variable field in-

between the spark-plug gap (∼1.4 mm):

$$\widetilde{c}_{\mathrm{ign}} = c_0 \left(1 - \tanh\left(\frac{|x_i - x_{i,\mathrm{sp}}|}{\Delta_{\mathrm{sp}}}\right)\right) \tag{8.11}$$

In eqn. 8.11, Δ_{sp} is the cell size in the vicinity of the spark-plug, $x_{i,\mathrm{sp}}$ is the spark location and c_0 is a model constant, which is set to 0.01. The imposed profile is purely seen as an initialisation of the $\widetilde{c}$-field and cannot account for the transition of the laminar spherical flame kernel into a wrinkled self-sustaining flame front. To avoid any misfire, an ignition reaction source term is introduced, which reads:

$$\overline{\dot{\omega}}_{\mathrm{ign}} = \overline{\rho}\frac{\widetilde{c}_{\mathrm{ign}}}{\Delta t} \tag{8.12}$$

The reaction source term is used for a duration of 5°CA after ignition. The post-oxidation of the fuel, the flame quenching at the walls or the reduction of the flame speed close to the walls due to heat losses [28] are not taken into account. The intake and exhaust ports are removed from the computational domain.

8.5 Results and discussion

First the flow fields are discussed under motored operating conditions and compared against PIV and MRV measurements. A vortex centre tracking algorithm is applied to the flow fields within the compression stroke and auto-correlation curves are calculated to quantify the tumble break-down in both cylinder-head configurations. Finally, the simulated flame front propagation inside both cylinder-head geometries is compared against each other.

8.5.1 Flow field comparison - Motored case

Figure 8.3 shows the phase-averaged mean velocity at 270°bTDC within the tumble symmetry plane for the LES (average of 15 cycles) and PIV measurements (average of 2700 cycles) together with the velocity vectors. For both cylinder-head configurations, the spark-plug was kept in the domain, but in the experiments (MRV and PIV) removed. The influence on the spark-plug to the flow field can already be seen in region 4 of figure 8.3, where the intake jet is disturbed and changes its penetration angle towards the piston. A deeper penetration of the intake jet towards the exhaust side appears for the LES with spark-plug compared to the PIV measurement without spark-plug. Higher velocities of the intake jet are preserved for the wall-guided configuration at the liner walls, underneath the exhaust side. Therefore, the redirected flow at the piston top can reach closer to the liner at the intake side, which is denoted as region 6 in figure 8.3. The region of the redirected flow is much wider for the wall-guided head and lifts-up the stagnation line (region 5). More flow enters the combustion chamber at the intake side for the spray-guided head.

Evidently, the geometrical changes of the valves and the valve seats have a great influence on the development of the in-cylinder flow. Since it is very difficult to apply PIV to the upper part of the cylinder-head and to the valve seat region, the comparison and the discussion of the LES of both cylinder-heads is continued with the MRV data. Figure 8.4 shows the ensemble-averaged flow fields of the MRV measurements in the upper part of the cylinder-head in a cut through the mid-valve plane at a moment, which mimics the flow conditions at 270°bTDC of the spray- and wall-guided head configurations. At first glance, higher flow velocities are observed in the intake port upstream of the spray-guided

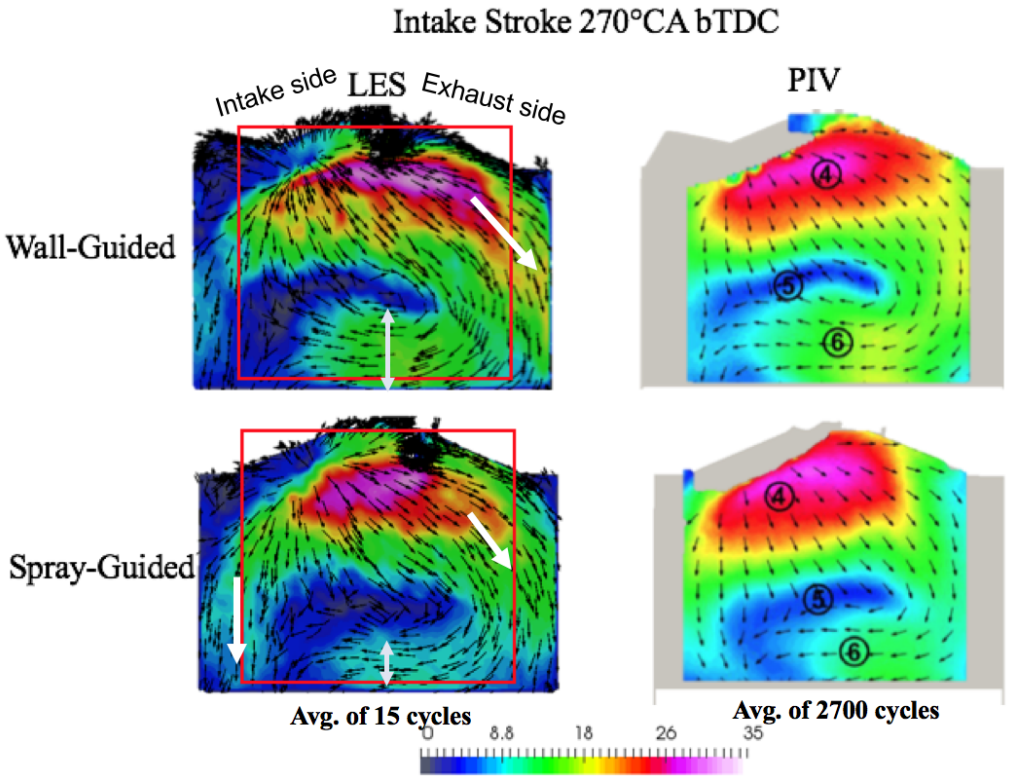

Figure 8.3: Phase averaged mean flow fields of the LES taken from 15 cycles compared to PIV measurements of the spray- and wall-guided head configurations [65] within the tumble symmetry plane at 270 °bTDC.

head compared to the intake port of the wall-guided head configuration. The smoother transition of the intake port to the spray-guided head has also led to a smaller recirculation zone in the underflow region (point 2 in figure 8.4), which explains the deeper intake-jet penetration at the liner walls for the spray-guide head underneath the intake valves in the tumble-symmetry plane of figure 8.3. The earlier change of the flow direction is induced by the different valve seat angles, which are illustrated in figure 8.2. The virtually extended line of the valve seat angle of the spray-guided head in figure 8.2 points towards the tip of the intake valves and so does the flow in the LES and MRV measurements, which is shown in figure 8.4.

The change of the valve seat angle has led to a significant change of the intake tumble structure. For the wall-guided head, one main flow, which leaves the upper part of the intake valve, is observed. The flow is being guided by the cylinder-head towards the liner, flowing down towards the piston, getting redirected by the piston and, finally, impinging on the flow coming from the lower part of the intake seat. The intake jet of the spray-guided head, however, has two distinct flow branches. As the flow is disturbed by the upper tip of the valve, the intake-jet quickly forms a recirculation zone and another part of the flow aligns with the liner walls. The lower intake-jet forms a stagnation line with the flow redirected by the piston. The redirected flow is more shifted towards the centre of the cylinder for the spray-guided head.

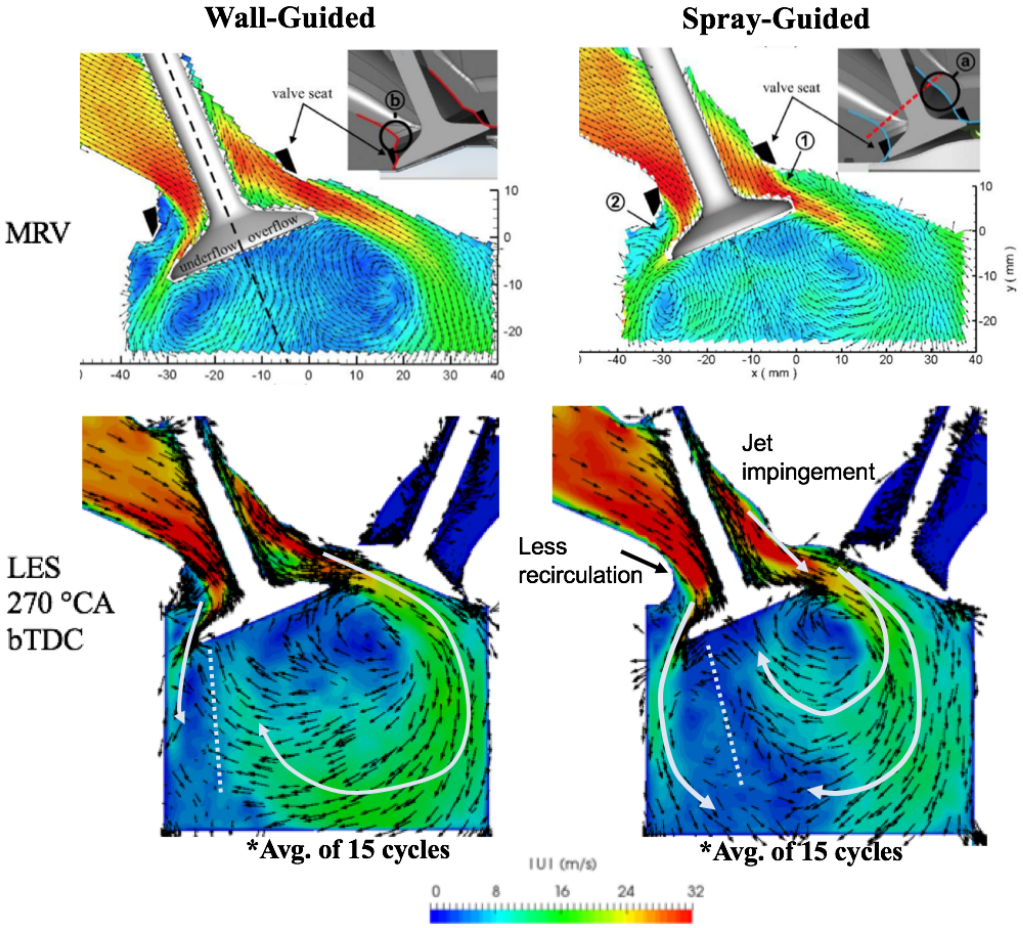

Figure 8.4: Ensemble-averaged mean flow fields obtained form MRV measurements [65] and phase-averaged mean flow fields obtained from the LES for the spray- and wall-guided head configurations. The black vectors indicate the flow direction and the white arrows highlight flow field differences.

8.5.2 Tumble formation - Motored case

Since the geometrical features around the valve seat and the cylinder-head are designed to form a favourable turbulent flow field for the combustion, the important question is now, how do the different flows for the spray- and wall-guided head evolve during the compression stroke. Figure 8.5 shows phase-averaged flow fields at 90°bTDC within the tumble-symmetry plane obtained from PIV and the LES of the two cylinder-head configurations. The biggest difference in the flow fields for both configurations is related to the tumble core, which is more pronounced for the wall-guided head with a tiny local region of very small velocities. On the contrary, the spray-guided configuration shows a much wider centre of low velocities. Region 1 in figure 8.5 pinpoints these centres of the tumble vortex. The position of the tumble core, is for the wall-guided head, in a good agreement with the experiment (already shown in a prevoious work 6 [94]), but for the results of the spray-guided LES, the core is shifted towards the cylinder-head in comparison to the PIV measurement. The shift of the vortex centre could be caused by the spark-plug, which was not mounted for the PIV measurement or by the impingement of the intake flow on the valve tip, which might be not accurately modelled. However, the LES simulation of the spray-guided head shows a wider region of low velocities in the tumble core as well. Apart

of the differences related to the vortex core, higher velocities are found for the spray-guided configuration below the cylinder-head at the intake side, whereas the highest velocities for the wall-guided configuration exist at the piston. The main differences are also here marked by bold white vectors.

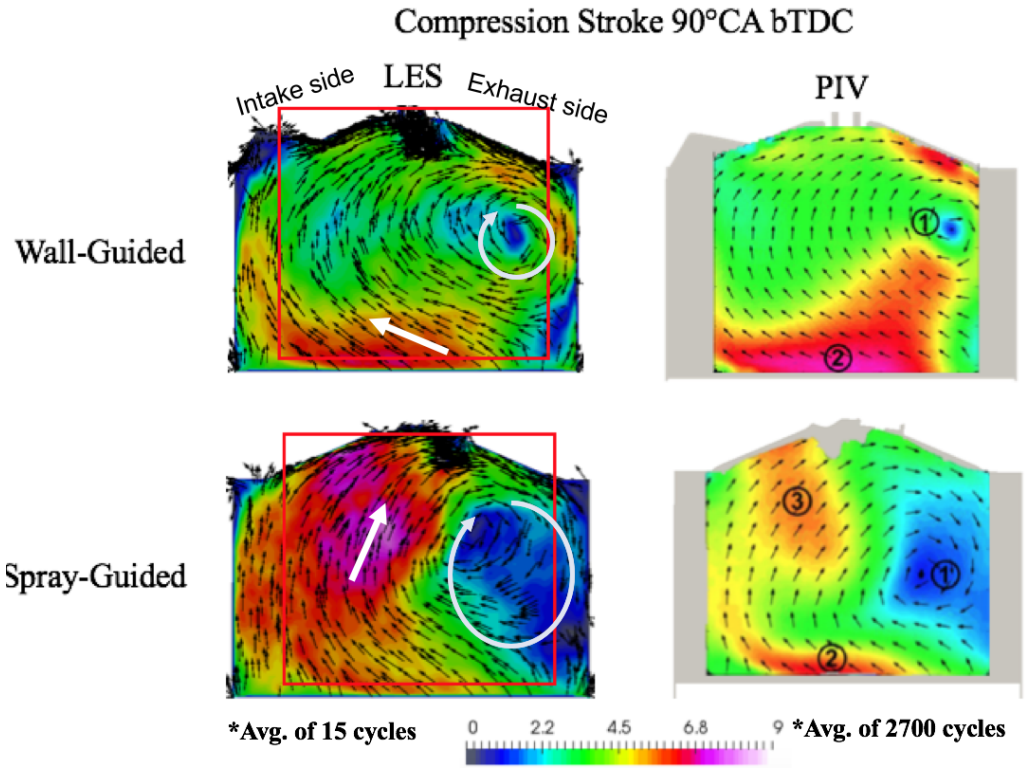

Figure 8.5: Phase averaged mean flow fields of the LES taken from 15 cycles compared to PIV measurements for the spray- and wall guided configurations within the tumble symmetry plane at 90°bTDC.

Tumble visualization

Since the history of the tumble motion and the tumble break-up is of key-importance for the combustion, it is not sufficient to consider the tumbling motion only on one 2D plane. Therefore, the evolution and the shape of the tumble is assessed with the help of the Γ-criterion, which was developed for vortex-tracking by Graftieaux et al. [77], and used in a previous study [94] for the visualisation of the tumble flow. The Γ-criterion is applied on 2D planes every 1 mm parallel to the tumble plane. The algorithm was solely applied on the displacement volume and the pent-roof chamber volume has been discarded. Therefore, a visualization of the tumble flow is from 45°bTDC to TDC not possible. From the individual planes, a closed 3D surface with an Γ iso-value of -0.65 is constructed at 125°bTDC and 90°bTDC and with a Γ iso-value of -0.35 for 45°bTDC for both cylinder-head configurations. The phase-averaged velocity data of 15 consecutive motored cycles is taken for the calculation of the Γ-field for the two cylinder-head configurations. It is important to mention again, that this tumble visualization strategy assumes that the tumble has its rotational axis perpendicular to the sampling planes (see figure 8.5).

Figure 8.6 shows iso-contours of the reconstructed Γ-field for the wall-guided (red) and the spray-guided (blue) cylinder-head configuration at 125, 90 and 45°bTDC inside the

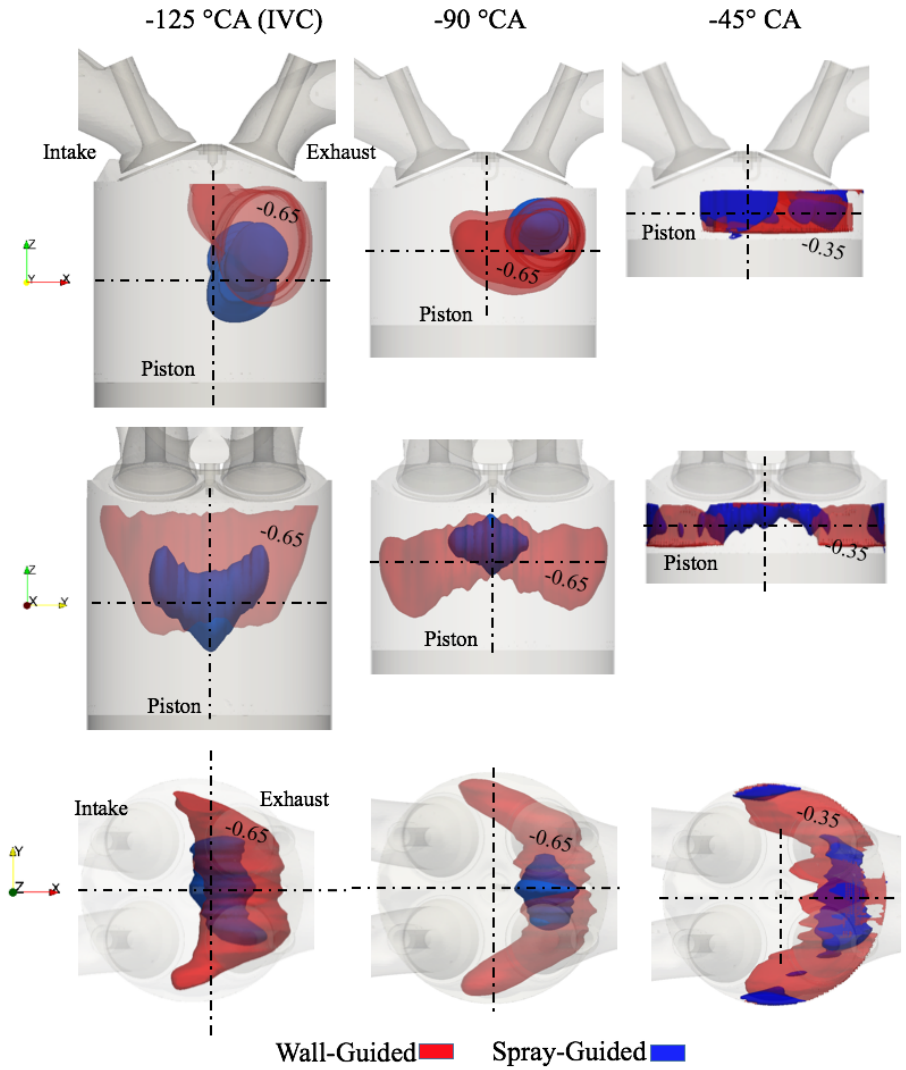

Figure 8.6: The Γ iso-contour for the wall- (red) and spray-guided (blue) heads at 125, 90 and 45 °bTDC shown from different directions inside the transparent wall-guided engine configuration.

engine. At IVC, the tumble vortex centre is found underneath the exhaust valves for the wall-guided head, where it fills up almost the complete upper half of the cylinder displacement volume. Also for the spray-guided configuration, the tumble vortex core is found at the exhaust side. Furthermore, the tumble flow is not attached to the liner walls but rather lies in-between the exhaust valves. At 90°bTDC, the tumble vortex gets squeezed by the upcoming piston. For the wall-guided head, the "belly" shape of the tumble vortex gets noticeably thinner and starts forming a "croissant-like" shape [94]. For the spray-guided configuration, the vortex core has now shrinked towards the centre tumble plane and lost its "v-shape". The tumble vortex of the spray-guided head is not branching towards the cylinder liner, which can be explained by looking at the velocity vector field at a Γ iso-contour of -0.5 shown in figure 8.7. Here, two vortices marked with X, which do not have their rotational axis perpendicular to the sample planes, but to a plane which is rotated relative to the tumble-symmetry by ∼40°. Since the Γ-criterion only detects the centre of the vortex perpendicular to the symmetry-tumble plane, it will not detect a

vortex that is strongly rotated to the plane. This does not mean that a rotational tumble structure does not exist anymore, but the intuitive understanding of a tumble flow along the horizontal cylinder-axis (as it is seen for the wall-guided head and known from the classical literature) is not longer applicable to the spray-guided head. At 45°bTDC, the tumble vortex is further squeezed and in full contact with the combustion chamber walls. From here, the tumble starts to move towards the spark-plug.

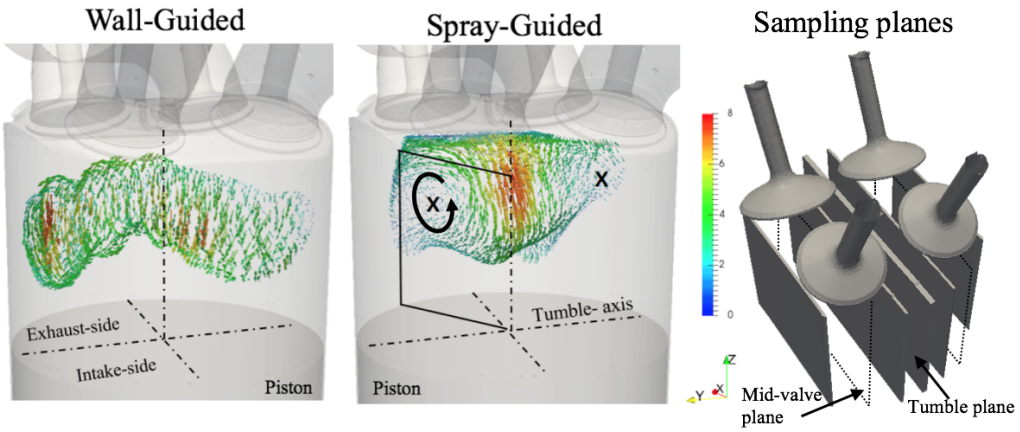

Figure 8.7: Velocity vector field colored with its magnitude (m/s) of the phase averaged mean velocity field (15 cycles) at 90°bTDC within a volume reconstructed by a Γ iso-contour of -0.5 for the wall- and spray-guided head and the corresponding sampling planes (only a few shown) on which the Γ-field was calculated.

8.5.3 Length scales - Motored Case

In order to quantify the differences between the in-cylinder flow fields of the two cylinder-head geometries, integral length scales are calculated based on two-point auto-correlation functions along the tumble-axis, bounded by the liner walls. Therefore, a modified version [94] of the auto-correlation function is taken. Figure 8.8 shows the lateral auto correlation coefficients R_{yy} using u^{δ} (vertical component) of the two different cylinder-head geometries at three different horizontal lines within the tumble symmetry plane. Each auto-correlation curve denotes one moment during the compression stroke (from 125°bTDC to 5°bTDC) and is averaged over 15 cycles. Looking on the correlation coefficients taken from the centre of the cylinder (y^*=0.5), it can be observed, that for the spray-guided head the correlation curves are overlapping each other until 75°bTDC. The auto-correlation curves for the wall-guided head, however, are changing their shape already at 100°bTDC. The auto-correlation curves for the spray-guided head configuration are falling steeper by approaching TDC and starting oscillating around 50°bTDC and at 25°bTDC for the wall-guided head. Within the scope of this work, the start of the oscillations is denoted as the start of the tumble break-up. Basically, the trend for both heads is similar, but the transition of the smooth correlation curves to the steeply falling oscillating curves happens at different moments and is most evident within the middle of the cylinder. The auto-correlations at the same y^* positions within the mid-valve planes were also calculated and a similar trend of the curves is obtained. However, for the spray-guided head, the auto-correlation curves start oscillating very late at 5°bTDC, which might be attributed to a small tumble flow underneath the valves as shown in figure 8.7.

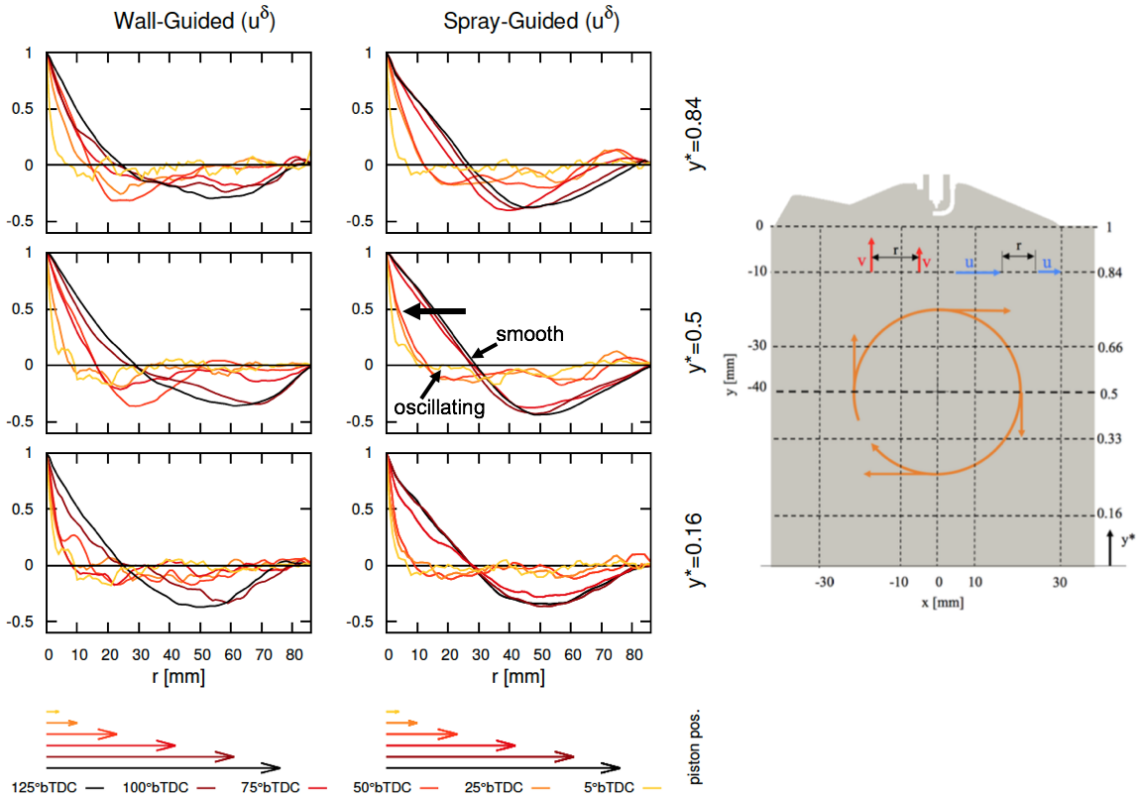

Figure 8.8: Auto-correlation coefficient curves (R_{yy}) obtained from the vertical velocity components at horizontal lines at the y^* positions 0.84, 0.5 and 0.33 (averaged over 15 cycles) for the wall- and spray-guided head configurations (left) and a sketch of the sampling positions within the tumble symmetry plane (right).

The evolution of the tumble becomes even more distinct by looking at the length scales that can be obtained by integrating the auto-correlation curves up to the first intersection with the zero line. Figure 8.9. shows the length scales calculated from the auto-correlation curves shown in figure 8.8. For the spray-guided head, the lateral length scales are remaining almost constant from 125°bTDC to 75 °bTDC on a first plateau and then sharply decreasing down to ∼ 4 mm to a second plateau, from where (20°bTDC) they finally decrease to ∼2 mm. The decay of the length scales with the two distinct plateaus is also observed for the wall-guided head, but at different locations.

The first decay from the first plateau to the second one starts already at 100°bTDC from ∼10 mm to ∼8 mm, then stays almost constant until ∼45°bTDC, before it finally decreases to ∼2 mm. The integral length scales of the wall-guided head are very similar to the integral length scales of the spray-guided head at the mid-valve planes and are linearly decreasing from ∼12 mm to ∼2 mm at 5°bTDC.

The first phase (plateau) is assigned to a moment, when the tumble moves freely inside the cylinder and is not changing its size. Once the piston starts to compress the tumble and the tumble touches the walls, the length scales are decreasing, which is indicated by the first sharp drop of the length scales. During the second plateau, the onset of the tumble break-up takes place.

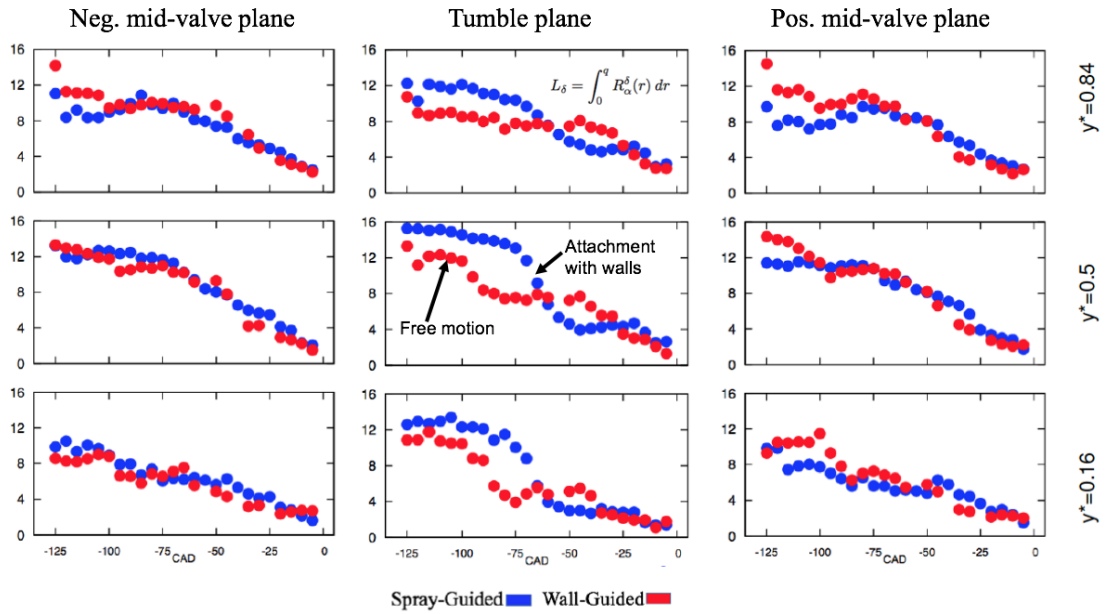

Figure 8.9: Integral length scales within the negative and positive mid-valve planes and within the tumble plane calculated from the auto-correlation coefficient curves R_{yy} at the horizontal sampling positions according to figure 8.8 during the compression stroke (averaged over 15 cycles).

8.5.4 Comparison of the flame propagation inside the spray- and wall-guided heads

Figure 8.10 shows the phase-averaged progress variable field at 10, 5 and 0°bTDC taken from 10 individual cycles for the spray- and wall-guided head within the tumble-symmetry plane. The red zone denotes a region through which the flame has propagated (for all cycles) and consumed the air/fuel mixture. For the wall-guided head, it can be observed that a flame kernel has developed after 6°CA after the ignition time and tends to move towards the intake side. At TDC most of the flame (for some cycles) has already reached the edge of the piston and has started to propagate into the crevice. Also for the spray-guided head, the flame tends to move towards the intake side at the beginning (5°bTDC), but it is lifted upwards, only partially reaching the piston head. The upwards lifted flame of the spray-guided head can be explained by the velocity vector field within the tumble-symmetry plane, which is shown in figure 8.11. For the spray-guided head configuration, the flow field is pointing upwards to the spark-plug. For the wall-guided head, however, the flow is parallel to the piston.

In figure 8.12, the contour surface of the averaged progress variable field ($\langle\tilde{c}\rangle$=0.2) is shown at 10, 5 and 0°bTDC, which now enables a 3D representation of the flame propagation inside the two different cylinder-head configurations. For a better comparison, the two contour surfaces of the progress variable are shown together in the transparent spray-guided cylinder volume. Here, it can be seen how the two flames develop from their ignition location.

Figure 8.13 shows the combustion progress of the spray- and wall-guided head, where the transition of the flame kernel into a freely-propagating flame starts earlier for the

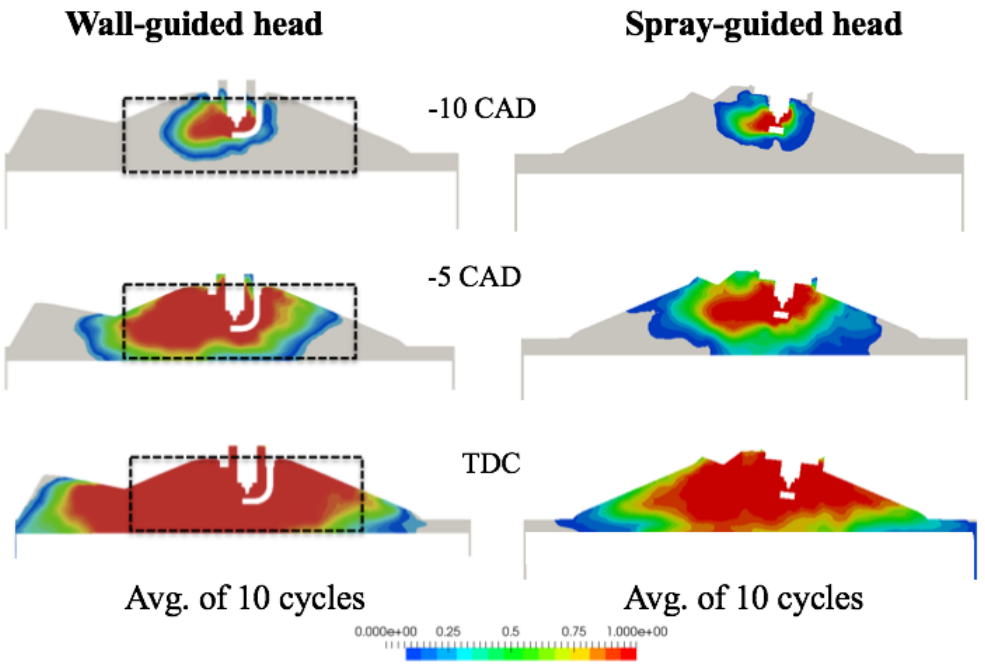

Figure 8.10: Phase averaged progress variable field of 10 individual cycles for the wall- and spray-guided head in a cut through the tumble symmetry plane at 10, 5 and 0°bTDC. Operating conditions: engine is running at 800 rpm, λ=1, no internal gas recirculation, spark timing at 16°bTDC and flow field initialized at 20°bTDC from the cold flow simulations presented in setion 8.5.1.

wall-guided head configuration ($\sim$ 8°bTDC), in comparison to the spray-guided head ($\sim$ 3°bTDC). From here, the combustion progress curves have a very similar slope, which implies that the flame inside the two cylinder-heads has a similar turbulent flame speed. Both curves are slowing down at the moment where 80% of the mixture is consumed. At this moment, the flame has almost consumed all the mixture in the combustion chamber. The further slow decrease is attributed to a burning flame inside the piston top-land crevice and in the late expansion stroke by the outgassing crevice air/fuel mixture, which then burns slowly at the edge of the crevice. The air/fuel mixture can literally escape from the combustion chamber into the piston-top land and then become available again later during the expansion stroke, when it will be pushed out by inertia forces. Thus, disregarding this volume will completely change the combustion phasing and will lead to an explicit change of the combustion chamber design.

8.6 Conclusions

The flow fields during the intake and the compression stroke were in a good qualitative agreement with the PIV and the MRV data. The impingement of the intake jet inside the spray-guided configuration has led to a branching of the main redirected flow inside the combustion chamber and yielded a bigger vortex core with low velocities during the compression stroke.

The tumble-visualization strategy can reveal the regions where the tumble vortex core changes its alignment with the tumble-symmetry plane. For the spray-guided head, the

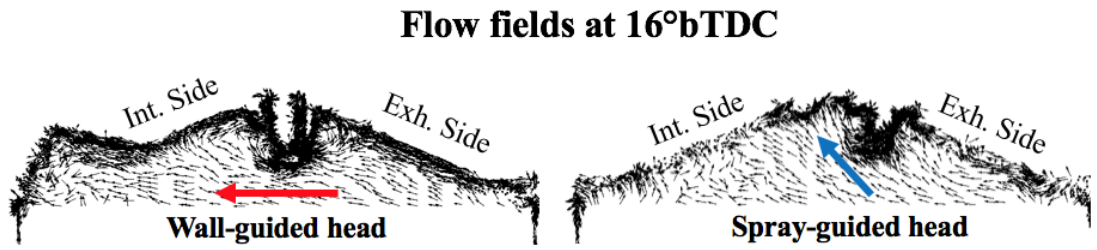

Figure 8.11: Velocity vector field for the wall- and spray-guided head at ignition time (16°bTDC) in a cut through the tumble plane.

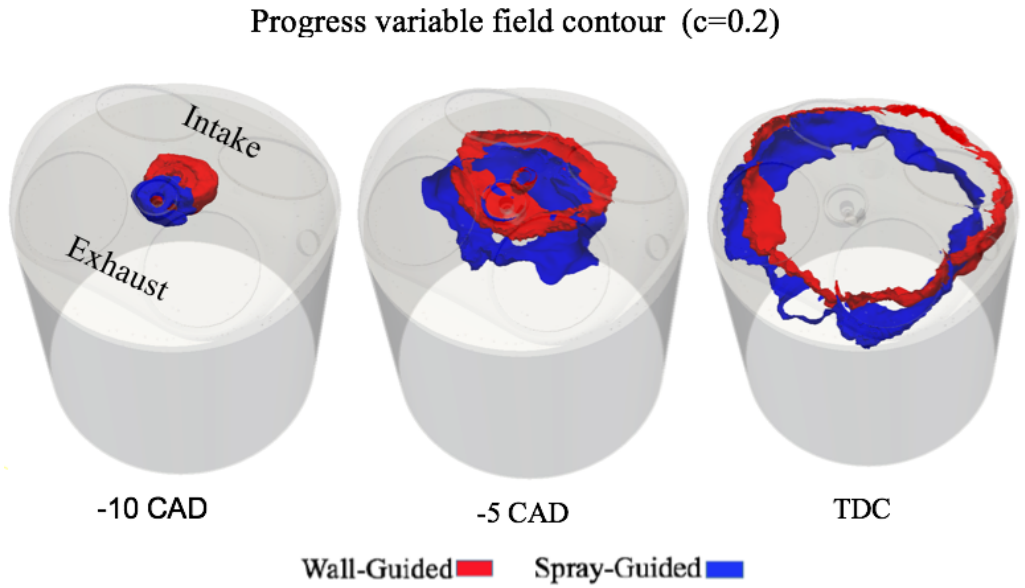

Figure 8.12: Iso-contour of the averaged progress variable ($\langle\widetilde{c}\rangle$=0.2) obtained from 10 cycles for the spray- (blue) and the wall-guided (red) head configurations at 10, 5 and 0°bTDC inside the transparent spray-guided head engine configuration.

typical tumble flow only appeared in-between the exhaust valves with the rotational axis being perpendicular to the tumble-symmetry plane.

A two-stage decay of the length scales was observed for the wall- and spray-guided head, where the first plateau could be assigned to the free motion of the tumble. The first decay of the length scales could be assigned to the attachment of the tumble with the liner walls and with the upwards coming piston. The tumble break-up took place within the second stage and decay and is more visible in the auto-correlation curves. The shapes of the auto-correlation curves enable a better distinguishing between the tumble break-up and the tumble compression, where the curves stay rather smooth during the compression and start oscillating heavily at the onset of the tumble break-up.

The cold-flow results were used for individual single-cycle combustion simulations, where the flame inside the wall-guided head tended to spread towards the intake side and, for the spray-guided head, towards the exhaust side. Furthermore, the local flow field pushed the flame into the direction of the cylinder-head in the spray-guided head. Inside the wall-

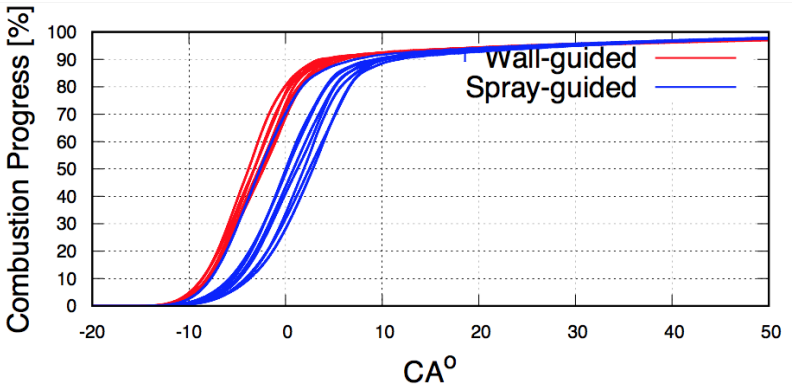

Figure 8.13: Combustion progress of the wall- and spray guided head.

guided head, the flow at the ignition timing was rather aligned with the piston head and streamed towards the intake side. Overall, it took 5 degrees longer for the spray-guided head configuration to burn the first 10% of the in-cylinder charge. After this point, the turbulent flame speed was for both head configurations very similar until crevice and wall effects became important.

9

Penetration of the Flame into the Top-Land Crevice - Large-Eddy Simulation and Experimental High-Speed Visualization

Authors: Peter Janas, Mateus Dias Ribeiro, Andreas Kempf, Martin Schild, Sebastian A. Kaiser
This chapter including all figures and tables was previously published in the International Journal of Engines SAE: "Penetration of the Flame Into the Top-Land Crevice - Large-Eddy Simulation and Experimental High-Speed Visualization,"SAE Technical Paper 2015-01-1907, 2015, doi:10.4271/2015-01-1907. The author P. Janas developed the code, ran all the simulations, wrote the paper and generated all figures and tables related to the simulation. Mateus Dias Ribeiro assisted in creating the computational grids. Martin Schild and Sebastian A. Kaiser made the experiments, created all the figures related to the experiment, contributed corrections, discussions and proof-reading. Andreas Kempf contributed corrections, discussions and proof-reading, too.

9.1 Introduction

Optically accessible engines will normally necessitate unconventional geometries, for example with enlarged piston clearance and ring packs located lower on the piston. These modifications are meant to not influence the in-cylinder processes, but UHC-emissions are sensitive to the size of the top-land piston crevice volume [14],[50],[197],[22],[81]. At top dead center, the crevice volume may take up to 10-20% of the combustion chamber volume of an optical engine. If these gases are unburned (and dense), the crevice can include half of the entire charge (by mass). This means that the heat release and hence the in-cylinder pressure are directly affected by the crevice volume. The crevice volumes of such optically accessible engines may be 40 times larger than those of production engines [185],[108]. Nevertheless, even the much smaller crevice volume of production engines is still very relevant for UHC emissions. The relevant geometry of piston, cylinder, and combustion chamber is

illustrated in Figure 9.1. During compression, unburned charge is pushed into the top land crevice. Depending on the piston clearance δ, the surface-to-volume ratio of the crevice changes, affecting convective heat transfer between the charge, the piston, and the cylinder wall. During combustion, dilatation pushes even more of the unburned gas into the crevice. Depending on δ, the flame can either propagate into the volume, be quenched by the walls, or propagate at a reduced effective flame speed. The strength of the quenching depends on the crevice geometry, the composition of the unburned mixture, the temperature, and the pressure [14],[87]. The importance of flame-wall-interaction for UHC emissions, in particu-

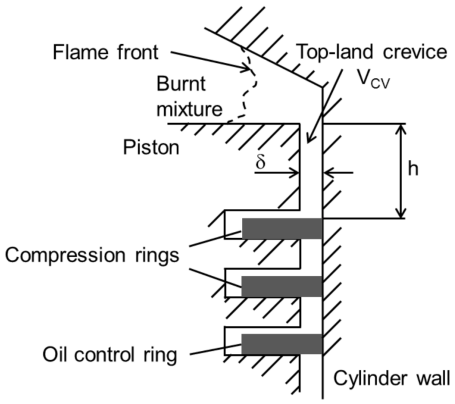

Figure 9.1: Geometry of the piston and top-land crevice.

lar in the top-land crevice, is widely recognized [14],[50]. Wentworth [197] and Boam et al. [22] examined the influence of the piston crevices on exhaust hydrocarbon emissions: they eliminated the piston crevice by a customized piston ring, which lead to much reduced UHC-emissions. Boam et al. give a reduction in UHC-emissions by up to 30% at cold start conditions [22]. In 1980 Yoshida [205] found that decreasing the top-land crevice height from 9.5 mm to 3.0 mm or increasing the radial clearance from 0.3 mm to 0.5 mm reduced the UHC-emissions by 16% and 23%, respectively. The latter finding indicates that improving conditions for flame propagation in the crevice indeed yields less unburned mixture. A detailed overview of experimental studies on the effect of the top-land crevice geometry on UHC-emissions is given by Alkidas [14].

Haskell and Legate [81] introduced a method to determine quenching distances under engine conditions. They successively increased the piston clearance and measured the resulting UHC-emissions. They observed quenching for clearances smaller than 0.18 mm, which is close to the two-plate quenching distance estimated by the Peclet number [87]. Goolsby and Haskell [72] and later Ishizawa [90] studied the influence of equivalence ratio, exhaust gas recirculation rate, charge efficiency, ignition timing, and wall temperature on flame quenching in gasoline engines. They used ion probe sensors mounted at the center of a variably adjustable crevice to detect the flame propagation in the crevice. Ishizawa developed an empirical equation for the two-wall quenching distance for stoichiometric combustion without charge dilution in combustion engines. This equation is quite similar to the earlier correlations of Goolsby and Haskel [72] and of Friedman and Johnston [66], who detected visible radiation from some fuel conversion processes in crevices. First high-speed imaging of the flame progress towards the cylinder walls was performed by Daniel [44]. He determined the quenching distances for single walls. Later Sterlepper et al. [176] investigated the influence of crevice geometry on UHC-emissions with multiple optical fibers. They detected light from the top-land crevice and correlated it with the

This chapter was previously published [92] and is reprinted with permission of the journal

measured pressure trace to indicate flame quenching in the warm-up phase.

Wall quenching is the last phase of combustion in a spark ignition engine. The entire combustion process can be subdivided in three stages, which consist of rapid flame acceleration during and just after ignition, followed by a phase of constant burning velocity, and finally deceleration of the flame as it approaches the walls. Liu et al. [121] studied the different stages of combustion in an optical engine. The deceleration of the flame brush due to near-wall effects is difficult to visualize. The beginning of the deceleration of the flame was estimated by Liu to start a distance of 7 mm to the piston and by Foucher et al. [63] at 2 mm distance. This last stage of combustion happens at decreasing burning velocities, which emphasizes the importance of accurate wall description and crevice volume around the piston. However, many numerical studies of flame-front propagation in optical research engines focused on the first stages of combustion, where the flame is freely propagating and is primarily effected by turbulence [188],[55],[160],[54].

A review of existing combustion models for spark ignition engines can be found in [49], [198]. None of them focused on flame-front propagation into the piston top-land crevice in LES. In spark ignition engines, only 1D calculations specifically of the combustion process inside the crevice volume have been performed [39] (to the authors' knowledge). The few 3D calculations that considered the crevice volume focused mainly on HCCI [207],[12], soot entrainment through the top-land crevice into the crankcase [181], or the post-combustion oxidation of the UHC from it [203]. Rakopoulos et al. [158] proposed a simple phenomenological model for the mass transfer between the combustion chamber and crankcase, to be incorporated as a source term in the continuity equation. They used this crevice model for a 3D-RANS CFD with combustion [110]. However, this model cannot account for local effects by the in- and outflow of the crevice volume, which can affect in-cylinder mixture preparation and boundary layer thickness at the liner walls.

The paper presents an investigation of flame propagation inside the crevice, based on high-speed visualization experiments, large eddy simulation, and information taken from the literature. The qualitative findings from the simulations and experiments are then compared to each to see if either complete flame quenching or unperturbed combustion inside the crevice can adequately describe the situation. The findings imply that the flame continues to burn inside the crevice.

9.2 Engine and imaging experiment

Chemiluminescence measurements were performed in a passenger-car sized optically accessible single-cylinder gasoline engine with a pent roof four-valve head and a flat piston top [97]. During operation in a work-rest strategy (alternation of many fired and many motored engine cycles), the engine was fed with iso-octane premixed with air in a small mixing chamber about 50 cm upstream of the intake valves. The relative in-cylinder pressure was measured with a piezo-capacitive sensor (AVL GH12D) in the cylinder head. Absolute intake and exhaust pressure traces were taken by piezo-resistive transducers (Kistler 4007). The temporal resolution of the pressure measurement was 1°CA. Table 9.2 lists the engine's operating conditions and valve timings. The engine was throttled to an intake pressure of 700 mbar. Additional throttling by reduced lift of the intake valves (3.0 mm) and the exhaust (3.5 mm) valves resulted in part-load conditions. The intake air-flow was preheated to 300 K to ensure steady-state operation, despite the chosen work-rest strategy (140 cy-

Table 9.1: Engine operating point. Zero °CA is taken to be at compression top-dead center, i.e., crank angles during intake and compression are negative.

Engine speed	1500 min^{-1}
Intake pressure	700 mbar
Intake temperature	300 K
Fuel	Iso-octane
Relative air-fuel ratio	1.0
Ignition timing	-45°CA
Intake valve opening/closing	350°CA / -176°CA
Exhaust valve opening/closing	172°CA / -320°CA

Table 9.2: Cylinder and combustion-chamber geometry

Compression ratio	10.0
Displacement	499 cm^3
Stroke	90 mm
Bore	84 mm
Clearance height	1.4 mm
Top land height h	31.5 mm
Radial clearance	0.5 mm
Crevice volume V_{cv}	4.13 cm^3

cles fired / 140 cycles motored). Some key specifications including engine and top-land geometry are listed in Table 9.2.

In this experiment, the upper part of the cylinder was from quartz, which enabled viewing the pent-roof combustion chamber and the complete width of the bore to about 29 mm down from the fire deck (Figure 9.2). As it is common in an optically accessible engine, the radial piston clearance is enlarged and the uppermost compression ring is located very low to avoid that the piston or the ring, respectively, touch the glass surfaces. Time-resolved flame front visualization was performed in the visible spectrum (400-700 nm) with a high-speed CMOS camera (Vision Research Phantom v.7.3, 800 x 600 pixels) combined with a commercial camera lens (Nikon 50 mm, f/1.2). The projected pixel size of the measurement was 313 μm^2. The exposure time was set to 15μs. The repetition rate of 18 kHz corresponds to 0.5°CA at the engine speed of 1500 rpm. Each time-resolved data set includes 120 snap-shots per cycle, from -50°CA to 9.5°CA after TDC.

Broadband sensing in the visible part of the spectrum mainly detects the luminescent species CH*, CO, CO2, and H2O. These may not be directly associated with the flame front. Figure 9.2 shows a false-color example of a snapshot taken 20°CA after ignition. Here, the focal plane is mid-cylinder, such that the ignition event and early flame kernel are sharply in focus.
Figure 9.3 shows two images from later in the cycle. Both have the same field of view, which is corresponds to a section of the top-land crevice as indicated in Figure 9.2. In Figure 9.3 a), the focal plane is again mid-cylinder. Indistinct spots of elevated brightness can be seen in the crevice.

Figure 9.3 b) is from the same crank angle and location, but the camera has been refocused to 42 mm in front of the mid-cylinder plane, i.e., the front most part of the crevice. We

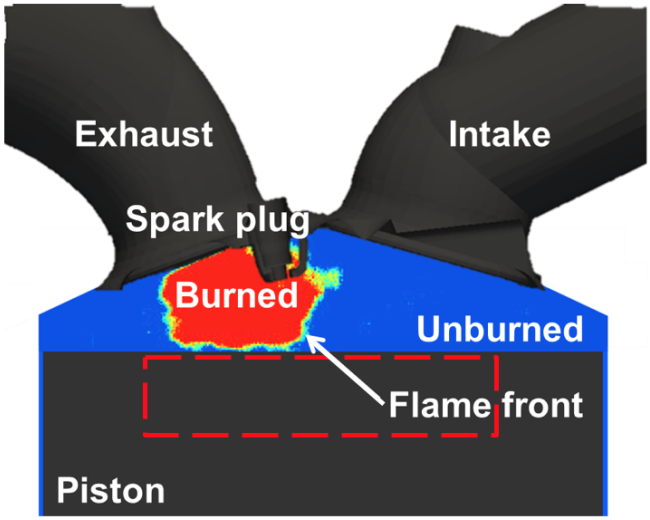

Figure 9.2: Snapshot during early flame propagation at 20°CA superimposed in false color on a CAD rendering of the engine geometry. The dotted-line rectangle indicates the field of view of the images in Figure 9.3.

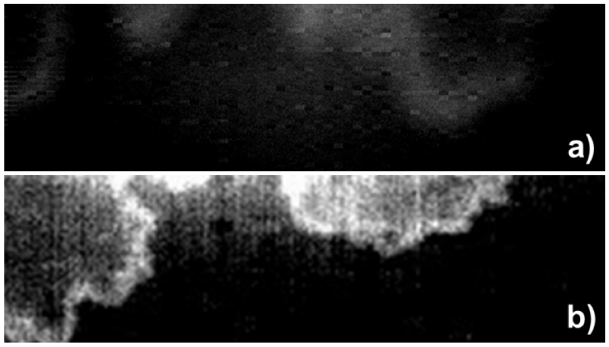

Figure 9.3: Chemiluminescence imaging in the top-land crevice. a) Focal plane mid-cylinder, at the spark plug and b) focus on the crevice volume.

now can clearly see well-defined, curved structures of high brightness, which previously simply were out of focus. The large relative aperture (f/1.2) of the lens, optimized for low-light imaging, contributes to a shallow depth-of-field and thus the pronounced defocussing in Figure 9.3a). The need for refocusing and possibly altering exposure settings may well explain why such "flame-in-crevice" images have not been published before (to the authors' knowledge). The latter focus setting enabled detailed observation of late flame propagation and what may be penetration into the top land crevice.

Figure 9.4 b) shows how islands of hot gas are pushed into the crevice. At TDC, one can distinguish at least three such islands, their outlines being marked by a luminous region. The "gulf" between the islands indicates a region of unburned gases. At 2.5°CA, the gulf has disappeared, and the burned-gas islands seem to have merged. This merging implies that the luminous boundaries are not just advected, but propagate actively, giving strong evidence that the luminous boundaries are in fact a propagating flame, not just leftover,

This chapter was previously published [92] and is reprinted with permission of the journal

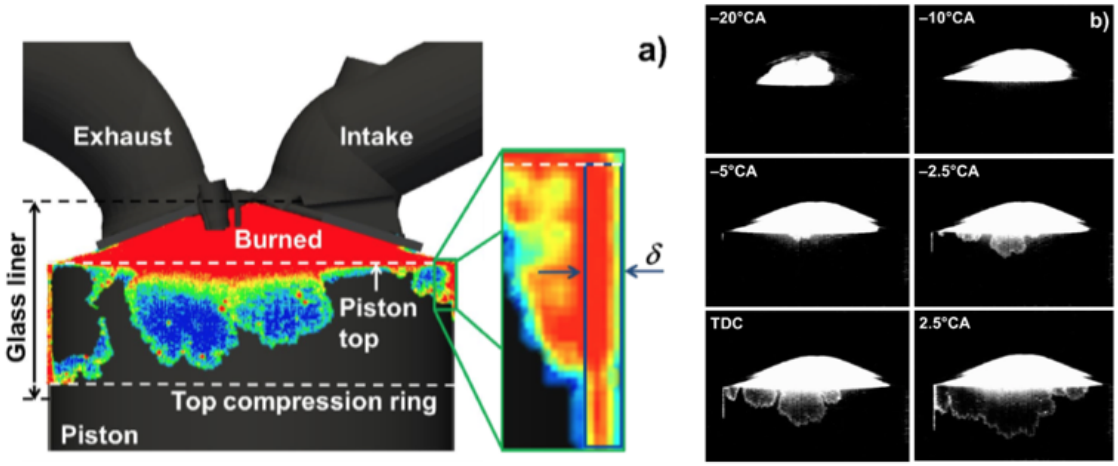

Figure 9.4: a) Snapshot at TDC superimposed in false color on a CAD rendering of the engine geometry. b) Flame development in a single cycle with expansion into the large crevice region.

chemiluminescent gases. So we have some direct evidence that the flame does indeed continue to burn within the crevice. This observation can be related to evidence obtained from calculating the two-wall quench distance (d_q) determined by the empirical equation of Ishizawa [90] for similar operating conditions:

$$d_q = 14.8 \cdot P_{max}^{-0.9} \cdot T_W^{-0.5} \tag{9.1}$$

For an in-cylinder peak pressure of P_{max}=18 bar and a crevice wall temperature of T_W=450 K, a quench distance of 0.41 mm is calculated - which is considerably smaller than the crevice width of 0.5 mm, so that the flame can be expected to burn into the crevice. Like all of SI combustion, also this crevice flame is subject to strong cyclic variations. Figure 9.5 shows three different cycles between -5°CA and 2.5°CA. Although the general morphology is the same, temporal onset and specific flame morphology seem to be randomly different for each cycle.

9.3 Modeling

For the large-eddy simulation of the flow and flame propagation, the Favre-filtered Navier-Stokes equations are solved, which read for mass (9.2), momentum (9.3) and energy (9.4):

$$\frac{\partial(\overline{\rho})}{\partial t} + \frac{\partial(\overline{\rho}\widetilde{u}_j)}{\partial x_j} = 0 \tag{9.2}$$

$$\frac{\partial\left(\overline{\rho}\widetilde{u}_i\right)}{\partial t} + \frac{\partial(\overline{\rho}\widetilde{u}_i\widetilde{u}_j)}{\partial x_j} = \frac{\partial\overline{\tau_{ij}}}{\partial x_j} + \frac{\partial\tau_{ij}^{\mathrm{sgs}}}{\partial x_j} - \frac{\partial\overline{p}}{\partial x_i} \tag{9.3}$$

This chapter was previously published [92] and is reprinted with permission of the journal

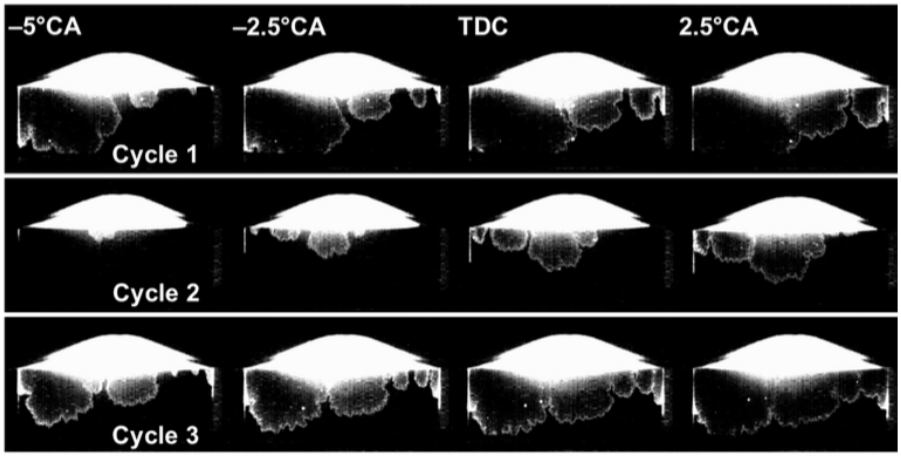

Figure 9.5: Cyclic fluctuations of flame progress in the crevice for three different cycles.

$$\frac{\partial(\overline{\rho}\widetilde{h}_t)}{\partial t} + \frac{\partial(\overline{\rho}\widetilde{u}_j\widetilde{h}_t)}{\partial x_j} + \frac{\partial(\overline{\rho}\widetilde{K})}{\partial t} + \frac{\partial(\overline{\rho}\widetilde{K}\widetilde{u}_j)}{\partial x_j} = \frac{\partial}{\partial x_j}\left(\alpha_{\text{eff}}\frac{\partial\widetilde{h}_t}{\partial x_j}\right) + \frac{\partial\overline{p}}{\partial t} \tag{9.4}$$

The governing equations are solved on a moving grid, where the fluxes over the faces are made relative to the motion of the control volume [47]. Within the governing equations $\overline{\rho}$ denotes the density of the gas mixture, $\widetilde{u}_i$ stands for the velocity vector, $\overline{p}$ for the pressure and τ_{ij} for the viscous shear stress tensor. The unresolved subgrid stresses τ_{ij}^{sgs} are calculated by the standard Smagorinsky model [174]. The pressure is obtained by a pressure-velocity-density coupling for flows at arbitrary Mach number proposed by Demirdžić et al. [47], [46]. This procedure allows marching in time with larger time steps than in a density-based approach. The energy equation (9.4), is solved for the absolute enthalpy h_t , which is composed of the sensible enthalpy and the chemical energy of the mixture. By using the absolute enthalpy, no reaction source term appears in the energy equation. The kinetic energy is given by $\widetilde{K} = 1/2\widetilde{u}_j^2$, and α_{eff} is the sum of the turbulent and laminar thermal diffusivities. The viscosity of the mixture is obtained by the Sutherland law [178]. The mixture inside the engine is assumed to consist of three components, which are air (oxidant), iso-octane (fuel), and burned gas (products). The JANAF coefficients are used to calculate the specific heat capacity and the temperature of the mixture. The composition inside the engine is determined by the Favre-filtered progress variable $\widetilde{c}$ and by the fuel mass fraction f_t. The fuel mass fraction (f_t) is the ratio of the fuel mass (m_{fuel}) to the entire in-cylinder mass, which includes the mass of the air (m_{air}). Thus, the mean molecular weight (W_m) of the mixture can be computed by the following equations (9.5-9.8), where λ_{st} denotes the stoichiometric air to fuel ratio. The mass fractions of the fuel, air, and burned gases are given by $\widetilde{Y}_{\text{fuel}}$, $\widetilde{Y}_{\text{air}}$ and $\widetilde{Y}_{\text{burnt}}$, respectively.

$$\widetilde{Y}_{\text{fuel}} = (1-\widetilde{c})f_t + \widetilde{c}\left(f_t - \frac{1-f_t}{\lambda_{st}}\right) \tag{9.5}$$

$$\widetilde{Y}_{\text{air}} = (1-f_t) - (f_t - \widetilde{Y}_{\text{fuel}})\lambda_{st} \tag{9.6}$$

This chapter was previously published [92] and is reprinted with permission of the journal

$$\widetilde{Y}_{\text{burnt}} = 1 - \widetilde{Y}_{\text{fuel}} - \widetilde{Y}_{\text{air}} \tag{9.7}$$

$$\frac{1}{W_m} = \frac{\widetilde{Y}_{\text{fuel}}}{W_{\text{fuel}}} + \frac{\widetilde{Y}_{\text{air}}}{W_{\text{air}}} + \frac{\widetilde{Y}_{\text{burnt}}}{W_{\text{burnt}}} \tag{9.8}$$

Fuel injection, about 50 cm upstream of the intake valves in the experiment, is not specifically taken into account by the simulation. We assume a homogeneous air/fuel mixture inside the entire combustion chamber prior to ignition. The flame-front propagation is modeled by a transport equation for the Favre-filtered progress variable $\widetilde{c}$ which reads:

$$\frac{\partial(\overline{\rho}\widetilde{c})}{\partial t} + \frac{\partial(\overline{\rho}\widetilde{u}_j\widetilde{c})}{\partial x_j} + \frac{\partial}{\partial x_j}\left(\overline{\rho}\widetilde{u_j c} - \overline{\rho}\widetilde{u}_j\widetilde{c}\right) = \frac{\partial}{\partial x_j}\overline{\left(\rho D\frac{\partial c}{\partial x_j}\right)} + \overline{\dot{\omega}} \tag{9.9}$$

The right-hand side of equation 9.9 includes the molecular diffusivity D and the reaction source term $\overline{\dot{\omega}}$. It is described by the generalized flame surface density (FSD) formulation (eqn. 9.10), with S_l as the laminar flame speed and ρ_u as the density of the unburned mixture:

$$\frac{\partial}{\partial x_j}\overline{\left(\rho D\frac{\partial c}{\partial x_j}\right)} + \overline{\dot{\omega}} \approx \rho_u S_l \Sigma_{\text{gen}} \tag{9.10}$$

The generalized flame surface density Σ_{gen} considers the flame wrinkling induced by the turbulence and can be modeled by an algebraic equation. Here, the Weller flame surface density model [194] is chosen:

$$\Sigma_{\text{gen}} = 1 + 2\widetilde{c}\left(1 + 0.62\sqrt{\frac{u'_\Delta}{S_l}}Re_\eta\right)\left|\frac{\partial \overline{c}}{\partial x_j}\right| \tag{9.11}$$

In equation (9.11), $u'_\Delta = (2/3k_{\text{sgs}})^{0.5}$ denotes the subgrid velocity fluctuations and $Re_\eta = u'_\Delta/(\tau_\eta \epsilon_{\text{sgs}})$ the Kolmogorov Reynolds number. The turbulent kinetic subgrid energy and dissipation are k_{sgs} and ϵ_{sgs}. The Kolmogorov time scale is computed by $\tau_\eta = (\mu_u/(\rho_u \epsilon_{sgs}))^{0.5}$, with μ_u for the viscosity and ρ_u for the density of the unburned mixture.

The scalar subgrid fluxes $(\overline{\rho}\widetilde{u_j c} - \overline{\rho}\widetilde{u}_j\widetilde{c})$ in equation (9.9) are modeled by a gradient assumption with a counter gradient transport (CGT) model proposed by Richard [160]. The CGT term has to be included, since the gradient of the Reynolds-filtered progress variables $\nabla\overline{c}$ used within the Weller flame surface density model. The modeled subgrid fluxes include the turbulent thermal diffusivity α_t, the flame surface normal vector n_j, which is pointing towards the unburned mixture, read:

$$\left(\overline{\rho}\widetilde{u_j c} - \overline{\rho}\widetilde{u}_j\widetilde{c}\right) = -\alpha_t\frac{\partial \widetilde{c}}{\partial x_j} - S_l\rho_u(\overline{c} - \widetilde{c})n_j \tag{9.12}$$

This chapter was previously published [92] and is reprinted with permission of the journal

The Reynolds-filtered progress variable $\overline{c}$ is deduced from the Favre-filtered progress variable according to Chakraborty et al. [35]. The laminar flame speed S_l (eqn. 9.13) is obtained by Gulder's flame speed correlation [79] for unstrainend premixed flames. The parameters for iso-octane are: $W = 0.4658$, $\eta = -0.326$, $\xi = 4.48$, $\alpha = 1.56$, $\gamma = -0.22$, $p_{ref} = 1.0131\text{bar}$, $T_{ref} = 300\text{K}$ and Φ as the equivalence ratio.

$$S_l = W\Phi^{\eta} \cdot \exp(-\xi \cdot (\Phi - 1.075)^2) \cdot \left(\frac{T_u}{T_{ref}}\right)^{\alpha} \left(\frac{p}{p_{ref}}\right)^{\gamma} \tag{9.13}$$

The unburned temperature T_u is obtained by solving an additional energy equation for the unburned absolute enthalpy $\widetilde{h}_u$, which is solely solved while combustion occurs and reads:

$$\frac{\partial(\overline{\rho}\widetilde{h_u})}{\partial t} + \frac{\partial(\overline{\rho}\widetilde{u}_j\widetilde{h_u})}{\partial x_j} + \left(\frac{\partial(\overline{\rho}\widetilde{K})}{\partial t} + \frac{\partial(\overline{\rho}\widetilde{K}\widetilde{u}_j)}{\partial x_j}\right)\left(\frac{\overline{\rho}}{\overline{\rho}_u}\right) = \frac{\partial}{\partial x_j}\left(\alpha_{\text{eff}}\frac{\partial\widetilde{h_u}}{\partial x_j}\right) + \frac{\partial\overline{p}}{\partial t}\left(\frac{\overline{\rho}}{\overline{\rho}_u}\right) \tag{9.14}$$

Ignition is triggered by setting the reaction source term to a sufficiently high value in the vicinity of the spark plug. The size of the flame kernel (V_{kernel}) is taken from flame kernel visualizations in the experiment. Figure 9.6 shows the flame kernel at the spark plug 1°CA after ignition and the flame front 9°CA later.

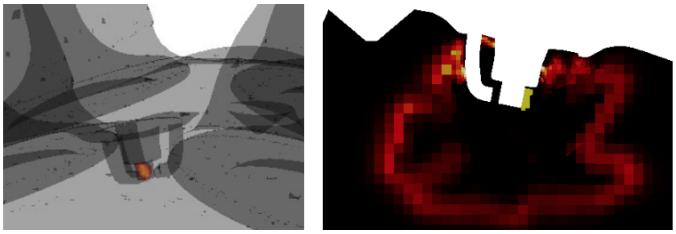

Figure 9.6: Spark plug with flame kernel after ignition (left) and reaction source term (right).

For the crevice zone, the reaction source term of the progress variable transport equation can be switched off. The following scenarios can be studied with this approach:

1. Flame front propagation inside the crevice by setting $\overline{\dot{\omega}}_{\text{Crevice}} = \rho_u S_l \Sigma_{\text{gen}}$
2. The flame is quenched inside the crevice by setting $\overline{\dot{\omega}}_{\text{Crevice}} = 0$ and solely considering the molecular and turbulent diffusion and convective transport of $\widetilde{c}$

9.4 Numerical Solution

The engine grid has to maintain high mesh quality (low skewness, high orthogonality) for high-order numerical schemes for a LES. In order to avoid mesh-induced errors by highly deformed cells, the engine cycle is split into predefined intervals, each with good quality. At the end of each interval, the results are mapped onto a new grid, on which the simulation continues. The grid interval size was set to 5°CA. Fully automated mesh generation based on OpenFOAM's internal grid generator is used to build the individual grids consisting of unstructured hexahedral cells with mesh refinement [124],[145]. Valve closure is achieved by curtains around the valve seats, which act as an internal wall. The minimum valve lift of the numerical model is 0.3 mm. Inside the crevice gap the average cell size is 0.2 mm, at

the valve seat 0.125 mm (minimum valve lift), around the spark plug 0.2 mm, and inside the ports and cylinder 0.85 mm. The total domain consists of 1.1 million cells at TDC and 2.2 million cells at BDC, including 100 mm of the intake and 200 mm of the exhaust ports. Figure 9.7 shows a grid cut through the intake and exhaust valves at TDC.

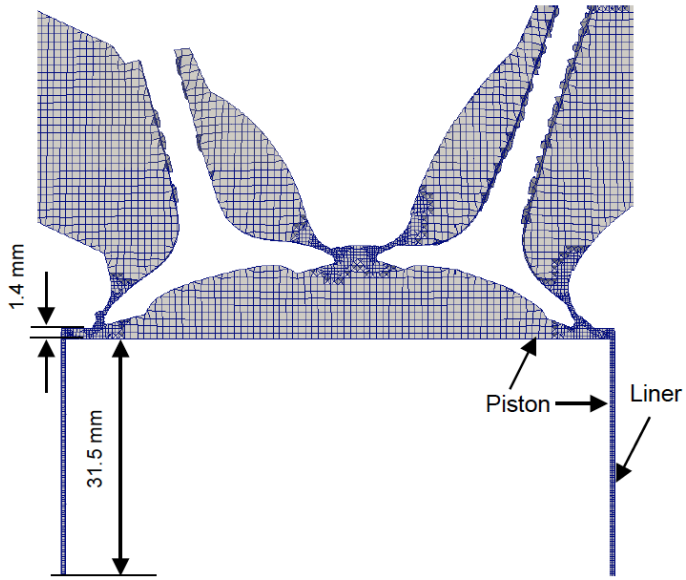

Figure 9.7: Section of the computational domain for the optical engine, including the crevice volume. The grid was locally refined from 0.85 mm to 0.125 mm.

For the motion of the internal grid points a Laplace equation for a cell velocity field u_{cell} is solved based on the boundary motion of the piston and valves [96]. The mesh-motion Laplace equation incorporates a mesh diffusion constant γ, which is used to control the mesh motion.

$$\frac{\partial}{\partial x_j}\left(\gamma \frac{\partial u_{\text{cell,j}}}{\partial x_j}\right) = 0 \tag{9.15}$$

The velocity field obtained this way is then used to calculate the position of the new grid points.

9.5 Simulation Setup

The simulations are conducted with OpenFOAM-2.3.x, which features a parallelized mapping procedure. An implicit, second-order backward scheme is applied for the time discretization. The convective scalar-fluxes are treated with a TVD-scheme, using the Sweby limiter [179]. For the momentum equation a CDS-scheme is taken, since a TVD-scheme is too dissipative for a LES. However, the lower numerical dissipation of the CDS- scheme can yield stability problems at high flow velocities. Therefore, a switch between the CDS and TVD-scheme is implemented as a function of the Mach number. In regions of high flow velocities (Ma $>$ 0.5) the TVD-scheme will be applied for the momentum equation and for the rest of the domain the CDS-scheme [145].

This chapter was previously published [92] and is reprinted with permission of the journal

The simulation is started at TDC, when the intake and exhaust valves are opened. A time-varying absolute pressure boundary condition is imposed at the intake and exhaust ports, with the pressure taken from the measurements. The intake temperature is fixed at 300 K and for all walls a temperature of 333 K is imposed. A non-slip velocity boundary condition is applied at all walls. The engine is running at 1500 rpm. For simplicity, a stoichiometric homogeneously distributed air/fuel mixture with a fuel mass fraction of 0.0623 is initialized inside the complete combustion chamber. The ignition kernel has a diameter of 2 mm. Inside the ignition volume, the reaction source term $\overline{\dot{\omega}}_{\text{ignition}}$ is set to 8000 kg $\text{m}^{-3}\text{s}^{-1}$. The ignition timing was set to the nominal start of ignition in the experiments, 45°CA before TDC. From the start of ignition the reaction source term $\overline{\dot{\omega}}_{\text{ignition}}$ is kept constant for 1°CA, ensuring that the flame kernel does not extinguish. A comparison of the flame penetration was carried out based on two simulations of the same cycle with and without reaction source term inside the crevice gap.

9.6 Results

In Figure 9.8, the LES of one cycle is qualitatively compared to the high-speed visualization by rendering an iso-surface of the reaction progress variable. Inside the crevice, the reaction source term $\overline{\dot{\omega}}_{\text{Crevice}}$ was "switched on", thus representing the case of a burning flame inside the piston-top land crevice. In the simulation the flame brush is penetrating into the crevice shortly before TDC, which is about 5°CA later than in the experiment. However, the structure of the flame given by the simulation and the experiment is surprisingly similar inside the top-land crevice. Single flame "islands" along the edge of the piston penetrate into the crevice and combine later to form a closed surface. The formation of the distinct "islands" around the crevice can be explained by Figure 9.9, where it can be seen that the flame is not uniformly propagating towards the piston, thus reaching the entrance of the crevice at different times and locations.

In a next step, the simulation was restarted when the flame brush reached the crevice entrance, but this time, in the crevice the reaction source term $\overline{\dot{\omega}}_{\text{Crevice}}$ was "switched off". Thus, only the transport of the progress variable $\widetilde{c}$ is considered, i.e., the flame is perfectly quenched by the crevice. In Figure 9.10, the location of flame inside the crevice is shown just after TDC in the case with and without the reaction source $\overline{\dot{\omega}}_{\text{Crevice}}$.
The flame has entered the crevice at the same location for both cases, but now extends less deep for the case without reaction source term. In the simulation, the flow reaches velocities up to 25 m/s at TDC near the entrance of the crevice gap. Therefore, for the given combustion phasing, the boundary between burned and unburned gas would be pushed into the crevice for any turbulent flame speed that could realistically be achieved at this low-speed operating point (1500 rpm). Additionally, the morphological appearance of this interface in experiment and simulation is consistent with an actively burning flame.

In Figure 9.11 the progress variable at the outer wall is shown for the case with and without source term. The light region denotes the burned gas and the black color the remaining unburned charge. In the case with source term the "flame islands" come closer together, where they do not seem to join in the case without reaction source term. The complete merging of the "flame islands" was also observed in the high-speed visualization (see Figure 9.4), which supports our conclusion of an actively burning flame in the crevice.

The presence or absence of a flame in the crevice changes the flow from or into the crevice.

This chapter was previously published [92] and is reprinted with permission of the journal

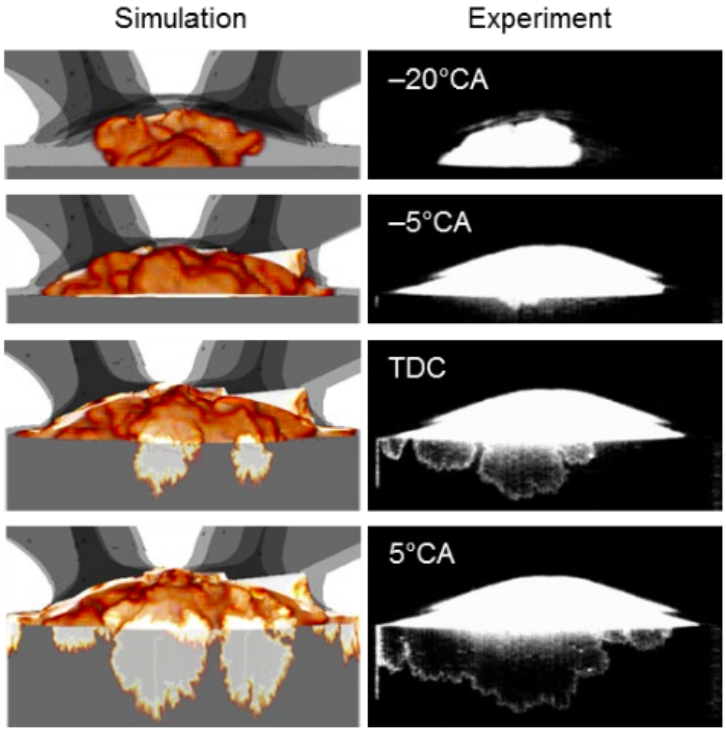

Figure 9.8: Simulation (left): Rendering of an iso-surface of the reaction progress variable. Experiment (right): High- speed visualization of visible chemiluminescence.

Figure 9.11 quantifies this with data from the simulation. Shown here is the density-weighted average vertical component of the gas velocity in the crevice just below the top of the piston crown. The data have been conditioned on the progress variable, thus distinguishing between burned and unburned mixture.

In addition to the cases discussed so far we also evaluated a motored case for reference. As expected, the corresponding (green) trace is symmetric with respect to zero velocity at TDC. During compression, the average velocity is always negative, as the mixture is pushed into the constant-volume crevice, while in the expansion stroke outgassing takes place.

In the fired cases, the velocity magnitude increases beyond this compression-induced velocity as the combustion-induced expansion in the cylinder is pushing gas into the crevice. Outgassing does take place, but only after TDC. Shortly before TDC, the flame reaches the crevice. Within a few degrees crank angle, the crevice-quenched case (reaction term switched off), represented in Figure 9.12a, significantly differs from the case with reaction in the crevice, Figure 9.12b. Without reaction, burned as well as unburned mixture is pushed into the crevice by the still ongoing combustion-induced gas expansion in the bulk of the cylinder. Outgassing starts at 11°CA. At first, all of the outflowing crevice gas is burned mixture, but a few degrees CA later unburned mixture is ejected, too, eventually comprising the entire outflow. This temporal sequence indicates that in the perfectly quenched crevice the pockets of burned gas on average are not pushed in very far. The maximum circumference-averaged outgassing velocities are between 5 and 10 m/s, but the precision of these values should not be over-estimated, given the poor grid resolution in

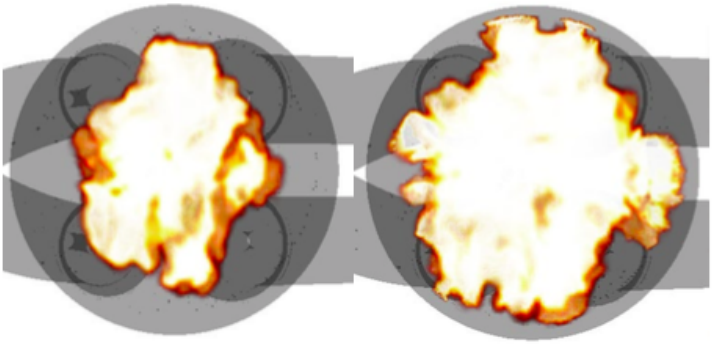

Figure 9.9: Rendering of an iso-surface of the simulation's reaction progress variable at -10°CA (left) and at TDC (right). View from the bottom.

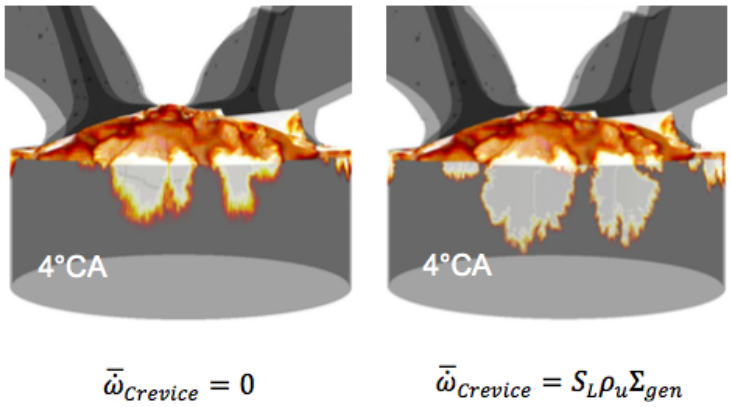

Figure 9.10: Flame penetration with zero reaction source term (left) compared to flame penetration with source term in the crevice gap (right) at 4°CA after TDC.

the crevice.

When reaction is allowed to proceed in the crevice, combustion-induced expansion is not only taking place in the bulk, but also in the crevice. Thus, at 5°CA after TDC, the average flow direction reverses earlier than without reaction. Averaged over all locations in which the crevice entrance contains burned mixture, there is never much inflow of burned mixture. (The fact that the burned velocity is almost exactly zero for an extended time is probably coincidence, depending combustion phasing and flame speed). However, as in the crevice-quenched case, when outgassing starts, almost immediately the entire outflow is burned mixture, indicating that in this simulation significant combustion occurs in the crevice. At about 17 m/s, the maximum average outflow velocity is much higher than in the quenched case, and it occurs later, too. This implies that crevice combustion is still taking place late in the simulated cycle.

9.7 Conclusions

High-speed visualizations in a spark ignition research engine showed a luminous front inside the top-land crevice volume. The structure and its propagation resembled that of a wrinkled flame inside the crevice - rather than just a luminous zone of residual gases that

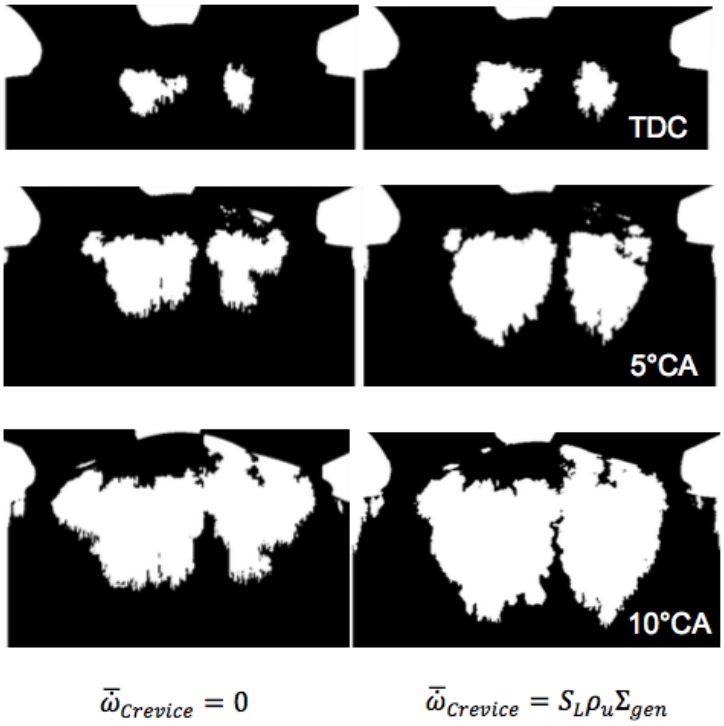

Figure 9.11: Flame penetration in the simulation at the wall at 10°CA. Left: without reaction source term. Right: with reaction source term. Note that these are not volume renderings, as in Figure 9.8 through Figure 9.10. Instead, just the layer of cells next to the wall is represented here.

are pushed into the crevice. The available literature supported our tentative conclusion that there is an actively burning flame inside the crevice. A large-eddy simulation was conducted, which allowed comparing scenarios with and without reaction source term. They revealed that at 4°CA after TDC the flame has penetrated almost twice as deep into the crevice than it has without reaction source term. Single "flame islands" are formed near the edge of the piston and penetrate into the crevice, where they meet and merge. This is consistent with the observations made in the experiments.

Clearly, the above results are far from generally applicable: Optically accessible research engines of the Bowditch-type feature crevice dimensions that are heavily modified from production engines, and the materials and internal cooling also is not representative of all-metal engines. The combustion phasing, which is difficult to control in an optical engine, happened to be such that the flame front reached the crevice within a few degrees crank-angle around TDC. We have not systematically explored variations of the phasing. The same is true of variations in fuel/air-ratio or fuel composition.

Including the top-land crevice in numerical simulations can be expensive, but the current work indicates that at least some validated crevice model may be necessary to predict emissions or even heat release with high fidelity. The top-land crevice in production engines is much smaller than the one investigated here, but with current emissions legislation very small amounts of cold-start UHC need to be predicted and eliminated.

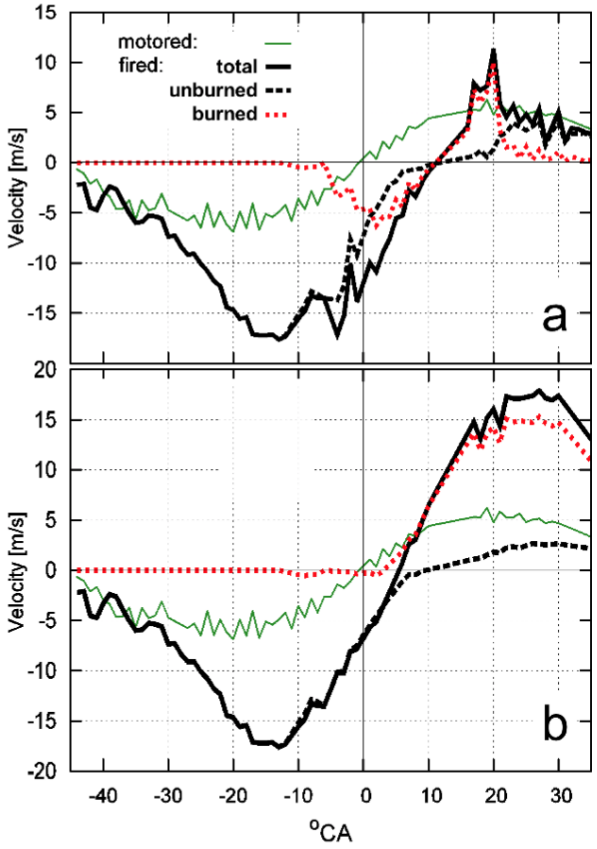

Figure 9.12: Circumference-averaged crevice outgassing velocities in the simulation. (a) without, (b) with source term in the crevice. For reference, a motored cycle (no source term anywhere in the domain) is also shown.

10

Conclusion

This is the final chapter of this thesis, where the main achievements are presented and summarised. Finally, an outlook on future work is given.

10.1 Summary

Within the scope of this work, a simulation strategy for large eddy simulations of cold flow and reactive engine simulations was developed. The main achievements are summarised in the following list:

- A generic grid-generation and mesh-motion approach for engines with inclined valves including a mapping-based simulation strategy was developed and implemented (see chapter 4.9).
- A spatial discretization scheme was proposed to overcome stability problems at the valve opening and closing events, while maintaining sufficient accuracy for LES (see chapter 4.2).
- The numerical approach was successfully validated for cold-flow simulations against PIV and MRV measurements (see chapter 6).
- A criterion for estimating the number of cycles needed in a simulation was proposed (see chapter 6.4).
- A visualization strategy for the three-dimensional tumble flow was developed based on a 2D-vortex-centre-identification algorithm (see chapters 6.4.5 and 8.5.2).
- Auto-correlation curves were calculated based on a new velocity, that considered coherent flow structures (not only the turbulent fluctuations) and were used to characterise the tumble break-down (see chapters 6.4.6 and 8.5.3).
- The influence of the valve seat region on the in-cylinder flow field and the combustion was studied (see chapter 8.5.4).
- The flame penetration inside the large piston top-land crevice of optically accessible research engines was investigated (see chapter 9).
- Multi-cycle simulations with combustion and internal gas recirculation were performed using a new algebraic flame-surface-density model (see chapter 7.5.3).

The developed simulation workflow (see section 4.9) has been applied to different engine geometries. One of the key-elements for the success of this approach is that the meshing works automatically and only a STL representation of the engine is needed. However, a drawback of the automated meshing approach is that the grid quality is difficult to control, especially in the valve seat region for very small valve lifts. A high grid quality can be ensured by decreasing the mesh motion interval. Within this work, a fixed interval of 5°CA worked well, which is quite low compared to the interval size from other simulations [54], but an automated meshing was considered to be more important than the number of the intervals. Due to the large number of intervals, it is very important that the mapping is (a) conservative, (b) a good overlap between the source and the target grids is achieved and (c) works in parallel. A positive effect of the short intervals is that the LES filter width does not change significantly.

The opening and the closing of the valves can lead to oscillations due to high velocities and steep gradients, while using central differencing for the convective fluxes of the momentum equation, which is necessary for LES. Therefore, a switch based on the Mach-number was implemented, to locally change the discretisation scheme of the momentum equation. It was decided for $Ma > 0.3$ to switch to a TVD-scheme, where compressibility effects become important. Technically, it is only applied in the valve seat region at small valve lifts, where the rest of the domain can still benefit from the low numerical dissipation and high accuracy of the CDS-scheme. This method allows a stable solution and can be regarded as a good compromise.

The combination of the CDS-scheme and a TVD-scheme on the equidistant cubic cells inside the combustion chamber has turned out to be a good choice, based on the good qualitative and quantitative agreements of the LES simulations of the wall-guided head configuration compared to PIV and MRV flow measurements (see chapter 6.4). The standard Smagorinsky model performed very well and no significant changes to the σ-model were observed, except for the turbulent viscosity at the walls. A grid resolution of 1 mm has shown to provide a good compromise between the accuracy and the computational cost with a minimum valve lift of 0.3 mm and a resolution of 0.125 mm inside the valve seat. No turbulent fluctuations were imposed at the inlet boundary, which are usually necessary for an LES. Since most of the turbulence is generated in the shear layers, when the flow enters the cylinder, the disregard of the turbulent fluctuations might not be of big importance.

For the comparison with the experimental findings, the simulated flow fields were phase-averaged. Up to 20 cycles were used to calculate the mean values and the ensemble-averaged fluctuations. For the mean velocities, the number of cycles appeared to be sufficient, but the fluctuations required more cycles. Since in the past, different numbers of cycles have been simulated without a rational explanation, a criterion for choosing an appropriate number of cycles needed for the simulation was proposed. The criterion developed within this thesis is therefore a first attempt to have a direct assessment if the number of cycles is sufficient. Thus, the proposed criterion can help to save time and highlight those regions that require further attention. It has to be stressed, that the criterion requires experimental data.

A visualisation strategy was developed to track the 3D tumble flow and enabled a better understanding of the tumble formation. Most of the time the tumble is only regarded in the tumble-symmetry plane or by integral numbers, e.g. the tumble-number. With this strategy the cycle-to-cycle fluctuations of the 3D tumble volume can be observed, where some cycles had a rather symmetric tumble volume and other cycles had an asymmetric

shape. Since the algorithm relies on a 2D-vortex centre tracking algorithm, the sampling planes have to be placed parallel to each other - only one rotational axis for the tumble. It was shown for two different cylinder head configurations, that this limitation can be used to find regions, where the tumble vortex starts to change its rotational axis.

The visualization of the tumble enabled drawing only qualitative conclusions about the flow behaviour and therefore a new method to quantify the tumble was proposed. Since the tumble flow is considered to be a coherent vortex, which changes its size and the length scales, a tool based on two-point auto-correlations seemed to be appropriate for the tumble quantification. The calculation of the length scales, however, is based on the fluctuating velocity, which is not easy to calculate due to CCV and the required number of cycles to simulate (hundreds or even thousands). Therefore, a new definition of the velocity fluctuation is proposed, which contains information on the coherent flow structures (see chapter 6.4.6). The new velocity fluctuations were used for the calculation of the auto-correlation coefficients and the integral length scales for horizontal lines during the compression stroke. Interesting observations were made after only 15 to 20 cycles. Herby, a two-stage decay of the length scales was observed, where the first plateau was assigned to the free motion of the tumble and the first decay was assigned to the attachment of the tumble to the walls and the upwards-coming piston. Within the second plateau and decay, the tumble break-up took place, which became very evident in the plots of the auto-correlation curves. The shapes of the auto-correlation curves allowed to better distinguish between the tumble break-up and the tumble compression, where the curves stayed rather smooth during the compression and started oscillating heavily at the onset of the tumble break-up. The two developed post-processing methods (tumble visualisation and auto-correlations) were tested based on the flow fields of two different cylinder head geometries. Clear differences between the flow fields could be quickly detected and clearly presented with the two post-processing methods, where surprisingly, a big difference between the two flow fields was observed - compared to the rather small geometric variations (see chapter 8.5.3). The methods can be used to quickly assess the design of a new cylinder-head.

Finally, combustion was studied by an FSD-approach. The cold-flow velocity fields were directly used to initialize the combustion simulations, but real multi-cycle simulations were also carried out. Good results for the pressure and the flame position using the Keppeler FSD-model were obtained during the free-flame propagating phase by the multi-cycle approach. For the single-cycle approach, the peak-pressure was mostly over-predicted, which could be assigned to neglecting the internal gas recirculation, which lowered the laminar flame speed and the energy content of the fresh charge. Around 15% of the burnt gases from the previous cycle stayed or streamed back into the cylinder. The flame propagation phase seemed to work reasonably well using the FSD-approach compared to the morphology and the position of the flame given by the experiment. However, a big disadvantage of the used combustion model was its inability to predict the initial flame kernel growth correctly. At the walls, no quenching or reduction of the flame wrinkling towards the walls was considered, which was also responsible for the over-prediction of the peak-cylinder pressure.

An interesting observation of the combustion progress was made, where the combustion slowed down rapidly at a point where around 90% of the air/fuel mixture was burned. Due to the lowered piston-ring-package in optically accessible engines, a big crevice volume was created and changed the combustion phasing completely. The slow combustion could be assigned to flame propagation inside the piston top-land. Obviously, it is a feature of the

optically accessible engines and does not appear to such an extent in a real engine, but it cannot be neglected for the simulation of optically accessible research engines, where an impact on the in-cylinder pressure was already observed under motored operating conditions (see chapter 7.5.1). The piston top-land crevice increases the surface-to-volume ratio and therefore amplifies the heat exchange during the compression and the expansion stroke. Neglecting the piston top-land crevice volume has led to an over-prediction of the peak in-cylinder pressure of roughly 2 bar (see figure 7.2).

10.2 Outlook

As a next step, more extensive grid sensitivity studies should be carried out, in particular in the valve seat region and upper cylinder head. High shear stresses of the intake jet with the surrounding in-cylinder gas are responsible for the generation of the turbulence and dominating the evolution of tumble development. An alignment of the cells with the intake jet should be considered as well. These investigations could be carried out together with different sub-grid scale turbulence models, such as the Sigma or WALE models, the usage of turbulent fluctuations at the inlet and a variation of the engine speed.
For the comparison with the experiments, flow fields have to be compared in the late compression stroke and at TDC, where the in-cylinder temperature also needs to be predicted precisely, as it has an impact on the viscosity, hence on the turbulence. Comparisons so far were only made in the early compression and in the intake stroke, where the in-cylinder temperature is rather dominated by the inlet conditions.
The number of cycles presented in this work was enough to capture the most important flow features, but for the study of CCV the number of simulated cycles is not sufficient. Therefore, more cycles need to be calculated, on which the tumble visualization and the auto-correlation coefficients could be applied to find correlations of the shape and length scales to CCV.In a further step, the tumble development and shape could be correlated to combustion. Therefore, it is inevitable to model the ignition phase more acurately, which is also highly influenced by CCV. Algebraic FSD-models are not able to predict the ignition process, because they assume an equilibrium between the production and destruction of the flame surface density. Therefore, a better choice could be the ECFM-LES model combined with the Imposed Stretch Spark Ignition Model (ISSIM). Furthermore, during the last stage of the combustion process, the flame quenching to the walls and the reduction of the flame surface need to be taken into account, which will improve the combustion phasing of the peak in-cylinder pressure and the over-prediction of the pressure during the expansion stroke.

Bibliography

[1] Ansys - Commercial CFD code. http://www.ansys.com. Accessed: 2016-07-22

[2] AVBP - CFD code of the research centre CERFACS. http://www.cerfacs.fr/avbp7x/index.php. Accessed: 2017-01-22

[3] AVL Fire - Commercial CFD code dedicated to combustion engines. https://www.avl.com/fire2. Accessed: 2016-07-22

[4] Convergence Science - Commercial CFD code dedicated to combustion engines. https://convergecfd.com. Accessed: 2016-07-22

[5] Esi Group - Leading Innovator in Virtual Prototyping Software and Services. https://www.esi-group.com. Accessed: 2016-07-22

[6] Internal Combustion Engine Group of Politecnico di Milano. http://www.engines.polimi.it/index.php. Accessed: 2016-07-23

[7] KIVA - Commercial CFD code dedicated to combustion engines. https://www.erc.wisc.edu/modeling/kiva.php. Accessed: 2016-07-22

[8] OICA - Organisation Internationale des Constructeurs d'Automobiles. http://www.oica.net/category/production-statistics/2015-statistics/. Accessed: 2016-12-16

[9] OpenFOAM - Free CFD Software. http://www.openfoam.com. Accessed: 2017-01-16

[10] OpenFOAM Foundation. http://openfoam.org. Accessed: 2017-01-16

[11] Star-CD - Commercial CFD code. http://www.cd-adapco.com. Accessed: 2016-07-22

[12] Aceves, S.M., Flowers, D.L., Espinosa-Loza, F., Martinez-Frias, J., Dibble, R.W., Christensen, M., Johansson, B., Hessel, R.P.: Piston-liner crevice geometry effect on HCCI combustion by multi-zone analysis. Tech. rep., SAE Technical Paper (2002). DOI 10.4271/2002-01-2869

[13] Adamczyk, A., Kaiser, E., Lavoie, G.: A combustion bomb study of the hydrocarbon emissions from engine crevices. Combustion science and technology **33**(5-6), 261–277 (1983)

[14] Alkidas, A.: Combustion-chamber crevices: the major source of engine-out hydrocarbon emissions under fully warmed conditions. Progress in energy and combustion science **25**(3), 253–273 (1999)

[15] Alkidas, A., Drews, R., Miller, W.: Effects of Piston Crevice Geometry on the Steady-State Engine-Out Hydrocarbons Emissions of a SI Engine. Tech. rep., SAE Technical Paper (1995). DOI 10.4271/952537

[16] Angelberger, C., Veynante, D., Egolfopoulos, F., Poinsot, T.: Large eddy simulations of combustion instabilities in premixed flames. In: Proc. of the Summer Program, pp. 61–82. Citeseer (1998)

[17] Auriemma, M., Corcione, F., Macchioni, R., Valentino, G.: Assessment of k-ε Turbulence Model in KIVA-II by in-Cylinder LDV Measurements. Tech. rep., SAE Technical Paper (1995). DOI 10.4271/952385

[18] Baum, E., Peterson, B., Böhm, B., Dreizler, A.: On the validation of les applied to internal combustion engine flows: Part 1: Comprehensive experimental database. Flow, Turbulence and Combustion **92**(1), 269–297 (2014). DOI 10.1007/s10494-013-9468-6

[19] Baumann, M., di Mare, F., Janicka, J.: On the validation of large eddy simulation applied to internal combustion engine flows part ii: Numerical analysis. Flow, Turbulence and Combustion **92**(1), 299–317 (2014). DOI 10.1007/s10494-013-9472-x

[20] Bensing, D.: Aufbau eines optisch zugänglichen Einzylinder-Viertaktmotors und charakterisierende Messungen. Ph.D. thesis, Universität Duisburg-Essen, Fakultät für Ingenieurwissenschaften, Maschinenbau und Verfahrenstechnik (2014)

[21] Blender Online Community: Blender - A 3D modelling and rendering package. Blender Foundation, Blender Institute, Amsterdam (2016). URL `http://www.blender.org`

[22] Boam, D., Finlay, I., Biddulph, T., Ma, T., Lee, R., Richardson, S., Bloomfield, J., Green, J., Wallace, S., Woods, W., et al.: The sources of unburnt hydrocarbon emissions from spark ignition engines during cold starts and warm-up. Proceedings of the Institution of Mechanical Engineers, Part D: Journal of Automobile Engineering **208**(1), 1–11 (1994)

[23] Boger, M., Veynante, D., Boughanem, H., Trouvé, A.: Direct numerical simulation analysis of flame surface density concept for large eddy simulation of turbulent premixed combustion. Symposium (International) on Combustion **27**(1), 917 – 925 (1998). DOI 10.1016/S0082-0784(98)80489-X

[24] Bourhis, G., Solari, J.P., Dauphin, R.: Measurement of RON Requirements for Turbocharged SI Engines: One Step to the Octane on Demand Concept. In: SIA POWERTRAIN - The low CO2 spark ignition engine and its hybridization. SIA, Versailles, France (2015)

[25] Boussinesq, J.: Essai sur la théorie des eaux courantes. Imprimerie nationale (1877)

[26] Bowditch, F.W.: Cylinder and piston assembly (1960). US Patent 2,919,688

[27] Bray, K., Champion, M., Libby, P.A.: Pre-mixed flames in stagnating turbulence: Part V - Evaluation of models for the chemical source term. Combustion and Flame **127**(1 - 2), 2023 – 2040 (2001). DOI 10.1016/S0010-2180(01)00304-2

[28] Bruneaux, G., Poinsot, T., Ferziger, J.: Premixed flame–wall interaction in a turbulent channel flow: budget for the flame surface density evolution equation and modelling. Journal of Fluid Mechanics **349**, 191–219 (1997)

[29] Böhm, B.: Private communication at the Fifth Darmstadt-Engine-Workshop (2016). URL http://www.rsm.tu-darmstadt.de/rsm

[30] Bücker, I., Karhoff, D.C., Klaas, M., Schröder, W.: Stereoscopic multi-planar PIV measurements of in-cylinder tumbling flow. Experiments in Fluids **53**(6), 1993–2009 (2012). DOI 10.1007/s00348-012-1402-5

[31] Buhl, S., Hartmann, F., Hasse, C.: Identification of Large-Scale Structure Fluctuations in IC Engines using POD-Based Conditional Averaging. Oil & Gas Science and Technology–Revue d'FP Energies nouvelles **71**(1), 1 (2016). DOI 10.2516/ogst/2015021

[32] Burcat, A., Ruscic, B.: Third millenium ideal gas and condensed phase thermochemical database for combustion with updates from active thermochemical tables. Argonne National Laboratory Argonne, IL (2005). DOI 10.2172/925269

[33] Butler, T., O'Rourke, P.: A numerical method for two dimensional unsteady reacting flows. In: Symposium (International) on Combustion, vol. 16, pp. 1503–1515 (1977). DOI 10.1016/S0082-0784(77)80432-3

[34] Candel, S.M., Poinsot, T.J.: Flame stretch and the balance equation for the flame area. Combustion Science and Technology **70**(1-3), 1–15 (1990). DOI 10.1080/00102209008951608

[35] Chakraborty, N., Cant, R.: A priori analysis of the curvature and propagation terms of the flame surface density transport equation for large eddy simulation. Physics of Fluids **19**(10), 105,101–105,101 (2007). DOI 10.1063/1.2772326

[36] Chakraborty, N., Klein, M.: A priori direct numerical simulation assessment of algebraic flame surface density models for turbulent premixed flames in the context of large eddy simulation. Physics of Fluids **20**(8) (2008). DOI 10.1063/1.2969474

[37] Chakraborty, N., Klein, M.: A priori direct numerical simulation assessment of algebraic flame surface density models for turbulent premixed flames in the context of large eddy simulation. Physics of fluids **20**, 085,108 (2008)

[38] Charlette, F., Meneveau, C., Veynante, D.: A power-law flame wrinkling model for LES of premixed turbulent combustion Part I: non-dynamic formulation and initial tests. Combustion and Flame **131**(1), 159–180 (2002). DOI 10.1016/S0010-2180(02)00400-5

[39] Chauvy, M., Delhom, B., Reveillon, J., Demoulin, F.X.: Flame/wall interactions: laminar study of unburnt HC formation. Flow, Turbulence and Combustion **84**(3), 369–396 (2010). DOI 10.1007/s10494-009-9245-8

[40] Colin, O., Benkenida, A., Angelberger, C.: 3D modeling of mixing, ignition and combustion phenomena in highly stratified gasoline engines. Oil & gas science and technology **58**(1), 47–62 (2003). DOI /10.2516/ogst:2003004

[41] Colin, O., Ducros, F., Veynante, D., Poinsot, T.: A thickened flame model for large eddy simulations of turbulent premixed combustion. Physics of Fluids **12**(7), 1843–1863 (2000). DOI 10.1063/1.870436

[42] Colin, O., Truffin, K.: A spark ignition model for large eddy simulation based on an FSD transport equation (ISSIM-LES). Proceedings of the Combustion Institute **33**(2), 3097–3104 (2011). DOI 10.1016/j.proci.2010.07.023

[43] Corcione, F.E., Valentino, G.: Turbulence length scale measurements by two-probe-volume lda technique in a diesel engine. In: SAE Technical Paper. SAE International (1990). DOI 10.4271/902080

[44] Daniel, W.: Flame quenching at the walls of an internal combustion engine. Symposium (International) on Combustion **6**(1), 886 – 894 (1957). DOI 10.1016/S0082-0784(57)80125-8

[45] Davidson, P.: Turbulence: an introduction for scientists and engineers. Oxford University Press (2015)

[46] Demirdžić, I., Lilek, Ž., Perić, M.: A collocated finite volume method for predicting flows at all speeds. International Journal for Numerical Methods in Fluids **16**(12), 1029–1050 (1993). DOI 10.1002/fld.1650161202

[47] Demirdžić, I., Perić, M.: Space conservation law in finite volume calculations of fluid flow. International journal for numerical methods in fluids **8**(9), 1037–1050 (1988). DOI 10.1002/fld.1650080906

[48] Ding, C.: Laserbasierte Untersuchung der Flammenausbreitung in einem optisch zugänglichen direkt-einspritzenden Ottomotor. Master Thesis, Technische Universität Darmstadt (2012)

[49] Drake, M., Haworth, D.: Advanced gasoline engine development using optical diagnostics and numerical modeling. Proceedings of the Combustion Institute **31**(1), 99–124 (2007). DOI 10.1016/j.proci.2006.08.120

[50] Dreizler, A., Böhm, B.: Advanced laser diagnostics for an improved understanding of premixed flame-wall interactions. Proceedings of the Combustion Institute **35**(1), 37–64 (2015). DOI 10.1016/j.proci.2014.08.014

[51] Driscoll, J.F.: Turbulent premixed combustion: Flamelet structure and its effect on turbulent burning velocities. Progress in Energy and Combustion Science **34**(1), 91–134 (2008). DOI 10.1016/j.pecs.2007.04.002

[52] Druault, P., Guibert, P., Alizon, F.: Use of proper orthogonal decomposition for time interpolation from PIV data. Experiments in fluids **39**(6), 1009–1023 (2005). DOI 10.1007/s00348-005-0035-3

[53] Duclos, J., Colin, O.: Arc and kernel tracking ignition model for 3D spark-ignition engine calculations. In: Fifth Int. Symp. on Diagnostics, Modelling of Combustion in Internal Combustion Engines (COMODIA), pp. 343–350 (2001)

[54] Enaux, B., Granet, V., Vermorel, O., Lacour, C., Pera, C., Angelberger, C., Poinsot, T.: LES study of cycle-to-cycle variations in a spark ignition engine. Proc. Combust. Inst **33**(2), 3115–3122 (2011). DOI 10.1016/j.proci.2010.07.038

[55] Enaux, B., Granet, V., Vermorel, O., Lacour, C., Thobois, L., Dugué, V., Poinsot, T.: Large eddy simulation of a motored single-cylinder piston engine: numerical strategies and validation. Flow, turbulence and combustion **86**(2), 153–177 (2011). DOI 10.1007/s10494-010-9299-7

[56] Fansler, T.D., Wagner, R.M.: Cyclic dispersion in engine combustion-introduction by the special issue editors (2015)

[57] Favre, A.: The equations of compressible turbulent gases. Tech. rep., DTIC Document (1965)

[58] Fendell, F., Fink, S., Feldman, P.: A Note on Unburned Hydrocarbon Emissions from Automotive Engines. Combustion Science and Technology **30**(1-6), 47–57 (1983). DOI 10.1080/00102208308923611

[59] Ferziger, J.H., Peric, M.: Computational methods for fluid dynamics. Springer Science & Business Media (2012)

[60] Fontanesi, S., d'Adamo, A., Rutland, C.J.: Large-eddy simulation analysis of spark configuration effect on cycle-to-cycle variability of combustion and knock. International Journal of Engine Research **16**(3), 403–418 (2015). DOI 10.1177/1468087414566253

[61] Fontanesi, S., Paltrinieri, S., d'Adamo, A., Duranti, S.: Investigation of boundary condition and field distribution effects on the cycle-to-cycle variability of a turbocharged gdi engine using les. Oil & Gas Science and Technology–Revue d'IFP Energies nouvelles **69**(1), 107–128 (2014). DOI 10.2516/ogst/2013142

[62] Fontanesi, S., Paltrinieri, S., Tiberi, A., d'Adamo, A.: LES multi-cycle Analysis of a High Performance GDI Engine. In: SAE Technical Paper. SAE International (2013). DOI 10.4271/2013-01-1080

[63] Foucher, F., Mounaïm-Rousselle, C.: Fractal approach to the evaluation of burning rates in the vicinity of the piston in a spark-ignition engine. Combustion and flame **143**(3), 323–332 (2005). DOI 10.1016/j.combustflame.2005.06.007

[64] Freudenhammer, D., Baum, E., Peterson, B., Böhm, B., Jung, B., Grundmann, S.: Volumetric intake flow measurements of an IC engine using magnetic resonance velocimetry. Experiments in Fluids **55**(5), 1–18 (2014). DOI 10.1007/s00348-014-1724-6

[65] Freudenhammer, D., Peterson, B., Ding, C.P., Boehm, B., Grundmann, S.: The Influence of Cylinder Head Geometry Variations on the Volumetric Intake Flow Captured by Magnetic Resonance Velocimetry. SAE International Journal of Engines **8**(2015-01-1697), 1826–1836 (2015). DOI 10.4271/2015-01-1697

[66] Friedman, R., Johnston, W.: The Wall-Quenching of Laminar Propane Flames as a Function of Pressure, Temperature, and Air-Fuel Ratio. Journal of Applied Physics **21**(8), 791–795 (1950). DOI 10.1063/1.1699760

[67] Fureby, C.: A fractal flame-wrinkling large eddy simulation model for premixed turbulent combustion. Proceedings of the Combustion Institute **30**(1), 593–601 (2005). DOI 10.1016/j.proci.2004.08.068

[68] Fureby, C.: A fractal flame-wrinkling large eddy simulation model for premixed turbulent combustion. Proceedings of the Combustion Institute **30**(1), 593–601 (2005)

[69] Germano, M., Piomelli, U., Moin, P., Cabot, W.H.: A dynamic subgrid-scale eddy viscosity model. Physics of Fluids A: Fluid Dynamics (1989-1993) **3**(7), 1760–1765 (1991). DOI 10.1063/1.857955

[70] Geurts, B.J., Fröhlich, J.: A framework for predicting accuracy limitations in large-eddy simulation. Physics of Fluids **14**(6), 41–44 (2002). DOI 10.1063/1.1480830

[71] Giacomazzi, E., Bruno, C., Favini, B.: Fractal modelling of turbulent combustion. Combustion Theory and Modelling **4**(4), 391–412 (2000). DOI 10.1088/1364-7830/4/4/302

[72] Goolsby, A., Haskell, W.: Flame-quench distance measurements in a cfr engine. Combustion and Flame **26**, 105–114 (1976). DOI 10.1016/0010-2180(76)90060-2

[73] Goryntsev, D., Sadiki, A., Janicka, J.: Towards Large Eddy Simulation of Spray Combustion in Direct Injection Spark Ignition Engine. In: SAE Technical Paper. SAE International (2011). DOI 10.4271/2011-01-1884

[74] Goryntsev, D., Sadiki, A., Klein, M., Janicka, J.: Large eddy simulation based analysis of the effects of cycle-to-cycle variations on air–fuel mixing in realistic DISI IC-engines. Proc. Combust. Inst **32**(2), 2759–2766 (2009). DOI 10.1016/j.proci.2008.06.185

[75] Goryntsev, D., Stein, O., Klein, M., Janicka, J.: Characterization of cyclic fluctuations of the in-cylinder flow field of a direct injection SI engine using large eddy simulation. In: 7th Int. Congress: Engine Combustion Process, Munich, Germany, pp. 335–344 (2005)

[76] Gouldin, F., Bray, K., Chen, J.Y.: Chemical closure model for fractal flamelets. Combustion and flame **77**(3), 241–259 (1989). DOI 10.1016/0010-2180(89)90132-6

[77] Graftieaux, L., Michard, M., Grosjean, N.: Combining PIV, POD and vortex identification algorithms for the study of unsteady turbulent swirling flows. Measurement Science and Technology **12**(9), 1422 (2001)

[78] Granet, V., Vermorel, O., Lacour, C., Enaux, B., Dugué, V., Poinsot, T.: Large-eddy simulation and experimental study of cycle-to-cycle variations of stable and unstable operating points in a spark ignition engine. Combustion and Flame **159**(4), 1562–1575 (2012). DOI 10.1016/j.combustflame.2011.11.018

[79] Gülder, O.L.: Correlations of Laminar Combustion Data for Alternative S.I. Engine Fuels. In: SAE Technical Paper. SAE International (1984). DOI 10.4271/841000

[80] Hartmann, F., Buhl, S., Gleiss, F., Barth, P., Schild, M., Kaiser, S.A., Hasse, C.: Spatially resolved experimental and numerical investigation of the flow through the intake port of an internal combustion engine. Oil Gas Sci. Technol.-Rev. IFP Energies nouvelles **71**(1), 2 (2016)

[81] Haskell, W.W., Legate, C.E.: Exhaust Hydrocarbon Emissions from Gasoline Engines - Surface Phenomena. In: SAE Technical Paper. SAE International (1972). DOI 10.4271/720255

[82] Hasse, C.: Scale-resolving simulations in engine combustion process design based on a systematic approach for model development. International Journal of Engine Research **17**(1), 44–62 (2016). DOI 10.1177/1468087415597842

[83] Hawkes, E., Cant, R.: A flame surface density approach to large-eddy simulation of premixed turbulent combustion. Proceedings of the Combustion Institute **28**(1), 51–58 (2000)

[84] Hawkes, E.R., Chatakonda, O., Kolla, H., Kerstein, A.R., Chen, J.H.: A petascale direct numerical simulation study of the modelling of flame wrinkling for large-eddy simulations in intense turbulence. Combustion and flame **159**(8), 2690–2703 (2012). DOI 10.1016/j.combustflame.2011.11.020

[85] Haworth, D.: Large-eddy simulation of in-cylinder flows. Oil & Gas Science and Technology **54**(2), 175–185 (1999). DOI 10.2516/ogst:1999012

[86] Haworth, D., Jansen, K.: Les on unstructured deforming meshes: towards reciprocating ic engines (1996)

[87] Heywood, J.B.: Internal combustion engine fundamentals

[88] Hirschfelder, J., Bird, R.B., Curtiss, C.F.: Molecular theory of gases and liquids (1964)

[89] Hong, C., Chen, D.: Direct measurements of in-cylinder integral length scales of a transparent engine. Experiments in Fluids **23**(2), 113–120 (1997). DOI 10.1007/s003480050092

[90] Ishizawa, S.: An experimental study on quenching crevice widths in the combustion chamber of a spark-ignition engine. In: Symposium (International) on Combustion, vol. 26, pp. 2605–2611 (1996). DOI 10.1016/S0082-0784(96)80094-4

[91] Issa, R.I.: Solution of the implicitly discretised fluid flow equations by operator-splitting. Journal of Computational Physics **62**(1), 40–65 (1986). DOI 10.1016/0021-9991(86)90099-9

[92] Janas, P., Ribeiro, M.D., Kempf, A., Schild, M., Kaiser, S.A.: Penetration of the Flame Into the Top-Land Crevice-Large-Eddy Simulation and Experimental High-Speed Visualization. In: SAE Technical Paper. SAE International (2015). DOI 10.4271/2015-01-1907. URL `http://dx.doi.org/10.4271/2015-01-1907`

[93] Janas, P., Schild, M., S., K., Kempf, A.: Numerical simulation of flame front propagation in a spark ignition engine. Proceedings of the Europeen Combustion Institute, vol. 6 (2013)

[94] Janas, P., Wlokas, I., Böhm, B., Kempf, A.: On the Evolution of the Flow Field in a Spark Ignition Engine. Flow, Turbulence and Combustion **98**(1), 237–264 (2017). DOI 10.1007/s10494-016-9744-3

[95] Jasak, H.: Error analysis and estimation for the finite volume method with applications to fluid flows, 1996. Ph.D. thesis, University of London Imperial College (1996)

[96] Jasak, H., Tuković: Automatic mesh motion for the unstructured finite volume method. Transactions of FAMENA **30**(2), 1–20 (2006)

[97] Kaiser, S., Schild, M., Schulz, C.: Thermal stratification in an internal combustion engine due to wall heat transfer measured by laser-induced fluorescence. Proceedings of the Combustion Institute **34**(2), 2911–2919 (2013). DOI 10.1016/j.proci.2012.05.059

[98] Kashdan, J., Thirouard, B.: Optical Engines as Representative Tools in the Development of New Combustion Engine Concepts. Oil & Gas Science and Technology–Revue d'IFP Energies nouvelles **66**(5), 759–777 (2011). DOI 10.2516/ogst/2011134

[99] Kempf, A., Flemming, F., Janicka, J.: Investigation of lengthscales, scalar dissipation, and flame orientation in a piloted diffusion flame by LES. Proceedings of the Combustion Institute **30**(1), 557–565 (2005). DOI 10.1016/j.proci.2004.08.182

[100] Keppeler, R., Tangermann, E., Allaudin, U., Pfitzner, M.: LES of Low High Turbulent Combustion in an Elevated Pressure Environment. Flow, Turbulence and Combustion **92**(3), 767–802 (2014). DOI 10.1007/s10494-013-9525-1

[101] Keppeler, R., Tangermann, E., Pfitzner, M.: Exension of a large eddy simulation combustion model for high pressures and for low reynolds number flames. In: Proceedings of European Combustion Meeting, Cardiff (2011)

[102] Keskinen, J.P., Vuorinen, V., Kaario, O., Larmi, M.: Large eddy simulation of a piston–cylinder assembly: The sensitivity of the in-cylinder flow field for residual intake and in-cylinder velocity structures. Computers & Fluids **122**, 123–135 (2015)

[103] Keskinen, J.P., Vuorinen, V., Kaario, O., Larmi, M.: Influence of mesh deformation on the quality of large eddy simulations. International Journal for Numerical Methods in Fluids (2016). DOI 10.1002/fld.4215

[104] Klein, M.: An attempt to assess the quality of large eddy simulations in the context of implicit filtering. Flow, Turbulence and Combustion **75**(1-4), 131–147 (2005). DOI 10.1007/s10494-005-8581-6

[105] Klein, M., Meyers, J., Geurts, B.J.: Assessment of LES Quality Measures Using the Error Landscape Approach, pp. 131–142. Springer Netherlands, Dordrecht (2008). DOI 10.1007/978-1-4020-8578-9_11

[106] Kobayashi, H., Kawazoe, H.: Flame instability effects on the smallest wrinkling scale and burning velocity of high-pressure turbulent premixed flames. Proceedings of the Combustion Institute **28**(1), 375–382 (2000). DOI 10.1016/S0082-0784(00)80233-7

[107] Koch, J., Schmitt, M., Wright, Y.M., Steurs, K., Boulouchos, K.: LES multi-cycle analysis of the combustion process in a small SI engine. SAE International Journal of Engines **7**, 269–285 (2014). DOI 10.4271/2014-01-1138

[108] Köhler, E., Flierl, R.: Verbrennungsmotoren: Motormechanik, Berechnung und Auslegung des Hubkolbenmotors. Springer-Verlag (2007). DOI 978-3-8348-8309-4

[109] Kolmogorov, A.N.: The local structure of turbulence in incompressible viscous fluid for very large Reynolds numbers. In: Dokl. Akad. Nauk SSSR, vol. 30, pp. 301–305. JSTOR (1941)

[110] Kosmadakis, G., Pariotis, E., Rakopoulos, C.: Heat transfer and crevice flow in a hydrogen-fueled spark-ignition engine: Effect on the engine performance and NO exhaust emissions. International Journal of Hydrogen Energy **38**(18), 7477–7489 (2013). DOI 10.1016/j.ijhydene.2013.03.129

[111] Kuo, K.K.: Principles of combustion (1986)

[112] Lafossas, F.A., Castagne, M., Dumas, J.P., Henriot, S.: Development and validation of a knock model in spark ignition engines using a CFD code. Tech. rep., SAE Technical Paper (2002). DOI 10.4271/2002-01-2701

[113] Laget, O., Reveille, B., Martinez, L., Truffin, K., Habchi, C., Angelberger, C.: LES Calculations of a four cylinder engine. Tech. rep., SAE Technical Paper (2011). DOI 10.4271/2011-01-0832

[114] Launder, B.E., Spalding, D.: The numerical computation of turbulent flows. Computer Methods in Applied Mechanics and Engineering **3**(2), 269–289 (1974). DOI 10.1016/0045-7825(74)90029-2

[115] Lavoie, G.A.: Correlations of combustion data for SI engine calculations-laminar flame speed, quench distance and global reaction rates. Tech. rep. (1978). DOI 10.4271/780229

[116] Lecocq, G., Richard, S., Michel, J.B., Vervisch, L.: A new LES model coupling flame surface density and tabulated kinetics approaches to investigate knock and pre-ignition in piston engines. Proceedings of the Combustion Institute **33**(2), 3105–3114 (2011). DOI 10.1016/j.proci.2010.07.022

[117] Legier, J.P., Poinsot, T., Veynante, D.: Dynamically thickened flame les model for premixed and non-premixed turbulent combustion. In: Proc. of the summer program, pp. 157–168 (2000)

[118] Leonard, S., Terracol, M., Sagaut, P.: Commutation error in LES with time-dependent filter width. Computers & Fluids **36**(3), 513–519 (2007). DOI 10.1016/j.compfluid.2005.06.010

[119] Li, W., Li, Y., Wang, T., Jia, M., Che, Z., Liu, D.: Investigation of the Effect of the In-Cylinder Tumble Motion on Cycle-to-Cycle Variations in a Direct Injection Spark Ignition (DISI) Engine Using Large eddy simulation (LES). Flow, Turbulence and Combustion pp. 1–31 (2016). DOI 10.1007/s10494-016-9773-y

[120] Lindstedt, R., VÃ¡os, E.: Modeling of premixed turbulent flames with second moment methods. Combustion and Flame **116**(4), 461 – 485 (1999). DOI http://dx.doi.org/10.1016/S0010-2180(98)00058-3

[121] Liu, K., Burluka, A., Sheppard, C.: Turbulent flame and mass burning rate in a spark ignition engine. Fuel **107**, 202–208 (2013). DOI 10.1016/j.fuel.2013.01.042

[122] Lucchini, T., D'Errico, G., Brusiani, F., Bianchi, G.: A finite-element based mesh motion technique for internal combustion engine simulations. COMODIA, Japan pp. 28–31 (2008)

[123] Lucchini, T., D'Errico, G., Jasak, H., Tukovic, Z.: Automatic mesh motion with topological changes for engine simulation. Tech. rep. (2007). DOI 10.4271/2007-01-0170.

[124] Lucchini, T., Fiocco, M., Torelli, R., D'Errico, G.: Automatic mech generation for full-cycle CFD modeling of IC engines: application to the TCC test case. Tech. rep., SAE Technical Paper (2014). DOI 10.4271/2014-01-1131

[125] Lumley, J.L.: Engines: an introduction. Cambridge University Press (1999)

[126] Ma, T., Stein, O., Chakraborty, N., Kempf, A.: A posteriori testing of algebraic flame surface density models for les. Combustion Theory and Modelling (ahead-of-print), 1–52 (2013)

[127] Ma, T., Stein, O., Chakraborty, N., Kempf, A.: A posteriori testing of the flame surface density transport equation for LES. Combustion Theory and Modelling (2013)

[128] Mahle: Motorische Erprobung, pp. 123–295. Springer Fachmedien Wiesbaden, Wiesbaden (2015). DOI 10.1007/978-3-658-09558-1_7

[129] Mandelbrot, B.B.: On the geometry of homogeneous turbulence, with stress on the fractal dimension of the iso-surfaces of scalars. Journal of Fluid Mechanics **72**(03), 401–416 (1975). DOI 10.1017/S0022112075003047

[130] di Mare, F., Goryntsev, D., Janicka, J.: LES of the flow in a DISI engine: analysis of turbulent scalar-velocity correlations. In: Proceedings of the LES4ICE International Conference. IFP (2010)

[131] di Mare, F., Knappstein, R., Baumann, M.: Application of les-quality criteria to internal combustion engine flows. Computers & Fluids **89**, 200–213 (2014). DOI 10.1016/j.compfluid.2013.11.003

[132] McAllister, S., Chen, J.Y., Fernandez-Pello, A.C.: Thermodynamics of Combustion, pp. 15–47. Springer New York, New York, NY (2011). DOI 10.1007/978-1-4419-7943-8_2

[133] Merker, G.P., Schwarz, C., Teichmann, R.: Grundlagen verbrennungsmotoren. Auflage, Vieweg+ Teubner, Wiesbaden (2009). DOI 10.1007/978-3-8348-9344-4

[134] Metghalchi, M., Keck, J.C.: Burning velocities of mixtures of air with methanol, isooctane, and indolene at high pressure and temperature. Combustion and Flame **48**, 191–210 (1982). DOI 10.1016/0010-2180(82)90127-4

[135] Min, K., Cheng, W.: Oxidation of the piston crevice hydrocarbon during the expansion process in a spark ignition engine. Combustion Science and Technology **106**(4-6), 307–326 (1995). DOI 10.1080/00102209508907784

[136] Misdariis, A., Robert, A., Vermorel, O., Richard, S., Poinsot, T.: Numerical methods and turbulence modeling for LES of piston engines: impact on flow motion and combustion. Oil & Gas Science and Technology Journal **69**, 83–105 (2014). DOI 10.2516/ogst/2013121

[137] Mittal, V., Kang, S., Doran, E., Cook, D., Pitsch, H.: LES of gas exchange in IC engines. Oil & Gas Science and Technology–Revue d'IFP Energies nouvelles **69**(1), 29–40. DOI 10.2516/ogst/2013122

[138] Montorfano, A., Piscaglia, F., Onorati, A.: An extension of the dynamic mesh handling with topological changes for LES of ICE in OpenFOAM®. Tech. rep., SAE Technical Paper (2015). DOI 10.4271/2015-01-0384

[139] Montorfano, A., Piscaglia, F., Schmitt, M., Wright, Y.M., Frouzakis, C.E., Tomboulides, A.G., Boulouchos, K., Onorati, A.: Comparison of Direct and Large Eddy Simulations of the Turbulent Flow in a Valve/Piston Assembly. Flow, Turbulence and Combustion **95**(2-3), 461–480 (2015). DOI 10.1007/s10494-015-9620-6

[140] Morse, P.M., Feshbach, H., et al.: Methods of theoretical physics, vol. 1. McGraw-Hill New York (1953)

[141] Moureau, V., Barton, I., Angelberger, C., Poinsot, T.: Towards large eddy simulation in internal-combustion engines: simulation of a compressed tumble flow. Tech. rep., SAE Technical Paper (2004). DOI 10.4271/2004-01-1995

[142] Muppala, S., Aluri, N.K., Dinkelacker, F., Leipertz, A.: Development of an algebraic reaction rate closure for the numerical calculation of turbulent premixed methane, ethylene, and propane/air flames for pressures up to 1.0 mpa. Combustion and Flame **140**(4), 257–266 (2005). DOI 10.1016/j.combustflame.2004.11.005

[143] Murayama, M., Takeno, T.: Fractal-like character of flamelets in turbulent premixed combustion. In: Symposium (International) on Combustion, vol. 22, pp. 551–559. Elsevier (1989). DOI 10.1016/S0082-0784(89)80062-1

[144] Naitoh, K., Itoh, T., Takagi, Y., Kuwahara, K.: Large eddy simulation of premixed-flame in engine based on the multi-level formulation and the renormalization group theory. Tech. rep., SAE Technical Paper (1992). DOI 10.4271/920590

[145] Nguyen, T., Janas, P., Lucchini, T., D'Errico, G., Kaiser, S., Kempf, A.: LES of flow processes in an SI engine using two approaches: OpenFOAM and PsiPhi. Tech. rep., SAE Technical Paper (2014). DOI 10.4271/2014-01-1121

[146] Nguyen, T.M., Proch, F., Wlokas, I., Kempf, A.M.: Large eddy simulation of an internal combustion engine using an efficient immersed boundary technique. Flow, Turbulence and Combustion **97**(1), 191–230 (2016). DOI 10.1007/s10494-015-9683-4

[147] Nicoud, F., Ducros, F.: Subgrid-scale stress modelling based on the square of the velocity gradient tensor. Flow, Turbulence and Combustion **62**(3), 183–200 (1999). DOI 10.1023/A:1009995426001

[148] Nicoud, F., Toda, H.B., Cabrit, O., Bose, S., Lee, J.: Using singular values to build a subgrid-scale model for large eddy simulations. Physics of Fluids **23**(8) (2011). DOI 10.1063/1.3623274

[149] North, G., Santavicca, D.: The fractal nature of premixed turbulent flames. Combustion Science and Technology **72**(4-6), 215–232 (1990). DOI 10.1080/00102209008951648

[150] Payri, F., Olmeda, P., Martin, J., Garcia, A.: A complete 0D thermodynamic predictive model for direct injection diesel engines. Applied Energy **88**(12), 4632–4641 (2011). DOI 10.1016/j.apenergy.2011.06.005

[151] Peters, N.: Turbulent Combustion. Cambridge University Press (2000)

[152] Pettit, M., Coriton, B., Gomez, A., Kempf, A.: Large-eddy simulation and experiments on non-premixed highly turbulent opposed jet flows. Proc. Combust. Inst **33**(1), 1391–1399 (2011). DOI 10.1016/j.proci.2010.06.140

[153] Piscaglia, F., Montorfano, A., Onorati, A.: Towards the LES simulation of IC Engines with parallel topologically changing meshes. SAE Int. J. Engines **6**(2), 926–940 (2013). DOI 10.4271/2013-01-1096

[154] Piscaglia, F., Montorfano, A., Onorati, A., Brusiani, F.: Boundary conditions and sgs models for LES of wall-bounded separated flows: An application to engine-like geometries. Oil Gas Sci. Technol.-Rev. IFP Energies nouvelles **69**(1), 11–27 (2014). DOI 10.2516/ogst/2013143

[155] Poinsot, T., Veynante, D.: Theoretical and numerical combustion. RT Edwards Incorporated (2005)

[156] Pope, S.: The evolution of surfaces in turbulence. International Journal of Engineering Science **26**(5), 445–469 (1988). DOI 10.1016/0020-7225(88)90004-3

[157] Pope, S.B.: Turbulent Flows. Cambridge University Press (2000)

[158] Rakopoulos, C., Kosmadakis, G., Dimaratos, A., Pariotis, E.: Investigating the effect of crevice flow on internal combustion engines using a new simple crevice model implemented in a CFD code. Applied Energy **88**(1), 111–126 (2011). DOI 10.1016/j.apenergy.2010.07.012

[159] Reitz, R., Corcione, F., Valentino, G., et al.: Interpretation of k-ε computed turbulence length-scale predictions for engine flows. In: Symposium (International) on Combustion, vol. 26, pp. 2717–2723. Elsevier (1996). DOI 10.1016/S0082-0784(96)80108-1

[160] Richard, S., Colin, O., Vermorel, O., Benkenida, A., Angelberger, C., Veynante, D.: Towards large eddy simulation of combustion in spark ignition engines. Proceedings of the Combustion Institute **31**(2), 3059–3066 (2007). DOI 10.1016/j.proci.2006.07.086

[161] Richardson, L.F.: Weather prediction by numerical process cambridge university press. CambridgeRichardsonWeather prediction by numerical process1922 (1922)

[162] Robert, A., Richard, S., Colin, O., Martinez, L., De Francqueville, L.: LES prediction and analysis of knocking combustion in a spark ignition engine. Proceedings of the Combustion Institute **35**(3), 2941–2948 (2015). DOI 10.1016/j.proci.2014.05.154

[163] Robert, A., Richard, S., Colin, O., Poinsot, T.: LES study of deflagration to detonation mechanisms in a downsized spark ignition engine. Combustion and Flame **162**(7), 2788–2807 (2015). DOI 10.1016/j.combustflame.2015.04.010

[164] Rutland, C.: Large-eddy simulations for internal combustion engines–a review. International Journal of Engine Research (2011)

[165] Sagaut, P.: Large eddy simulation for incompressible flows: an introduction. Springer Science & Business Media (2006)

[166] Saika, T., Korematsu, K.: Flame propagation into the ring crevice of a spark ignition engine. Tech. rep., SAE Technical Paper (1986). DOI 10.4271/861528

[167] Schmitt, M., Frouzakis, C.E., Tomboulides, A.G., Wright, Y.M., Boulouchos, K.: Direct numerical simulation of the effect of compression on the flow, temperature and composition under engine-like conditions. Proceedings of the Combustion Institute **35**(3), 3069–3077 (2015). DOI 10.1016/j.proci.2014.06.097

[168] Schmitt, M., Frouzakis, C.E., Wright, Y.M., Tomboulides, A., Boulouchos, K.: Direct numerical simulation of the compression stroke under engine relevant conditions: Local wall heat flux distribution. International Journal of Heat and Mass Transfer **91**, 948–960 (2016). DOI 10.1016/j.ijheatmasstransfer.2015.08.031

[169] Schmitt, M., Frouzakis, C.E., Wright, Y.M., Tomboulides, A.G., Boulouchos, K.: Direct numerical simulation of the compression stroke under engine-relevant conditions: Evolution of the velocity and thermal boundary layers. International Journal of Heat and Mass Transfer **91**, 948–960 (2015). DOI 10.1016/j.ijheatmasstransfer.2015.08.031

[170] Schmitt, M., Frouzakis, C.E., Wright, Y.M., Tomboulides, A.G., Boulouchos, K.: Investigation of wall heat transfer and thermal stratification under engine-relevant conditions using DNS. International Journal of Engine Research **17**, 63–75 (2015). DOI 10.1177/1468087415588710

[171] Schmitt, M., Hu, R., Wright, Y.M., Soltic, P., Boulouchos, K.: Multiple Cycle LES Simulations of a Direct Injection Natural Gas Engine. Flow, Turbulence and Combustion **95**(4), 645–668 (2015). DOI 10.1007/s10494-015-9625-1

[172] Senecal, P., Richards, K., Pomraning, E., Yang, T., Dai, M., McDavid, R., Patterson, M., Hou, S., Shethaji, T.: A new parallel cut-cell Cartesian CFD code for rapid grid generation applied to in-cylinder diesel engine simulations. Tech. rep., SAE Technical Paper (2007). DOI 10.4271/2007-01-0159

[173] Sick, V., Reuss, D., Rutland, C., Haworth, D., Oefelein, J., Janicka, J., Kuo, T., Yang, X., Freitag, M.: A common engine platform for engine les development and validation. In: International Conference on Large-Eddy Simulation for Internal Combustion Engine Flows (LES4ICE), Rueil-Maimaison, France, November, pp. 18–19 (2010)

[174] Smagorinsky, J.: General circulation experiments with the primitive equations: I. the basic experiment*. Monthly weather review **91**(3), 99–164 (1963)

[175] Sone, K., Patel, N., Menon, S.: Large-eddy simulation of fuel-air mixing in an internal combustion engine. In: 39th Aerospace Sciences Meeting and Exhibit. DOI 10.2514/6.2001-635

[176] Sterlepper, J., Neußer, H.J., Ruhland, H.: HC-Emissions of SI Engines-Optical Investigation of Flame Propagations in Piston Top Land Crevice. Tech. rep., SAE Technical Paper (1994). DOI 10.4271/941994

[177] Stiehl, R., Bode, J., Schorr, J., Krüger, C., Dreizler, A., Böhm, B.: Influence of intake geometry variations on in-cylinder flow and flow-spray interactions in a stratified direct-injection spark-ignition engine captured by time-resolved particle image velocimetry. International Journal of Engine Research (2016). DOI 10.1177/1468087416633541

[178] Sutherland, W.: The viscosity of gases and molecular force. The London, Edinburgh, and Dublin Philosophical Magazine and Journal of Science **36**(223), 507–531 (1893)

[179] Sweby, P.K.: High resolution schemes using flux limiters for hyperbolic conservation laws. SIAM journal on numerical analysis **21**(5), 995–1011 (1984). DOI 10.1137/0721062

[180] Tabaczynski, R.J., Heywood, J.B., Keck, J.C.: Time-resolved measurements of Hydrocarbon mass flowrate in the exhaust of a spark-ignition engine. Tech. rep., SAE Technical Paper (1972). DOI 10.4271/720112

[181] Tan, S.M., Ng, H.K., Gan, S.: CFD modelling of soot entrainment via thermophoretic deposition and crevice flow in a diesel engine. Journal of Aerosol Science **66**, 83–95 (2013). DOI 10.1016/j.jaerosci.2013.08.007

[182] Tatschl, R., Bogensperger, M., Pavlovic, Z., Priesching, P., Schuemie, H., Vitek, O., Macek, J.: LES simulation of flame propagation in a direct-injection SI-engine to identify the causes of cycle-to-cycle combustion variations. Tech. rep., SAE Technical Paper (2013). DOI 10.4271/2013-01-1084

[183] Thobois, L., Lauvergne, R., Poinsot, T.: Using LES to investigate reacting flow physics in engine design process. Tech. rep., SAE Technical Paper (2007). DOI 10.4271/2007-01-0166

[184] Toda, H.B., Cabrit, O., Balarac, G., Bose, S., Lee, J., Choi, H., Nicoud, F.: A subgrid-scale model based on singular values for les in complex geometries. In: Proc. of the Summer Program, pp. 193–202 (2010)

[185] Todsen, U.: Verbrennungsmotoren. Carl Hanser Verlag GmbH Co KG (2012)

[186] Toledo, M.S., Le Penven, L., Buffat, M., Cadiou, A., Padilla, J.: Large eddy simulation of the generation and breakdown of a tumbling flow. International Journal of Heat and Fluid Flow **28**(1), 113–126 (2007). DOI 10.1016/j.ijheatfluidflow.2006.03.029

[187] Van Driest, E.R.: On turbulent flow near a wall. Journal of the Aeronautical Sciences (2012)

[188] Vermorel, O., Richard, S., Colin, O., Angelberger, C., Benkenida, A., Veynante, D.: Towards the understanding of cyclic variability in a spark ignited engine using multi-cycle LES. Combustion and Flame **156**(8), 1525–1541 (2009). DOI 10.1016/j.combustflame.2009.04.007

[189] Versteeg, H.K., Malalasekera, W.: An Introduction to Computational Fluid Dynamics. The Finite Volume Method. Pearson Education (2007)

[190] Verzicco, R., Mohd-Yusof, J., Orlandi, P., Haworth, D.: Large eddy simulation in complex geometric configurations using boundary body forces. AIAA journal **38**(3), 427–433 (2000). DOI 10.2514/2.1001

[191] Veynante, D., Vervisch, L.: Turbulent combustion modeling. Progress in energy and combustion science **28**(3), 193–266 (2002). DOI 10.1016/S0360-1285(01)00017-X

[192] Wadekar, S.: Large-eddy simulation of the ignition and turbulent premixed combustion in a spark ignition engine - using a transport equation for the flame surface density. Master Thesis, University Duisburg-Essen, 2015

[193] Weclas, M., Melling, A., Durst, F.: Flow separation in the inlet valve gap of piston engines. Progress in Energy and Combustion Science **24**(3), 165–195 (1998). DOI 10.1016/S0360-1285(97)00023-3

[194] Weller, H., Tabor, G., Gosman, A., Fureby, C.: Application of a flame-wrinkling LES combustion model to a turbulent mixing layer. In: Proc. Combust. Inst, vol. 27, pp. 899–907. Elsevier (1998). DOI 10.1016/S0082-0784(98)80487-6

[195] Weller, H.G., Tabor, G., Jasak, H., Fureby, C.: A tensorial approach to computational continuum mechanics using object-oriented techniques. Computers in physics **12**(6), 620–631 (1998)

[196] Wentworth, J.: Piston and ring variables affect exhaust hydrocarbon emissions. Tech. rep., SAE Technical Paper (1968). DOI 10.4271/680109

[197] Wentworth, J.: The piston crevice volume effect on exhaust hydrocarbon emission. Combustion Science and Technology **4**(1), 97–100 (1971). DOI 10.1080/00102207108952475

[198] Westbrook, C.K., Mizobuchi, Y., Poinsot, T.J., Smith, P.J., Warnatz, J.: Computational combustion. Proceedings of the Combustion Institute **30**(1), 125–157 (2005). DOI 10.1016/j.proci.2004.08.275

[199] Whitelaw, J., Yianneskis, M.: Turbulent flow measurements by laser-floppier anemometry in motored piston-cylinder assemblies. Journal of Fluids Engineering **101**, 208–216 (1979). DOI 10.1115/1.3448937

[200] Willcock, M., Tidmarsh, D., Foss, P.: The variation of hydrocarbon emissions from different piston designs in a spark ignition engine. Proceedings of the Institution of Mechanical Engineers, Part D: Journal of Automobile Engineering **210**(3), 235–242 (1996). DOI 10.1243/PIME_PROC_1996_210_267_02

[201] Williams, F.A.: Combustion theory, (1985). Cummings Publ. Co (1985)

[202] Woschni, G.: A universally applicable equation for the instantaneous heat transfer coefficient in the internal combustion engine. Tech. rep., SAE Technical paper (1967). DOI 10.4271/670931

[203] Wu, K.C., Hochgreb, S.: Numerical simulation of post-flame oxidation of hydrocarbons in spark ignition engines. Tech. rep., SAE Technical Paper (1997). DOI 10.4271/970886

[204] Yao, M., Zheng, Z., Liu, H.: Progress and recent trends in homogeneous charge compression ignition (HCCI) engines. Progress in Energy and Combustion Science **35**(5), 398–437 (2009). DOI 10.1016/j.pecs.2009.05.001

[205] Yoshida, M.: An effect of the top-land form of the piston on hydrocarbon emissions of a spark-ignition engine. Motortechnische Zeitschrift **41**, 93–95 (1980)

[206] Yoshizawa, A.: Statistical theory for compressible turbulent shear flows, with the application to subgrid modeling. Physics of Fluids **29**(7), 2152–2164. DOI 10.1063/1.865552

[207] Zhang, Y., Kung, E., Haworth, D.: A PDF method for multidimensional modeling of HCCI engine combustion: effects of turbulence/chemistry interactions on ignition timing and emissions. Proceedings of the Combustion Institute **30**(2), 2763–2771 (2005). DOI 10.1016/j.proci.2004.08.236

[208] Zhao, H.: HCCI and CAI engines for the automotive industry. Elsevier (2007)

[209] Zimont, V., Lipatnikov, A.: A numerical model of premixed turbulent combustion of gases. Chem. Phys. Rep **14**(7), 993–1025 (1995)

Curriculum Vitae

Der Lebenslauf ist in der Online-Version aus Gründen des Datenschutzes nicht enthalten.